PADERBORN
UNIVERSITY

WATER UNDER METAL-ORGANIC FRAMEWORK CONFINEMENT: SYSTEMATIC STUDIES OF THE WATER SORPTION BEHAVIOR AND WATER INTERACTIONS IN ONE-DIMENSIONAL PORES

PhD Thesis
approved for the attainment of the degree of
Doctor of Natural Science
(Dr. rer. nat.)
from the Faculty of Science of the University of Paderborn

submitted by
Marvin Kloß
born 17.08.1994 in Dortmund

Paderborn, November 4, 2024

The experimental investigations for this thesis were carried out between April 2020 to September 2024 in the working group of Prof. Dr. Michael Tiemann at Paderborn University, Paderborn, Germany.

Chair of the audit committee	Prof. Dr. Martin Brehm
First Reviewer	Prof. Dr. Michael Tiemann
Second Reviewer	Prof. Dr. Sebastian Henke
Member of the audit committee	PD Dr. Hans Egold

Submitted	November 4, 2024
Disputation	December 6, 2024

STATEMENT OF AUTHORSHIP

With this signature, I declare that I have completed this thesis independently and with all mentioned support and resources. The thesis has never been submitted to any examination authority in the same or similar form.

Paderborn, November 4, 2024

DANKSAGUNG

Mit der Abgabe meiner Promotionsarbeit nutze ich auch die Möglichkeit, mich bei denjenigen zu bedanken, ohne welche diese Dissertation in ihrer hier dargelegten Form nicht möglich gewesen wäre.

Zu aller erst möchte ich mich bei *Prof. Dr. Michael Tiemann* für die Chance bedanken, unter seiner Leitung promovieren zu dürfen. Dies beinhaltet die zahlreichen fruchtbaren Diskussionen mit dir, sowie deine Anmerkungen und Hilfestellungen zu meinen Arbeiten. Ebenso möchte ich dir für die Möglichkeit danken, unsere Arbeiten auf zahlreichen Konferenzen vorstellen zu können. Meine Zeit in Paderborn sowie die zahlreichen schönen Unternehmungen unserer Gruppe werde ich immer positiv in Erinnerung behalten.

Ebenso möchte ich mich bei *Prof. Dr. Sebastian Henke* für die Übernahme des Zweitgutachtens bedanken. Wir kennen uns schon seit vielen Jahren und es hat mich immer wieder gefreut, dich auf Konferenzen zu treffen. Ich weiß es sehr zu schätzen, dass du dir die Zeit genommen hast.

Weiterhin möchte ich mich bei den Mitgliedern der Prüfungskommission *Prof. Dr. Martin Brehm* und *PD Dr. Hans Egold* für Ihren Prüfungsbeisitz bedanken.

Als nächstes möchte ich mich bei *Dr. Christian Weinberger* für seine zahlreichen Hilfestellungen und Ratschläge bedanken. Durch dich konnte ich viel lernen und diverse Dinge aus einem neuen Blickwinkel betrachten. Ebenso bist du einer der Gründe, wieso ich mit dem Laufen begonnen habe und dabei geblieben bin.

Ein besonderer Dank gilt allen Mitgliedern unseres Arbeitskreises, die für unzählige schöne Momente und Diskussionen (nicht immer über die Arbeit) gesorgt haben. Nachfolgend noch ein paar Worte für jeden von euch:

Bei *Dominik Baier* möchte ich für seine Unterstützung bei zahlreichen Messungen bedanken. Auch wenn viele Versuche nicht von Erfolg gekrönt waren, so konnte ich doch einiges lernen und hatte Spaß daran, mit dir zu arbeiten. Denk immer dran: 13 mal 1 ist auch Null.

Liebe *Linda Kothe*, bei dir möchte ich mich insbesondere für unsere gemeinsamen Unternehmungen mit unseren RISE Studentinnen Sarah und Alex sowie deine Hilfe bei meinen LaTex Problemen bedanken. Melde dich, wenn du mal einen Wal wegschieben musst.

Ebenso bedanke ich mich bei *Tobias Wagner*. Es war schon einige Male beängstigend, wie gleich wir beide denken können. Doch fast immer gab es großes Gelächter (auch wenn wir nicht immer von den anderen verstanden wurden). Halt dein Fahrrad bereit, wir holen uns bald ein Happy-Meal.

Lieber *Zhenyu Zhao*, als du deine Bachelorarbeit bei mir begonnen hast, konnte ich dir noch einiges beibringen. Auch wenn wir am Anfang einige Kommunikationsprobleme hatten, haben wir alles gemeistert! Inzwischen konnte ich auch vieles von dir lernen und weiß deinen Rat sehr zu schätzen. Ich hoffe du bleibst die verschlafene Katze, die du bist.

Bei *Maria Beyer* möchte ich mich für Ihre Unterstützung und die gemeinsame Zeit bedanken. Auch wenn du noch nicht lange bei uns bist, ist schon klar, dass du super in unser Team passt. Für deine weitere Zeit wünsche ich dir alles Gute.

Weiterhin möchte ich *Lara Schäfers* für ihr Mitwirken an einigen Projekten im Rahmen ihrer Abschlussarbeiten und die entspannte Zeit danken. Ich weiß deine Mühen zu schätzen und wünsche dir für deinen weiteren Weg nur das Beste.

Liebe *Christiane Gloger*, dir gilt ein besonderer Dank als unser guter Engel der Chemie. Wann immer man dich braucht, auf dich ist Verlass. Beinahe immer sorgst du durch deine frohe Art dafür, dass auch jeder noch so verregnete Herbsttag ein guter wird.

Bei *Jannik Breda* möchte ich mich für seine Unterstützung im Labor sowie die unterhaltsamen Gespräche und die tolle Zeit, die wir miteinander verbringen konnten, bedanken. Auch *Andrea Harbarth* danke ich für ihren Einsatz und die vielen unkomplizierten Messungen meiner Proben. Danke auch der gesamten Zentralen Analytik unseres Departments für ihren Einsatz.

Auch unseren ehemaligen Arbeitskreismitgliedern *Josefin Klippstein*, *Dominik Rengel*, *Dr. Ali Javed* und *Bertram Schwind* möchte ich für die schöne Atmosphäre und tolle Gespräche danken.

Weiterhin danke ich *Michael Beerbaum*, *Dr. Frederik Zysk*, *Dr. Hossam Elgabarty* und *Prof. Dr. Thomas Kühne* für die erfolgreiche Kooperation, die wir gemeinsam aufbauen konnten. Besonders bedanken möchte ich mich bei dir *Michael*. Durch unsere enge Zusammenarbeit und den regen Austausch habe ich einiges lernen können und konnte mein Verständnis der theoretischen Chemie erweitern.

Die besten Mensafreund der Welt würde ich niemals vergessen. *André Platzek*, *Lars Janiak*, *Stefan Koop* und *Jonathan Wattenberg*, ich hoffe ihr wisst, wie viel ihr Jungs mir bedeutet. Über jeden einzelnen von euch könnte ich Seiten füllen, möchte mich hier aber kurz halten. Ich bin dankbar für jeden Moment, jede Reise, jedes Abenteuer mit euch und jeden Ratschlag von euch. Ich bin mir sicher, dass unsere Reise noch lange nicht vorbei ist und wir noch einiges gemeinsam erleben werden und darauf freue ich mich so richtig. Unser Zug rollt und niemand hält ihn auf. Danke, dass es euch vier gibt!

Abschließend möchte ich mich noch bei meiner Familie bedanken, die mich während dieser Arbeit motiviert und immer an mich geglaubt hat. Ein besonderer Dank gilt dabei meinen Eltern *Martin* und *Heike*, meinem Schwesterherz *Katharina* und meiner Stiefmutter *Ute*. Einfach Danke, dass ihr immer für mich da seid. ♡

Leb deinen Traum, denn er wird wahr
Gehe deinen Weg, stelle dich der Gefahr
Alles was wichtig ist
Wirst du erkennen, wenn die Zeit gekommen ist, ja
Greif nach den Sternen, du bist bereit
Glaub an dich, bald ist es so weit
Wir werden bei dir sein
Sei bereit!

Diese Arbeit widme ich meinen Eltern Martin und Heike,
meiner Schwester Katharina und meiner Stiefmutter Ute

11011969 – 25022008 = ♡

LIST OF PUBLICATIONS

Academic Publications

- M. Kloß, Z. Zhao, L. Schäfers, C. Weinberger, M. Tiemann, Water Sorption on Isoreticular CPO-27-type MOFs: From Discrete Sorption Sites to Water-Bridge-Mediated Pore Condensation *Nanomaterials*, **2024**, *14*, 1791.

- M. Kloß, C. Weinberger, M. Tiemann, Water in the Micropores of CPO-27 Metal-Organic Frameworks: A Comprehensive Study, *Microporous Mesoporous Mater.*, **2025**, *381*, 113352.

- M. Kloß, M. Beerbaum, D. Baier, C. Weinberger, F. Zysk, H. Elgabarty, T. Kühne, M. Tiemann, Understanding Hydration in CPO-27 Metal-Organic Frameworks: Strong Impact of the Chemical Nature of the Metal (Cu, Zn), *Adv. Mat. Interfaces*, **2024**, 2400476.

- R. Pallach, J. Keupp, K. Terlinden, L. Frentzel-Beyme, M. Kloß, A. Machalica, J. Kotschy, S. K. Vasa, P. A. Chater, C. Sternemann, M. T. Wharmby, R. Linser, R. Schmid, S. Henke, Frustrated flexibility in metal-organic frameworks, *Nat. Commun.*, **2021**, *12*, 4097.

- R. Giereth, A. K. Mengele, W. Frey, M. Kloß, A. Steffen, M. Karnahl, S. Tschierlei, Copper(I) Phosphinooxazoline Complexes: Impact of the Ligand Substitution and Steric Demand on the Electrochemical and Photophysical Properties, *Chem. Eur. J.*, **2020**, *26*, 2675-2684.

- L. Frentzel-Beyme, M. Kloß, P. Kolodzeiski, R. Pallach, S. Henke, Meltable Mixed-Linker Zeolitic Imidazolate Frameworks and Their Microporous Glasses: From Melting Point Engineering to Selective Hydrocarbon Sorption, *J. Am. Chem. Soc.*, **2019**, *141*, 12362-12371.

- L. Frentzel-Beyme, M. Kloß, R. Pallach, S. Salamon, H. Moldenhauer, J. Landers, H. Wende, J. Debus, S. Henke, Meltable Mixed-Linker Zeolitic Imidazolate Frameworks and Their Microporous Glasses: From Melting Point Engineering to Selective Hydrocarbon Sorption, *J. Mater. Chem. A*, **2019**, *141*, 985-990.

Oral Presentations

- M. Kloß, M. Beerbaum, D. Baier, F. Zysk, C. Weinberger, T. Kühne, M. Tiemann, *Metal Center-dictated Water Adsorption in CPO-27-M and its Effect on the Water Structure within the One-dimensional Channels*, 35th German Zeolite Conference, Jena (Germany), February 29, 2024.

Poster Presentations

- D. Baier, M. Huck, L. Kieke, S. Voth, M. Kloß, H.-G. Steinrück, M. Tiemann, Microporous Frameworks as Filter Layers for Selective Hydrogen Sensing, Sensor und Test, Congress Center Nuremberg, June 11-13, 2024.
- M. Kloß, D. Baier, C. Weinberger, M. Tiemann, Small Changes, Strong Impact: Adsorption of Water and Its Behavior inside the One-Dimensional Pores of CPO-27, 34th German Zeolite Conference, University of Vienna (Austria), September 21-23, 2023.
- M. Kloß, D. Baier, C. Weinberger, M. Tiemann, The Effect of the Metal Center on the Adsorption of Water in the CPO-27(M) Framework Series, 8th International MOF Conference, International Congress Center Dresden (Germany), September 4-7, 2022.

CONTENTS

LIST OF ABBREVIATIONS

CN	coordination number
CPO	coordination polymer of Oslo
DFT	density functional theory
DMF	*N,N*-dimethylformamide
DUT	Dresden University of Technology
DVS	dynamic vapour sorption
FTIR	Fourier transform infrared
FMOF	fluorinated MOF
IRMOF	isoreticular MOF
IUPAC	International Union of Pure and Applied Chemistry
MD	molecular dynamics
MIL	Matériaux de l'Institut Lavoisier
MOF	metal-organic framework
MCM	Mobil Composition of Matter
NMR	nuclear magnetic resonance
OMS	open metal site
PMO	periodic mesoporous organosilica
PXRD	powder X-ray diffraction
SBA	Santa Barbara Amorphous
SBU	secondary building unit
SSS	saturated salt slurries
TGA	thermogravimetric analysis

UiO	Universitetet i Oslo
ZIF	zeolitic imidazolate framework

ABSTRACT

Numerous studies revealed the potential of metal-organic frameworks (MOFs) with strong binding sites for sorption-based applications. To evaluate this, a fundamental understanding of their water sorption characteristics is mandatory, as water-adsorbent interactions play a key role.

This work gathers a comprehensive understanding about the hydration behavior of CPO-27-type frameworks. It is found that the incorporated metal center in CPO-27-*M* (*M* = Co, Cu, Mg, Mn, Ni, Zn) orchestrates the water uptake into the one-dimensional micropores, governed by coordination of the open metal site. CPO-27-Zn reveals a prototypical behavior, showing occupation of distinct positions in distinguishable sorption steps. Most other materials (*M* = Co, Mg, Mn, Ni) show severe differences, depending on the metal center. Contrary, water uptake in CPO-27-Cu proceeds entirely differently in one step without participation of the metal center. Additionally, the precise arrangement of water molecules, *i.e.*, their interactions with the host framework, affects the hydrolytic stability of CPO-27-*M*.

Further, the hydration behavior of CPO-27-type frameworks is altered by their pore size and incorporated defect sites. More defect sites alter the adsorption mechanism of CPO-27-Ni. Increasing pore size results in enthalpy-driven hydration without water-pore wall interactions, showing classical pore condensation, initiated by the formation of water bridges between water molecules coordinating to the metal center.

KURZFASSUNG

Das Potenzial von metall-organischen Gerüstverbindungen (kurz MOFs) mit attraktiven Bindungsstellen für sorptionsbasierte Anwendungen wurde in zahlreichen Studien nachgewiesen. Zur Beurteilung ebendieser Netzwerke ist eine detaillierte Kenntnis ihrer Wassersorptionseigenschaften nötig, da vorhandene Wasser-MOF Wechselwirkungen eine Schlüsselrolle spielen.

In dieser Arbeit wird ein umfassendes Verständnis des Hydratationsverhaltens von CPO-27-artigen Netzwerken gewonnen. Es zeigt sich, dass das in CPO-27-*M* (*M* = Co, Cu, Mg, Mn, Ni, Zn) enthaltene Metallzentrum die Wasseraufnahme in den eindimensionalen Mikroporen steuert, welche durch die Besetzung der offenen Koordinationsstelle am Metall eingeleitet wird. CPO-27-Zn zeigt ein einzigartiges Verhalten unter der Besetzung verschiedener Positionen in klar definierten Sorptionsschritten. Die meisten anderen Materialien (*M* = Co, Mg, Mn, Ni) zeigen Unterschiede in Abhängigkeit vom Metallzentrum. Im Gegensatz dazu zeigt CPO-27-Cu eine Porenkondensation von Wasser ohne Beteiligung des Metallzentrums. Zusätzlich beeinflusst die Struktur adsorbierter Wassermoleküle, insbesondere ihre Wechselwirkungen mit dem MOF, die hydrolytische Stabilität von CPO-27-*M* entscheidend.

Darüber hinaus wird das Hydratationsverhalten von CPO-27-artigen MOFs durch die Porengröße und durch eingebaute Defekte verändert. Eine Vielzahl an Defektstellen beeinflusst den Adsorptionsmechanismus von CPO-27-Ni. Mit zunehmender Porengröße erfolgt eine enthalpiegesteuerte Hydratation ohne Wasser-Porenwand-Wechselwirkungen, was in einer Porenkondensation resultiert, welche durch die Bildung von Wasserbrücken zwischen Wassermolekülen, die an das Metallzentrum koordinieren, initiiert wird.

CHAPTER 1

INTRODUCTION

1.1 Metal-organic Frameworks

Metal-organic frameworks (briefly MOFs) are inorganic-organic hybrid materials that gathered severe research interest over the past decades. These compounds are formed through a self-assembling reaction mechanism of inorganic building blocks (*e.g.*, metal cations, metal-(oxo)-clusters) and organic, multitopic linker molecules. Coordination of these linkers to the inorganic units results in crystalline, two- or three-dimensional frameworks, characterized by permanent accessible porosity (Figure 1.1).[1]

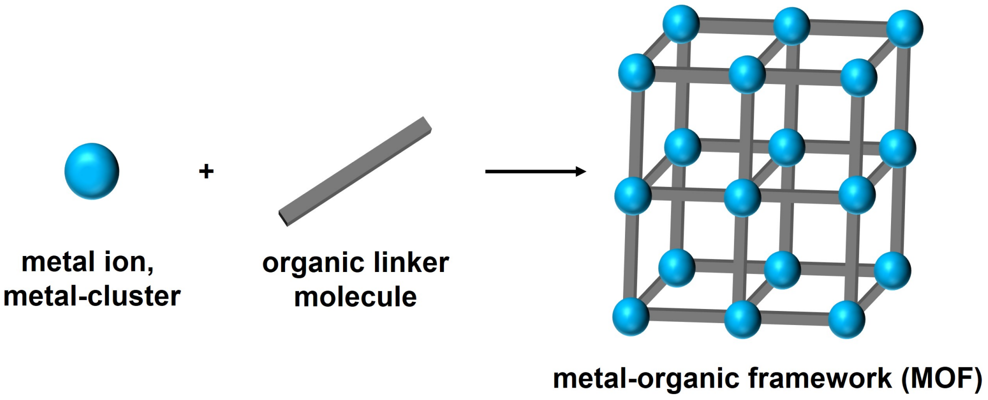

Figure 1.1: Schematic illustration of MOFs built by a self-assembling reaction mechanism of inorganic (metal ions or -clusters) and organic (linker molecules) building units.

The large surface areas and pore volumes along with diverse structure and, in some cases, high thermal stability make these hybrid materials particularly interesting for many applications.[2–4] This includes the separation of gases,[5,6] gas storage,[5,6] catalysis[7–9] or water harvesting.[10,11]

1.1.1 Structure and Properties of CPO-27

One prominent and heavily studied example for these porous hybrid materials is CPO-27[12] (CPO = coordination polymer of Oslo), which is also known by its synonym MOF-74.[13] It is well established due to its vast variety of usable bivalent metal centers (M^{2+}), including M = Cd,[14,15] Co,[12] Cu,[16] Fe,[17,18] Mg,[19] Mn,[20] Ni,[21] and Zn.[13] The inorganic building unit adopts a rod-like alignment formed by corner-sharing octahedra of six-fold coordinated metal ions (*i.e.*, MO_6) in a helical arrangement (Figure 1.2).

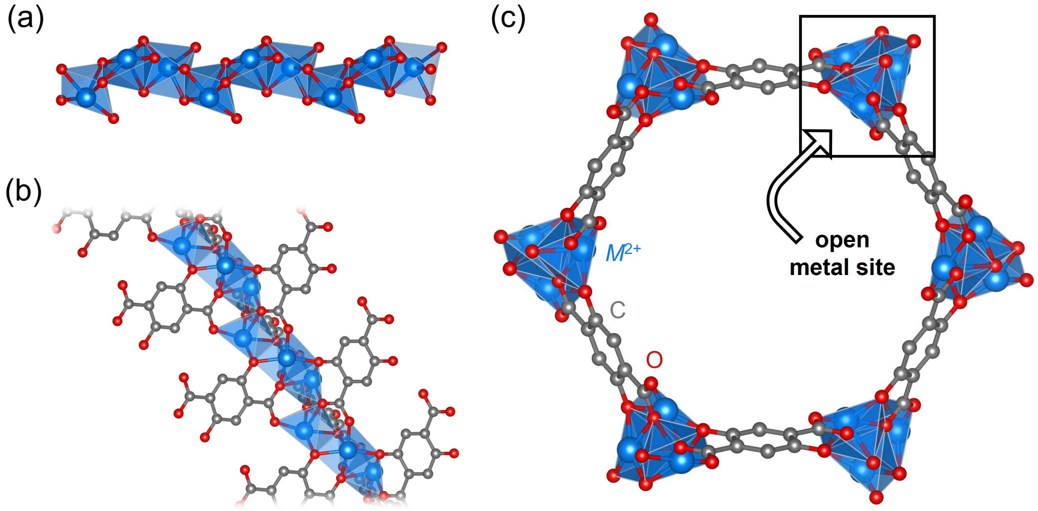

Figure 1.2: Representation of the (a) rod-like inorganic building unit of desolvated CPO-27-*M*. (b) Connectivity within the rod-like unit, showing multiple coordinative bonds of the $dhtp^{4-}$ linker molecule toward different metal centers. (c) Illustration of the one-dimensional channels along the crystallographic *c*-axis, highlighting undercoordinated metal centers, *i.e.*, open metal sites.

These metal octahedra are formed by coordination of three carboxylate oxygen atoms and two phenolate groups, both provided by the 2,5-dihydroxyterephthalate ($dhtp^{4-}$ or $dobdc^{4-}$) linker molecules and one coordinating solvent molecule (usually *N,N*-dimethylformamide (DMF) or water, stemming from the reaction solution) to saturate the coordination sphere. The thus-formed framework possess a honeycomb-like cross-section, exhibiting cylindrical, one-dimensional, *i.e.*, individual micropores that are parallel to each other.

Post-synthetic removal of the coordinating solvent molecules by different methods such as thermal activation or solvent exchange procedures generates an open metal site (OMS),[22] *i.e.*, under-coordinated metal cations, directed toward the pore space. These highly attractive sites are accessible for a variety of different guest molecules (including H_2O and CO_2).

The framework can be further modified by incorporation of multiple metal cations[23,24] to obtain mixed-metal MOFs, or by the selective introduction of structural defects with (partial) use of linker molecules with a lower topotacticity,[25–28] *i.e.*, missing carboxylate and/or phenolate coordinating groups. This gives rise to materials with tailor-made properties such as thermal stability, stability against water, and reactivities.

1.1.2 Properties of CPO-27 and Its Interactions with Small Molecules

The easy accessibility of generated OMS makes CPO-27-*M* an interesting material in terms of sorption-based applications. MATZGER *et al.* analyzed the CO_2 uptake of a series of CPO-27-*M* (*M* = Co, Mg, Ni, Zn) frameworks, depending on the exposure toward humidity.[29] They first analyzed the effect of different relative humidities on the uptake of CPO-27-Mg and found that even exposure to low relative humidities resulted in a significant loss of the CO_2 uptake after thermal regeneration (150°C, under a dry Argon stream). Afterward, the performance of all frameworks was analyzed at 70% relative humidity (Figure 1.3), suggesting that the hydrolytic stability of these frameworks decreases as follows: Co > Ni > Mg > Zn. Powder X-ray diffraction (PXRD) experiments revealed that the crystallinity of all compounds is indeed maintained, although peak broadening is visible in some cases. Finally, CPO-27-Co was subjected to multiple humidity/regeneration cycles, showing a complete loss of the CO_2 uptake after 20 cycles.

Further studies comparing the hydrolytic stability of CPO-27-Mg and CPO-27-Ni suggested a higher stability of the nickel-based framework.[30] The authors attributed this to the generally higher stability of divalent metal oxides with increasing electronegativity of the M^{2+} center, since the rod-like inorganic units are dominated

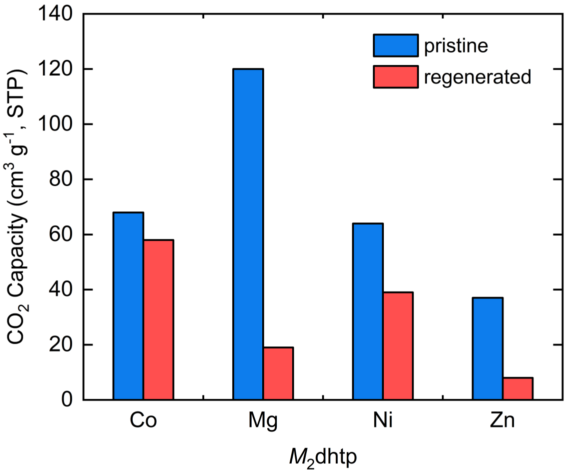

Figure 1.3: Comparison of CO_2 capacities of pristine and regenerated samples of CPO-27-*M* after exposure to 70% relative humidity.[29]

by *M*-O bonding. Consequently, framework decomposition is thermodynamically driven and not solely dictated by kinetics. These observations are further supported by the high water adsorption/desorption cyclability of CPO-27-Ni.[31] (A more detailed view on the water adsorption/desorption behavior of CPO-27-*M* is given in Section 1.2.5.)

Later, a more detailed approach was applied on CPO-27-Mg.[32] The effect of the humidity and temperature on the framework characteristics was studied. Results indicate lower thermal stabilities for aged samples as well as a nearly complete loss of porosity. Further, PXRD experiments confirmed lower crystallinity of aged compounds, shown by severely decreased intensity of the [110] reflection, which generally reflects the ordering of the cylindrical micropores. These changes became apparent after only one day, remaining mainly unchanged for longer aging times. Since Fourier transform infrared (FTIR) spectroscopy revealed no changes in the carboxylate region, the authors suggested a decomposition mechanism initiated by coordination of water molecules to the open metal site, facilitating water clustering (Figure 1.4a). In combination with the high bonding degree of the Mg^{2+} center, *i.e.*, bond orders of 1 to 1.5, distortion of the inorganic unit is initiated, eventually resulting in cleavage of the axial Mg-O bonds. As a consequence of the broken bonds between adjacent one-dimensional pores, individual channels tilt against each other and (partially) block their respective pore openings, leading to a complete loss of accessible porosity. However, molecular dynamics (MD) simulations on CPO-27-Zn suggested a different mechanism, characterized by dissociation of water into H^+ and

OH^- ions, influenced by the Lewis acidic M^{2+}center (Figure 1.4b).[33] Thus, formed ions result in the formation of metal hydroxides and protonated linker molecules, leading to a complete collapse of the porous framework.

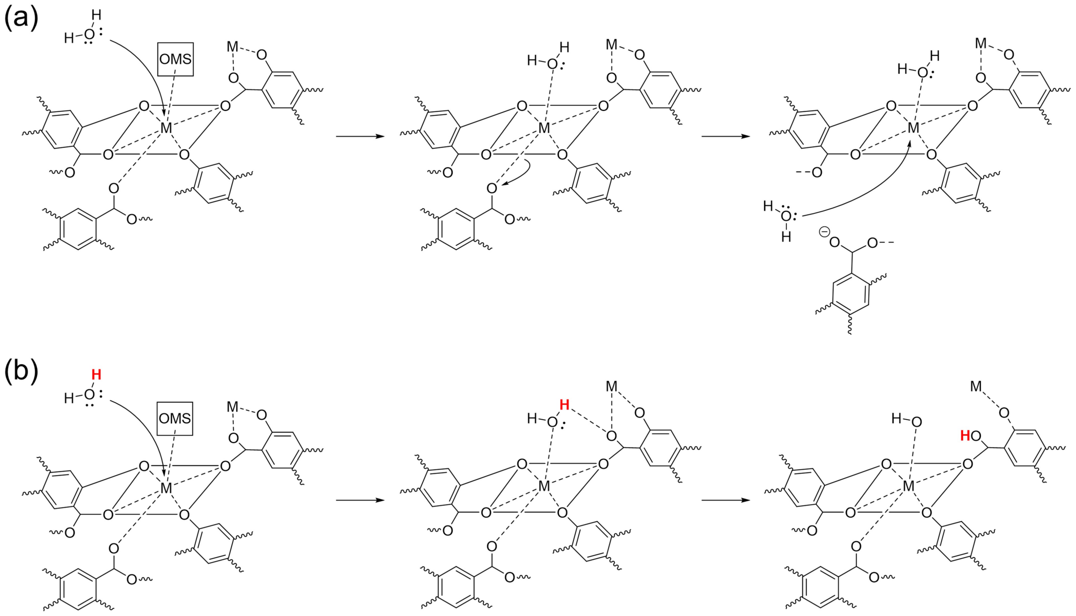

Figure 1.4: Proposed decomposition mechanisms for (a) CPO-27-Mg,[32] based on the dissociation of the axial M-O_{dhtp} bond, resulting in rotation of individual pores against each other. (b) Suggested decomposition mechanism of CPO-27-Zn,[33] involving the protonation of the linker molecules, resulting in a complete loss of crystallinity. Only relevant atoms and bonds are displayed. Waved bonds indicate the extended structure of the framework.

However, approaches emerged in order to overcome the lack of hydrolytic stability. One of these is the use of multiple metal centers during the framework synthesis.[34,35] Studies highlighted that even incorporation of small amounts of Cu^{2+} or Ni^{2+} into the CPO-27-Mg structure resulted in significantly higher stabilities in aqueous solution.

Further computational studies analyzed the behavior of small guest molecules in CPO-27-M. Application of density functional theory (DFT) to CPO-27-M focused on the adsorption energies and preferred adsorption sites of small molecules (*e.g.*, CO_2,[36,37] N_2,[36,37] and H_2[36,38]). While most metal centers revealed a rather similar behavior, CPO-27-Cu offered distinct differences. In this particular case, a lower positive charge of the Cu^{2+} centers resulted in structural changes of the framework with one oxygen atom of the inorganic units blocking the metal center and further acting as an adsorption site for H_2 *via* H-bonding.[39]

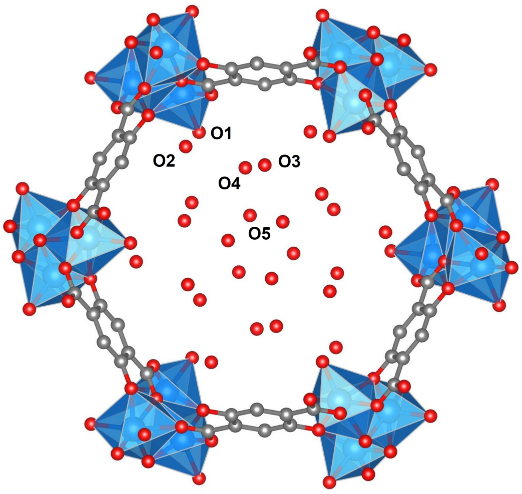

Figure 1.5: Representation of the crystal structure of hydrated CPO-27-*M*, showing the five crystallographically independent water positions, indicated by their respective oxygen atoms (O1 – O5).[40,41]

Considering water as a potential guest molecule, DIETZEL *et al.*[40,41] studied the dehydration behavior of CPO-27-*M* (*M* = Co, Cu, Mg, Mn, Ni, Zn) and found five crystallographically defined water molecules per M^{2+}center in fully hydrated frameworks. They categorized these five molecules in three distinguishable groups, with respect to their strength of interaction with the host material and with adjacent water molecules (Figure 1.5): (i) One water molecule binds to the OMS *via* a coordinative bond, possessing the strongest adsorption strength (*i.e.*, chemisorption, O1). (ii) Next, two more water molecules (O2, O3) form strong H-bonds with the coordinating water molecule, revealing weaker adsorption strengths. (iii) Lastly, the remaining two water molecules (O4, O5) solely interact with the last-mentioned two water molecules by H-bonding. Hence, these are more loosely bonded and show the weakest adsorption strength. Considering this, the chemical formula of completely hydrated CPO-27-*M* is $[M_2(\text{dhtp})(\text{H}_2\text{O})_2] \cdot 8\ \text{H}_2\text{O}$, indicating that two water molecules (one per M^{2+}) strongly bind to the metal center and are therefore a crucial part of the coordination environment, while eight additional molecules (four per M^{2+}) are considered as crystal water molecules within the microporous framework pores.

1.1.3 Reticular Synthesis

One of the most important concepts in describing MOF chemistry is the concept of reticular synthesis,[42,43] established by YAGHI. Within certain boundaries, it enables to pre-determine the structure of these frameworks by selection of its building blocks. This concept provides a simplification of the often complex structures found in MOFs[44–48] by viewing these as simplified geometric objects. These building blocks are called secondary building units (SBUs) and refer back to the respective geometry and connectivity of the inorganic and organic moieties based on extension points (*e.g.*, carboxylate carbon atoms, see Figure 1.6). Assuming that these units are rigid, they can be viewed as interchangeable. Consideration of the structure and connectivity of the underlying periodic net, *i.e.*, the network topology,[49,50] then allows a clarified view of the structure of these porous compounds in terms of connectivity and periodic alignment of individual SBUs. This facilitates synthesis by design with precise fine-tuning of the framework properties, generating isoreticular frameworks (*i.e.*, frameworks that adopt the same topology). These opportunities include the introduction of new functionalities,[51–56] the modification of the pore size,[10,51,57] and the use of different metal cations[58] during MOF synthesis.

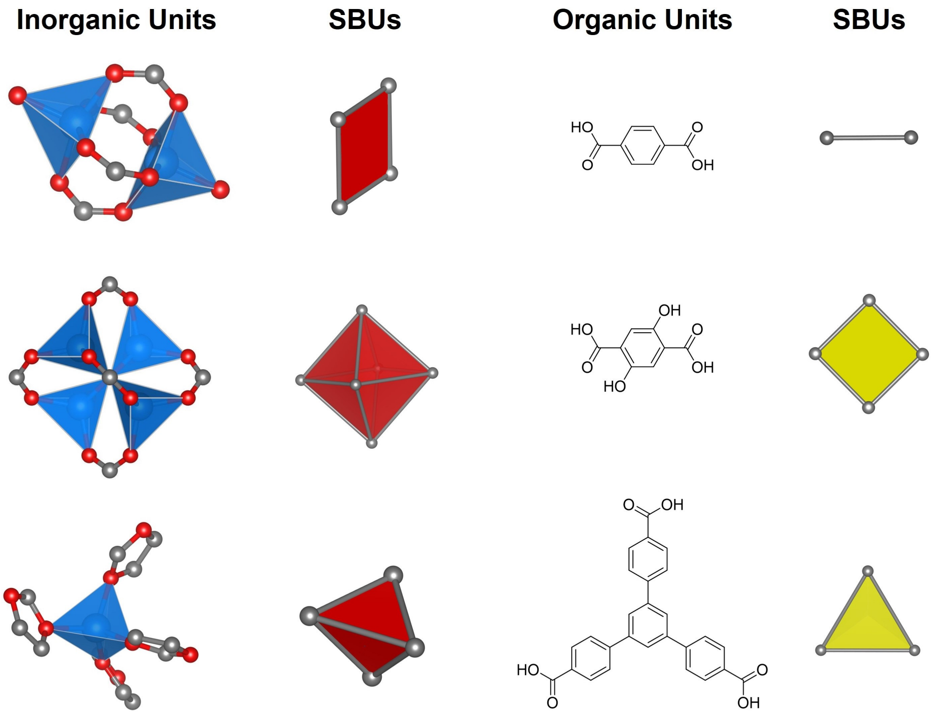

Figure 1.6: Representation of typical inorganic and organic building units found in MOFs and their simplified interpretation as secondary building units (SBUs).[42]

A well known material to highlight the applicability of this concept is the previously discussed CPO-27 (or MOF-74). Substitution of the organic SBU, *i.e.*, of the linker molecules (Figure 1.7a), results in isoreticular frameworks, so-called IRMOFs-74, with different pore sizes and functionalities such as found for M_2dondc[59] (dondc = 1,5-dihydroxynaphthalene-2,6-dicarboxylate), M_2bpp[15,57,60–63] (bpp = 3,3'-dihydroxy-[1,1'-biphenyl]-4,4'-dicarboxylate) and M_2tpp[15,57,61,62] (tpp = 3,3"-dihydroxy-2',5'-dimethyl-[1,1':4',1"-terphenyl]-4,4"-dicarboxylate). In addition, modification of the linker substitution pattern (*i.e.*, from para- toward meta-arrangement of carboxylate groups), results in the formation of frameworks with curved, »banana-like« pore walls (Figure 1.7b), as demonstrated in M_2dhip[64] (dhip = 4,6-dihydroxy-isophthalate) and M_2bpm[62,65,66] (bpm = 4,4'-dihydroxy[1,1'-biphenyl]-3,3'-dicarboxylate). These pore engineering possibilities enable to selectively tune the frameworks surface area from 1100 ... 2400 cm^3 g^{-1} as well as their respective pore diameters, within the range from 10 to 23 Å, and beyond.

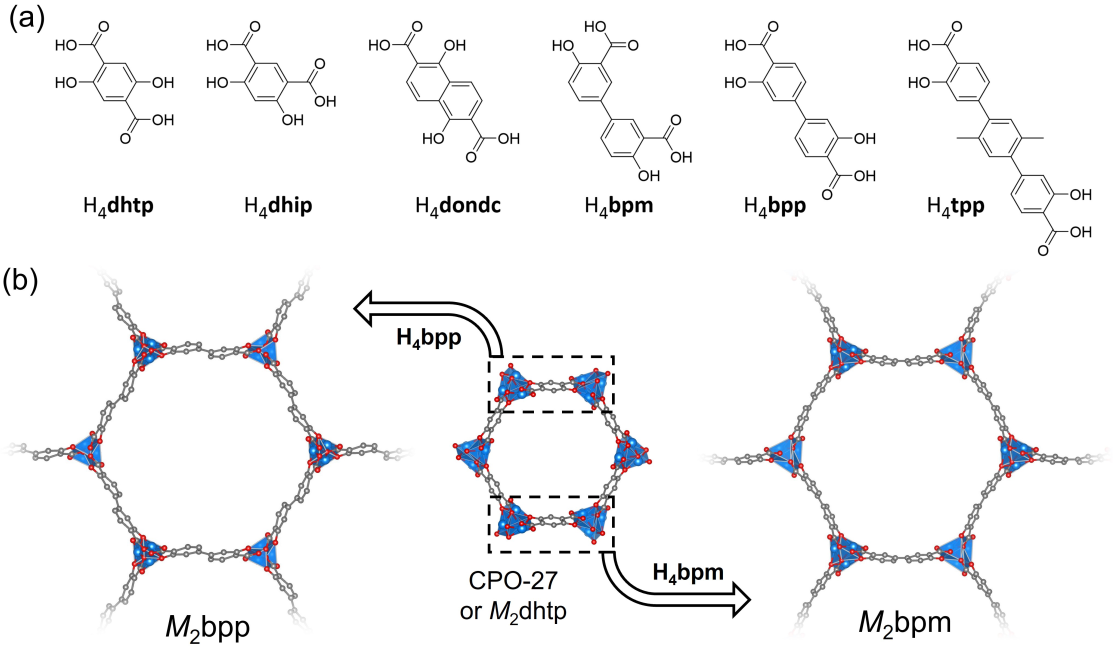

Figure 1.7: (a) Examples of linker molecules known to generate CPO-27-type framework structures. (b) Illustration of the curved, »banana-like« pore walls found in M_2bpm in comparison with M_2bpp, enforced by the different arrangement of functional groups.

1.2 Water Sorption of Porous Materials

Porous materials are often used for sorption-based applications, since they offer benefits such as high surface to volume ratios, high surface areas coupled with large porosity and often highly-ordered, uniform pores.[67] Independently from the desired application, the adsorption of water is an important process to understand.[68–71] This is due to the interaction of water molecules, *i.e.*, the adsorptive, with the solid interface, *i.e.*, the adsorbent, in particular on the internal surface of porous materials (Figure 1.8).

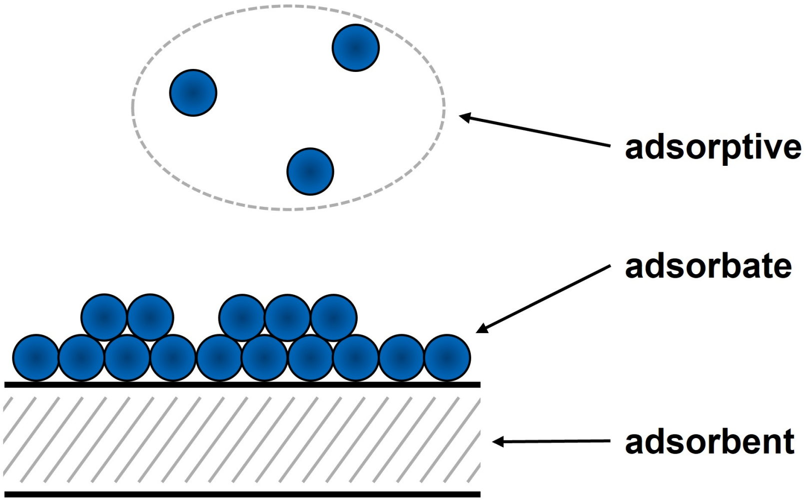

Figure 1.8: Schematic representation of the molecular adsorption process of molecules from the gas phase onto a solid interface.

On the one side, a large variety of applications for porous materials are based on the preferential uptake of water, *i.e.*, strong water-adsorbent interactions. Examples for these are proton conduction,[72–74] humidity sensing,[69,75] water harvesting[11,76,77] or adsorption-driven heat pumps.[78,79] On the other side, numerous other applications like the detection of gases (except for water),[69,75,80,81] gas capturing and storage,[82–84] gas separation[85–87] or catalysis[7,88–90] typically aim for the absence of water as it is a disruptive factor. This is a consequence of water competing with the desired target molecules for attractive sorption sites, influencing selectivity. Additionally, water may negatively affect the materials' stability. Hence, a comprehensive understanding of the water sorption behavior is necessary to evaluate potential candidates for industrial applications by detecting possible drawbacks and benefits. For example, water sorption analysis can provide valuable insight into the stability of a material by analyzing its durability[91–93] under concrete water concentrations, *i.e.*, a given relative humidity, providing information on the long-term applicability of the material. In addition, this method allows to classify the polarity of the pore environment. This ultimately enables researchers to pre-select the most promising candidates for a desired application, making water sorption analysis a mandatory characterization method.

To monitor the water sorption properties of porous materials, many techniques have been used in the past, all possessing advantages and drawbacks with respect to other methods. One of the first applied techniques is the standard gravimetric method that uses saturated salt slurries (SSS), enabling the measurement of equilibrium water sorption isotherms.[94] Therefore, SSS are prepared to generate well-known relative humidities in closed sample chambers, enabling simultaneous measurement of various samples. However, since any given salt yields only one specific humidity value at a given temperature, multiple salt solutions are required to obtain complete isotherms. Additionally, large sample amounts are needed to accurately measure the water uptakes with sufficient precision. This results in time-consuming measurements, *i.e.*, extended equilibrium times (days to weeks), with intensive laboratory use and difficulties in reproducibility.[95–98]

In order to overcome these limitations, more advanced gravimetric methods were developed. The most explored method is the dynamic vapour sorption (DVS) apparatus,[97] using a series of desired humidity values. In order to proceed with the measurement, the sample has to reach a mass equilibrium, which is measured by a highly sensitive, digital microbalance. As a result, automatic and time-effective (days to weeks) measurements are possible that yield accurate and reliable water sorption isotherms using reasonable sample amounts. However, a severe drawback of this method is the lack of resolution in the low pressure range, *i.e.*, under low water concentrations, due to the used humidity sensors.[99]

Lastly, manometric methods are more frequently used to generate water sorption data for various different porous compounds.[100–104] This approach provides data with comparable accuracy as aforementioned gravimetric methods, but offers reasonably faster measurement times. In addition, this approach has proven to be a powerful tool to provide high accuracy for very low amounts of water, as needed for a detailed characterization of nano- and microporous materials.

1.2.1 Water Sorption Isotherms

Independently from the used method, the adsorption of water proceeds *via* different mechanisms that depend on multiple factors, including the pore size (micropores, mesopores, macropores), the shape of individual pores, their connectivity (cages, channels) and the polarity of the pore surface, *i.e.*, hydrophilicity/hydrophobicity of the adsorbent. All of these material properties affect the interplay between the adsorbate-adsorbate (here: water-water) and adsorbate-adsorbent (water-interface) interactions, resulting in differently shaped sorption isotherms. These different types are classified into seven distinguishable isotherm shapes by the International Union of Pure and Applied Chemistry (IUPAC), referring to the polarity, *i.e.*, surface hydrophilicity/hydrophobicity, of the adsorbent (see Figure 1.9).[105] As water isotherms for hydrolytically stable porous compounds differ drastically from those found for other gases, the respective isotherm shapes found in water sorption measurements do not allow to determine the kind of porosity in any given samples, as it is possible by nitrogen sorption measurements.[106]

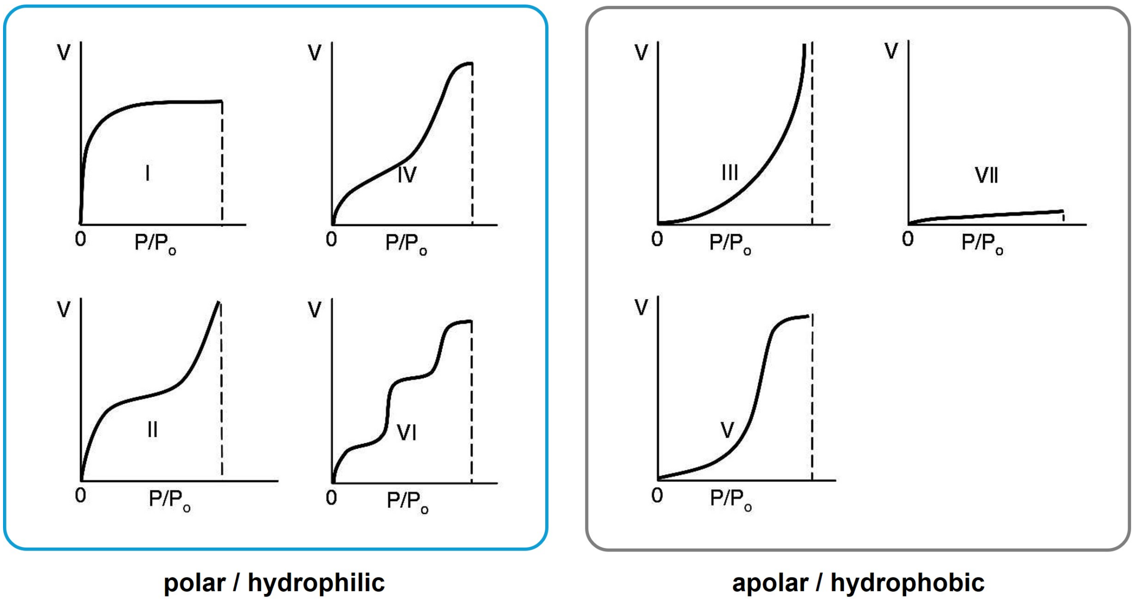

Figure 1.9: Different types of water adsorption isotherms classified according to IUPAC with respect to the hydrophilicity/hydrophobicity of the material surface. (Type I - very hydrophilic; type II and IV - hydrophilic; type III and V - hydrophobic/low hydrophilic with weak water-adsorbent interactions; type VI - hydrophilic with multiple water-adsorbent interactions and a step-wise adsorption process; type VII - very hydrophobic.) Figure reprinted with permission from reference [105].

In general, the different shapes of water vapor sorption isotherms reflect the complex interplay between the structural and functional properties. Different isotherm shapes refer to hydrophilic materials (types I, II, IV and VI), which are characterized by selective water adsorption at low relative water pressures p/p_0, and hydrophobic materials (types III, V and VII). The maximum water uptake in the type I isotherm is obtained at very low water vapor pressures, indicating highly attractive water-adsorbent interactions (*i.e.*, hydrophilic interface). Compared to the type I isotherm, type II and IV isotherms show lower slopes at low relative pressures, indicating a less hydrophilic character. Hydrophilic materials offering multiple attractive adsorbent-water interactions (or differently sized pores) typically show a type VI isotherm with step-wise water adsorption. Moderately hydrophobic materials reveal a type III isotherm with very low uptakes at low p/p_0, drastically increasing with pressure. The characteristic S-shape of the type V isotherm possesses similar features in the low pressure range as a type III isotherm, presenting weak adsorbent-water interactions, as found in hydrophobic or low hydrophilic adsorbents. With increasing pressure, a stable plateau is reached after a distinct sorption step, indicating the condensation of water in the pores. Lastly, strongly hydrophobic materials show a type VII isotherm with a nearly linear water uptake until saturation.[105]

To compare the relative hydrophilicity (or polarity) of different materials, the steepness of the water vapor adsorption isotherm at low relative pressure is of severe importance. Therefore, the inflection point α of water sorption steps is determined.[43] Its position is defined as the point at which half of the maximum absorption, *i.e.*, 50% uptake during this step, is reached. Knowing the respective isotherm shapes and the inflection point α for porous materials allows to evaluate their utility for water-sorption-related applications, which require specific material properties. For instance, highly hydrophilic materials that adsorb water at very low vapor pressures ($\alpha < 0.05$) are particularly useful as desiccants, while materials that reveal a steep uptake in the medium pressure range ($0.1 < \alpha < 0.5$) are great candidates for desalination of water, heat transformation or atmospheric water harvesting.[107]

1.2.2 Porous Carbons

Porous carbons are a class of materials that has been comprehensively studied in water sorption experiments as a consequence of their high availability. They offer a highly non-polar (hydrophobic) surface structure, which typically results in low water uptakes at low relative pressures $p/p_0 < 0.3$. With increasing vapor pressure, they reveal a steep uptake, depending on the pore geometry and functional group density (*e.g.*, N- or O-atoms) on the surface (Figure 1.10).[108] As soon as their pores are wide enough, *i.e.*, greater than 5 Å, porous carbons additionally reveal a hysteresis loop with its onset and shape also depending on the pore diameter.[109,110]

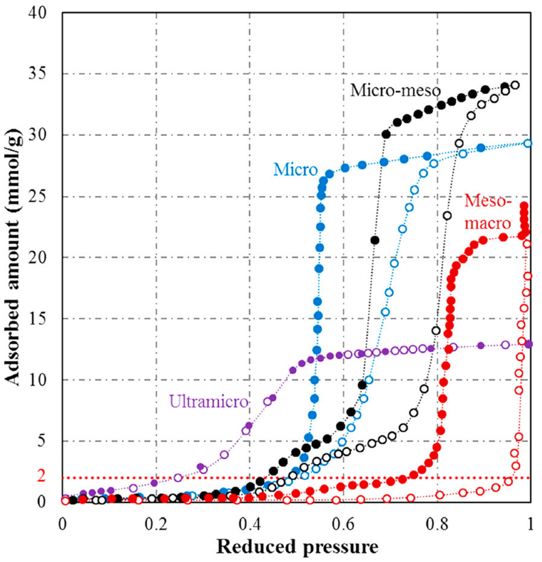

Figure 1.10: Schematic representation of water sorption isotherms of ordered, porous carbons with different pore sizes. Figure reprinted with permission from reference [108].

As a result, most porous carbons reveal a type V adsorption isotherm (*i.e.*, S-shaped).[108] Typically, the adsorption mechanism proceeds as follows: Adsorption of water molecules to functional groups (*e.g.*, N- or O-atoms) is followed by binding of additional molecules *via* hydrogen bonds to previously adsorbed ones. This provides formation of discrete water clusters. Next, the pores are filled by pore-condensation, which eventually results in a stable plateau after complete saturation.[111,112] As their pore size increases to the mesopore range, their previously described characteristics remain similar, additionally showing significantly larger hysteresis loops and water uptakes.[112,113] These hysteresis loops are also affected by the measurement temperature. An increase in temperature results in a shift of the desorption branch toward higher p/p_0, while the adsorption branch remains unchanged. This is a consequence of the differences in the adsorption and desorption mechanism, with the former being governed by the temperature-independent pore-condensation, solely affected by water-water and water-surface interactions, while the latter is described by a temperature-dependent evaporation of adsorbed water molecules.[108,114]

However, different circumstances are found as soon as the surface of the materials is drastically altered. Introduction of polar (hydrophilic) functional groups (*e.g.*, O or N containing ones) provides attractive nucleation sites for water cluster formation *via* hydrogen bonds, being a result of more favorable water-surface interactions. This forces the formation of hydration layers along the pore walls and eventually results in capillary condensation at lower p/p_0 when compared to non-functionalized carbons.[115,116] Hence, different water sorption isotherm shapes might be observed, with their precise characteristics determined by type and density of surface functional groups.

1.2.3 Porous Silica-based Compounds

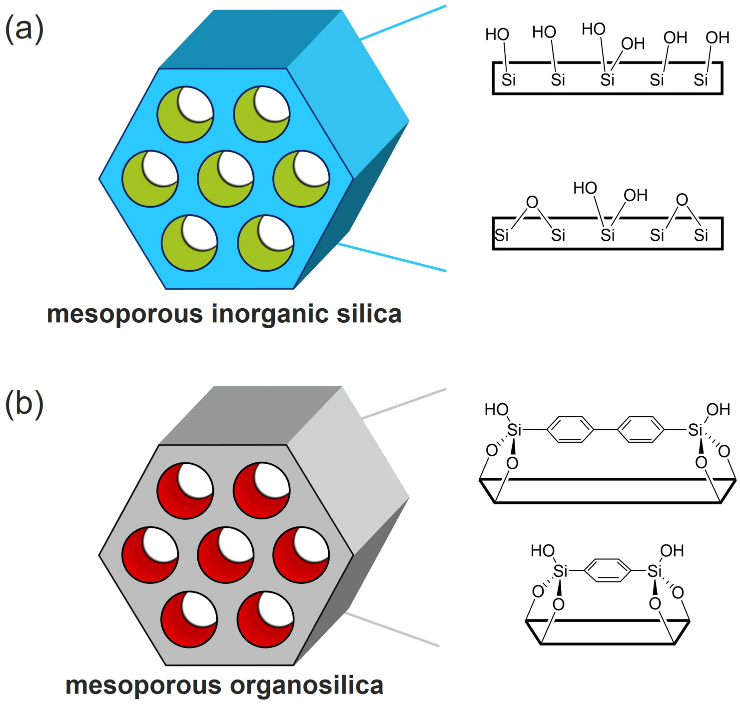

Figure 1.11: (a) Mesoporous inorganic silica with variable surface silanol concentrations, achieved *via* thermal treatment, and (b) mesoporous organosilica, with different incorporated organic moieties.[117]

If highly polar adsorbents are needed for water adsorption, either zeolites or mesoporous silica are the preferred choice. However, the high activation temperatures and limited pore space of zeolites is a significant drawback in some applications.[118] Contrary, mesoporous silica offer milder regeneration conditions, high water sorption capacities along with tuneable pore size,[119] pore structure[120] and surface polarity.[121]

The pore surface polarity can be altered by different methods such as thermal treatment to remove surface-bonded silanol groups, *i.e.*, dehydroxylation,[122] or by functionalization (during or post synthetic)[121,123] of the pore walls (Figure 1.11). Another method is the use of organically functionalized building blocks instead of regular silica sources, leading to the formation of organosilica hybrid materials, also referred to as periodic mesoporous organosilicas (PMOs), that offer cylindrical pores with organic moieties as an intrinsic part of (crystalline) pore walls.[124,125] Generally speaking, mesoporous silica often reveal type V water sorption isotherms with pronounced hysteresis and capillary condensation, both dependent on the pore size, thus behaving similarly as the above-described porous carbons.[126]

1.2.4 Metal-Organic Frameworks

While the water sorption behavior of many porous materials such as porous carbons or porous silica has been investigated for decades, MOFs initially gathered little interest, as early research focused on the discovery of novel structures. This changed as the research interest shifted toward potential applications.[11,77,127] Contrary to the previously discussed materials, MOFs show no uniform sorption behavior, which stems from the large range of polarities enforced by the different SBUs.[42,43] This results in various isotherm shapes, differing in concrete shape, *i.e.*, onset of water uptake, steepness, hysteresis and inflection point. However, as discussed in Chapter 1.1.2, some structures lack sufficient water stability due to the dynamic nature of the assembled coordinative bonds.[128] Nevertheless, their tuneable properties (see Section 1.1.3) offer enormous potential for MOFs in industrial applications, making them interesting research objects.

One example for this is the mesoporous MIL-101-Cr[131] (MIL = Matériaux de l'Institut Lavoisier), a well-studied mesoporous terephthalate-based (bdc^{2-}) MOF. When activated, it offers vacant Cr^{3+} sites and two differently sized cages of 29 and 34 Å diameter (Figure 1.12a). Researchers analyzed the effect of functional groups on the water sorption behavior of this framework (Figure 1.12b-c).[130] The pristine

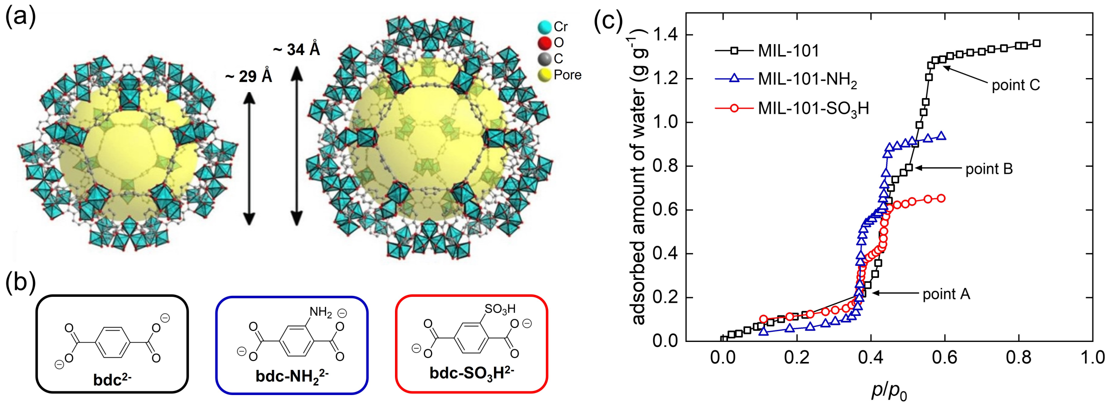

Figure 1.12: (a) Illustration of the differently sized pores of MIL-101-Cr. Figure is taken from Reference [129]. (b) Selected dicarboxylate-based linker molecules used for the synthesis of functionalized MIL-101-Cr frameworks. (c) Water adsorption isotherms for desolvated MIL-101-Cr, MIL-101-Cr-NH_2 and MIL-101-Cr-SO_3H measured at 25 °C.[130]

MIL-101-Cr reveals a step-wise water adsorption due to the different diameter of its two cages. After adsorption of water molecules to the OMS below $p/p_0 < 0.4$ (point A), additional water molecules start to adsorb thereon, resulting in the formation of distinct water clusters.[132] Then, pore condensation starts in two distinguishable steps. First, the smaller cages (diameter of 29 Å) are filled completely ($p/p_0 \approx 0.5$, point B). Afterward, water molecules adsorb to the larger cages (diameter of 34 Å) until complete saturation (point C). When the framework is functionalized with hydrophilic groups (*e.g.*, -NH_2 or -SO_3H), a shift of the adsorption isotherm towards lower p/p_0 is observed when compared to the pristine framework (Figure 1.12c). This indicates higher hydrophilicity at the pore surface, consequently leading to stronger water-framework interactions.

Microporous MOFs typically yield S-shaped water sorption isotherm (type IV and V) with inflection points α within a pressure range p/p_0 = 0.1 ... 0.3. This is a result of the different polarities of their building blocks, *i.e.*, hydrophilic inorganic SBUs and hydrophobic linker moieties, present inside the framework pores. These effects have been extensively studied for the cubic UiO-66,[134] a framework based on metal-oxo-clusters, *i.e.*, $[Zr_6O_4(OH)_4]$, formed of Zr^{4+} cations coordinated by oxido and hydroxido anions (Figure 1.13a-c). Those inorganic building blocks are interconnected by a total of 12 deprotonated terephthalic acid (bdc^{2-}) moieties to form a framework of *fcu* topology with tetrahedral and octahedral cages, possessing a diameter of 7.2 and 8.4 Å, respectively.

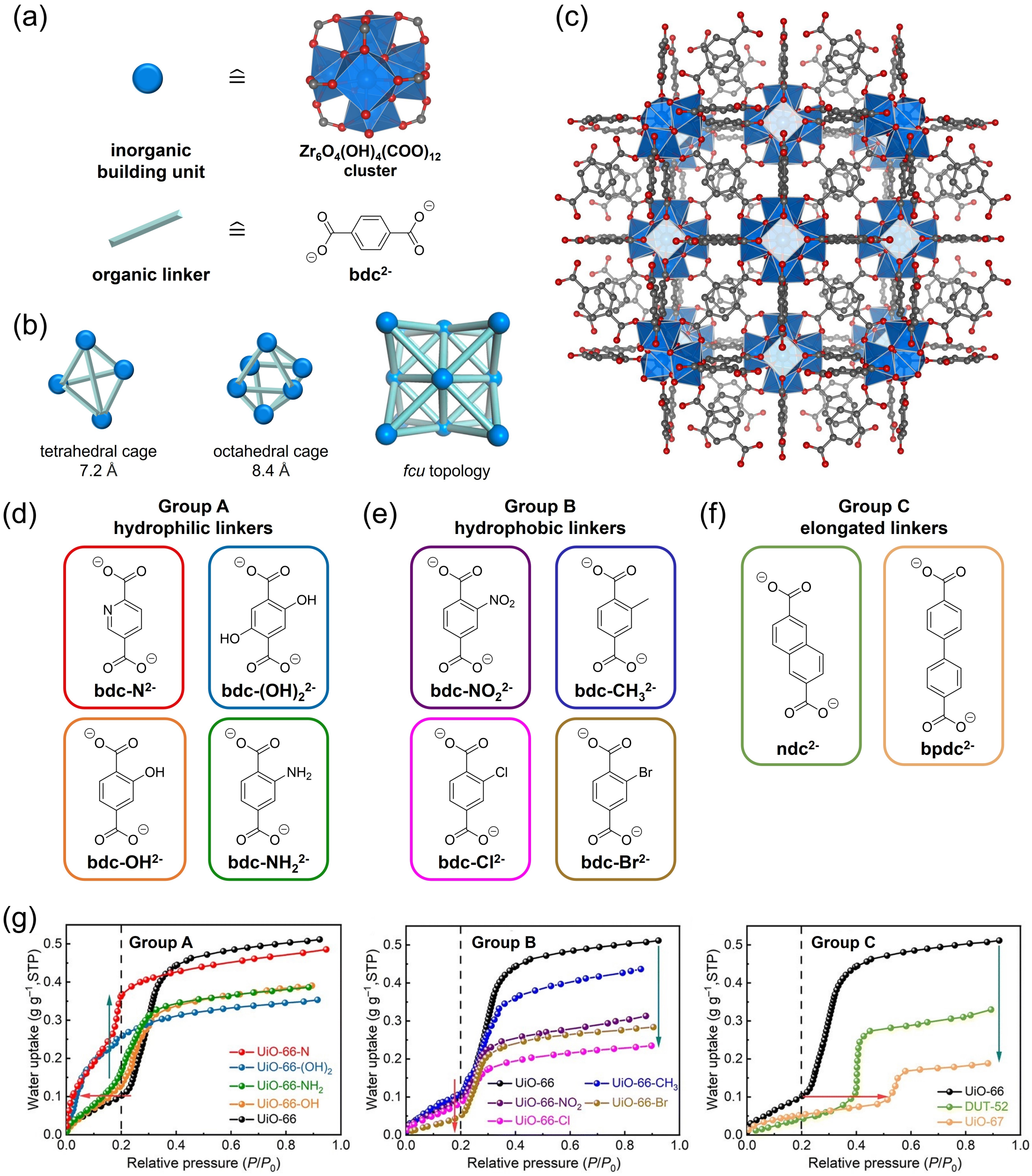

Figure 1.13: (a) Building units of UiO-66, showing its inorganic, *i.e.*, 12-connected [$Zr_6O_4(OH)_4(COO^-)_{12}$] SBU and the organic bdc^{2-} linker molecule. (b) Illustration of the tetrahedral and octahedral cages, found in the *fcu* topology, adopted by UiO-66. (c) Crystal structure of unmodified UiO-66-Zr. Representation of different hydrophilic (d), hydrophobic (e) and elongated linker molecules (f), incorporated into the UiO-66 framework structure. (g) Water vapor adsorption isotherms of pristine and functionalized UiO-66 materials, measured at 25 °C, reprinted with permission from reference [133].

LU *et. al*[133] systematically analyzed the water sorption behavior of UiO-66-Zr and isoreticular frameworks by measuring water sorption isotherms at 25 °C. They classified all investigated materials into three different groups (Figure 1.13e-f). First, they compared functionalized frameworks (UiO-66-R) containing linker molecules with hydrophilic (group A; R = OH, NH_2, OH_2, ...) and hydrophobic moieties (group B; *e.g.*, R = CH_3, Cl, Br, ...) with the pristine framework. Pristine UiO-66 showed a S-shaped water sorption isotherm (type IV), indicating a hydrophilic framework with multiple water sorption sites (Figure 1.13g). After a gradual increase of the adsorbed water until $p/p_0 \approx 0.2$, a steep adsorption step is visible in the range of p/p_0 0.25 ... 0.4. Afterward, small amounts of water are adsorbed, resulting in a maximum water uptake of 0.51 g g^{-1} (at p/p_0 = 0.9). Functionalized materials of group A, *i.e.*, hydrophilic functional groups, revealed a decreased total uptake, stemming from the lower surface areas (Figure 1.13g). Further, a shift of the sorption step, *i.e.*, inflection point, toward lower p/p_0 was detected. However, most members exhibit a similar isotherm shape as the pristine MOF, while solely UiO-66-$(OH)_2$ revealed a type I isotherm with no clear sorption step, suggesting a much higher surface polarity.[133] Similar observations on the dependence of the substituent's polarity on the isotherm type and inflection point were made in other studies.[135,136] Continuing with group B, *i.e.*, hydrophobic functional groups, materials also revealed a decreased total water uptake when compared to UiO-66. This effect is more pronounced than for group A, further increasing with substituent size. However, the pressure range of the sorption step remains nearly unchanged for all materials.

Lastly, they studied the influence of the pore size and surface area on the sorption properties by incorporation of elongated linker molecules (group C). For this purpose, they used biphenylene ($bpdc^{2-}$ resulting in UiO-67[134]) and naphthalene-based (ndc^{2-} resulting in DUT-52[137]; DUT = Dresden University of Technology) dicarboxylate linker molecules, yielding frameworks with extended pore structures of 8.2/10.0 Å (for DUT-52) and 11.2/21.0 Å (for UiO-67). Their results highlighted that the total water capacities decreased remarkably with increasing pore size: 0.51 g g^{-1} (UiO-66) > 0.33 g g^{-1} (DUT-52) > 0.19 g g^{-1} (UiO-67, see Figure 1.13g). As discussed for porous carbons and silica (see Sections 1.2.2 and 1.2.3), the sorption step is shifted towards higher p/p_0 with increasing pore size. These results suggest a primary role of the pore size on the micropore filling that affects the binding affinity of water, which decreases with increasing pore size as a consequence of larger hydrophobic domains, *i.e.*, extended organic linker backbones.[133] However, different results suggest that this behavior can be fine-tuned by introduction of functional groups in different ratios.[133,138]

1.2.5 Water Sorption Behavior of CPO-27-type Frameworks

Despite the previously mentioned issues with its hydrolytic stability (see Section 1.1.1), CPO-27 is another heavily studied material with respect to its water adsorption/desorption properties. One of the first measurement sequences on CPO-27-*M* (*M* = Co, Mg, Ni, Zn) was performed by YAGHI *et al.*.[139] Although all materials revealed a fast saturation with water at low relative humidities, their experiments did not consider the effect of the OMS on the sorption behavior, as samples were stored in air prior to the measurements. Further studies on the CPO-27-*M* series (*M* = Co,[140] Mg,[141,142] Ni,[15,31,143,144] Zn[145]) considered these circumstances and observed significantly higher overall water uptakes for all materials, additionally revealing type I[105] water sorption isotherms, highlighting the high hydrophilicity of these compounds.

In addition to these experimental studies, computational investigations focused on the adsorption of water and its interactions with the CPO-27-*M* (*M* = Mg, Zn) framework.[39,145,146] These studies revealed discrete sorption sites, similar to the above-described crystallographic water positions found in fully hydrated CPO-27-*M* (see Section 1.1.2).[41] These sites are located (i) at the open metal site, (ii) near the oxygen atoms of the inorganic SBUs and (iii) near the phenylene backbone. Distinct differences between the occupation of these sorption sites became apparent for different metal cations. On the one hand, for CPO-27-Zn[145] an energetically favorable adsorption to the OMS was found. On the other hand, results for CPO-27-Mg[39,146] suggest otherwise, revealing similar sorption energies for water molecules at the OMS and near the inorganic SBU, after adsorption of few water molecules to the open metal site. This suggests a simultaneous occupation of both sites, with far less attractive interactions near the phenylene moieties forming the pore walls.

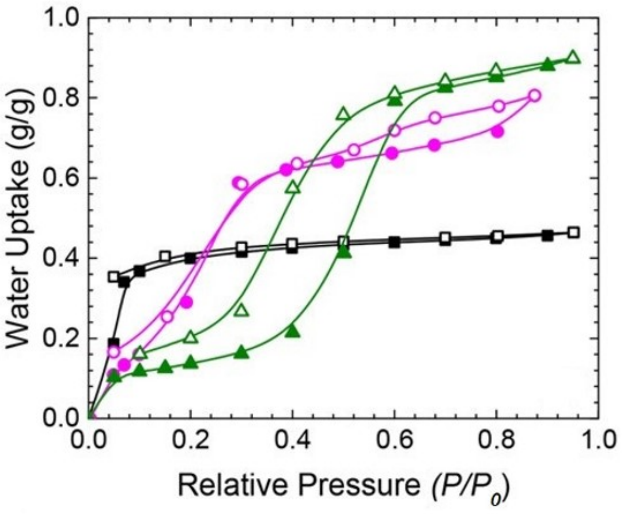

Figure 1.14: Water adsorption/desorption isotherms, closed and open symbols respectively, of Ni_2dhtp (black), Ni_2bpp (purple) and Ni_2tpp (green), measured at 25°C. Figure reprinted with permission from reference [15].

Further investigations on different isoreticular MOFs, *i.e.*, IRMOFs-74[15] were made, revealing a type IV water sorption isotherm for frameworks with larger pores, *i.e.*, Ni_2bpp and Ni_2tpp, rather than a type I isotherm for Ni_2dhtp (*i.e.*, CPO-27-Ni; see Figure 1.14). In addition, the inflection point α is shifted toward higher p/p_0 with increasing linker size, thus being in agreement with the above-stated observations for porous carbons (see Chapter 1.2.2) and MOFs (see Chapter 1.2.4).[133]

1.3 Chemistry of Water in Confined Spaces

In order to fully explore the water sorption behavior of porous materials, an understanding of the chemistry of water in nanoscopic confined spaces, *i.e.*, voids with limited entry and exit points (*e.g.*, pore opening), is required (Figure 1.15). Under such circumstances, the molecular behavior is controlled by a complex interplay of multiple factors rather than by distinct forces or interactions. This results in sometimes drastically different reactivities,[147] selectivities[148] and stabilities[149] of confined molecules when compared to respective bulk-phases. Such confined spaces are found in nature, *e.g.*, enzymes[150] or zeolites,[149] as well as in artificially made porous compounds such as MOFs,[1] carbons[108] and silica.[125] Despite the rather complex situation, those environments offer unique possibilities to control molecular behavior.[151]

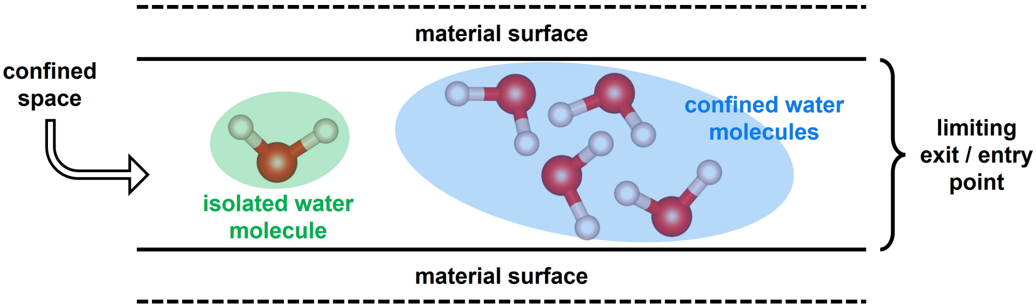

Figure 1.15: Schematic illustration showing water molecules in a confined space, highlighting the limited space as a result of entry and exit points.

In the particular case of water in confinement, its behavior stems from the high degree of molecules interacting with the interface of the porous host structure.[152,153] These interactions are altered by different factors such as the surface polarity, pore geometry and pore dimensions of the confining structure.[117,154,155] This is a direct consequence of competing water-surface and water-water interactions of adsorbed water, affecting the local H-bonding network. Hence, water under confinement shows different arrangements than found in the bulk-phase, leading to altered structural and dynamic properties of these molecules.[154–157] Examples for these effects include the formation of monocrystalline water at room temperature,[152] drastically modified diffusion properties,[153,158] and diverse water structures.[159]

1.3.1 Water under Anisotropic Confinement

Multiple studies on water under confinement focus on inorganic porous compounds such as carbon nanotubes and porous silica. This is a consequence of two things: (i) The highly anisotropic environment inside defined pore channels with spatial limitations along the pore perpendicular to the pore axis with fewer restrictions along the pore axis. (ii) The option to modify the pore surface polarity (as discussed in Chapter 1.2).

FRÖBA *et al.*[160] demonstrated the effect of pore wall functionality in silica compounds (mesoporous silica and PMOs) on the arrangement of water in the cylindrical mesopores. They compared MCM-41 (MCM = Mobil Composition of Matter) with three PMOs, *i.e.*, phenylene (PMO-phen), biphenylene (PMO-biphen) and divinylaniline (PMO-$(NH_3)_2$), of comparable pore size. All materials exhibited the expected behavior, showing pore condensation and type V isotherms, with the onset shifted toward higher p/p_0 with increasing hydrophobicity. However, despite similar water sorption characteristics, the arrangement of water was found to be drastically different. For the less polar (or more hydrophobic) materials PMO-phen and PMO-biphen, water was found to adsorb near the inorganic silica moieties with no indication of water residing near the hydrophobic pore walls. Contrary, for PMO-$(NH_2)_2$ a strong interaction with the inorganic walls is initiated by H-bonds toward the amine group. Thus, pore filling occurs uniformly along the pore walls.

Similar observations were made by TIEMANN *et al.*.[121] They studied the effect of the pore wall surface polarity in MCM-41 on the arrangement of water molecules by functionalization of mesoporous silica with trimethylsilyl moieties. Their study combined experimental and theoretical methods and revealed that hydrophilic pore wall surfaces lead to an »ice-like« water arrangement, being a consequence of comparably strong water-water and water-surface interactions. Contrary, the functionalized and more hydrophobic silica showed a water arrangement more comparable to liquid water due to less strong water-surface interactions. Further, they found that the average coordination number (CN), *i.e.*, the number of H-bonds with adjacent atoms from other water molecules or the solid interface, is affected by the number of surface-bond silanol or methyl groups, since these groups alter the pore wall polarity.

Additional studies by SCOTT *et al.*[117] investigated the arrangement of water in dependence of differently sized organosilane backbones within SBA-15 (SBA = Santa Barbara Amorphous). Results indicated that highly ordered water molecules

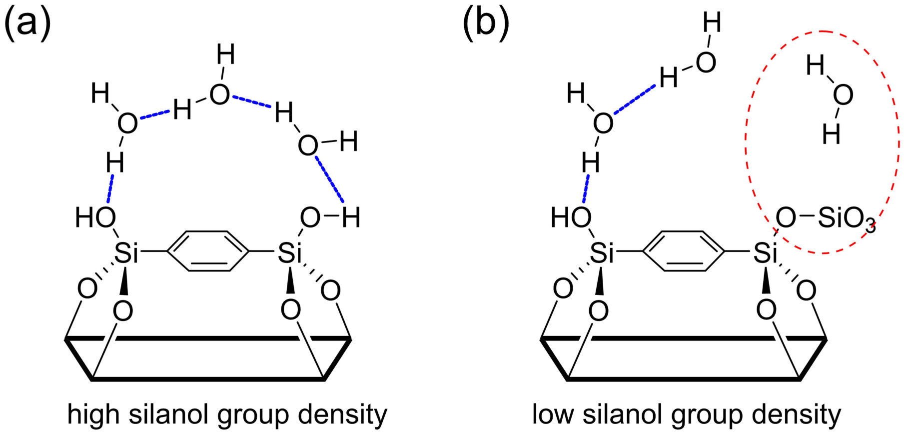

Figure 1.16: (a) Chain of H-bonded water molecules anchored at silanol groups (the blue dotted lines represent hydrogen bonds) and (b) reduced ordering as a result of partial dehydroxylation of the organosilica. The red dotted oval highlights the loss of a hydrogen bond anchoring.[117]

are located around the organic moieties, forming water-bridges between adjacent silanol groups, only possible for a sufficient silanol group density on the surface (Figure 1.16). Similar observations were made for water molecules adsorbing to a functionalized carbon surface.[116] These effects are due to the entropy-driven hydration of small hydrophobic domains, viewing them as discrete perturbations, resulting in the adsorption of high-entropy water. As the hydrophobic domains increase in size, the Gibbs hydration energy ($\Delta G_{\mathrm{hydration}}$) becomes dominated by the enthalpy term, leading to water molecules avoiding the pore walls. The reversal of this effect is observed at a domain length of *ca.* 10 Å.[161–163]

1.3.2 Behavior of Adsorbed Water in Metal-Organic Frameworks

The huge variety of different pore sizes and functionalities of MOFs makes them particularly relevant for the investigation of confinement effects. While the adsorbed amount of water in highly hydrophobic, *i.e.*, non-polar MOFs, such as FMOF-1[164] (FMOF = fluorinated MOF, *i.e.*, $Ag_2[Ag_4tz]$, tz = 3,5-bis(trifluoromethyl)-1,2,4-triazolate, see Figure 1.17) is negligible compared to other porous materials, the behavior of water is rather unique.[165] At low vapor pressures, isolated water molecules adsorb to small micropores of the framework (see Figure 1.17c), which is explainable by the absence of H-bonding. This is possible, due to structural changes of the framework, caused by adsorption of (mostly) pentameric water structures into larger micropores of the framework. Similar water cluster formation was also observed in hydrophobic, nanoporous carbons.[158] With increasing p/p_0, the concentration of isolated water molecules increases. In addition, more water clusters form in the larger pores, indicating the possibility of fluorine atoms acting as H-bonding sites. During the desorption, isolated water molecules are desorbed preferentially due to the lack of positive interactions, while water molecules in the larger pore seem to agglomerate near the pore center, being a consequence of the highly hydrophobic pore surface, *i.e.*, fluorine atoms.

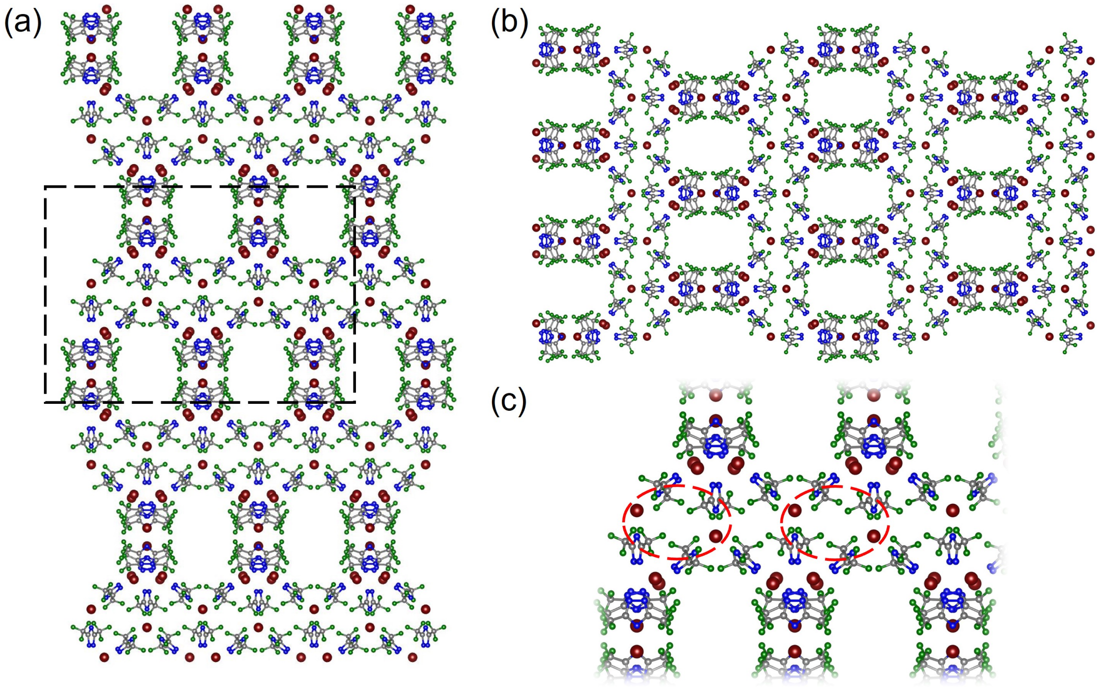

Figure 1.17: View along the crystalligraphic a-axis (a) and b-axis (b) of FMOF-1. (c) Zoom of the marked region, highlighting the small micro pore space (red ellipsis), yielding room for the adsorption of an individual water water molecule *via* structural changes in the framework structure. Silver is displayed in brown, carbon grey, nitrogen blue, fluorine green.[165]

Further studies on water in MOFs focused on the adsorption mechanism and water interactions within the aldehyde containing ZIF-90 (ZIF = zeolitic imidazolate framework, *i.e.*, Zn(imCa)$_2$, imCa = imidazolate-2-carboxaldehyde), using D_2O.[166,167] They combined experimental and theoretical data and suggested the following mechanism: Minor adsorption is found at low relative pressures $p/p_0 < 0.3$.

Afterward, pore condensation is apparent, resulting in a type V isotherm shape. Condensation is initiated by the entropically favorable adsorption of water molecules to the interior surface of the framework and results in weak H-bonding interactions towards aldehyde groups, when compared to water-water interactions in the bulk phase. After the initial adsorption, entropic gain enables the additional uptake of water to the interior pore surface, resulting in further H-bonding opportunities for subsequent molecules. As a consequence, additional molecules preferentially form H-bonds with surface-bound molecules rather than with aldehyde groups in adjacent pores. This leads to simultaneous water clustering and pore condensation, characterized by subsequent filling of individual pores instead of simultaneous pore filing. Similar observations were made for other isoreticular ZIFs.[168]

1.3.3 O–H Vibration Band of Water in Different Environments

A powerful experimental method to identify the interactions of water molecules at surfaces and within pores is Fourier transform infrared (FTIR) spectroscopy. For this purpose, the characteristic O–H stretching vibration band of water, found in the range of 2800 ... 3700 cm^{-1}, is analyzed. This band is a superposition of at least three vibrational bands corresponding to H_2O molecules in varying H-bonding environments. Their respective vibrational frequencies are blue-shifted, *i.e.*, toward higher wavenumbers, with decreasing number of H-bonding partners. Following the commonly used classification proposed by BRUBACH *et al.*[169] for three bands, these are assigned to the following three situations: (i) Water molecules that display a coordination number (CN) ≥ 4 (here: number of H-bonding partners) are noted as »network water«. This type of water reveals the lowest O–H stretching vibration frequencies, typically around 3300 cm^{-1}. (ii) Water molecules that are poorly connected with their respective environment, exhibiting only few H-bonds (*e.g.*, as found in dimeric or trimeric water structures) are referred to as »multimer water«. These have the highest vibration frequencies located around 3590 cm^{-1}. This resembles to water molecules terminating a liquid-like network at a liquid-solid/gas interface. (iii) The third type of water molecules presents an intermediate H-bonding situation, *i.e.*, between network and multimer water. Hence, they are accordingly termed »intermediate water«. Water molecules located farther apart from the interface are associated to this type, revealing vibration frequencies around 3460 cm^{-1}.

Analysis of the respective contributions of the different modes, *i.e.*, their peak

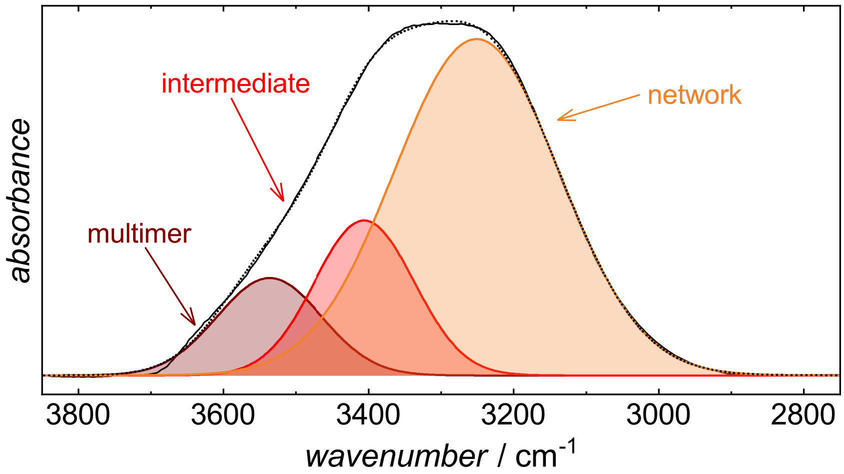

Figure 1.18: Example for the deconvolution of the O–H stretching vibration of liquid water (solid line), showing three types of water molecules, referring to water in different H-bonding situations. Network, intermediate and multimer water are displayed in orange, red and purple, respectively. The cumulative fit is shown as a doted line.[169]

areas, provides valuable insight about the H-bonding framework of water. This information is obtained by deconvolution of the broad O–H stretching vibration band, using least-square fits of at least three Gaussian profiles (Figure 1.18). Further research validated the applicability of this method to water in a confined geometry, as found in inverse micelles[170,171] or in mesoporous silica.[121,172] Results reveal that the respective contributions of the three water types primarily depend on three factors: (i) The surface polarity and functionality of the porous compounds, (ii) the dimension of the confined space, *i.e.*, pore size, and (iii) the »loading«, *i.e.*, relative amounts of adsorbed water. A combination of these factors determines the arrangement of water in limited spaces and ultimately allows the polarity of the environment to be classified. Further information is obtained by consideration of the respective differences between the peak center locations of different vibrational modes x and y, *i.e.*, the wavenumber splitting $\Delta\tilde{v}_{\mathrm{xy}}$. This approach enables to classify the average H-bonding symmetry of water molecules. Generally, lower $\Delta\tilde{v}_{\mathrm{xy}}$ values suggest a higher symmetry in the local H-bonding of water and *vice versa*.[173,174]

CHAPTER

2

MOTIVATION

Understanding of the precise hydration mechanism of porous adsorbents is crucial to evaluate their potential in industrial applications. For MOFs, recent research addressed this issue. However, these hybrid materials offer a vast variety of different building blocks that enforce a complex interplay of hydrophobic (linker molecules) and hydrophilic (typically the inorganic SBUs) sites. This severely affects the observed interactions with water which play a crucial role in microporous frameworks. In addition, the arrangement of water is influenced by large confinement effects, resulting in drastically different sorption mechanisms.

2.1 Influence of the Metal Center on the Properties of CPO-27-*M*

This thesis aims to collect a comprehensive understanding of the water sorption behavior and the interactions of adsorbed water molecules within MOFs. For the first part of this work, CPO-27-*M* is selected as a promising compound, since it offers highly attractive binding sites, *i.e.*, open metal sites (OMS). Additionally, recent work revealed the existence of discrete, crystallographic positions of water in fully hydrated materials. Encouraged by this, the effect of the given metal center in CPO-27-*M* (*M* = Cu, Co, Mg, Mn, Ni, Zn) on the water sorption properties of this framework is investigated by water vapor sorption analysis (Figure 2.1). To gain more insight into the mechanism, density functional theory (DFT) based molecular dynamics (MD) simulations are performed on selected materials by collaborating partners. Present interactions of water molecules with their respective environment are further evaluated by Fourier transform infrared (FTIR) spectroscopy. Combination of these methods allows to precisely analyze the sorption behavior of individual frameworks and identification of the responsible reasons for water-host interactions. This provides a comprehensive knowledge of the effect of the incorporated metal center on the observed water sorption behavior. Finally, the influence of the arrangement of water molecules in the micropores of these frameworks is used to compare their respective hydrolytic stabilities with each other and highlight the key factors, affecting the materials durability.

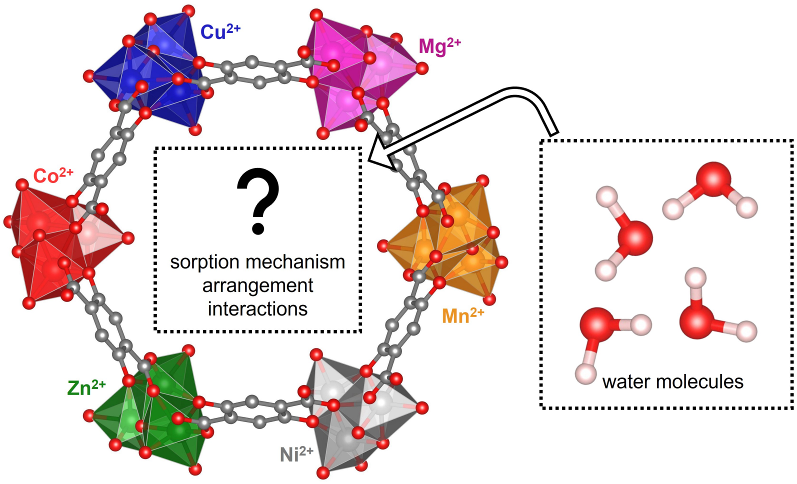

Figure 2.1: Illustration of the different bivalent metal cations (M^{2+}) selected for CPO-27-M synthesis to analyze metal center dependent differences in the hydration behavior.

2.2 Water Sorption Behavior of Pore Engineered CPO-27-Ni

The second part of this work analyzes the effect of the pore size and hydrophobic domain size on the water adsorption/desorption behavior of different CPO-27-type frameworks. Again, particular interest lies in the analysis of interactions of adsorbed water molecules with each other and the MOF surface. Ni^{2+} is selected as the metal center as current research progress suggests high hydrolytic stabilities of these materials. Combination of different metal sources with various linker molecules (L), all unique in substitution pattern and/or molecular size, allows to synthesize isoreticular compounds (*i.e.*, Ni_2L, see Figure 2.2) with tuneable pore size and pore wall hydrophobicity. Finally, precise analysis of incorporated defect sites is performed by solution ^1H nuclear magnetic resonance (NMR) spectroscopy on acid decomposed MOF samples to investigate their effects on the water adsorption mechanism.

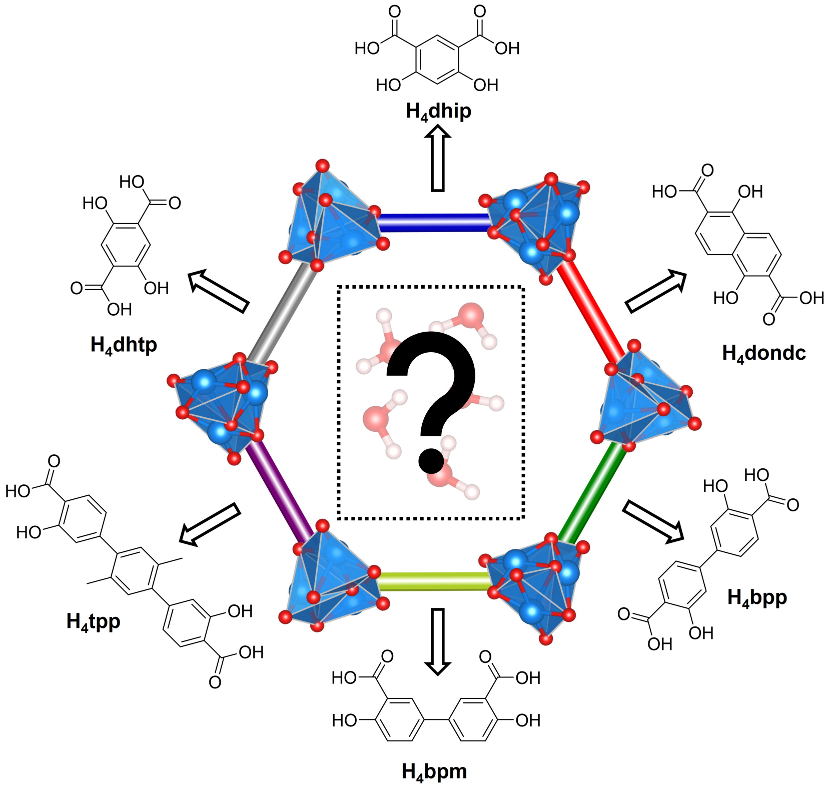

Figure 2.2: Utilized linker molecules for the synthesis of CPO-27-type frameworks to study pore size dependent effects on their respective water adsorption/desorption behavior.

CHAPTER

3

HYDRATION BEHAVIOR OF CPO-27-*M*

The porous coordination polymer CPO-27 has been extensively studied by many researchers with respect to its applicability in sorption-based applications, revealing metal-center depending differences. This is a direct consequence of the chemical nature of the metal ions and the accessible OMS, generated by removal of the coordinating solvent molecules, presenting highly attractive binding sites for a variety of guest molecules (*e.g.*, CO_2, H_2 and H_2O). To be promising for industrial applications, a material must fulfill several criteria, such as: (i) Moderate to good hydrolytic stability, (ii) easy accessibility and (iii) good cyclability, *i.e.*, easy regeneration after use. A majority of possible applications either rely on strong water-adsorbent interactions (*e.g.*, water harvesting) or try to avoid any interaction with the material to maintain large selectivities, sorption capacities or stability (*e.g.*, catalysis and carbon capture). Hence, a comprehensive understanding of the interactions of individual water molecules with the framework and neighboring molecules is needed.

3.1 Impact of the Metal Center on the Hydration of CPO-27-*M* (Cu, Zn)

Previous results revealed large differences in the general sorption behavior of the isoreticular CPO-27-*M* series, with CPO-27-Cu acting drastically different. This knowledge makes them interesting candidates for studying their precise hydration behavior, starting with selected CPO-27-*M* (*M* = Cu and Zn) frameworks. This was accomplished by analyzing their water adsorption/desorption behavior with water vapor sorption analysis. Further insight on the arrangement of water molecules and its interactions with the MOF host was gained by Fourier transform infrared (FTIR) spectroscopy. In addition, density functional theory (DFT) based molecular dynamics (MD) simulations were employed by collaborating partners, allowing the determination of net atomic charges of the framework atoms and adsorbed water molecules, quantifying electronic differences. Results reveal entirely different sorption mechanisms, resulting from changes in their electronic charges and the M^{2+} coordination environment. CPO-27-Zn showed a step-wise sorption mechanism, initiated by saturation of OMS, characterized by occupation of discrete positions for adsorbed water molecules. This is a direct consequence of strong framework-water interactions. Contrary, micropore filling in CPO-27-Cu occurs all at once, like classical pore condensation, with the adsorbed water forming elongated, bulk-like, water clusters along the pore channels.

M. Kloß, M. Beerbaum, D. Baier, C. Weinberger, F. Zysk, H. Elgabarty, T. D. Kühne, M. Tiemann Understanding Hydration in CPO-27 Metal-Organic Frameworks: Strong Impact of the Chemical Nature of the Metal (Cu, Zn) *Adv. Mater. Interfaces* **2024**, 2400476.

- Digital Object Identifier: 10.1002/admi.202400476

Participation in this publication

M. Kloß, D. Baier, C. Weinberger, M. Tiemann: Experimental work, data evaluation, writing and editing of the manuscript, project idea and conceptualization

M. Beerbaum, F. Zysk, H. Elgabarty, T. D. Kühne: DFT based MD simulations (conceptualization, execution, evaluation), contributions to the manuscript

RESEARCH ARTICLE

ADVANCED MATERIALS INTERFACES
Open Access
www.advmatinterfaces.de

Understanding Hydration in CPO-27 Metal-Organic Frameworks: Strong Impact of the Chemical Nature of the Metal (Cu, Zn)

Marvin Kloß, Michael Beerbaum, Dominik Baier, Christian Weinberger, Frederik Zysk, Hossam Elgabarty, Thomas D. Kühne, and Michael Tiemann**

CPO-27 is a metal-organic framework (MOF) with coordinatively unsaturated metal centers (open metal sites). It is therefore an ideal host material for small guest molecules, including water. This opens up numerous possible applications, such as proton conduction, humidity sensing, water harvesting, or adsorption-driven heat pumps. For all of these applications, profound knowledge of the adsorption and desorption of water in the micropores is mandatory. The hydration and water structure in CPO-27-*M* (*M* = Zn or Cu) is investigated using water vapor sorption, Fourier transform infrared (FTIR) spectroscopy, density functional theory (DFT) calculations, and molecular dynamics simulation. In the pores of CPO-27-Zn, water binds as a ligand to the Zn center. Additional water molecules are stepwise incorporated at defined positions, forming a network of H-bonds with the framework and with each other. In CPO-27-Cu, hydration proceeds by an entirely different mechanism. Here, water does not coordinate to the metal center, but only forms H-bonds with the framework; pore filling occurs mostly in a single step, with the open metal site remaining unoccupied. Water in the pores forms clusters with extensive intra-cluster H-bonding.

1. Introduction

Within the constantly growing diversity of metal-organic frameworks (MOFs),[1,2] materials with open metal sites, that is coordinatively unsaturated metal centers, are particularly interesting.[3] One fascinating example is CPO-27,[4] also known as MOF-74.[5] It contains the linker ligand 2,5-dioxido-1,4-benzenedicarboxylate (dobdc^{4-}) and has been synthesized using a large number of metals, including Zn[5] and Cu.[6] CPO-27 has 1D micropores arranged in parallel with a honeycomb-like cross section. The metal centers are coordinated by three carboxylate and two phenolate groups of the linker molecules, as well as by a solvent molecule from the synthesis (dimethylformamide (DMF) or water). Removal of this molecule through thermal activation creates the open metal site that is exposed to (and therefore accessible through) the pores. Thus, a variety of guest molecules, including H_2O, can coordinate to the open metal sites.[7-9] Numerous applications are based on the uptake of water, such as humidity sensing,[10,11] water harvesting,[12,13] proton conduction,[14-18] or adsorption-driven heat pumps.[19] Other applications aim at the uptake of other molecules, for example, gas sensing (other than water),[20,21] carbon capture,[22,23] or catalysis.[24] In these latter cases, water can be an interfering component that competes with the target molecule for sorption sites. In addition, the structural integrity of the framework materials may be affected by humidity.[25] Hence, it is mandatory to understand the behavior of water inside the pores of the CPO-27 host material.

CPO-27 may be regarded as an ideal system for comprehensive hydration/dehydration studies, because intra-pore water molecules are known to occupy well-defined sites. Dietzel *et al.*

M. Kloß, D. Baier, C. Weinberger, M. Tiemann
Department of Chemistry – Inorganic Chemistry
Faculty of Science
Paderborn University
Warburger Str. 100, 33098 Paderborn, Germany
E-mail: michael.tiemann@upb.de

The ORCID identification number(s) for the author(s) of this article can be found under https://doi.org/10.1002/admi.202400476

DOI: 10.1002/admi.202400476

M. Beerbaum, T. D. Kühne
Center for Advanced Systems Understanding (CASUS)
Untermarkt 20, 02826 Görlitz, Germany
E-mail: t.kuehne@hzdr.de

M. Beerbaum, T. D. Kühne
Helmholtz Zentrum Dresden-Rossendorf
Bautzner Landstr. 400, 01328 Dresden, Germany

F. Zysk, H. Elgabarty
Department of Chemistry – Theoretical Chemistry
Faculty of Science
Paderborn University
Warburger Str. 100, 33098 Paderborn, Germany

identified five crystallographically defined water molecules per Zn center in fully hydrated CPO-27-Zn.[25] Based on temperature-dependent, in situ powder X-ray diffraction (XRD) and thermal analysis data, they categorized the five molecules in three distinct groups, according to their strength of interaction with the host material and with neighboring water molecules:[9] (i) The water molecule that coordinates to the metal center exhibits the strongest adsorption strength (chemisorption). (ii) Two more molecules interact with the coordinating one by H-bonding and show a weaker adsorption strength. (iii) Finally, the last two water molecules interact only with the last-mentioned two molecules by H-bonding and exhibit the weakest adsorption strength. The formula of CPO-27-Zn is therefore $[Zn_2(dobdc)(H_2O)_2]\cdot 8H_2O$, indicating that two water molecules (one per Zn) coordinate, while eight molecules (four per Zn) are considered as crystal water molecules inside the pores.

Obviously, measuring the adsorption (and desorption) of water from the gas phase is a very promising means of studying the hydration (and dehydration) behavior of MOFs.[26,27] However, for CPO-27, water sorption studies to date have mostly employed the gravimetric method (microbalance), with particular focus on the structural integrity of the framework.[28,29] The manometric technique, on the other hand, has proven to be a very powerful means of studying water vapor sorption in many porous media including some MOFs;[30,31] however, to the best of our knowledge, it has not been applied systematically to CPO-27. The manometric technique provides very high accuracy especially for very low amounts of water, that is, low water vapor pressure. This is particularly helpful for detailed hydration/dehydration studies in CPO-27, due to the strong water-metal interaction.

Further insight in the unique behavior of water in confined space is obtained by computational methods. Density functional theory (DFT) has been applied to CPO-27-*M* (*M* = Cu, Mg, Zn) to study adsorption energies and preferred adsorption sites of small molecules (*e.g.* CO_2,[32,33] N_2,[32,33] and H_2[32,34]). Studies focusing on the adsorption of water in CPO-27-*M* (*M* = Mg, Zn)[35,36] outline differences between the first (open metal site), second (near the oxygen atoms of the inorganic building units) and third water sorption sites (near the phenylene backbone). While results on CPO-27-Zn[35] strongly suggest an energetically favorable adsorption to the first site, simulations for CPO-27-Mg[36,37] suggest otherwise. In the latter, similar sorption energies for the first two sorption sites, after adsorption of one water molecule, suggest a simultaneous occupancy of both positions, while the third sorption site is far less attractive. Depending on the metal center, these observations hint toward a different sorption process.

Here we present a study on the hydration behavior and water structure in CPO-27-Zn and CPO-27-Cu by a combined experimental and computational approach. The objectives of our investigation is to gain a better understanding of the interactions between water molecules and the framework (coordinative bonding, hydrogen bonds) on the one hand, and the H-bonding behavior of the water molecules among themselves on the other hand. In particular, water-induced structural changes in the framework are investigated. We study the adsorption and desorption of water by manometric vapor sorption analysis. In addition, water-induced structural distortion and changes in charge distribution of the materials are discussed by employing density functional theory (DFT). The DDEC6 atomic population analysis[38–43] obtains net atomic charges (NAC) by assigning valence electrons as a function of the total electron density distribution to the observed system. The obtained NAC are calculated on several criteria, such as transferability to different conformations of the same molecules. The electron density distribution needed for the analysis is obtained by DFT. Further, the spatial distribution of water molecules in the pores is analyzed using semi-empirical (PM6-FM) molecular dynamics (MD) simulations. Combination of static and dynamic calculations allows for a unique insight, understanding the differences in macroscopic behavior on an atomic levels.

2. Results and Discussion

2.1. General Characterization

CPO-27-Zn[44] and CPO-27-Cu[45] were prepared by modified solvothermal methods previously reported in the literature, as described in detail in the Supporting Information section. Powder X-ray diffraction (XRD) patterns (**Figure 1**a/b) confirm the framework structure of all materials with no evidence of crystalline impurities. To assess the stability of the frameworks to an excess of water, the materials were washed with water (approx. 50 mg sample with 8 to 10 mL H_2O) and then air-dried on filter paper at room temperature. XRD confirms that both materials remain crystalline. The microporous nature of the products is confirmed by N_2 physisorption analysis, revealing type-I sorption isotherms (Figure 1c).[46] The measurements prove high surface areas and large pore volumes (Table S1, Supporting Information).

Elemental analysis of the hydrated materials reveals C/H ratios that are reasonably consistent with mostly defect-free frameworks (Table S2, Supporting Information). The calculated number of water molecules per formula unit (M_2(dobdc)) is approximately ten for CPO-27-Zn, in accordance with literature data.[25] CPO-27-Cu-hyd has only 9 water molecules per formula unit, which can be explained by generally weak interaction of the Cu^{2+} open metal site with guest molecules[45,47] due to Jahn-Teller distortion.[48] Thermogravimetric analysis coupled with mass spectrometry (TGA/MS) of the hydrated frameworks reveal very similar results to those obtained by Dietzel *et al.* (Figure S1, Supporting Information).[9]

Fourier transform infrared (FTIR) spectra of the desolvated frameworks (**Figure 2**a) show the absence of the carboxyl O—H vibration, confirming the absence of unreacted (protonated) linker molecules. Spectra of the hydrated samples show typical vibration bands of water (for a closer inspection of the stretching modes, see below). Otherwise, the spectra show only slight differences (slight shifts in the oscillation frequencies) to those of the desolvated materials. In the low wavenumber region (Figure 2b), the M—O stretching vibration within the framework[8,49] is observed at slightly higher wavenumber for CPO-27-Cu (600 cm^{-1}) than for CPO-27-Zn (580 cm^{-1}), suggesting a higher Cu—O than Zn—O bond strength. This is consistent with the observation of shorter distances between the Cu center and the coordinating O atoms in the framework (see below).

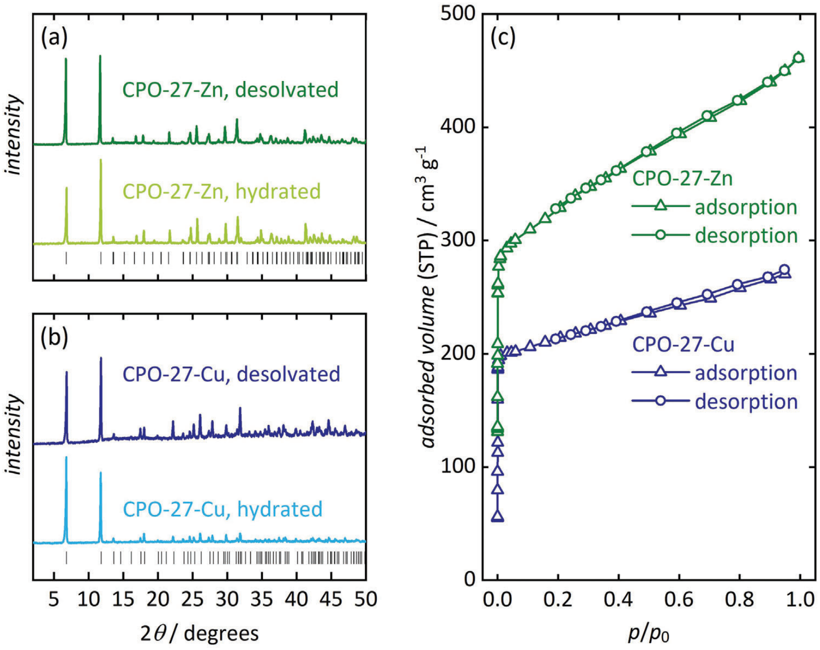

Figure 1. Powder X-ray diffraction patterns of desolvated and hydrated frameworks, (a) CPO-27-Zn and (b) CPO-27-Cu, confirming structural integrity after hydration. (c) N_2 sorption isotherms of CPO-27-Zn and CPO-27-Cu (the latter sample showed extra-pore condensation at the highest measured pressure, $p/p_0 = 0.995$; the respective data point was removed for clarity).

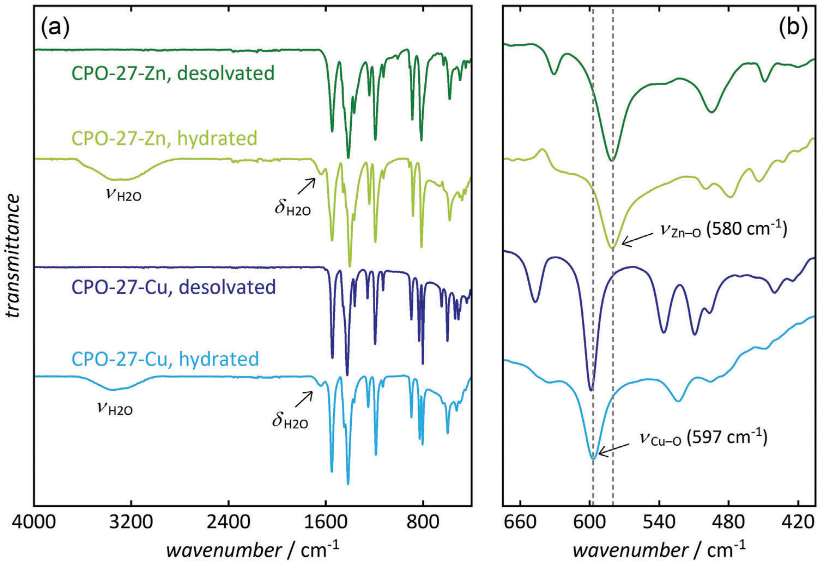

Figure 2. FTIR spectra of desolvated and hydrated CPO-27-Zn and CPO-27-Cu. Hydrated samples show typical H_2O vibration bands (a); the Cu—O stretching vibration occurs at slightly higher wavenumber than Zn—O (b).

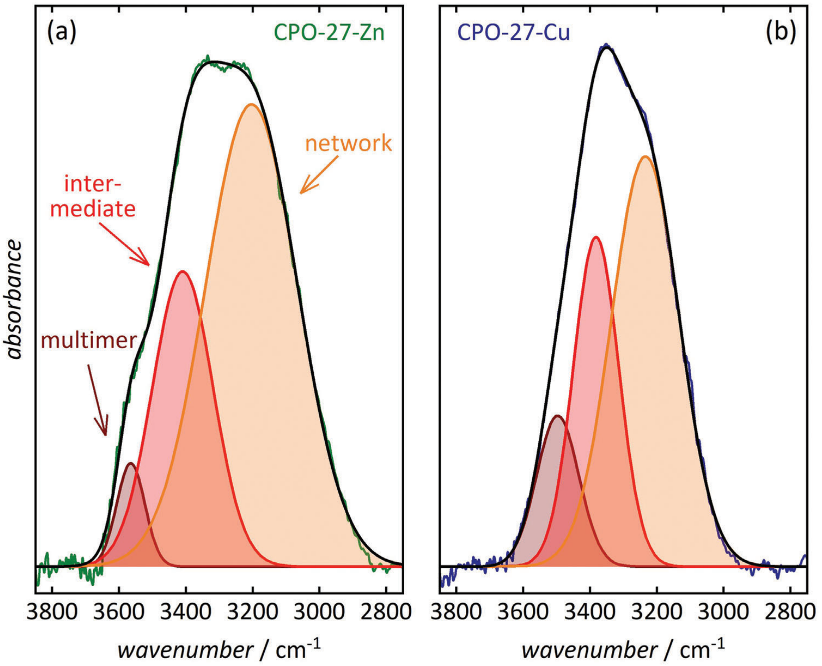

Figure 3. Deconvolution by least-square fitting of the FTIR O–H stretching vibration band of water in hydrated (a) CPO-27-Zn and (b) CPO-27-Cu, revealing a higher degree of H-bonding ('network water') in CPO-27-Zn than in CPO-27-Cu (black lines are the sums of the three fitted Gaussian profiles).

2.2. Experimental Studies of Hydration

A closer inspection of the stretching vibration bands of H_2O in the hydrated samples by FTIR in attenuated total reflection (ATR) mode provides some insight in the interactions of water molecules within the pores. Previous studies have shown that for water in confinement, the O—H stretching vibration band in the range of 2800 ... 3700 cm^{-1} can be deconvoluted into three contributions originating from water in different environments.[30,31,50] Three bands that result from least-square fitting of Gaussian profiles correspond to 'network water' (molecules that interact strongly with adjacent ones by approximately four H-bonds), 'multimer water' (molecules that are poorly connected by only a few H-bonds), and 'intermediate water' (H-bonding situation between 'network' and 'multimer'). **Figure 3** shows that the relative contribution from network water is higher in CPO-27-Zn (71%) than in CPO-27-Cu (55%), while the opposite is observed for the contribution from multimer water (Zn: 5%; Cu: 14%). Hence, water molecules in the pores of CPO-27-Zn seem to form more extensive H-bonding networks than in CPO-27-Cu, as discussed below.

To understand the hydration and dehydration of CPO-27-Zn and CPO-27-Cu in more detail, we carried out manometric water vapor sorption measurements at 25°C. Two consecutive cycles of adsorption/desorption were performed without removing the sample from the device between cycles, that is without additional thermal activation after the first cycle. This allows to identify water molecules that occupy the open sites, that is, coordinate to the metal centers, since these will not be removed by the desorption process. In this case, a different situation is expected for the second adsorption isotherm. For both materials, an overall higher total uptake is observed during the second adsorption/desorption cycle than during the first cycle (see below). We explain this finding by a partial degradation of the frameworks due to cleavage of metal-linker bonds during the time-consuming measurements (several days), leading to the formation of additional open metal sites. This is consistent with previous reports for MOFs with vacant coordination sites, including CPO-27-Mg.[29]

The water sorption isotherms of CPO-27-Zn show a stepwise progression (**Figure 4**a). Since most of the water is adsorbed at low relative pressure ($p/p_0 < 0.1$), we show all isotherms both in a linear and in a semi-logarithmic representation. (Figure 4b/c, Missing data points below *ca.* $p/p_0 = 0.002$, except in the first adsorption isotherms, are due to technical experimental restrictions) Initially, a step around $p/p_0 = 0.01$ is observed in the first adsorption isotherm, during which *ca.* 20% of the total water uptake takes place. This step is not reversible, that is these 20% of water remain in the sample after the completed first adsorption/desorption cycle. We assign this uptake to the coordination of water molecules to the open Zn^{2+} centers (first adsorption site). This is consistent with the above-mentioned findings that the coordinating molecule is one out of five crystallographically defined water molecules in the fully hydrated material.[25] Then, further water adsorption occurs in another three distinguishable steps: First, a well-defined step in the pressure range $p/p_0 = 0.01$ ... 0.025 is observed. During this step, another *ca.*

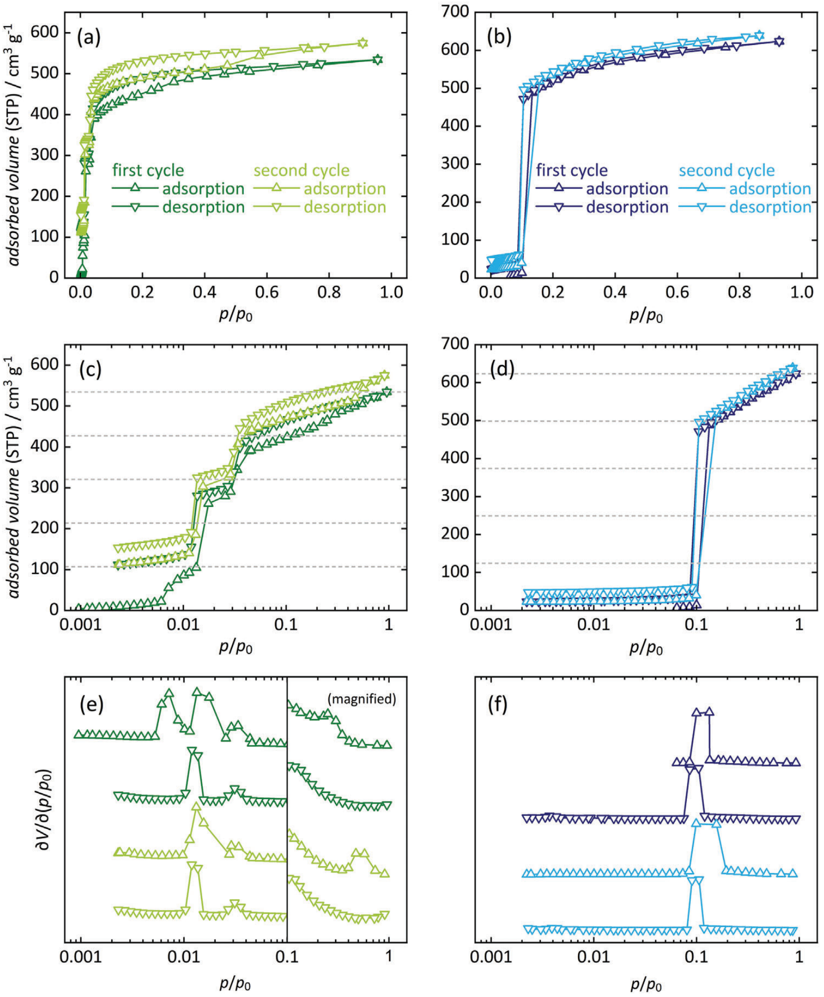

Figure 4. Water vapor sorption isotherms (25°C) of (a) CPO-27-Zn and (b) CPO-27-Cu (two consecutive adsorption/desorption cycles). Data are shown at linear scale, in semi-logarithmic representation (c,d), and as the normalized first derivatives (e,f). Horizontal lines mark 20%, 40%, 60%, 80%, and 100% of the total water uptake during the first cycle.

40% of the total water uptake takes place, which we attribute to two water molecules interacting quite strongly with the coordinating water molecule through H-bonding (second and third adsorption site), consistent with the above-mentioned observations made by Dietzel *et al.*[9] Next, there is another step at p/p_0 = 0.025 ... 0.05, whereby another approx. 20% of the total water uptake occurs (fourth sorption site). This uptake can be attributed to a water molecule with weaker interaction. Finally, the uptake of the remaining *ca.* 20% occurs gradually, over a wide pressure range of p/p_0 = 0.05 ... 1, which corresponds to one last water molecule with the weakest interaction to neighboring molecules.

Both consecutive cycles of adsorption/desorption in CPO-27-Zn show significant hysteresis, which may be interpreted as a configurational rearrangement of the adsorbed water molecules. Hysteresis in water sorption isotherms is often explained by a rearrangement of water molecules (from a metastable state, *i.e.*, preliminary pore saturation) with increasing vapor pressure (*i.e.*, during adsorption). If such a rearrangement leads to an increase in the density of the adsorbed water and is not reversible when the pressure decreases thereafter (*i.e.* during desorption), it will create hysteresis. This effect has been discussed mainly for larger pores and/or for hydrophobic pores (including micropores).[31,51-60] We hypothesize that a similar effect occurs in our case, since the pore walls of CPO-27 contain hydrophobic (phenylene) units between the (hydrophilic) coordinated metal centers. Assuming that all five water molecules are ultimately located at crystallographically defined positions, they may temporarily (partially) exist in a different, metastable configuration during the adsorption process.

CPO-27-Cu exhibits a completely different water sorption behavior than CPO-27-Zn (Figure 4b). Almost no uptake is observed at pressures up to *ca.* $p/p_0 = 0.1$. Then, adsorption of *ca.* 80% (*i.e.*, four molecules per Cu) occurs all at once, followed by the residual 20% (one molecule) in the remaining pressure range ($p/p_0 = 0.1 \ldots 1$). This behavior resembles classical pore condensation, with no option to distinguish between crystallographically distinct water sites. Almost no hysteresis is observed. Most notably, the adsorption of all five water molecules is reversible, that is, any water molecule near the open site at the Cu^{2+} center, binds only weakly, if at all (see below). This is in accordance with literature data that revealed weak interactions of H_2O with Cu^{2+} centers in other open-metal-site frameworks due to Jahn-Teller distortion.[61] This leads to steric constraints that result in drastically reduced Cu–O Coulomb interactions and significantly lower partial charge than for the other members of the isoreticular series.[34] As a consequence, one oxygen atom of the linker molecule is oriented into the pore, sterically blocking the metal site and inhibiting interactions with water, as will be confirmed by DFT calculation shown below. Ultimately, this oxygen atom acts as a nucleation site facilitating water cluster growth through hydrogen bonding.

Summarizing the water sorption data, we can conclude that the high water uptake at low relative pressure ($p/p_0 < 0.1$) is clear evidence of the hydrophilic nature of CPO-27-Zn. The affinity of the open metal site becomes evident by the coordination of water (strong bonding; 20% of total water uptake). The irreversibility of this sorption process verifies the existence of vacant coordination sites prior to sorption measurements (*i.e.* after activation). Deviating from this behavior, CPO-27-Cu shows a (nearly) reversible pore condensation behavior driven by water-water interactions. Distortion of the local coordination environment causes one oxygen atom from the inorganic building unit to be oriented into the pore, thereby initiating water cluster formation via hydrogen bonding without participation of the Cu^{2+} site (see theoretical calculations below).

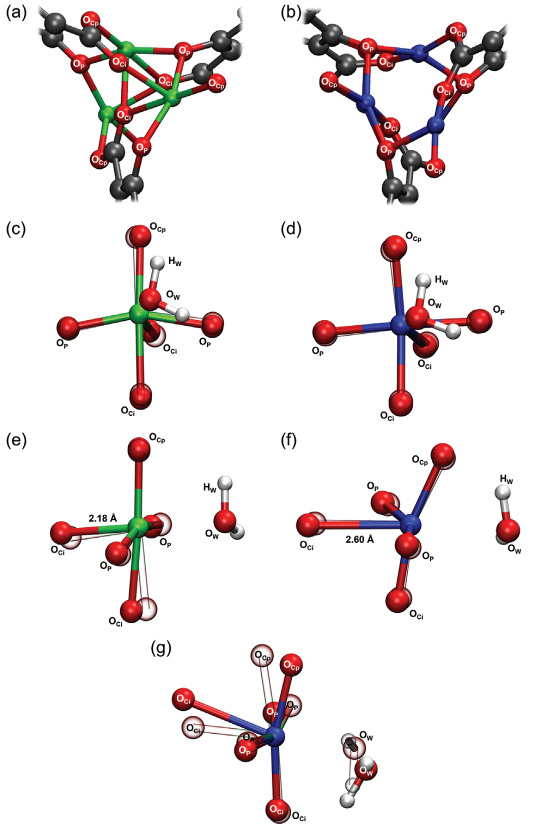

Figure 5. Distinguishable framework O atoms in hydrated (a) CPO-27-Zn and (b) CPO-27-Cu, not showing coordinating water molecules for clarity. Top views (c,d) and side-on views (e,f) of the changes in the local coordination environment before (transparent atoms/bonds) and after (colored atoms/bonds) hydration and geometric optimization. (g) Comparison of the coordination environment in hydrated CPO-27-Cu (solid color) and CPO-27-Zn (hollow). (Color code: O - red, C - dark gray, Zn - green, H - white).

2.3. Computational Studies

DFT simulation of the hydration utilizes supercells of the frameworks (1 × 1 × 4) under periodic boundary conditions (pbc); the studied structures possess a total of three independent pores with no defects. The supercells are based on crystallographic data of the dehydrated frameworks, that is with unoccupied, open metal sites (M_2(dobdc)).[47] We distinguish three types of framework oxygen atoms (O_{MOF}) according to their respective environment: (i) carboxylate oxygen atoms exposed to the pore (O_{Cp}), (ii) carboxylate oxygen atoms pointing “inward”, that is slightly away from the pore (O_{Ci}), and (iii) phenolate oxygen atoms (O_P), as displayed in **Figure** 5a/b. One water molecule was placed next to each metal site at a distance of 2 Å, resulting in the monohydrate framework (M_2(dobdc)$(H_2O)_2$, that is, one water molecule per metal center). The system was then allowed to relax into the geometrically optimized structure. Higher hydration degrees were obtained by filling the pores of less hydrated frameworks with bulk water from centroid molecular dynamics (cmd) simulations using the second-generation Car-Parinello-based quantum ring polymer contraction method, as described in the Supporting Information section.

For CPO-27-Zn, we observe that the water molecule forms a coordinative bond (Figure 5c/d) to the metal. Its oxygen atom O_{water} is at a distance to the Zn center of 2.32 Å (0.2 Å farther than in the hexaaqua zinc(II) complex[62]); its hydrogen atoms H_{water} are in proximity to one O_P and one O_{Cp} atom. This results in a distorted octahedral coordination geometry with most bonds being slightly elongated (see Table S3, Supporting Information). Seven O_{MOF}–H_{water} distances are below 3.0 Å, which indicates a strong affinity of the Zn site to water, in agreement with the water sorption data (Figure 4) and with previous studies.[35]

In addition, the coordination of water causes a change in the electron densities within the framework, which we quantify using the DDEC6 atomic population analysis charges (see Table S4, Supporting Information). Compared to the (original) desolvated structure, the charge of the O_{Cp} atoms is now significantly higher (−0.526 before → −0.560 after hydration). The same effect, though to a weaker extent, is observed for the O_P atoms (−0.603 → −0.610), while the O_{Ci} atoms are now slightly less negatively charged (−0.592 → −0.585). The Zn center is now slightly more positively charged (+0.977 → +0.987). The changes in electron densities result from both polarization and charge transfer effects due to the presence of the water molecule itself, and also from the subsequently induced geometrical relaxation of the framework, as shown in Table S4 (Supporting Information); the charge increases to +1.000 upon relaxation only, excluding the influence of water. These findings suggest a significant transfer of electron density from the coordinating water molecule to the CPO-27-Zn framework. In the monohydrate framework, this creates a positive net charge (+0.105) on the coordinating water molecule. Addition of more, non-coordinating water molecules, gradually reduces this net charge through H-bonding.[63] For 50% and 70% hydration ($Zn_2(dobdc)(H_2O)_5$, $Zn_2(dobdc)(H_2O)_7$, obtained by MD simulation), the net charge of the coordinating molecule is reduced to 0.071 and 0.051, respectively. In turn, a positively charged layer in the non-coordinating water domain is observed at a distance between *ca.* 3 and 5 Å from the pore center. However, we do not observe the creation of a negatively charged sublayer or significant changes in charges of all hydrogen atoms (Figures S2 and S3, Supporting Information). We note that our observations stand in slight contrast to previous DFT calculations on gas-phase fragments of desolvated CPO-27-*M*,[34] where higher charges for all atoms as well as a higher charge for O_{Cp} than for O_P were observed, contrary to our results. We attribute these differences to the different approach and applied methods (here: continuous framework) and to deviating degrees of pore filling.

CPO-27-Cu shows an entirely different picture, consistent with our experimental findings. After hydration and geometric relaxation, the local Cu environment undergoes a radical change from a distorted square-pyramidal to a highly distorted, nearly square-planar configuration (Figure 5d/f). This is a consequence of the elongation of the axial Cu—O_{Ci} bond from 2.42 to 2.60 Å (as the Cu center moves into the direction of the pore space) and the low affinity of the Cu center to water resulting in a large Cu—O_{water} distance of 2.64 Å (for the closest water molecule). Both axial bonds are *ca.* 0.2 Å longer than for the loosely bound axial water molecules in the hexaaqua copper(II) complex,[64-66] which is right at the boundary of the combined van-der-Waals radii.[67] Additionally, the water molecule is tilted toward the equatorial CuO_4 plane (bond lengths of 1.99 ± 0.02 Å) with one hydrogen atom pointing toward the O_{Cp} and O_P atoms, highlighted by two short O_{MOF}—H_{water} distances below 2.5 Å (see Table S3, Supporting Information). These observations verify our previously mentioned assumption that water does not coordinate to the open Cu metal site and instead interacts with the O atoms of the inorganic building unit via H-bonding.

Upon hydration, the atomic charge of the Cu center increases notably; for 20% hydration ($Cu_2(dobdc)(H_2O)_2$), the charge becomes less positive (+0.873 → +0.840, see Table S5, Supporting Information). Further, charges of O_P increase (−0.537 → −0.532) while the opposite is observed for O_{Cp} (−0.508 → −0.522). At the O_{Ci} atom, the charge also decreases (−0.601 → −0.587), with its negative charge remaining the highest observed. For 50% hydration ($Cu_2(dobdc)(H_2O)_5$, obtained by MD simulation), remarkably similar values are observed, which confirms that the impact of the first water molecule can hardly be distinguished from additional ones. Interestingly, we observe a broadening of the standard deviation for all oxygen atoms, which seems to depend on their accessibility to form H-bonds ($O_{Cp} > O_P > O_{Ci}$).[63] In addition, we observe a minor intra-molecular electron density transfer from the O to the H atoms, which is more pronounced for water molecules near the framework atoms, but does not affect the charge balance in water (Figure S4, Supporting Information). In contrast to previous experiments on water surfaces,[63] no (positively or negatively) charged sub-surfaces are observed in our study, which we attribute to (i) the confined space, as the reported depths for negatively charged subsurface layers lay between 3 and 8 Å,[63] and (ii) the limited interactions of the framework atoms with the confined water molecules. Except for the already mentioned significantly higher charges in previous DFT calculations,[34] we observe the same trends in our calculations on CPO-27-Cu.

In summary, the DFT data confirm significantly different situations for CPO-27-Zn and CPO-27-Cu (Figure 5g). Coordination of water to the open metal site in CPO-27-Zn results in a slightly distorted octahedral coordination environment of the Zn center, which becomes more positive in charge. Further, the more approachable O_{Cp} atoms possess the highest negative charge of all O atoms, thus favoring H-bonding with water, acting as secondary sorption sites. Otherwise, minor changes to the local Zn environment are observed. CPO-27-Cu shows a more drastic change. As a result of the higher electron densities of Cu and O_{Ci} after hydration, the Cu–O_{Ci} distance is strongly elongated, suggesting that O_{Ci} leaves the Cu coordination sphere. Further, no water molecules are in close proximity to the Cu center as water molecules interact with the O atoms of the framework (O_{Cp} and O_P) via H-bonding. As a consequence, the previously square-pyramidal environment of the Cu center is transformed to nearly square-planar geometry.

Next, we studied the spatial distribution of water molecules in the pores of CPO-27-Zn and CPO-27-Cu for different degrees of pore filling by molecular dynamics simulation. For CPO-27-Zn, the stepwise water uptake in the vapor sorption isotherm (Figure 4) suggests that the water molecules occupy defined, individual sites within the pores, similar to what crystallographic data revealed.[25] Addition of the first water molecule per Zn (*i.e.* $Zn_2(dobdc)(H_2O)_2$, monohydrate material) results in the saturation of the first site, which is the open metal site, as shown in the H_2O density probability histogram (**Figure 6a**). In the water sorption isotherm (Figure 4), this corresponds to the first, irreversible adsorption step (20% total water uptake). In the radial O_{water} density distribution (Figure S5, Supporting Information), this corresponds to the single, narrow peak at 5.5 Å distance from the pore center. We note that the coordinating water molecules show only slight vibrational displacement.

Addition of another *ca.* 1.5 water molecules per Zn (*i.e.* $Zn_2(dobdc)(H_2O)_5$) results in a weighted O occupancy of the other four sites. These are located at distances (from the pore center) of 5.5 Å (second site, same distance as the first site, compare

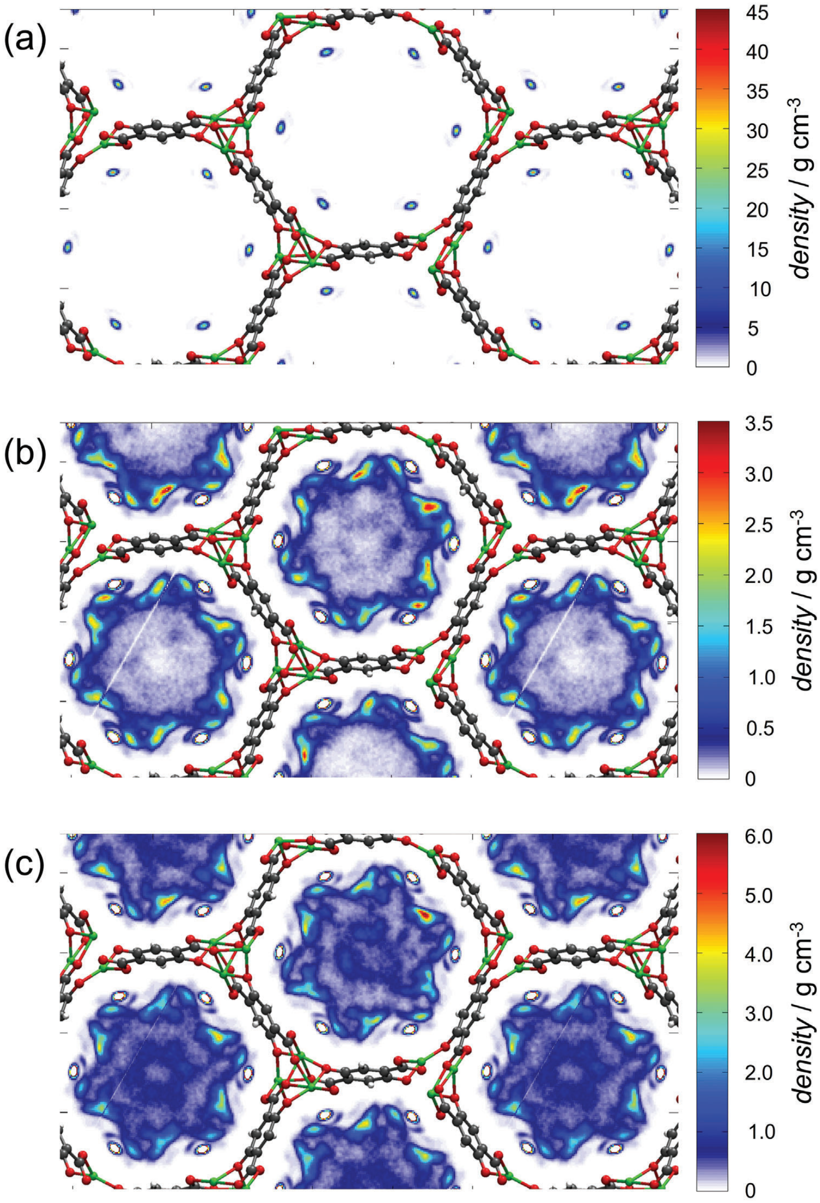

Figure 6. Probability density distribution histograms of water in CPO-27-Zn = $Zn_2(dobdc)(H_2O)_x$; (a) $x = 2$ (monohydrate), (b) $x = 5$, and (c) $x = 7$. For clarity, values > 3.5 and > 6.0 g cm^{-3} (occurring at the coordinating water molecule) are not shown in images (b) and (c), respectively; histograms with the full density value range are shown in Figure S7 (Supporting Information). (White lines are due to periodic boundary conditions of our simulations. Missing bonds in the framework structure are an artefact of the used VMD software package and do not refer to the real connectivity between the framework atoms. Unusually high densities stem from the small grid, that is, < 0.1 × 0.1 Å^2, that was used to track the position of the atomic nuclei, used for density calculations.).

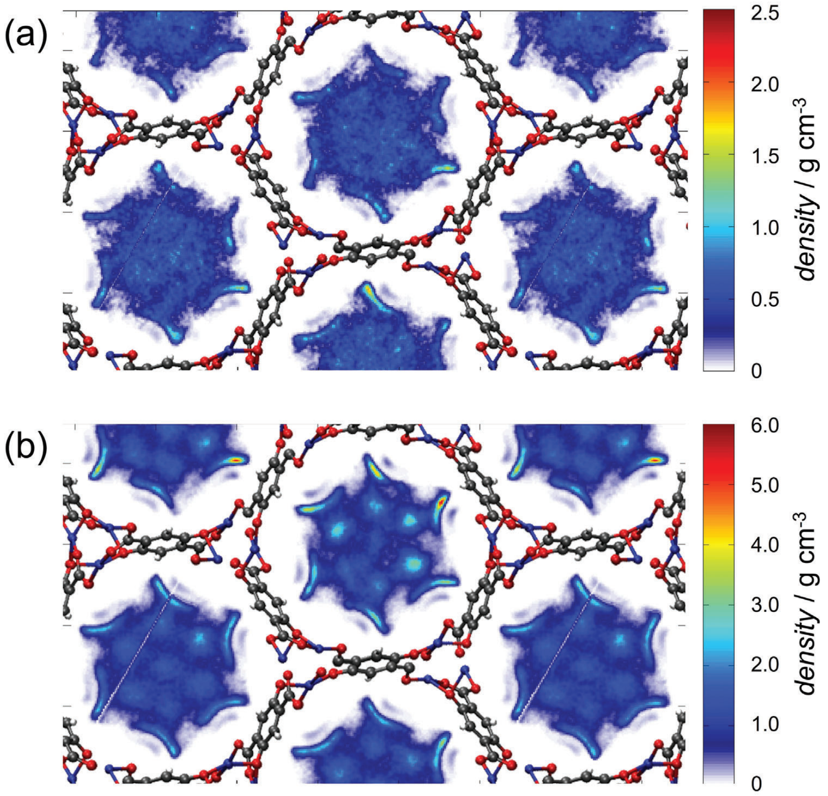

Figure 7. Probability density distribution histograms of water in CPO-27-Cu = $Cu_2(dobdc)(H_2O)_x$, (a) $x = 2$ (monohydrate) and (b) $x = 5$. Molecules form a star-like structure, resulting in seven pillars in the pore center. No molecules are found close to Cu, creating an empty space in its vicinity. Water shows a clear preference for H-bond formation with the framework carboxylate O atoms.

Figure S6, Supporting Information), 4.85 Å (third site), 4.05 Å (fourth site), and 1.3 Å (fifth site) (Figures S5 and S6, Supporting Information). This is supported by the density probability histogram (Figure 6b) that shows high occupancies at the second, third, and fourth site, because of the previously described H-bonding to framework oxygen atoms (O_{Cp} and O_P, see also H_{water} atom distribution, Figure S8, Supporting Information). The non-coordinating water molecules (*i.e.* second to fifth site) are 'mobile', that is, they exchange between sites,[35] resulting in broad density distributions along preferred paths. Negligible oxygen density is found near the center of the pore (fifth site), which makes it virtually indistinguishable from random movement through the pore. Again, this is consistent with the water sorption isotherms.

Further addition of another water molecule per Zn (*i.e.* $Zn_2(dobdc)(H_2O)_7$) increases the population of all available positions (Figure 6c). Those near the pore center experience the largest growth in occupancy (fourth and fifth adsorption site). In addition, the H_{water} atom distribution (Figure S8, Supporting Information) shows a strong preference for the added water molecules toward the pore center, resulting in the connection of all oxygen atoms via a H-bond network. This aligns with the third step in the water sorption isotherm (Figure 4a), expecting a preliminary pore saturation (*i.e.*, meta-stable state). We hypothesize that further addition of water to the framework will result in more distinct positions, matching those found in previous hydration experiments.[9] This is a gradual process that slowly progresses over a larger relative water pressure range as the movement of water molecules between different sorption sites becomes severely more hindered with each adsorbed water molecule. This is what the water sorption data (Figure 4a) suggest; future work will be dedicated to confirm this hypothesis by molecular dynamics simulation. We note that our radial water densities in CPO-27-Zn matches the general trend previously reported for CPO-27-Mg.[36] However, we observe a different weighting of the individual peaks, which may stem from (i) the incomplete pore filling in our system and/or (ii) the different metals discussed and/or (iii) the different methods used.

For CPO-27-Cu, addition of the first water molecule per Cu center (*i.e.* $Cu_2(dobdc)(H_2O)_2$, monohydrate material) does not suggest occupation of the open metal site (**Figure 7a**), consistent with the above-made observations. Rather, the water molecules tend to reside at the center of the pore (see also Figure S5, Supporting Information). We note that this state is not observed in the water sorption measurement, since adsorption of the first *ca.* 80% water occurs nearly simultaneously (Figure 4). Addition of another *ca.* 1.5 water molecules per Cu (*i.e.* $Cu_2(dobdc)(H_2O)_5$, Figure 7b) allows a more conclusive view on the interactions and arrangement of the water molecules, even though it marks a transition state during the sole sorption step in our experiments. As stated above, no oxygen atoms are found in proximity to the Cu center, resulting in an empty pocket. The nearest water molecules form H-bonds toward the O_P and O_{Cp} atoms, while others form additional H-bonds toward the O_{Cp} atoms. This eventually enforces a curved, star-like water arrangement (Figure S9b, Supporting Information). The pronounced peak in the radial density plots centered at 4.0 Å (see Figure S5, Supporting Information) indicates the accumulation of water close to the phenylene ring (third sorption site), which matches our findings on CPO-27-Zn and previous findings on CPO-27-Mg.[36] Close to the center of the pore, no preferred hydrogen atom orientations or positions are visible (Figure S9, Supporting Information). We observe the formation of seven pillar-like water clusters along the channel axis, one of which is located in the exact center of the pore (peaks at 2.5 and 0 Å, respectively, see Figure S5, Supporting Information). We assume that at higher loadings, the visible arrangement becomes more pronounced, as our results suggest that the perpendicular water clusters increase in intensity with water uptake. As soon as enough water molecules can be adsorbed (*ca.* 80% of total uptake with respect to our sorption experiments), accumulation of the aforementioned interactions results in pore condensation.

In summary, the molecular dynamics simulations confirm that water shows much stronger affinity to the open metal site in CPO-27-Zn than in CPO-27-Cu. As a result, the mechanism of pore filling and the structure of water in the filled pore are entirely different.

3. Conclusion

By combining experimental methods (manometric water vapor sorption analysis and FTIR spectroscopy) with DFT and MD calculations, we were able to obtain a comprehensive picture of the uptake of water in CPO-27-Zn and CPO-27-Cu. This includes the distinction of individual sorption sites and water-induced structural relaxation of the frameworks. CPO-27-Zn and CPO-27-Cu, though topologically identical, show completely different properties with respect to hydration. The uptake of water into the micropores occurs via different mechanisms, and the resulting structure of the water in the pores is also different. In CPO-27-Zn, water first coordinates to the Zn center. The coordinated water molecule serves as an anchor for adsorption of further water molecules by H-bonding, although the latter also form H-bonds with framework oxygen atoms. Adsorption occurs stepwise, with water molecules occupying defined positions inside the pores and exchanging between them. In CPO-27-Cu, water does not coordinate to the metal center for geometric reasons and for resulting electron density distribution; the respective position remains unoccupied. Water molecules adsorb to the pore wall by H-bonding to framework oxygen atoms. Pore filling occurs all at once, like classical pore condensation. Water in the pores of CPO-27-Cu show high mobility, forming clusters along the pore axis. The DFT as well as the MD calculations validate the distinct difference in behavior in the two CPO-27 materials. We have shown that the water in CPO-27-Zn accumulates at defined positions. The strength of interaction depends on the position inside the cell and relates to the electronic interactions between the framework and water molecules, which favor a step-wise pore condensation process. For CPO-27-Cu we observe a distinct difference in both structure and electronic interactions in the simulations. We found little interactions between MOF and water, which favor a complete pore condensation in one step.

Supporting Information

Supporting Information is available from the Wiley Online Library or from the author.

Acknowledgements

The generous allocation of computing time on the supercomputer "Noctua2" by the Paderborn Center for Parallel Computing (PC2) is kindly acknowledged.

Open access funding enabled and organized by Projekt DEAL.

Conflict of Interest

The authors declare no conflict of interest.

Data Availability Statement

The data that support the findings of this study are available in the supplementary material of this article.

Keywords

CPO-27, DFT calculations, metal-organic frameworks, MOF-74, molecular dynamics, open metal sites, water vapor sorption

Received: May 30, 2024
Revised: July 25, 2024
Published online:

---

[1] C. Janiak, J. K. Vieth, *New J. Chem.* **2010**, *34*, 2366.
[2] R. Freund, O. Zaremba, G. Arnauts, R. Ameloot, G. Skorupskii, M. Dinca, A. Bavykina, J. Gascon, A. Ejsmont, J. Goscianska, M. Kalmutzki, U. Lächelt, E. Ploetz, C. S. Diercks, S. Wuttke, *Angew. Chem., Int. Ed.* **2021**, *60*, 23975.
[3] Ü. Kökçam-Demir, A. Goldman, L. Esrafili, M. Gharib, A. Morsali, O. Weingart, C. Janiak, *Chem. Soc. Rev.* **2020**, *49*, 2751.
[4] P. D. C. Dietzel, Y. Morita, R. Blom, H. Fjellvåg, *Angew. Chem., Int. Ed.* **2005**, *44*, 6354.
[5] N. L. Rosi, J. Kim, M. Eddaoudi, B. Chen, M. O'Keeffe, O. M. Yaghi, *J. Am. Chem. Soc.* **2005**, *127*, 1504.
[6] G. Calleja, R. Sanz, G. Orcajo, D. Briones, P. Leo, F. Martínez, *Catal. Today.* **2014**, *227*, 130.
[7] E. O. Fetisov, M. S. Shah, J. R. Long, M. Tsapatsis, J. I. Siepmann, *Chem. Commun.* **2018**, *54*, 10816.

[8] I. Strauss, A. Mundstock, D. Hinrichs, R. Himstedt, A. Knebel, C. Reinhardt, D. Dorfs, J. Caro, *Angew. Chem., Int. Ed.* **2018**, *57*, 7434.

[9] M. H. Rosnes, B. Pato-Doldán, R. E. Johnsen, A. Mundstock, J. Caro, P. D. C. Dietzel, *Microp. Mesop. Mater.* **2020**, *309*, 110503.

[10] L. J. Small, M. E. Schindelholz, T. M. Nenoff, *Ind. Eng. Chem. Res.* **2021**, *60*, 7998.

[11] J. Yan, J. Feng, J. Ge, J. Chen, F. Wang, C. Xiang, D. Wang, Q. Yu, H. Zeng, *IEEE Photonics Technol. Lett.* **2022**, *34*, 77.

[12] M. J. Kalmutzki, C. S. Diercks, O. M. Yaghi, *Adv. Mater.* **2018**, *30*, 1704304.

[13] N. Hanikel, M. S. Prévot, O. M. Yaghi, *Nat. Nanotechnol.* **2020**, *15*, 348.

[14] C. Solís, D. Palaci, F. X. Llabres i Xamena, J. M. Serra, *J. Phys. Chem. C.* **2014**, *118*, 21663.

[15] S. Hwang, E. J. Lee, D. Song, N. C. Jeong, *ACS Appl. Mater. Interfaces.* **2018**, *10*, 35354.

[16] A. Javed, I. Strauss, H. Bunzen, J. Caro, M. Tiemann, *Nanomaterials.* **2020**, *10*, 1263.

[17] I. E. Khalil, J. Fonseca, M. R. Reithofer, T. Eder, J. M. Chin, *Coord. Chem. Rev.* **2023**, *481*, 215043.

[18] Y. R. Liu, Y. Y. Chen, H. Y. Zhao, G. Li, *Coord. Chem. Rev.* **2024**, *499*, 215516.

[19] M. F. Lange, K. J. F. M. Verouden, T. J. H. Vlugt, J. Gascon, F. Kapteijn, *Chem. Rev.* **2015**, *115*, 12205.

[20] I. Strauss, A. Mundstock, M. Treger, K. Lange, S. Hwang, C. Chmelik, P. Rusch, N. C. Bigall, T. Pichler, H. Shiozawa, J. Caro, *ACS Appl. Mater. Interfaces.* **2019**, *11*, 14175.

[21] L. T. Zhang, Y. Zhou, S. T. Han, *Angew. Chem., Int. Ed.* **2021**, *60*, 15192.

[22] T. M. McDonald, W. R. Lee, J. A. Mason, B. M. Wiers, C. S. Hong, J. R. Long, *J. Am. Chem. Soc.* **2012**, *134*, 7056.

[23] C. A. Trickett, A. Helal, B. A. Al-Maythalony, Z. H. Yamani, K. E. Cordova, O. M. Yaghi, *Nat. Rev. Mater.* **2017**, *2*, 17045.

[24] Y. S. Wei, M. Zhang, R. Zou, Q. Xu, *Chem. Rev.* **2020**, *120*, 12089.

[25] P. D. C. Dietzel, R. E. Johnsen, R. Blom, H. Fjellvåg, *Chem. - Eur. J.* **2008**, *14*, 2389.

[26] H. Furukawa, F. Gándara, Y. B. Zhang, J. Jiang, W. L. Queen, M. R. Hudson, O. M. Yaghi, *J. Am. Chem. Soc.* **2014**, *136*, 5271.

[27] B. Zhang, Z. Zhu, X. Wang, X. Liu, F. Kapteijn, *Adv. Funct. Mater.* **2023**, 2304788.

[28] J. B. DeCoste, G. W. Peterson, B. J. Schindler, K. L. Killops, M. A. Browe, J. J. Mahle, *J. Mater. Chem. A.* **2013**, *1*, 11922.

[29] P. M. Schoenecker, C. G. Carson, H. Jasuja, C. J. J. Flemming, K. S. Walton, *Ind. Eng. Chem. Res.* **2012**, *51*, 6513.

[30] A. Metrane, A. Delhali, M. Ouikhalfan, A. H. Assen, Y. Belmabkhout, *J. Chem. Eng. Data.* **2022**, *67*, 1617.

[31] C. Weinberger, F. Zysk, M. Hartmann, N. K. Kaliannan, W. Keil, T. D. Kühne, M. Tiemann, *Adv. Mater. Interfaces.* **2022**, *9*, 2200245.

[32] K. Lee, J. D. Howe, L.-C. Lin, B. Smit, J. B. Neaton, *Chem. Mater.* **2015**, *27*, 668.

[33] L. Valenzano, B. Civalleri, S. Chavan, G. T. Palomino, C. O. Areán, S. Bordiga, *J. Phys. Chem. C.* **2010**, *114*, 11185.

[34] T. Pham, K. A. Forrest, J. Eckert, B. Space, *Cryst. Growth Des.* **2016**, *16*, 867.

[35] Y. Li, X. Wang, D. Xu, J. D. Chung, M. Kaviany, B. Huang, *J. Phys. Chem. C.* **2015**, *119*, 13021.

[36] X. Peng, L. Lin, W. Sun, B. Smit, *AIChE J.* **2015**, *61*, 3708.

[37] M. G. Lopez, P. Canepa, T. Thonhauser, *J. Chem. Phys.* **2013**, *138*, 154704.

[38] T. A. Manz, N. G. Limas, *RSC Adv.* **2016**, *6*, 47771.

[39] N. G. Limas, T. A. Manz, *RSC Adv.* **2016**, *6*, 45727.

[40] T. A. Manz, D. S. Sholl, *J. Chem. Theory Comput.* **2010**, *6*, 2455.

[41] T. A. Manz, D. S. Sholl, *J. Chem. Theory Comput.* **2011**, *7*, 4146.

[42] T. A. Manz, D. S. Sholl, *J. Chem. Theory Comput.* **2012**, *8*, 2844.

[43] T. A. Manz, *RSC Adv.* **2017**, *7*, 45552.

[44] L. J. Wang, H. Deng, H. Furukawa, F. Gándara, K. E. Cordova, D. Peri, O. M. Yaghi, *Inorg. Chem.* **2014**, *53*, 10937.

[45] M. H. Rosnes, M. Opitz, M. Frontzek, W. Lohstroh, J. P. Embs, P. A. Georgiev, P. D. C. Dietzel, *J. Mater. Chem. A.* **2015**, *3*, 4827.

[46] M. Thommes, K. Kaneko, A. V. Neimark, J. P. Olivier, F. Rodriguez-Reinoso, J. Rouquerol, K. S. W. Sing, *Pure Appl. Chem.* **2015**, *87*, 1051.

[47] B. Pato-Doldán, M. H. Rosnes, P. D. C. Dietzel, *ChemSusChem.* **2017**, *10*, 1710.

[48] M. V. Veidis, G. H. Schreiber, T. E. Gough, G. J. Palenik, *J. Am. Chem. Soc.* **1969**, *91*, 1859.

[49] N. Heidary, D. Chartrand, A. Guiet, N. Kornienko, *Chem. Sci.* **2021**, *12*, 7324.

[50] G. Onori, A. Santucci, *J. Phys. Chem.* **1993**, *97*, 5430.

[51] T. Iiyama, M. Ruike, K. Kaneko, *Chem. Phys. Lett.* **2000**, *331*, 359.

[52] J. Alcañiz-Monge, A. Linares-Solano, B. Rand, *J. Phys. Chem. B.* **2002**, *106*, 3209.

[53] I. Brovchenko, A. Geiger, A. Oleinikova, *J. Phys. Condens. Matter.* **2004**, *16*, S5345.

[54] T. Ohba, H. Kanoh, K. Kaneko, *J. Phys. Chem. B.* **2004**, *108*, 14964.

[55] T. Ohba, H. Kanoh, K. Kaneko, *Nano Lett.* **2005**, *5*, 227.

[56] P. Gallo, M. Rovere, S.-H. Chen, *J. Phys. Condens. Matter.* **2010**, *22*, 284102.

[57] M. Sadeghi, G. A. Parsafar, *Phys. Chem. Chem. Phys.* **2013**, *15*, 7379.

[58] M. Thommes, J. Morell, K. A. Cychosz, M. Fröba, *Langmuir.* **2013**, *29*, 14893.

[59] J. B. Mietner, F. J. Brieler, Y. J. Lee, M. Fröba, *Angew. Chem., Int. Ed.* **2017**, *56*, 12348.

[60] B. Malfait, A. Moréac, A. Jani, R. Lefort, P. Huber, M. Fröba, D. Morineau, *J. Phys. Chem. C.* **2022**, *126*, 3520.

[61] K. Schlichte, T. Kratzke, S. Kaskel, *Microporous Mesoporous Mater.* **2004**, *73*, 81.

[62] M. Hartmann, T. Clark, R. van Eldik, *J. Am. Chem. Soc.* **1997**, *119*, 7843.

[63] R. Vàcha, O. Marsalek, A. P. Willard, D. J. Bonthuis, R. R. Netz, P. Jungwirth, *J. Phys. Chem. Lett.* **2012**, *3*, 107.

[64] T. K. Sham, J. B. Hastings, M. L. Perlman, *J. Am. Chem. Soc.* **1980**, *102*, 5904.

[65] A. Pasquarello, I. Petri, P. S. Salmon, O. Parisel, R. Car, É. Tóth, D. H. Powell, H. E. Fischer, L. Helm, A. E. Merbach, *Science.* **2001**, *291*, 856.

[66] S. Gómez-Salces, F. Aguado, R. Valiente, F. Rodríguez, *Angew. Chem., Int. Ed.* **2012**, *51*, 9335.

[67] A. Bondi, *J. Phys. Chem.* **1964**, *68*, 441.

ADVANCED MATERIALS INTERFACES
Open Access

Supporting Information

for *Adv. Mater. Interfaces*, DOI 10.1002/admi.202400476

Understanding Hydration in CPO-27 Metal-Organic Frameworks: Strong Impact of the Chemical Nature of the Metal (Cu, Zn)

Marvin Kloß, Michael Beerbaum, Dominik Baier, Christian Weinberger, Frederik Zysk, Hossam Elgabarty, Thomas D. Kühne and Michael Tiemann**

Understanding Hydration in CPO-27 Metal-Organic Frameworks: Strong Impact of the Chemical Nature of the Metal (Cu, Zn)

SUPPORTING INFORMATION

Marvin Kloß,[1] Michael Beerbaum,[2] Dominik Baier,[1] Christian Weinberger,[1] Frederik Zysk,[3]
Hossam Elgabarty,[3] Thomas D. Kühne*,[2] and Michael Tiemann*,[1]

[1] *Department of Chemistry – Inorganic Chemistry, Faculty of Science, Paderborn University*
Warburger Str. 100, 33098, Paderborn, Germany (michael.tiemann@upb.de)

[2] *Center for Advanced Systems Understanding (CASUS), Untermarkt 20, 02826 Görlitz, Germany;*
Helmholtz Zentrum Dresden-Rossendorf, Bautzner Landstr. 400, 01328 Dresden, Germany
(t.kuehne@hzdr.de)

[3] *Department of Chemistry – Theoretical Chemistry, Faculty of Science, Paderborn University*
Warburger Str. 100, 33098, Paderborn, Germany

METHODS: EXPERIMENTAL

Materials and Methods: CPO-27-Zn[1] and CPO-27-Cu[2] were synthesized under solvothermal conditions according to modified reported procedures. The solvent was removed by heating under dynamic vacuum conditions; the desolvated samples were stored in a glove box under Ar atmosphere. Products were characterized by PXRD and compared with literature data (CCDC numbers 1516648 for Cu[3] and 1863522 for Zn[4]) using simulated peak positions, obtained with the *VESTA* software package.[5] The linker molecule (2,5-dihydroxyterephthalic acid) was synthesized according to a modified literature procedure.[6] All other chemicals and solvents were purchased from commercial suppliers (as stated below) and used without further purification.

Synthesis of 2,5-dihydroxyterephthalic acid: Dimethyl 2,5-dioxo-cyclohexane-1,4-dicarboxylic acid (11.4 g, 51.4 mmol, 1.0 eq) was dissolved in glacial acetic acid (50 mL). The mixture was heated to 80 °C and *N*-chlorosuccinimide (NCS, 7.22 g, 54.2 mmol, 1.08 eq) was added portion-wise over the course of 30 minutes. During this process, a yellow precipitate was formed. After complete addition of NCS, the mixture was heated for additional 2 hours to 80 °C. After cooling back to room temperature, a bright yellow solid was filtered off and washed with copious amounts of deionized water (300-400 mL) and methanol (2 x 10 mL). The product was dried overnight at 60 °C. Dimethyl 2,5-dihydroxyterephthalate (8.34 g, 36.9 mmol, 74 %) was isolated as a bright yellow, crystalline solid. ^{1}H NMR (700 MHz, $CDCl_3$): δ = 10.05 (s, 2H), 7.46 (s, 2H), 3.97 (s, 6H) ppm. ^{13}C NMR (175 MHz, $CDCl_3$) δ = 169.7, 153.1, 118.5, 118.0, 53.0 ppm. Dimethyl 2,5-dihydroxyterephthalate (8.34 g, 36.9 mmol, 1 eq) was dissolved in a solution of sodium hydroxide (6.71 g, 167.7 mmol, 4.55 eq) in deionized water (130 mL). The mixture was heated to 80 °C for 6 h, during which the initially yellow solution turned into an orange and finally dark brown solution. After cooling to room temperature, the solution was poured into a mixture of concentrated aqueous hydrochloric acid and ice. During this process, a light-yellow precipitate was formed. The pH was adjusted to 1. The product was separated by filtration and washed with copious amounts of water (approx. 700 mL) until the pH was neutral. The product was dried overnight at 60 °C in an oven to afford 2,5-dihydroxyterephthalic acid (5.27 g, 26.6 mmol, 72 %) as a light-yellow solid. ^{1}H NMR (500 MHz, dmso-d$_6$): δ = 11.34 (brs, 2H), 7.27 (s, 2H) ppm. ^{13}C NMR (125 MHz, dmso-d$_6$) δ = 170.8, 152.5, 119.8, 117.8 ppm.

Preparation of CPO-27-Zn: Zinc(II) nitrate hexahydrate (4.19 g, 14.1 mmol, 1.0 eq) was dissolved in a mixture of DMF (30 mL) and deionized water (3.6 mL) and transferred to a Teflon-lined insert (125 mL). Then, 2,5-dihydroxyterephthalic acid (0.9 g, 4.55 mmol, 0.33 eq) was dissolved in a mixture of DMF (30 mL) and ethanol (3.6 mL). The obtained solution was transferred to the insert containing the zinc salt solution and the mixture was stirred briefly. The insert was placed in a stainless-steel reactor (*Parr Instruments*), sealed, and reacted in a preheated oven at 120 °C for 24 h. After cooling, the yellow solid was separated by filtration over a glass frit and washed with deionized water (4 x 30 mL) and methanol (30 mL). Afterwards, the solvent was exchanged by methanol (four times), leaving each portion to stand for 30 to 45 minutes. The obtained product was dried in multiple steps. For the first step, the product was placed in a round flask under dynamic vacuum for 20 h. Then, the product was heated in three steps from 60 °C (hold for 90 minutes) to 100 °C (hold for 90 minutes) and 150 °C (hold for 20 h). The desolvated product (orange-yellow solid) was stored in a glove box under argon atmosphere.

Synthesis of CPO-27-Cu: Copper(II) nitrate trihydrate (2.414 g, 10.0 mmol, 1.0 eq) was dissolved in DMF (15 mL) under sonification and transferred to a Teflon-lined insert (125 mL). Then, 2,5-dihydroxyterephthalic acid (0.99 g, 5.0 mmol, 0.5 eq) and 1,4-diazabicyclo[2.2.2]octan (dabco, 0.28 g, 2.5 mmol, 0.25 eq) were separately dissolved in DMF (2,5-dihydroxyterephthalic acid in 40 mL, dabco in 10 mL) under sonification. The obtained solutions were combined in the insert and the mixture was stirred briefly. The insert was placed in a stainless-steel reactor (*Parr Instruments*), sealed, and reacted in a preheated oven at 60 °C for 72 h. After cooling, the dark red solid was separated by filtration over a glass frit and washed with deionized water (4 x 30 mL) and methanol (30 mL). Afterwards, the solvent was exchanged by methanol (four times), leaving each portion to stand for 30 to 45 minutes. The obtained product was dried in multiple steps. For the first step, the product was placed in a round flask under dynamic vacuum for 20 h. Then, the product was heated in three steps from 60 °C (hold for 90 minutes) to 100 °C (hold for 90 minutes) and 120 °C (hold for 20 h). The desolvated product (dark brown solid) was stored in a glove box under argon atmosphere.

NMR: ^{1}H and ^{13}C NMR spectra were recorded using Bruker *Advance 500* and Bruker *Ascent 700* spectrometers. Chemical shifts were calibrated to the resonance of residual non-deuterated solvent.

FTIR: FTIR spectroscopy was performed with a Bruker *Vertex 70 spectrometer* in ATR mode using the *Platinum ATR unit A225* with a diamond ATR crystal. Powder samples were pressed on the crystal during the measurement. After the measurement of hydrated samples, an automatic baseline correction was applied using the *OPUS 7.2.1* software package. The correction was performed using a *concave rubberband correction*, using 10 iterations and 32 baseline points. Gaussian least-square fits of the water stretching band were performed using the *peak analyzer* function of the *Origin23b* software package. First, the data within the range from 4500 to 2400 cm^{-1} was taken and normalized. For the fitting procedure, the data from 3850 to 2750 cm^{-1}. Then, three peaks were set with starting positions at 3560 cm^{-1} (multimer water), 3390 cm^{-1} (intermediate water) and 3210 cm^{-1} (network water). Only positive peak areas were allowed while the previously freely adjusted baseline was set constant. No further restrictions were used. We note that the selection of different (reasonable) starting positions resulted in similar results. It is noted that the fit results possess a small error, caused by the overlap of the aromatic C-H vibration of the linker molecule with the water stretching bands.

XRD: Powder X-ray diffraction (XRD) data was collected on a Bruker *D8 Advance* diffractometer with a step size of 0.02° and a counting time of 1 or 3 seconds per step. Patterns are normalized for better comparison of relative intensities.

N_2 Physisorption: N_2 physisorption analysis was performed with a Quantachrome *Autosorb 6B* at 77 K. The relative pressure range suitable for the BET surface area calculation was determined using the Rouquerol criteria.[7] Total pore volumes were determined from the uptake at $p/p_0 \approx 0.5$. Activation of the samples was performed in a stepwise manner. The desolvated (ds) samples were transferred to the measurement cell and dispersed in methanol twice for 45 minutes. After each step, the solvent was removed under dynamic vacuum. The pre-dried samples were degassed for approximately 17 hours applying the following procedure: The samples were heated from room temperature to 60 °C with a heating rate of 2 °C min^{-1} after which the temperature was held for two hours. Then, the sample was heated to 100 °C with the same heating rate (2 °C min^{-1}) and the temperature held for another two hours. Finally, the sample was heated (2 °C min^{-1}) to 150 °C (or 120 °C for the copper derivative) and the temperature held for additional 12 hours, after which the sample was allowed to cool to room temperature.

H_2O vapor sorption: Water experiments were performed on a *3Flex instrument* (*Micromeritics*) at 298 K (25 °C) with double distilled (and degassed) water. The samples were heated from room temperature to 60 °C with a heating rate of 2 K min^{-1} after which the temperature was increased to 100 °C with the same heating rate (2 K min^{-1}) and, finally, heated (2 K min^{-1}) to 150 °C (or 120 °C for the copper derivative).

Thermal analysis: Thermogravimetric (TGA) analysis was performed using a *TGA PT1000* thermobalance from *Linseis*. The sample was placed in a corundum crucible. Measurements were performed under a constant Argon gas (Purity 5.0 from *Wöhning Gas*) flow (100 mL min^{-1}) in a temperature range from 25 °C to 800 °C using a heating rate of 5 °C min^{-1}. For mass spectroscopy, the instrument was coupled with a Pfeiffer *Vacuum Omnistar* mass spectrometer.

Elemental analysis: Elemental analysis was performed using an Elementar *vario MICRO Cube* of the company.

METHODS: SIMULATION

All simulations were performed on 1×1×4 supercells, based on the crystal structure data (CCDC Numbers 1516648 for Cu, 1516647 for Zn)[3,4] using periodic boundary conditions (pbc). The created cells are without defects. One water molecule was added to each metal center with a preselected distance of 2 Å. Geometry was optimized using KS-DFT, which is provided in the Quickstep (QS) module in cp2k. We employed the Gaussian and plane waves method.[8,9] We applied GTH-PBE potentials[10-12] with a DZVP-MOLOPT-GTH basis set,[13] which was set to the short-ranged basis set for the transition metals, which work well in condensed phases. For the XC potential we used the PBE potential with the DFTD3 correction provided by Grimme *et al.*.[14]

Additional water molecules were added to the pores in order to obtain various filling degrees. For the first fillings step, we generated bulk water *via* centroid molecular dynamics (cmd) simulations using the second-generation Car-Parinello-based quantum ring polymer contraction method by Kühne *et al.*.[15,16] We used the program zeo++ with the largest inner pore diameter and the largest free diffusive diameter to determine the free space filled by water.[17,18] This resulted in a loading of exactly 4.8 and 5.1 water molecules per formula unit for the copper and zinc compounds, respectively. For the higher filling degree of 7.2 water per formula unit of CPO-27-Zn (*i.e.* $Zn_2(dobdc)(H_2O)_7$), we used the NVT equilibrated structure of $Zn_2(dobdc)(H_2O)_5$ and added additional water molecules.

The cells were equilibrated using PM6-FM semiempirical MD calculations[19,20] for a timeframe of at least 20 ps. The CSVR thermostat[21] was applied at 300 K with a time constant of 30.0 fs and a temperature tolerance of 20 K in the NVT ensemble. The evaluated trajectory was set in the NVE ensemble at 300 K, with a timestep of 0.1 fs, for a total trajectory length of 300 ps. For both the equilibration and production run, we set the first 648 atoms, which belong to the atoms of the MOF structure, to static conditions, leaving only the water molecules mobile.

We furthermore determined the charges on the atoms by determining the electronic densities within cp2k with KS-DFT, using the same basis sets and potentials as previously mentioned. The charges were obtained using the DDEC6 charge partitioning method included in Chargemol 3.5[22,23] based on one frame each. For discussion, averages of the charges for all atoms of the same type and structural behavior were used.

Radial distribution function, as provided by the TRAVIS package,[24,25] with a resolution of 1 pm were calculated. We employed the correction for the radial distribution and averaged the distances. Finally, the radial density probability distributions as well as the topological density probability distributions (see Equations S1-S2) were calculated with a resolution of 0.1 Å for all calculations.

Radial particle density calculations were performed by employing a hollow cylindric approach around each pore axis:

$$\rho = \sum_i \frac{m_i}{V} \bullet \frac{1}{n_{timesteps}} = \sum_i M_i N_i \bullet \frac{1}{N_A \bullet n_{Pores} \pi (R^2 - r^2) h} \bullet \frac{1}{n_{timesteps}} \tag{S1}$$

with	ρ	local density	$[\frac{g}{cm^3}]$
	m_i	total mass of atoms i	[g]
	V	volume	$[cm^3]$
	$n_{timesteps}$	number of frames calculated	[-]
	M_i	molar mass of atoms i	$[\frac{g}{mol}]$
	N_i	number of atoms of type i per frame	[-]
	N_A	Avogadro number	$[\frac{1}{mol}]$
	n_{Pores}	number of pores per cell	[-]
	R	outer radius of the hollow cylinder	[Å]
	r	inner radius of the hollow cylinder	[Å]
	h	height of the cell	[Å]

Topological particle density calculations were performed by applying a fine grid with a size of Δ*x* and Δ*y* over the cell and tracking the positions of the individual atoms inside each grid cell:

$$\rho = \sum_i \frac{m_i}{V} \bullet \frac{1}{n_{timesteps}} = \sum_i M_i N_i \bullet \frac{1}{N_A \bullet \Delta x \Delta y \bullet h} \bullet \frac{1}{n_{timesteps}} \tag{S2}$$

with	Δx	grid size along axis x	[Å]
	Δy	grid size along axis y	[Å]

SUPPORTING DATA:

Table S1. Specific surface areas and pore volumes (determined at $p/p_0 \approx 0.5$) obtained from the N_2 sorption isotherms.

	S_{BET} / m^2 g^{-1}	V_{Pore} / m^3 g^{-1}
CPO-27-Zn	1240	0.59
CPO-27-Cu	860	0.37

Table S2. Elemental analysis (C, H) of hydrated CPO-27-Zn and CPO-27-Cu and the assigned amounts of water molecules *x* per formula unit $M_2(dobdc)(H_2O)_x$.

	C	H	*x*
Zn	19.03	4.41	10
	19.05	4.42	10
	19.32	5.44	10
	19.22	4.31	10
Cu	20.08	4.14	9
	20.14	4.13	9
	20.09	4.27	9
	19.95	4.12	9

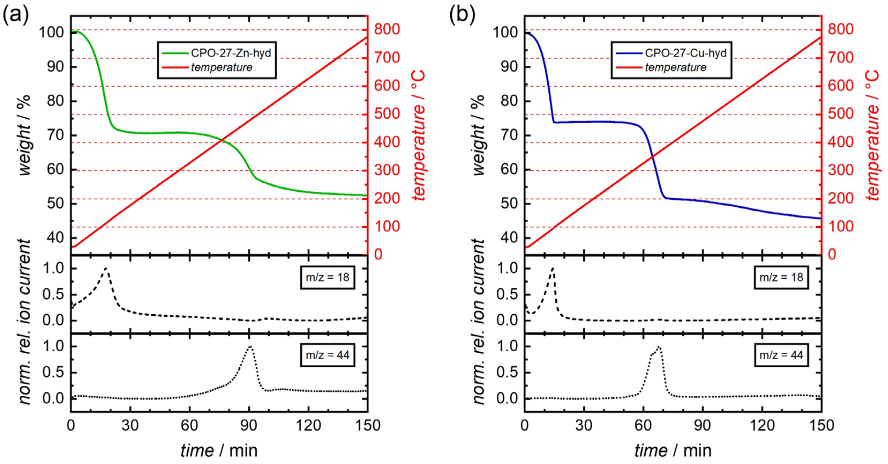

Figure S1. Thermogravimetric analysis coupled with mass ion detection (m/z = 18: H_2O^+, m/z = 44: CO_2^+) of hydrated **(a)** CPO-27-Zn and **(b)** CPO-27-Cu (heating rate: 5 °C min^{-1}).

Table S3. Interatomic distances in monohydrate CPO-27-Zn (= $Zn_2(dobdc)(H_2O)_2$) and monohydrate CPO-27-Cu (= $Cu_2(dobdc)(H_2O)_2$). The Zn centers possess a slightly distorted octahedral coordination sphere, with the water molecule tightly bound to the open metal site. In contrast, the Cu centers adopt a distorted planar square coordination environment, with the axial O_{Ci}^* leaving the coordinating sphere.

$Zn_2(dobdc)(H_2O)_2$				$Cu_2(dobdc)(H_2O)_2$		
atomic distance	crystal structure / Å	after hydration / Å		atomic distance	crystal structure / Å	after hydration / Å
$Zn - O_P$	2.03 ± 0.01	2.02 ± 0.03		$Cu - O_P$	1.94 ± 0.02	1.99 ± 0.02
$Zn - O_{Ci}$	2.15 ± 0.01	2.18 ± 0.03		$Cu - O_{Ci}$	1.94 ± 0.02	1.99 ± 0.02
$Zn - O_{Cp}$	1.96 ± 0.01	2.02 ± 0.03		$Cu - O_{Cp}$	1.94 ± 0.02	1.99 ± 0.02
$Zn - O_{Ci}^*$	2.03 ± 0.01	2.18 ± 0.03		$Cu - O_{Ci}^*$	2.42 ± 0.02	2.60 ± 0.03
$Zn - O_W$	-	2.32 ± 0.03		$Cu - O_W$	-	2.64 ± 0.07
$O_{MOF} - \underline{\mathbf{H}}_2O_W$	-	2.25 ± 0.01 2.35 ± 0.01 2.41 ± 0.01 2.45 ± 0.01 2.50 ± 0.01 2.65 ± 0.02 2.77 ± 0.01		$O_{MOF} - \underline{\mathbf{H}}_2O_W$		2.24 ± 0.05 2.39 ± 0.04

Table S4. Atomic charges (in electrons) of Zn, coordinating O atoms as well as net charges on the water molecules, determined for different amounts of water. The electronic structure in the framework changes upon hydration, as a consequence of both the presence of the water molecule itself and the thus-induced geometrical relaxation of the framework. (To discriminate between both factors, the water molecule was temporarily removed again, after geometric relaxation, keeping the (relaxed) structure unchanged.) Coordinating water transfers electron density to Zn. Further addition of water increases the electron density of the coordinating water molecules. After the addition of 7 water molecules per formula unit (*i.e.* $Zn_2(dobdc)(H_2O)_7$), the average charge in the non-coordinating water becomes near zero; however, this does not reflect the charge distribution close to the surface (see Figures S2 and S3).

atom	atomic charges / electrons				
	desolvated framework	relaxed framework*	partially hydrated framework $Zn_2(dobdc)(H_2O)_x$		
			$x = 2$	$x = 5$	$x = 7$
Zn	0.977 ± 0.001	1.000 ± 0.001	0.987 ± 0.001	0.987 ± 0.015	0.981 ± 0.013
O_P	-0.603 ± 0.001	-0.592 ± 0.001	-0.610 ± 0.002	-0.610 ± 0.008	-0.610 ± 0.009
O_{Cp}	-0.526 ± 0.001	-0.541 ± 0.001	-0.560 ± 0.001	-0.561 ± 0.011	-0.560 ± 0.010
O_{Ci}/O_{Ci}^*	-0.592 ± 0.002	-0.591 ± 0.001	-0.585 ± 0.001	-0.580 ± 0.009	-0.580 ± 0.010
O of coordinating H_2O (O_W)			-0.709 ± 0.001	-0.744 ± 0.006	-0.751 ± 0.004
H of coordinating H_2O (H_W)			0.407 ± 0.001	0.403 ± 0.003	0.395 ± 0.001
net charge coordinating H_2O			0.104 ± 0.002	0.071 ± 0.001	0.051 ± 0.002
O of non-coordinating H_2O				-0.761 ± 0.001	-0.755 ± 0.003
H of non-coordinating H_2O				0.390 ± 0.001	0.387 ± 0.001
net charge non-coordinating H_2O				0.019 ± 0.005	0.019 ± 0.005
O of all H_2O, average				-0.751 ± 0.029	-0.751 ± 0.026
H of all H_2O, average				0.395 ± 0.016	0.389 ± 0.015
net charge all H_2O, average				0.039 ± 0.002	0.028 ± 0.002

* in the absence of water

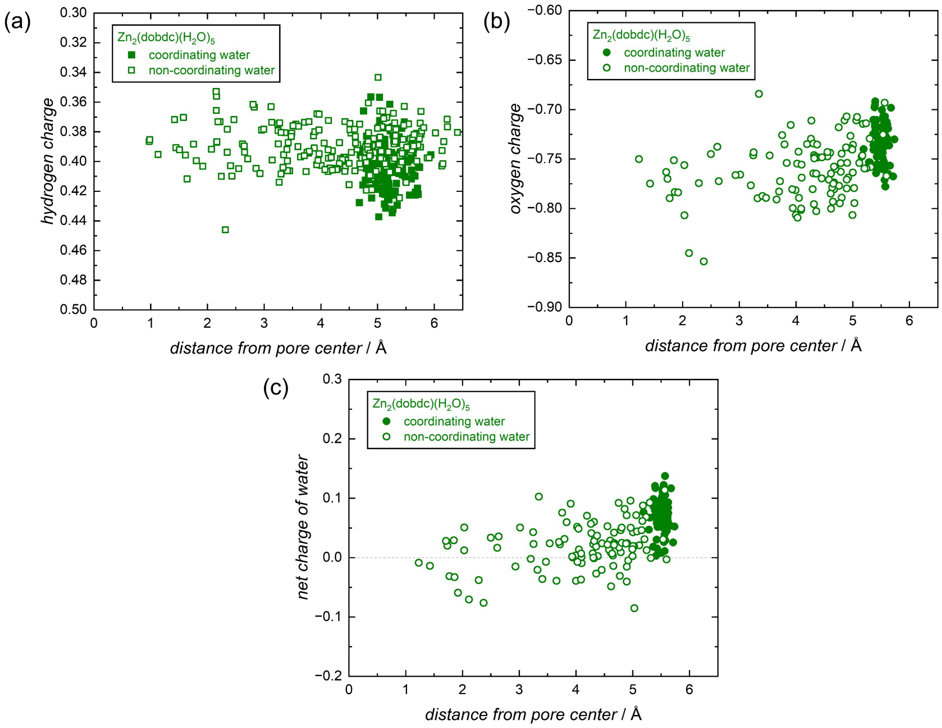

Figure S2. Charge distributions at coordinating and non-coordinating water molecules in $Zn_2(dobdc)(H_2O)_5$: (a) H_{water} atoms, (b) and O_{water} atoms, (c) resulting H_2O net charge. (For the net charges, those of both H atoms and the O atom were considered. The position relative to the pore center refers to the respective water O positions.) Charges of H_{water} atoms in non-coordinating water do not change in relation to their position and differ from those of H_{water} atoms in coordinating water. For the O_{water} atoms, we note a distinct decrease of electron charge density close to the pore walls of the framework, resulting in a net positive charge of the surface-near water layer (see **Table S4**).

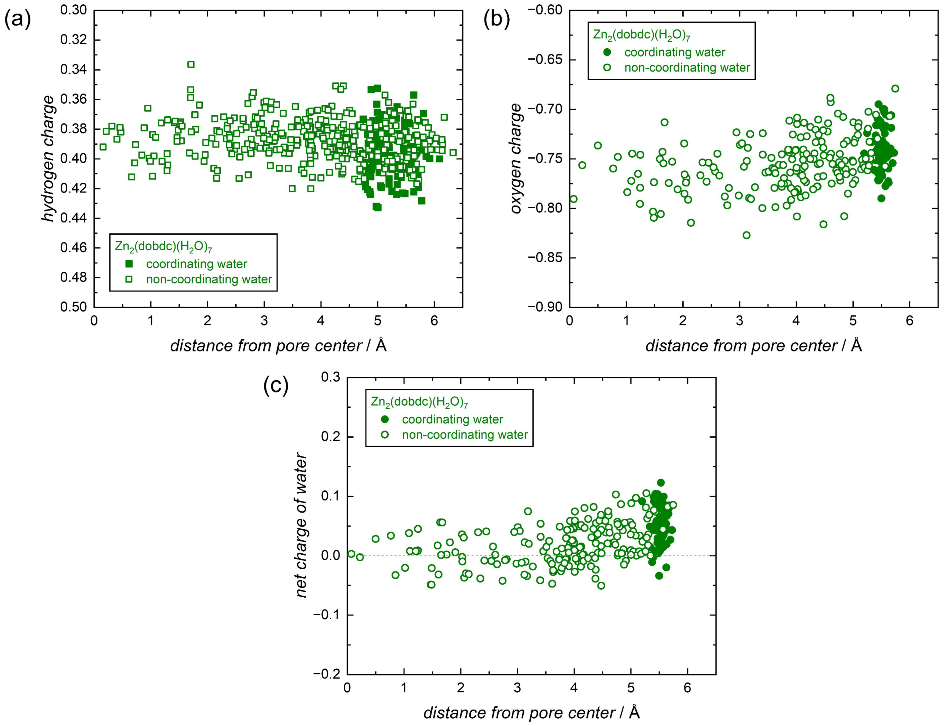

Figure S3. Charge distributions at coordinating and non-coordinating water molecules in $Zn_2(dobdc)(H_2O)_7$: (a) H_{water} atoms, (b) and O_{water} atoms, (c) resulting H_2O net charge. (For the net charges, those of both H atoms and the O atom were considered. The position relative to the pore center refers to the respective water O positions.) The H_{water} atoms show no charge dependency in respect to their location as the average charge of H_{water} atoms in coordinating water matches those found in non-coordinating water. When compared to lower water loading, the average charge of H_{water} atoms in coordinating water decreases (see **Table S4**). For O_{water} atoms up to a distance of *ca*. 3 Å, the average charge does not depend on their respective position, while a more positive charge is observed for water molecules near the pore walls of the framework (between *ca.* 3 Å and 5.5 Å).

Table S5. Atomic charges (in electrons) of the copper metal center, coordinating oxygen atoms as well as the charges on the water molecules, determined for different water amounts. The electronic structure in the MOF changes during reorientation of the structure. This is reflected by an increased electron density at the copper metal site. The addition of water has no effect on the average charges. Additionally, oxygen atoms involved in hydrogen bonding possess a broader charge distribution. The water molecules carry no net charge.

atom	atomic charges / electrons			
	pristine network	relaxed network	partially hydrated network $Cu_2(dobdc)(H_2O)_x$	
			$x = 2$	$x = 5$
Cu	0.873 ± 0.001	0.843 ± 0.006	0.840 ± 0.009	0.839 ± 0.003
O_P	-0.537 ± 0.001	-0.521 ± 0.003	- 0.532 ± 0.004	-0.520 ± 0.007
O_{Cp}	-0.508 ± 0.001	-0.520 ± 0.002	-0.522 ± 0.009	-0.525 ± 0.010
O_{Ci}	-0.601 ± 0.001	-0.589 ± 0.003	-0.587 ± 0.004	-0.584 ± 0.005
O of (non-coordinating) H_2O			-0.769 ± 0.002	-0.767 ± 0.002
H of (non-coordinating) H_2O			0.384 ± 0.001	0.383 ± 0.002
net charge (non-coordinating) H_2O			-0.001 ± 0.002	0.00 ± 0.002

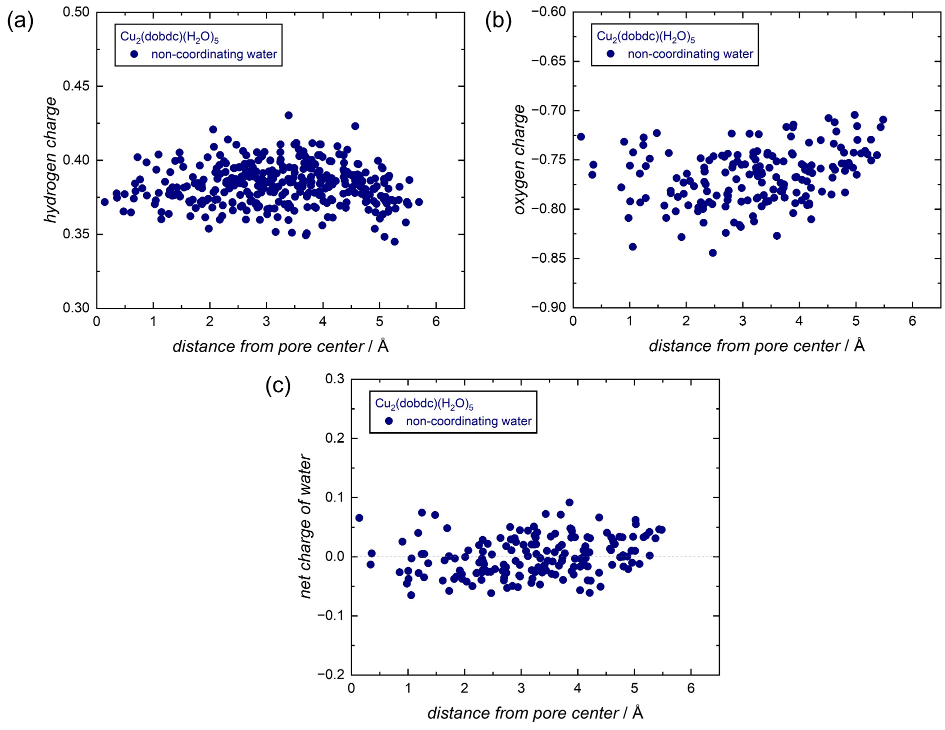

Figure S4. Charge distributions (non-coordinating) water molecules in $Cu_2(dobdc)(H_2O)_5$: (a) H_{water} atoms, (b) and O_{water} atoms, (c) resulting H_2O net charge. (For the net charges, those of both H atoms and the O atom were considered. The position relative to the pore center refers to the respective water O positions.) A slight increase in electron density is observed for hydrogen atoms located near the pore walls, while the opposite is the case for the oxygen atoms. Ultimately, the overall charge of the whole water molecule is unaffected.

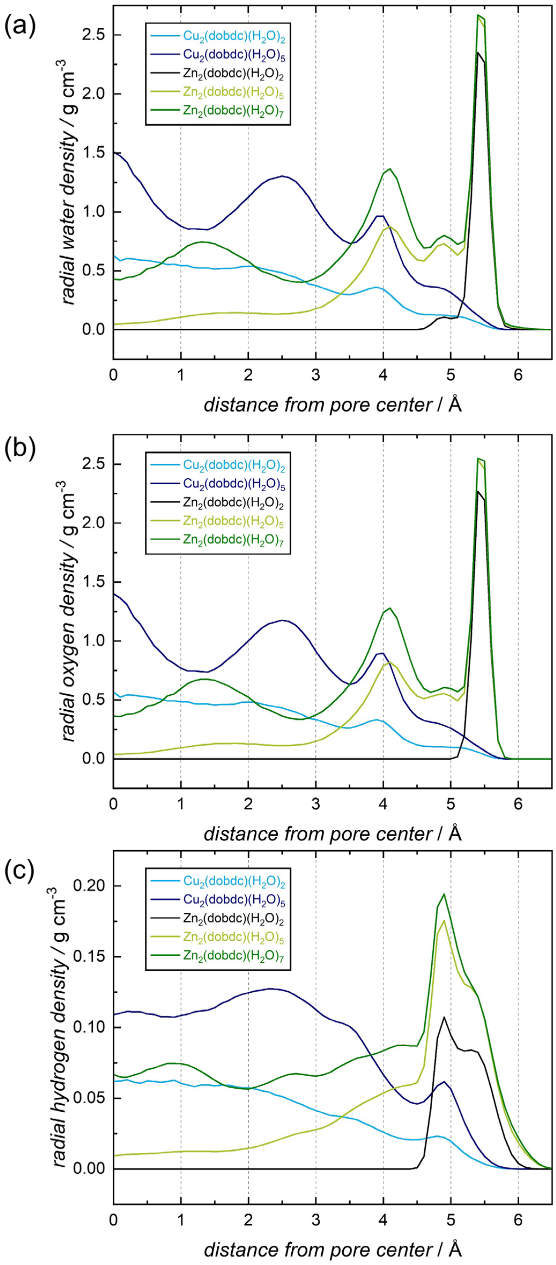

Figure S5. Radial average density probability distributions of (a) water molecules, (b) O_{water} atoms, and (c) H_{water} atoms in the pores of hydrated CPO-27-Zn and CPO-27-Cu with different amounts of water. In CPO-27-Zn, some water molecules are strongly bound to the open metal sites (*ca.* 5.5 Å); additional water is adsorbed near the pore walls at preferred positions (peaks at 4.85, 4.05 and 1.3 Å). H atoms are less fixed than the respective O atoms; the H atoms of the coordinating water molecules (preferred distances at 5 and 5.3 Å) point into the pores, overlapping with H atoms from molecules at the second site. In CPO-27-Cu, water molecules show no affinity to Cu and accumulate in the pore center, forming a total of seven pillars of water (peaks at 4, 2.5 and 0 Å); H-bonding to framework O atoms is reflected by a small peak at *ca.* 4.8 Å.

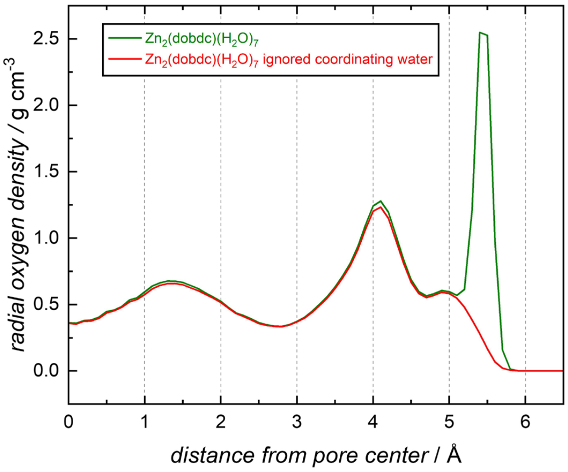

Figure S6. Radial average density probability distributions of O_{water} atoms in the pores of $Zn_2(dhtp)(H_2O)_7$, with and without consideration of the strongly bound, coordination water molecules located at the previously open metal sites (*ca*. 5.5 Å), highlighting water molecules located at the second sorption site.

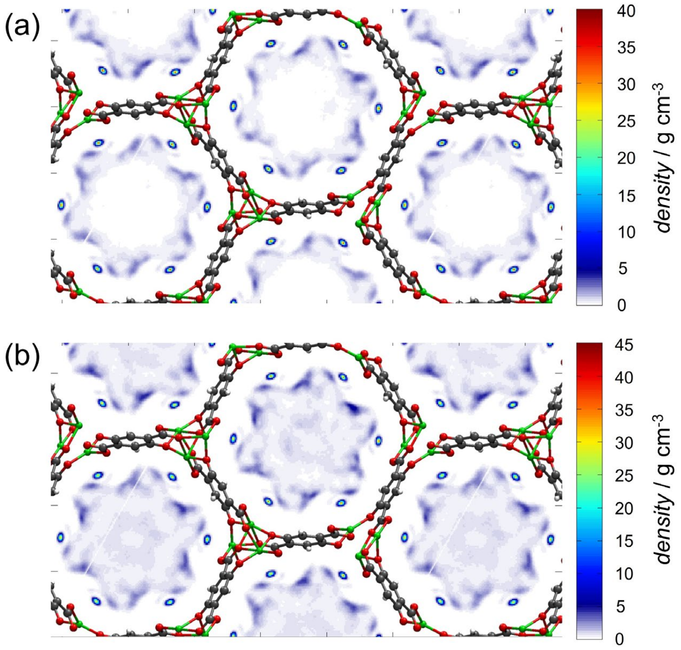

Figure S7. Probability density distribution histograms of water in CPO-27-Zn = $Zn_2(dobdc)(H_2O)_x$; (a) $x = 5$, and (b) $x = 7$.

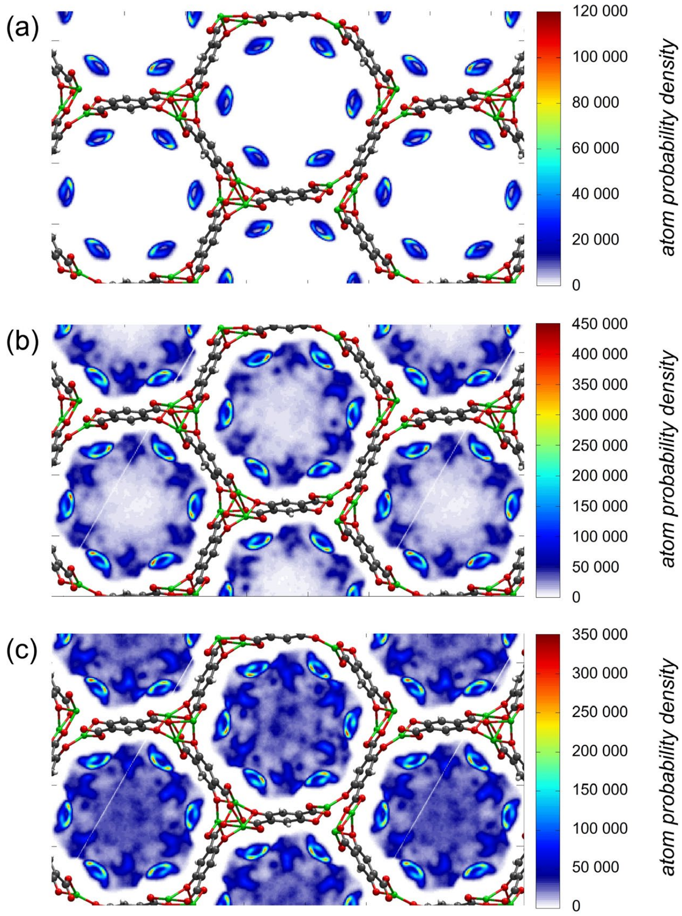

Figure S8. Atom probability density of H_{water} atoms in CPO-27-Zn = $Zn_2(dobdc)(H_2O)_x$. (a) x = 2 (monohydrate), (b) x = 5, and (c) x = 7. H atoms show preferences for several positions and orientations. Butterfly-like arrangements near the aromatic rings of the pore walls are created by an overlap of several preferred positions. Additionally, hydrogen atoms show a preference for the exposed O atoms of the inorganic building unit (*i.e.,* O_A and O_{Cp}). (c) x = 7: H atoms begin to form a continuous network which is pointing towards the center of the pore; in addition, accumulation close to the oxygen positions is observed.

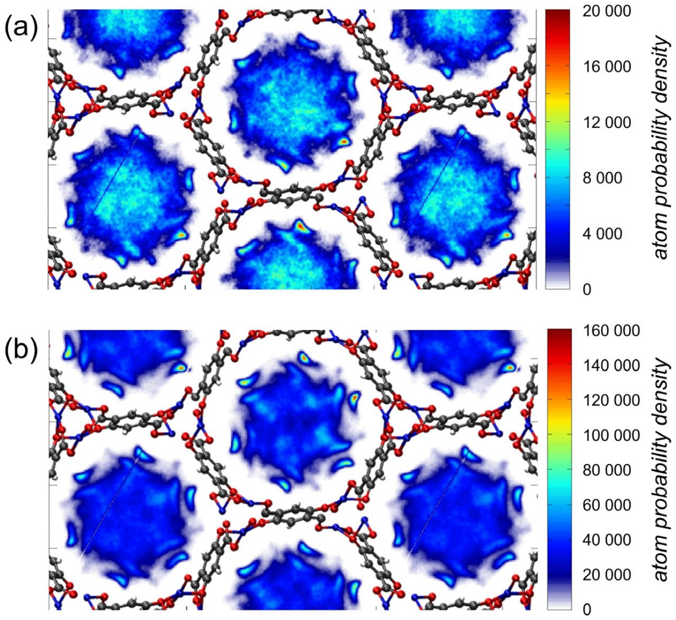

Figure S9. Atom density of H_{water} atoms in CPO-27-Cu = $Cu_2(dobdc)(H_2O)_x$, (a) $x = 2$ (monohydrate) and (b) $x = 5$. H atoms in the pore center are isotopically arranged. Near the pore walls, formation of H bonds with framework O_{Cp} atoms as well as (to lesser extent) with O_A atoms is observed.

References

[1] L. J. Wang, H. Deng, H. Furukawa, F. Gándara, K. E. Cordova, D. Peri, O. M. Yaghi, *Inorg. Chem.* **2014**, *53*, 5881–5883.

[2] M. H. Rosnes, M. Opitz, M. Frontzek, W. Lohstroh, J. P. Embs, P. A. Georgiev, P. D. C. Dietzel, *J. Mater. Chem. A* **2015**, *3*, 4827–4839.

[3] B. Pato-Doldán, M. H. Rosnes, P. D. C. Dietzel, *ChemSusChem* **2017**, *10*, 1710–1719.

[4] S. E. Henkelis, S. M. Vornholt, D. B. Cordes, A. M. Z. Slawin, P. S. Wheatley, R. E. Morris, *CrystEngComm* **2019**, *21*, 1857–1861.

[5] K. Momma, F. Izumi, *J. Appl. Crystallogr.* **2011**, *44*, 1272–1276.

[6] Q. Song, Y. Li, Z. Cao, H. Liu, C. Tian, Z. Yang, X. Qiang, Z. Tan, Y. Deng, *Bioorg. Med. Chem.* **2018**, *26*, 6115–6127.

[7] J. Rouquerol, P. Llewellyn, F. Rouquerol, *Stud. Surf. Sci. Catal.* **2007**, *160*, 49–56.

[8] G. Lippert, J. Hutter, M. Parrinello, *Mol. Phys.* **1997**, *92*, 477.

[9] J. VandeVondele, M. Krack, F. Mohamed, M. Parrinello, T. Chassaing, J. Hutter, *Comput. Phys. Commun.* **2005**, *167*, 103.

[10] S. Goedecker, M. Teter, J. Hutter, *Phys. Rev. B* **1996**, *54*, 1703.

[11] C. Hartwigsen, S. Goedecker, J. Hutter, *Phys. Rev. B* **1998**, *58*, 3641.

[12] M. Krack, *Theor Chem Acc* **2005**, *114*, 145.

[13] J. VandeVondele, J. Hutter, *J. Chem. Phys.* **2007**, *127*, 114105.

[14] S. Grimme, J. Antony, S. Ehrlich, H. Krieg, *J. Chem. Phys.* **2010**, *132*, 154104.

[15] C. John, T. Spura, S. Habershon, T. D. Kühne, *Phys. Rev. E* **2016**, *93*, 043305.

[16] T. D. Kühne, M. Krack, M. Parrinello, *J. Chem. Theory Comput.* **2009**, *5*, 235.

[17] T. F. Willems, C. H. Rycroft, M. Kazi, J. C. Meza, M. Haranczyk, *Microporous and Mesoporous Mater.* **2012**, *149*, 134.

[18] M. Pinheiro, R. L. Martin, C. H. Rycroft, M. Haranczyk, *CrystEngComm* **2013**, *15*, 7531.

[19] J. J. P. Stewart, *J. Mol. Model.* **2007**, *13*, 1173.

[20] M. Welborn, J. Chen, L.-P. Wang, T. Voorhis, *J. Comput. Chem.* **2015**, *36*, 934.

[21] G. Bussi, D. Donadio, M. Parrinello, *J. Chem. Phys.* **2007**, *126*, 014101.

[22] T. A. Manz, N. G. Limas, *RSC Adv.* **2016**, *6*, 47771.

[23] T. A. Manz, *RSC Adv.*, **2017**, *7*, 45552-45581.

[24] M. Brehm, M. Thomas, S. Gehrke, B. Kirchner, *J. Chem. Phys.* **2020**, *152*, 164105.

[25] M. Brehm, B. Kirchner, *J. Chem. Inf. Model.* **2011**, *51*, 2007.

3.2 Water in the Micropores of CPO-27 Metal-Organic Frameworks

Encouraged by the previous results on CPO-27-*M* (*M* = Cu and Zn), revealing that the adsorption of water within CPO-27-Zn proceeds by occupation of discrete positions, similar to those reported for fully hydrated CPO-27-*M* frameworks, the water adsorption/desorption behavior of four additional members (*M* = Co, Mg, Mn, Ni) was analyzed. For that purpose, water vapor sorption studies were applied. In addition, the effect of the water structure (analyzed by FTIR spectroscopy) and the contact time on the hydrolytic stability of these materials was studied, allowing to determine crucial factors for the durability of CPO-27-*M*. Obtained results highlight that the arrangement of adsorbed water molecules as well as the adsorption/desorption mechanism of the CPO-27-*M* series is dictated by the given metal center, with CPO-27-Zn revealing a prototypical behavior with easily distinguishable sorption steps. These differences are a consequence of altered water-framework interactions, providing distinct differences in H-bonding (with the framework atoms and adjacent water molecules). In contrast, CPO-27-Cu revealed an adsorption mechanism similar to classical pore condensation, with adsorbed water molecules showing a bulk-like behavior.

M. Kloß, C. Weinberger, M. Tiemann Water in the Micropores of CPO-27 Metal-Organic Frameworks: A Comprehensive Study *Microporous Mesoporous Mater.* **2025**, *381*, 113352.

- Digital Object Identifier: 10.1016/j.micromeso.2024.113352

Participation in this publication

M. Kloß, C. Weinberger, M. Tiemann: Experimental work (data evaluation and synthesis), writing and editing of the manuscript, project idea and conceptualization

Microporous and Mesoporous Materials 381 (2025) 113352

Contents lists available at ScienceDirect

Microporous and Mesoporous Materials

journal homepage: www.elsevier.com/locate/micromeso

Water in the micropores of CPO-27 metal-organic frameworks: A comprehensive study

Marvin Kloß, Christian Weinberger, Michael Tiemann *

Department of Chemistry – Inorganic Chemistry, Faculty of Science, Paderborn University, Warburger Str. 100, 33098, Paderborn, Germany

ARTICLE INFO

Keywords:
Metal-organic frameworks
CPO-27
Open metal sites
Water vapor sorption

ABSTRACT

The metal-organic framework CPO-27 exhibits free coordination sites (open metal sites) and can be prepared with a wide range of metals that influence its properties. It is therefore an intriguing structure to study sorption phenomena. We analyze the water resistance and sorption behavior of these frameworks, with particular attention to the sorption mechanism in detail and the structure of the confined water molecules. For this purpose, we use manometric water vapor sorption analysis and FTIR spectroscopy. The respective metal center orchestrates both the adsorption behavior and the arrangement of the water molecules in the micropores of the framework. The extent to which water molecules form hydrogen bonds (with each other and with framework oxygen atoms) plays a crucial role in the stability of the framework towards water. Water adsorption is governed by the coordination of water molecules to the open metal sites (except for CPO-27-Cu) and subsequent H-bonding. A stepwise adsorption of water is observed, with significant differences depending on the choice of metal.

1. Introduction

Metal-organic frameworks (MOFs) are known for their vast diversity of structures [1,2], including materials that exhibit open metal sites, *i.e.,* metals with unsaturated coordination spheres [3]. One example is CPO-27 [4], also called MOF-74 [5]. It is well known for its variety of possible bivalent metal centers (M^{2+}), including M = Co [4], Zn [5], Ni [6], Fe [7,8], Mn [9], Cu [10], Cd [11,12], and Mg [13]. The inorganic building unit adopts a rod-like structure with a helical arrangement, built by corner-sharing octahedra of coordinated metal ions. These are formed by coordination of three carboxylate oxygen atoms and two phenolate groups, originating from the 2,5-dihydroxylterephthalate (dhtp^{4-} or dobdc^{4-}) linker molecules, as well as from one solvent molecule (typically DMF or water). The resulting framework exhibits a honeycomb-like arrangement of building units, presenting cylindrical micropores. Removal of the coordinating solvent molecules (*e.g.* through thermal activation) generates open coordination sites exposed to the pores. These are accessible for coordination of guest molecules (*e.g.*, CO_2 [14–17], CO [18], H_2 [6,9,19], O_2 [7], NO [20], H_2O [16,21–23]), with manifold possible applications, including as catalysts [24–26], sensors [27,28], proton conductors [29–36], battery electrolytes [37], CO_2 sorbents [38,39], water harvesters [40,41] or for separation of light hydrocarbons [42,43]. Considering the strong binding of water towards the metal centers, it is crucial to analyze its behavior inside the cylindrical pores of the host material, to evaluate possible drawbacks and limitations in any given application.

The interaction of water molecules at surfaces and within pores can be analyzed by Fourier-transform infrared spectroscopy (FTIR). The characteristic O–H stretching vibration band of water (typically located in the range of 2800 … 3700 cm^{-1}) is a superposition of bands corresponding to H_2O molecules with different degrees of H-bonding. Following the designations proposed by Brubach *et al.* for liquid water in confinement or at solid surfaces [44], these bands correspond to the following situations: (i) ’Network water’ molecules exhibit approximately four H-bonds with adjacent atoms. This type of water shows the lowest O–H stretching vibration frequencies, typically around 3300 cm^{-1}. (ii) Poorly connected H_2O molecules with only few H-bonds (as present in dimers or trimers) are designated as ’multimer water’, showing the highest vibration frequencies around 3590 cm^{-1}. Water molecules that terminate a liquid-like network at an interface (to a solid or gas phase) belong to this type. (iii) Finally, H_2O molecules with an intermediate H-bonding situation are accordingly termed ’intermediate water’, with vibration frequencies around 3460 cm^{-1}. These molecules are farther apart from the interface. Deconvolution of the broad O–H

---

* Corresponding author.
E-mail address: michael.tiemann@upb.de (M. Tiemann).

https://doi.org/10.1016/j.micromeso.2024.113352
Received 29 June 2024; Received in revised form 27 July 2024; Accepted 25 September 2024
Available online 26 September 2024

stretching vibration band by least square-fitting of three Gaussian profiles allows determining the respective contribution of the three modes. This is also applicable to water in confinement, such as in inverse micelles [45,46] or in mesoporous silica [47]. It turned out that the respective contributions largely depend on two factors: the surface-chemical nature of the porous material and the relative amounts of water ('loading') in the pores. This then determines the arrangement of water in limited spaces and ultimately allows the polarity of the environment to be classified.

Previous studies on the fully hydrated structure of CPO-27-*M* (*i.e.* M_2(dhtp)(H_2O)$_{10}$), detected five water molecules (per metal center M^{2+}) located at crystallographically unique positions within the cylindrical pores. These five molecules were categorized using variable temperature, *in-situ* powder X-ray diffraction (VT-XRD), along with thermal analysis data. Three groups of water molecules can be distinguished with respect to their relative strength of interaction with neighboring water molecules [13,23]: (i) First, the coordinating water molecule located at the metal center revealing the strongest adsorption strength (chemisorption). (ii) Next, two water molecules interacting with the coordinating one *via* H-bonding, possessing a weaker adsorption strength. (iii) Lastly, the remaining two molecules, that solely interact with the previously mentioned two molecules through H-bonding and therefor having the weakest adsorption strength.

In order to thoroughly understand the hydration (and dehydration) behavior of any porous material, measuring the adsorption/desorption of water from the gas phase is an obvious method of choice [48,49]. In the particular case of CPO-27-*M*, water sorption studies so far have focused on gravimetric (microbalance) [50,51] and manometric techniques [52,47]. We recently highlighted the benefits of the latter method and its excellent accuracy at low water vapor pressures, *i.e.*, very low amounts of water, by analyzing the hydration/dehydration behavior of microporous CPO-27-*M* (Cu and Zn) [53]. Although both compounds adopt the same network topology, drastically different sorption behaviors were observed. CPO-27-Zn revealed a strong affinity towards the first sorption site (*i.e.,* open metal site) [54,55]. Additional water molecules predominantly occupy the second (near the oxygen atoms of the inorganic building units) and third sorption sites (near the phenylene backbone). Sorption energies for both sites are rather similar, as neither position is preferred, which deviates from previous computational studies on CPO-27-Mg [56,57], highlighting preferred sorption to the first two sorption sites. In contrast, CPO-27-Cu showed a one-step uptake of water over a small relative pressure range, reminiscent of classical pore condensation. This is enabled by distortion of the local copper coordination environment causing one oxygen atom to slightly move into the pore space, sterically blocking the Cu^{2+} site and serving as an anchor for H-bonding, facilitating water cluster formation. These observations hint towards a drastic impact of the metal center on the precise water sorption behavior/mechanism of the isoreticular CPO-27-*M* series.

Here we present a comprehensive study on the hydration behavior and water structure in the CPO-27-*M* series (*M* = Co, Cu, Mg, Mn, Ni, Zn), extending our previous study [53]. We use FT-IR spectroscopy to analyze the behavior of water in the one-dimensional pores and its effect on the framework stability against an excess of water. Further, adsorption and desorption of water by manometric vapor sorption analysis is studied to highlight differences in the adsorption mechanism (occupancy of different sorption sites) between the members in the isoreticular series.

2. Experimental

Synthesis: CPO-27-*M* materials were synthesized under solvothermal conditions according to modified reported procedures (*M* = Co [31], Cu [19], Mg [14], Mn [19], Ni [15], Zn [58]); details are given in the Supporting Information section. Solvent was removed by heating under dynamic vacuum conditions to obtain desolvated (ds) samples, which were stored in a glove box under Ar atmosphere. All products were characterized by powder X-ray diffraction (XRD) and compared with literature data (CCDC Numbers 1516643 for Co [15], 1516648 Cu [15], 1516645 Mg [15], 1031480 Mn [19], 1516644 Ni [15], 1863522 Zn [59]) using calculated peak positions, obtained with the *VESTA* software package [60]. The linker molecule (2,5-dihydroxyterephthalic acid, H_4dhtp or H_4dobdc) was synthesized according to modified literature procedures [61]; details are given in the Supporting Information section. All other chemicals and solvents were purchased from commercial suppliers and used without further purification.

General Characterization: ^{1}H and ^{13}C NMR spectra were recorded using Bruker *Advance 500* and Bruker *Ascent 700* spectrometers. Chemical shifts were calibrated to the resonance of residual non-deuterated solvent. Data derived from XRD measurements was collected on a Bruker *D8 Advance* diffractometer with a step size of 0.02° and a counting time of 1 or 3 s per step. Patterns are normalized (to 0–1 range) for better comparison of relative intensities. Elemental analysis was performed using an Elementar *vario MICRO Cube*. Thermogravimetric analysis (TGA) was performed using a *TGA PT1000* thermobalance from *Linseis*. The sample was placed in a corundum crucible. Measurements were performed under a constant Argon gas (purity 5.0 from *Wöhning Gas*) flow (100 mL min^{-1}) in a temperature range from 25 °C to 800 °C using a heating rate of 5 °C min^{-1}. For mass spectrometry, the instrument was coupled with a Pfeiffer *Vacuum Omnistar* mass spectrometer. N_2 physisorption analysis was performed with a Quantachrome *Autosorb 6B* at 77 K. The relative pressure range suitable for the BET surface area calculation was determined using the Rouquerol criteria [62]. Total pore volumes were determined from the uptake at $p/p_0 \approx 0.5$. Activation of the samples was performed in a stepwise manner. The desolvated (ds) samples were transferred to the measurement cell and dispersed in methanol twice for 45 min. After each step, the solvent was removed under dynamic vacuum. The pre-dried samples were degassed for approximately 17 h, using the following procedure: The samples were heated from room temperature to 60 °C with a heating rate of 2 °C min^{-1}, after which the temperature was held for 2 h. Then, the sample was heated to 100 °C with the same heating rate (2 °C min^{-1}), and the temperature was held for another 2 h. Finally, the sample was heated (2 °C min^{-1}) to 150 °C (or 120 °C for the copper derivative), and the temperature was held for additional 12 h, after which the sample was allowed to cool to room temperature.

FTIR: FTIR spectroscopy was performed with a Bruker *Vertex 70 spectrometer* in ATR mode using the *Platinum ATR unit A225* with a diamond ATR crystal. Powder samples were pressed on the crystal during the measurement. After the measurement of hydrated samples, an automatic baseline correction was applied using the *OPUS 7.2.1* software package. The correction was performed using a *concave rubberband correction*, using 10 iterations and 32 baseline points. Gaussian least-square fits of the water stretching band were performed using the *peak analyzer* function of the *Origin23b* software package. First, the data within the range from 4500 to 2400 cm^{-1} was taken and normalized. The data from 3950 to 2750 cm^{-1} was selected for the fitting procedure. Then, three peaks were set with reasonable starting points with respect to the different vibrational band: *ca* 3560 cm^{-1} (multimer water), *ca* 3390 cm^{-1} (intermediate water), and *ca* 3210 cm^{-1} (network water). Only positive peak areas were allowed while an automatic baseline correction was performed, after which the baseline was set to a constant value. No further restrictions were used. It is noted that the fit results potentially possess a small error caused by the overlap of the aromatic C-H vibration of the linker molecule with the water stretching bands.

H_2O vapor sorption: Water experiments were performed on a *3Flex instrument* (*Micromeritics*) at 298 K (25 °C) with double distilled (and degassed) water. Samples were degassed under vacuum by heating from room temperature to 60 °C, after which the temperature was increased to 100 °C and, finally, heated to 150 °C (or 120 °C for the copper derivative). The heating rate was kept at 2 K min^{-1} for all steps.

3. Results and discussion

3.1. General Characterization

A series of CPO-27-*M* materials (*M* = Co, Cu, Mg, Mn, Ni, Zn) was synthesized by modified solvothermal methods previously reported in the literature (see Experimental section). The crystal structures and phase purity of all materials are confirmed by powder X-ray diffraction (XRD); no evidence of crystalline impurities is observed (Supporting Information, Fig. S3a). Further, N_2 physisorption analysis reveals type-I sorption isotherms [63] for all compounds, consistent with micropores (pore diameters *ca.* 11 Å, depending on the metal *M*, Fig. S3b). In addition, the N_2 sorption measurements prove large BET surface areas (860 … 1780 $m^2\,g^{-1}$) and large pore volumes (0.37 … 0.90 $cm^3\,g^{-1}$) for all compounds, revealing accessible porosity (Supporting Information, Table S1).

3.2. Stability against water

Additional XRD studies were carried out to evaluate the stability of the frameworks against an excess of water. We prepared two sets of water-treated samples and compared them with the desolvated frameworks (CPO-27-*M*-ds), *i.e.,* samples with an open metal site. The first set of hydrated frameworks (CPO-27-*M*-hyd) was prepared in analogy to our previous studies [53] (*i.e., ca.* 50 mg sample washed with 8–10 mL H_2O of HPLC-grade water). For the second set, samples were dispersed and stored in water for 16 h (50 mg sample in 1 mL, CPO-27-*M*-disp). Both sets of samples were subsequently air-dried on filter paper at room temperature prior to further analysis. All frameworks remain crystalline after short exposure to water (CPO-27-*M*-hyd), with no significant shift in the XRD peak positions (Supporting Information, Figs. S4–S9). The two most intense reflections are most relevant, concerning the periodic structure of the framework. These belong to the (110) plane (*ca.* 6.8°) and the (300) plane (*ca.* 11.8°). These lattice planes reflect the ordered pore structure of the framework and the periodic alignment of the rod-like (inorganic) building units parallel to the crystallographic *c* axis, respectively (Fig. 1a and b). Both peaks remain mostly unchanged for the first set of samples (CPO-27-*M*-hyd), with only a few samples showing a slight change in relative intensities. Drastic differences become apparent after long exposure to water (*i.e.* CPO-27-*M*-disp). Here, we can categorize all investigated samples into two groups with respect to their stability. Group One (*M* = Cu, Mg, Ni) shows a shift in the peak positions as well as a pronounced change in the relative intensities of the (110) and (300) reflections (Fig. 1c), which is consistent with literature data [50]. We propose that the decomposition of this group of materials follows a mechanism previously described, according to which the open metal site is occupied by water, leading to cleavage of the axial *M*-O bond and thus creating an additional coordination site for water molecules [50]. A reduced connectivity of adjacent pores is the result, allowing them to rotate and (partially) block each other. This

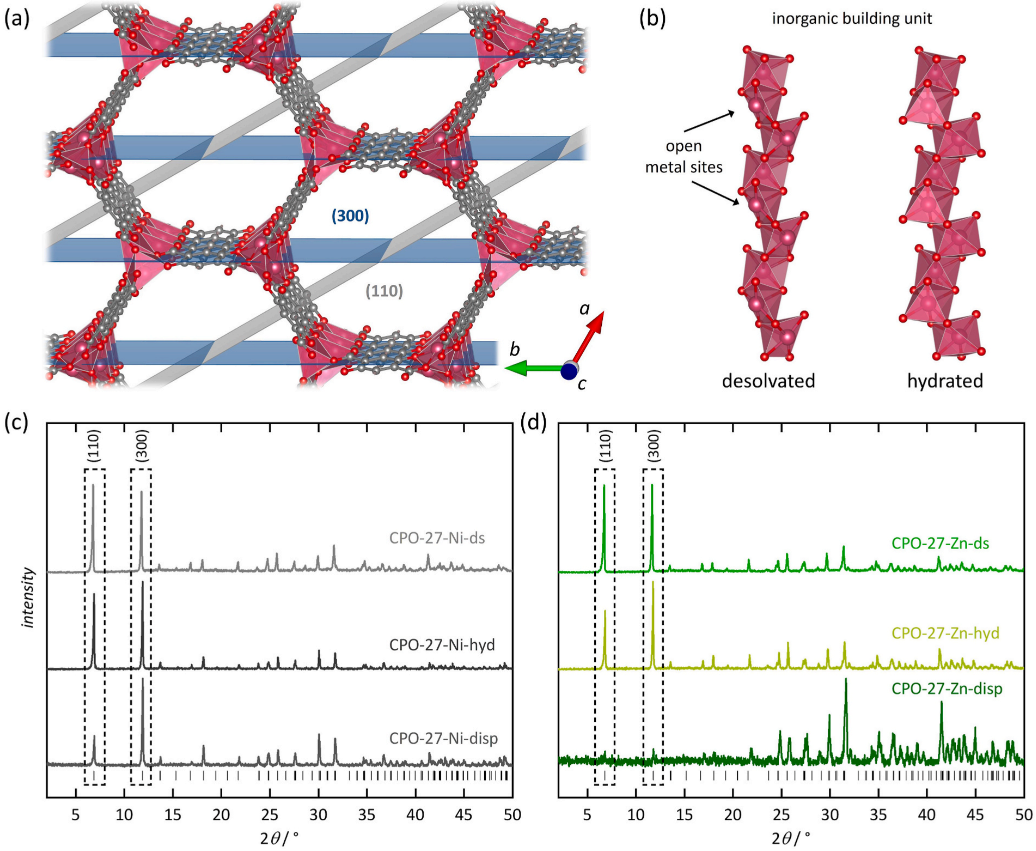

Fig. 1. **(a)** Illustration of the (110) and (300) planes in the crystal lattice of CPO-27-*M*. **(b)** Comparison of the desolvated and hydrated inorganic rod-like inorganic building units, viewed along the crystallographic *a*-axis. **(c,d)** Normalized powder XRD patterns of desolvated (ds), hydrated (hyd), and dispersed (disp) samples of CPO-27-Ni and CPO-27-Zn, given as selected representatives of their respective groups. Patterns are normalized for better comparison.

reduces the ordered arrangement of the pores, and parts of the porosity is lost. Up to a certain point, this process is reversible. However, XRD data (Supporting Information, Figs. S4–S6) do not indicate the formation of appreciable amounts of crystalline metal hydroxides ($M(OH)_x$) or oxides (MO_x). For group Two (M = Co, Mn, Zn), the (110) and (300) reflections are either completely missing or barely visible (Fig. 1d). Interestingly, all members show some Bragg reflections at higher angles that do not match the protonated linker molecule (Supporting Information, Fig. S10) but align well with the high-angle reflections of the respective dehydrated frameworks. Again, no indication of $M(OH)_x$ or MO_x formation is observed. CPO-27-Co-disp shows a nearly complete loss of crystallinity, while CPO-27-Mn-disp and CPO-27-Zn-disp still show weak (110) and (300) reflections, indicating that the stability within this group decreases from Zn → Mn → Co. Decomposition of these samples arguably follows a different mechanism [64]. Here, coordination of water molecules to the open metal sites is accompanied by their deprotonation, which results in strongly bound hydroxido ligands as well as protonation of the linker molecules, creating additional open metal sites. Eventually, this results in an irreversible, complete loss of crystallinity and pore structure. The remaining reflections indicate that some kind periodicity (*i.e.* pore walls and inorganic building units, see Fig. 1b) is maintained.

For both sets of samples (CPO-27-*M*-hyd and CPO-27-*M*-disp), elemental analysis reveals C/H ratios that are reasonably consistent with largely defect-free frameworks (Supporting Information, Table S2). Hence, we assume that only very small and/or stoichiometrically equal amounts of metal and linker ions leave the framework during treatment with water; we calculated the number x of water molecules per formula unit ($M_2(dhtp)(H_2O)_x$), assuming the detected carbon originates entirely from the pristine framework. For CPO-27-*M*-hyd, we observe approximately ten water molecules per formula unit for most materials, consistent with literature data [23]. However, there are two exceptions: (i) CPO-27-Cu-hyd has only nine water molecules [53], owing to the previously discussed absent water coordination to the Cu^{2+} open metal site. This is a consequence of the Jahn-Teller distortion [65], causing generally weak interactions of Cu^{2+} centers with small guest molecules [15,19,66,67]. (ii) CPO-27-Mg-hyd reveals more than ten water molecules, indicating either a higher water density inside the pores or adsorption of water at/between particle surfaces. For the CPO-27-*M*-disp samples, the calculated amount of water molecules is generally reduced by one. We attribute this to structural changes caused by the aforementioned (partial) decomposition. For group One (M = Cu, Mg, Ni), it can be assumed that the slightly lower amounts of adsorbed water result from damage of the pore system (*i.e.,* less ordered pore arrangement and additional open metal sites). In the case of group Two (M = Co, Mn, Zn), our observations suggest that the materials maintain a certain degree of porosity with less uniform (crystalline) pores that enables the adsorption of water (complete loss of porosity would yield significantly lower amounts of water). Further, some water molecules coordinate to (additional) open metal sites. Finally, the determined elemental ratios indicate the absence of significant amounts of $M(OH)_x$ and/or MO_x in any of the water-treated samples.

Further analysis of all samples was carried out by Fourier transform infrared (FTIR) spectroscopy. Spectra of the desolvated frameworks (Supporting Information, Figs. S11–S17) reveal the absence of the carboxyl O–H vibration, indicating that no unreacted (protonated) linker molecules are present within the samples. All water-treated samples (CPO-27-*M*-hyd and CPO-27-*M*-disp) show the typical vibration bands of water [44], *i.e.*, the stretching (3750 … 2800 cm^{-1}), bending (1700 … 1650 cm^{-1}), and libration bands (1000 … 400 cm^{-1}). Otherwise, the spectra reveal only slight differences (minor shifts in wavenumbers) to those of the respective pristine materials. The M–O stretching vibration is observed at 600 … 570 cm^{-1} (Fig. 2a–f), similar to previous reports for CPO-27-*M* (M = Co [22], Ni [68], Cu [53] and Zn [53]). The energy of this band depends on the respective metal and remains unchanged (within the measurement resolution) in the water-treated samples. Using Badger's rule [69], we can estimate the relative M–O bond strengths from the force constants, associated with the vibrational frequencies. This suggests that the Cu–O bond is the strongest (band at 600 cm^{-1}), followed by Ni–O (588 cm^{-1}), Mg–O (583 cm^{-1}), Co–O (582 cm^{-1}), and Zn–O (581 cm^{-1}). Finally, CPO-27-Mn reveals the weakest M–O bond (573 cm^{-1}) of all investigated frameworks. This agrees with crystal structure data (desolvated frameworks at 180 °C) which show a similar axial trend for the mean M–O distances [15]; the significantly longer axial Cu–O bond length (observed in the crystal structure) result from the Jahn-Teller distortion [65]. Our results suggest that stronger M–O interactions in group One (Cu, Mg, Ni) as compared to group Two (Co, Mn, Zn) result in less water-induced decomposition. The remaining signals in the low wavenumber range are attributed to the C–H out-of-plane deformation (>600 cm^{-1}) and

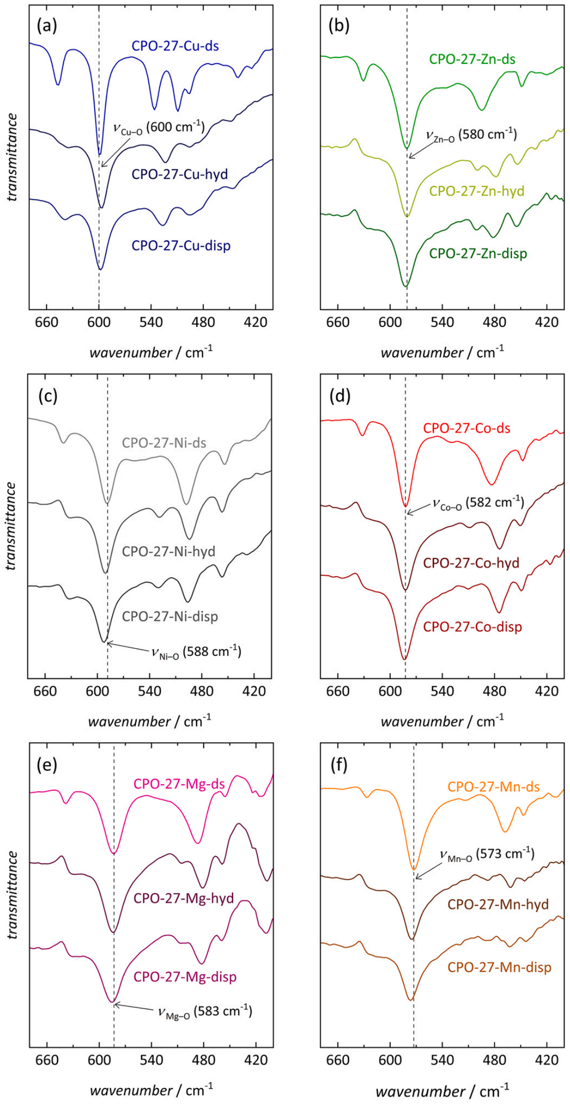

Fig. 2. FTIR spectra of desolvated (ds), hydrated (hyd), and dispersed (disp) CPO-27-*M* samples. The *M*–O vibrations are indicated by dashed lines. Data for (a) M = Cu and (b) M = Zn are reproduced from Ref. [53].

aromatic ring deformation vibrations (<550 cm^{-1}) of the linker molecule (see Supporting Information, Fig. S17) [70,71]. Furthermore, there is little to no indication of M(OH)$_x$ or MO$_x$ formation in the spectra of the water-treated frameworks, as no characteristic O–H vibration (*ca.* 3700 cm^{-1} or 3600 cm^{-1} in the case of CPO-27-Cu) [72–75] is observed (see Figs. S11–S16). Also, CPO-27-Co and CPO-27-Cu show no other characteristic vibrations. In case of CPO-27-Mg, two weak bands at 459 cm^{-1} and 408 cm^{-1} may indicate the formation of small amounts of Mg(OH)$_2$ [76]. However, these bands are the only evidence and since they also appear in the original sample, hydroxide formation seems altogether unlikely, in agreement with XRD data (Fig. S5). Similar observations are made for CPO-27-Mn and CPO-27-Zn. The former shows two vibration bands at 816 cm^{-1} and 885 cm^{-1}, which are also found in Mn(OH)$_2$ [73]. For CPO-27-Zn, a very weak band at 484 cm^{-1} is the only evidence of a hydroxide phase [77]. Lastly, CPO-27-Ni presents a slightly different situation. Here, a band at 528 cm^{-1} is visible, possibly arising from Ni-OH bending vibrations [78]; this band is absent in the pristine framework. Nevertheless, the XRD data and the absence of other characteristic bands suggest that hydroxide formation is at least questionable.

To further assess the structural stability of the materials, we performed thermogravimetric analysis coupled with mass spectrometry (TGA/MS) on the hydrated frameworks (CPO-27-M-hyd). Despite slightly different measuring conditions, we observe a similar thermal behavior (Supporting Information, Figs. S18–S24) as previously reported in the literature [23] (Fig. 3). We observe slightly lower dehydration temperatures (see Table S3), which is presumably due to a higher gas flow (100 mL min^{-1}) and higher initial heating rate (5 °C min^{-1}) compared to literature-based data. However, after the initial weight loss, we observe a small, steady release of water (detection of H$_2$O$^+$; m/z = 18) over a broader temperature range for all materials except CPO-27-Cu-hyd. (For CPO-27-Mg-hyd, the first 90 s of the m/z = 18 trace were discarded due to a high initial signal stemming from residual atmospheric water in the sample chamber.) Framework decomposition is indicated by the increase in the m/z = 44 (CO$_2^+$) mass signal, which is often accompanied by a weak m/z = 18 signal. This is probably due to the release of (strongly bond, coordinated) water molecules upon network collapse. The Cu- and Mg-based materials behave similarly to those reported previously. This is also true for CPO-27-Mn-hyd, considering that dehydration progresses slowly after the highlighted range. Previous reports show a slow mass decrease associated with CO$_2$ evolution before the pronounced decomposition step. However, some samples show differences in their decomposition behavior. Differences in the mass curves for CPO-27-Co-hyd and CPO-27-Zn-hyd from previously reported data may be due to the different synthesis methods (*i.e.*, here: DMF *vs.* Co: THF/water [4]; Zn: THF/water/NaOH [79]). Previous results on defects in CPO-27-M [80] showed that a low metal-to-linker ratio (here: 0.8) results in a small number of defects in the framework. In contrast, in water-based syntheses, a higher degree of defects is expected due to water-induced decomposition of the framework (as discussed above). Therefore, it is fair to assume that this will result in lower thermal stability [23]. For CPO-27-Ni-hyd, a unique thermal behavior is observed. There is a stronger, constant weight loss starting at 360 °C, accompanied by a m/z = 44 mass signal. This decrease in mass ultimately leads to the breakdown of the framework. We attribute this to defects caused by acetate anions (from the used metal source), as similar observations were made for *in-situ* formed formate anions (HCO$_2^-$) in reactions with a high metal-to-linker ratio [80]. Therefore, we attribute the first, less defined signal in the m/z = 44 MS curve to decomposition of acetate anions.

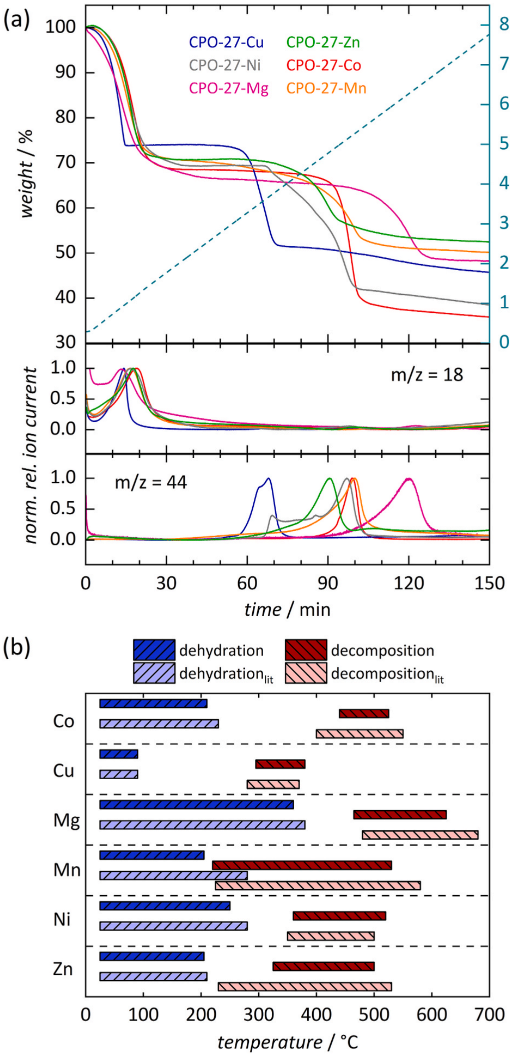

Fig. 3. **(a)** Thermogravimetric analysis coupled with mass ion detection (m/z = 18: H$_2$O$^+$, m/z = 44: CO$_2^+$) of the hydrated materials (CPO-27-M-hyd) (heating rate: 5 °C min^{-1}, Ar atmosphere). **(b)** Temperature ranges for the initial dehydration and decomposition of CPO-27-M-hyd. Light colors indicate previous dehydration studies by Dietzel *et al.* [23].

3.3. *FTIR studies of water in the pores*

All results presented so far suggest that in the water-treated CPO-27-M samples, the metal center not only determines the samples' stability (thermal and against water), but apparently also the decomposition mechanism of the respective framework. In addition, the contact time of the framework with water plays a major role. Except for CPO-27-Ni, no indication of M(OH)$_x$ or MO$_x$ is found in isolated samples. We assume that the ionic radii and the pore sizes of the respective materials play a key role in the observed mechanisms. This corresponds to the fact that materials in group One contain metal cations with smaller ionic radii (Cu^{2+}, Mg^{2+}, Ni^{2+}) [81] and possess smaller pores [15] than members of group Two (Co^{2+}, Mn^{2+}, Zn^{2+}). Based on our previous studies on CPO-27-M (M = Cu, Zn) [53] and studies on carbon nanotubes, that revealed a large effect of the channel size on water-water interactions and their dynamics [82–84], we propose that the water arrangement in the one-dimensional channels should be considered for the water-stability of the CPO-27-M series as well. Therefore, we carried out FTIR spectroscopic investigations on hydrated frameworks (CPO-27-M-hyd) in attenuated total reflection (ATR) mode. As discussed in the introduction, deconvolution of the O–H stretching vibration signal in the range of 2800 … 3700 cm^{-1} into three distinct bands allows further insight into the water arrangement in different environments [44–46,47]. By the degree of H-bond formation of water molecules with each other and with framework oxygen atoms, we distinguish 'network' water (approximately four H-bonds), 'multimer' water (few H-bonds), and 'intermediate' water (medium amount of H-bonds).

For a pure liquid water film at the surface of the ATR crystal (see Supporting Information, Fig. S25), the relative contributions (peak areas) are 13 % from multimer water (3535 cm^{-1}), 18 % from intermediate water (3405 cm^{-1}), and 69 % from network water (3251 cm^{-1}). We hypothesize that the multimer water in the liquid film is located at either of the interfaces, *i.e.*, to the ATR diamond crystal or to air. For the CPO-27-*M*-hyd materials with M = Co, Mg, Mn, and Ni, similarities to CPO-27-Zn [53] are observed. They show a lower contribution from network water (39 %–71 %) and a higher contribution from intermediate water (24 %–51 %) than the pure liquid water film, as shown in Fig. 4 (see also Supporting Information, Fig. S26 and Tables S4–S5). This is consistent with the fact that in a fully hydrated framework (*i.e.,* 100 % water uptake), water molecules are located at defined crystallographic positions within the pores [23] and therefore possess lower translational and rotational degree of freedom than in the bulk liquid state; the average number of H-bonds per H_2O molecule is lower. Further, the contribution from multimer water is also generally lower (5 %–6 %) in the CPO-27-*M*-hyd materials than in the pure water film (except CPO-27-Cu-hyd with 14 %). This suggests that water molecules near the pore walls possess a high tendency to form H-bonds (with framework atoms and with each other), more than interface-near water molecules in a pure liquid film. This is in accordance with our previous studies that revealed extended H-bond networks with strong interactions for hydrated CPO-27-Zn [53]. However, the overall different contributions suggest that the tendencies to form H-bonds vary for any given metal center.

Concerning the differences between the members of the series with respect to the relative amounts of intermediate and network water (Supporting Information, Table S4 and Fig. S27), we find the highest contribution of network water for M = Zn (71 %), followed by Mn (66 %) and Co (65 %). Interestingly, these are the less water-stable materials (group Two, see above), clearly highlighting the importance of H-bond networks (water clusters), especially H-bond formation of water molecules near the framework atoms (*i.e.* located at the first three sorption sites), on the water durability of these materials by promoting framework decomposition. Lower relative amounts of network water are observed for the more water-stable materials (M = Cu (55 %), Mg (53 %) and Ni (44 %); group One), which indicates that occupation of the water sorption sites near the pore walls in these frameworks proceeds differently, presumably due to weaker water-framework interactions, and consequently a lower H-bond tendency, than for the other members.

In addition to the relative contributions (peak areas) of the three vibration bands, we may also consider their respective wavenumbers $\tilde{\nu}$ (peak positions, see Supporting Information, Table S5). Compared to the pure water film, all CPO-27-*M*-hyd samples show a redshift of the network water peak (*i.e.*, towards lower $\tilde{\nu}$), and a slight blueshift of the multimer water peak (towards higher $\tilde{\nu}$), except for CPO-27-Cu-hyd which shows a redshift. The wavenumber of the intermediate water peak is mostly unchanged, except for CPO-27-Cu-hyd and CPO-27-Ni-hyd which both show a redshift. Valuable information arises from the respective differences between the three wavenumbers for each material, *i.e.*, from the wavenumber splitting $\Delta\tilde{\nu}_{xy}$ (**Table 1**). In general, higher $\Delta\tilde{\nu}$ values suggest a higher asymmetry in the local H-bonding of water [85,86]. We observe generally higher values for all CPO-27-*M*-hyd materials than for the pure water film (except for CPO-27-Cu-hyd), indicative of higher degrees of H-bonding asymmetry. This is consistent with the notion of water molecules residing at crystallographically defined positions with a highly asymmetric local environment. For

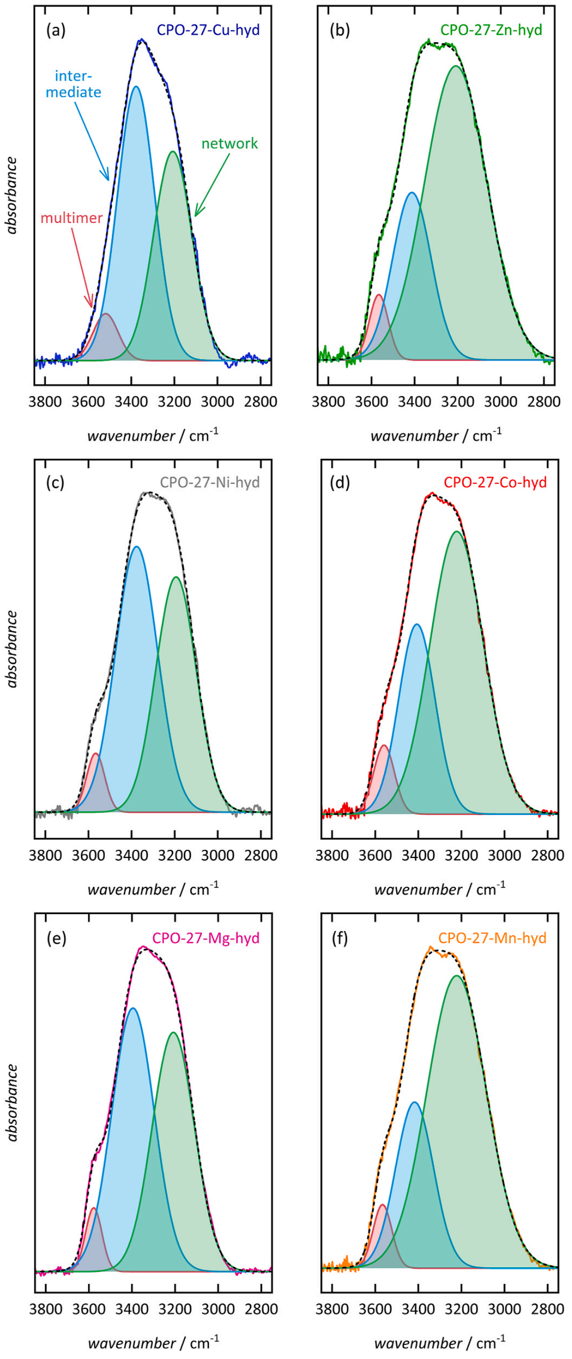

Fig. 4. Deconvolution by least-square fitting of the FTIR O–H stretching vibration band of water in hydrated CPO-27-*M* samples, revealing the respective contributions of multimer, intermediate, and network water; dotted lines are the sums of the three Gaussian profiles. Data for (a) M = Cu and (b) M = Zn are reproduced from Ref. [53].

Table 1

Wavenumber splitting $\Delta\tilde{\nu}$ of the stretching vibration bands of water in the CPO-27-*M*-hyd materials and of pure water.

	$\Delta\tilde{\nu}_{\text{multimer-network}}$ (cm^{-1})	$\Delta\tilde{\nu}_{\text{multimer-intermed.}}$ (cm^{-1})	$\Delta\tilde{\nu}_{\text{network-intermed.}}$ (cm^{-1})
Co	336.6 ± 2.4	152.6 ± 1.5	184.0 ± 2.4
Cu	258.5 ± 5.3	116.0 ± 6.7	142.5 ± 5.3
Mg	357.4 ± 3.1	168.9 ± 2.0	188.4 ± 3.1
Mn	340.1 ± 2.6	151.8 ± 1.5	188.3 ± 2.6
Ni	373.6 ± 5.1	190.8 ± 3.6	182.8 ± 5.1
Zn	352.8 ± 2.1	152.5 ± 1.2	200.3 ± 2.1
water	284.4 ± 1.5	130.2 ± 2.9	154.2 ± 1.5

CPO-27-Cu-hyd, a more symmetric H-bonding is present, which is a result of weaker water interactions with framework atoms, resulting in a more bulk-like water configuration [53].

Summarizing the FTIR studies, a higher contribution of the multimer water peak in CPO-27-*M* suggests a weaker interaction of water molecules with the open metal site (as revealed for CPO-27-Cu, with no coordination to the Cu^{2+} site [53]). The higher acidity of chemisorbed water as compared to bulk water seems to affect the decomposition mechanism, as it either inhibits protonation of the carboxylate/alkoxide groups (group One; Cu^{2+}, Mg^{2+}, Ni^{2+}) or facilitates it (group Two; Co^{2+}, Mn^{2+}, Zn^{2+}) [87]. In addition, the relative strength of the network water band is clearly correlated with the formation of extended H-bonding of water molecules (*ca.* four H-bonds) with surrounding water molecules and framework oxygen atoms. The thus-formed water clusters play a key role in the decomposition behavior, as materials with more extended H-bond networks are severely more prone to water-related decomposition (presumably due to the proximity of water molecules to the inorganic building units). Based on our findings, we assume that the other members of the CPO-27-*M* series (*M* = Co, Mg, Mn, Ni) will reveal a water sorption behavior more similar to CPO-27-Zn than to CPO-27-Cu [53], as will be elucidated in the following.

3.4. *Water vapor sorption studies*

We performed manometric water vapor sorption measurements at 25 °C for all CPO-27-*M* materials, *i.e.*, *M* = Co, Mg, Mn, Ni, Zn, and Cu. We have recently presented the respective results for Zn and Cu elsewhere [53] but will briefly include them in this study for comparison. Two consecutive adsorption/desorption cycles were measured without removing the sample from the device between both cycles, *i.e.*, without additional thermal activation after the first cycle. This takes into account that the coordinating water molecule that saturates the open metal site is irreversibly bound (as in the case of CPO-27-Zn) which will result in a different starting situation for the second sorption isotherm. All materials, except *M* = Cu, show an increased total water uptake during the second adsorption/desorption cycle, when compared to the first (see below). We attribute this to the partial degradation of the frameworks because of cleavage of metal-linker bonds during the time-consuming measurements (6–15 days), resulting in the formation of additional open metal sites (as discussed above). This goes along with a decreased crystallinity of the samples after the water sorption experiment (see Supporting Information, Fig. S28), being in agreement with previous reports on CPO-27-Mg [51] and other MOFs with vacant coordination sites [88]. To account for the fact that most of the water is adsorbed at low relative pressure ($p/p_0 < 0.1$), we display all isotherms both with a linear and with a semi-logarithmic scale, as the latter is necessary to obtain a full picture of the sorption behavior. First derivatives of the isotherms ($\delta V/\delta(p/p_0)$) were calculated to visualize distinct water adsorption steps in all sorption isotherms. (As a result of technical experimental restrictions, data points below *ca.* $p/p_0 = 0.002$ are missing in all, but the first adsorption isotherms.)

Our previous studies [53] have shown that water uptake by CPO-27-Zn proceeds in a stepwise manner. Molecular dynamics simulation revealed that the water molecules progressively occupy distinct sites within the pores (in agreement with crystal structure data for fully hydrated CPO-27-Zn [79]). This is shown schematically in Fig. 5. (Limited computing time did not allow us to carry out similar MD studies for all six materials; data in Ref. [53] are therefore limited to CPO-27-Zn and CPO-27-Cu as these two materials show the largest differences in the experimental data from each other.) In the water vapor sorption isotherms of CPO-27-Zn (Fig. 6a), the first step corresponds to the coordination of water to the Zn center (*ca.* $p/p_0 = 0.01$). This uptake is irreversible upon subsequent desorption and accounts for approx. 20 % of the total uptake, consistent with the fact that one out of five water molecules per metal center is coordinating ($M_2(dhtp)(H_2O)_{10}$; Fig. 5b). Then follows the adsorption of another *ca.* 40 % of the total water uptake (in the pressure range $p/p_0 = 0.01 \ldots 0.025$); these water molecules mostly reside at the second and third site, where they interact strongly with the coordinating water molecule and with framework oxygen atoms through H-bonding, resulting in a continuous water cluster along the pore walls (Fig. 5c). Next, another approx. 20 % of the total water uptake occurs ($p/p_0 = 0.025 \ldots 0.05$), with increasing occupation of the fourth and fifth sites (Fig. 5d). Finally, the remaining *ca.* 20 % of uptake occurs gradually over a wide pressure range ($p/p_0 = 0.05 \ldots 1$), with a rearrangement of the water molecules in the interior regions of the pores, resulting in a decreased mobility and orientational freedom, with more asymmetric H-bonding (Fig. 5e). This creates hysteresis, observed in both pairs of isotherms, due to a non-reversible increase in density

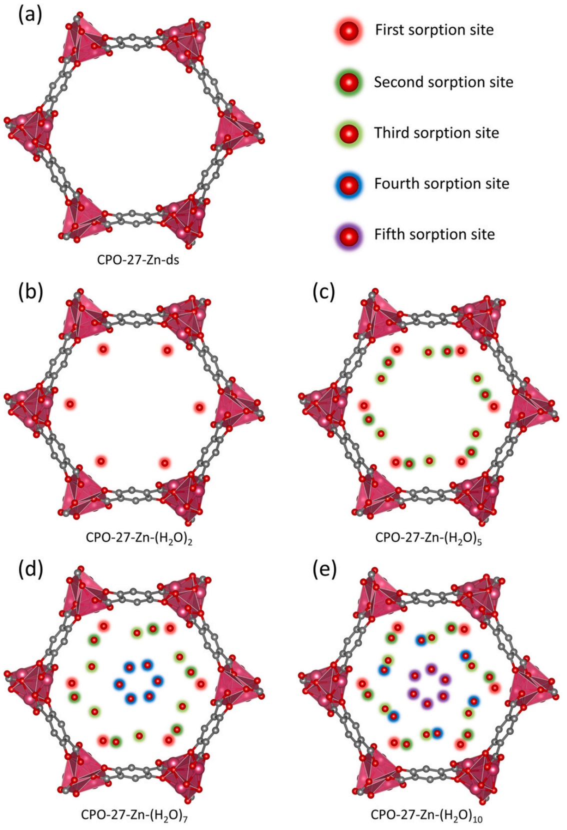

Fig. 5. Schematic of the subsequent occupation of distinct sites during hydration of CPO-27-Zn. Positions with the highest occupancy are displayed for (a) the desolvated framework, (b) 20 %, (c) 50 %, (d) 70 %, and (e) 100 % of the total water uptake.

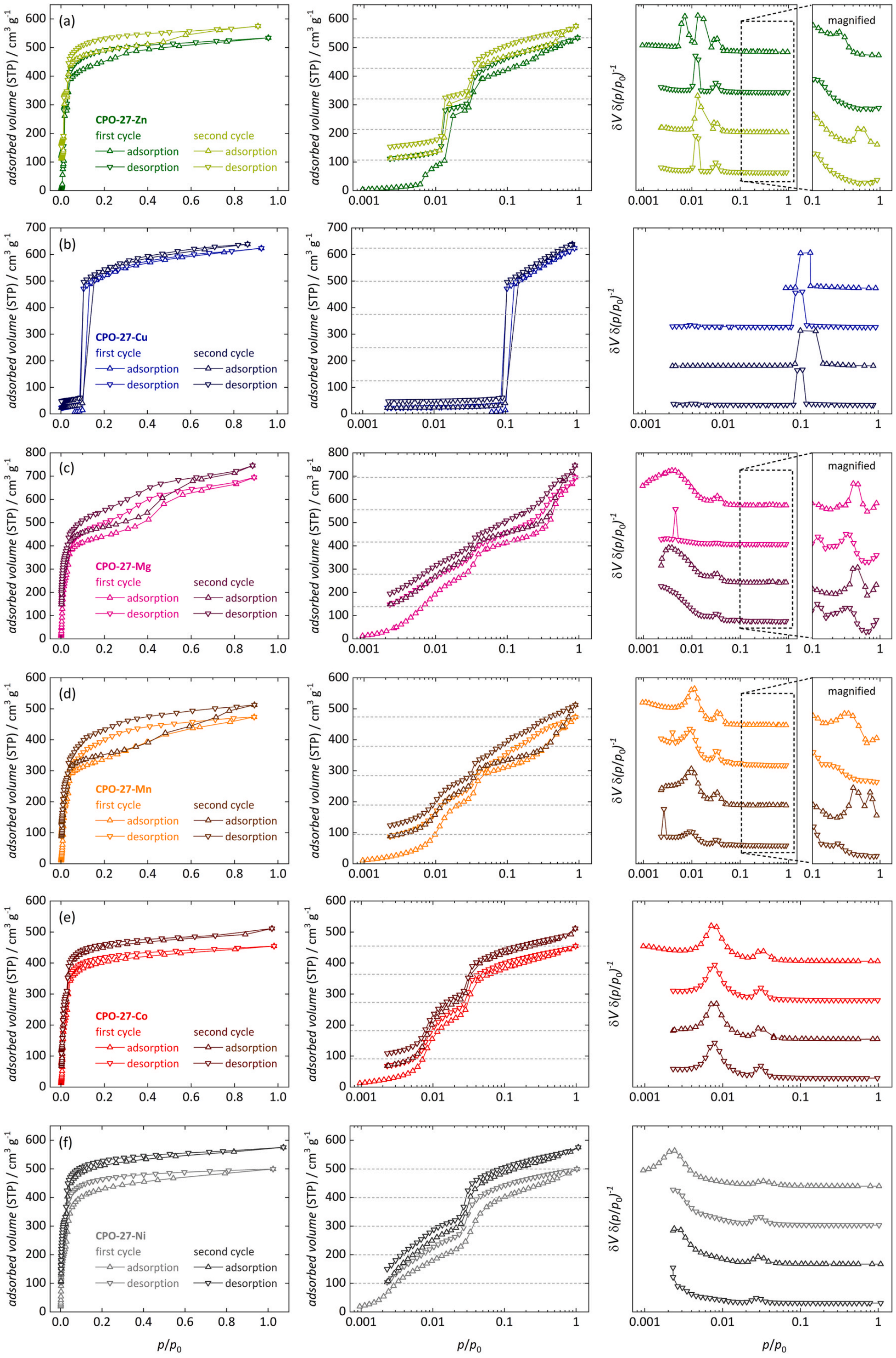

Fig. 6. Water vapor sorption isotherms (25 °C) of (a) CPO-27-Zn, (b) CPO-27-Cu, (c) CPO-27-Mg, (d) CPO-27-Mn, (e) CPO-27-Co, and (f) CPO-27-Ni (two consecutive adsorption/desorption cycles each). Data are shown at linear scale (left), in semi-logarithmic representation (middle), and as the first derivative (right). Horizontal lines mark 20 %, 40 %, 60 %, 80 %, and 100 % of the total water uptake during the first cycle. (Data for (a) M = Cu and (b) M = Zn are reproduced from Ref. [53].).

during rearrangement. Similar effects have been discussed previously for large pores and hydrophilic micropores [47,83,89–97].

For CPO-27-Cu (Fig. 6b), our previous study [79] showed an entirely different sorption behavior. Here, water sorption is negligible up to a pressure of *ca.* $p/p_0 = 0.1$. Then, adsorption of *ca.* 80 % (*i.e.*, four molecules per Cu center) occurs all at once, revealing classical pore condensation behavior, making it impossible to distinguish between distinct water molecules. This is due to a different local coordination environment of Cu^{2+} and different atomic charges [53,66], resulting in one O atom of the linker molecule being slightly shifted towards the pore center. This O atom acts as a nucleation site for water cluster formation (*via* H-bonding) and also sterically blocks the metal site, inhibiting coordination. The residual 20 % (one molecule) are adsorbed gradually (pressure range $p/p_0 = 0.1 \dots 1$), resulting in the formation of pillar-like water clusters with minimal interaction of water with the surrounding framework. Finally, adsorption of all water molecules is nearly completely reversible with almost no observable hysteresis.

Following that, we analyzed the water adsorption behavior of the other four materials in our study (M = Mg, Mn, Co, Ni). Starting with the water sorption isotherms of CPO-27-Mg (Fig. 6c) and CPO-27-Mn (Fig. 6d), both materials reveal a shape similar to each other but different from both CPO-27-Zn and CPO-27-Cu [53]. Initially, uptake of two molecules (*i.e.*, 40 % of the total uptake) in the pressure range of $p/p_0 = 0.001 \dots 0.02$ is observed. The adsorption of one of these two water molecules is irreversible, indicating that coordination to the open metal sites overlaps with adsorption of another water molecule. In the particular case of CPO-27-Mg, this is consistent with previous observations [16,57], highlighting a high affinity of the Mg^{2+} metal site towards water even in a competitive environment (*i.e.*, CO_2/H_2O mixture of 150/1; *ca.* 1 % relative humidity [16]). Based on previous findings on CPO-27-Zn [53] and CPO-27-Mg [55,56], we suggest the following mechanism: Some water molecules coordinate to the metal center (*i.e.*, partial occupation of the first site). The second site (near the inorganic building unit) is occupied simultaneously, which is a result of the similar adsorption energies of both sites. Subsequently, a third molecule is adsorbed in a defined step at *ca.* $p/p_0 = 0.02 \dots 0.05$. This water molecule occupies the third site (near the phenylene backbone) and possesses a lower binding energy than the previous ones [56]. Formation of the above-mentioned water clusters along the pore walls of the framework, with a weighted occupancy of all five positions (predominant occupation of first three sites, *i.e.,* comparable to Fig. 5c), is observed at that point. Then, adsorption of the last two molecules (40 %) is observed in the remaining pressure range in two reasonably distinguishable steps at $p/p_0 = 0.05 \dots 0.4$ (comparable to Fig. 5d) and, finally, between $p/p_0 = 0.4 \dots 1$ (comparable to Fig. 5e). As for CPO-27-Zn, strong hysteresis occurs in the latter region for both cycles, which suggests a similar rearrangement of a metastable water configuration into a denser configuration, restricting their mobility during the adsorption process.

Next, CPO-27-Co shows a water sorption behavior (Fig. 6e) which is partly comparable to CPO-27-Zn but differs from those observed for the other CPO-27-*M* (M = Mg, Mn, Cu) materials. Here, uptake of the first molecule does not occur in a well-defined step as the initial adsorption isotherm (first cycle) reveals the uptake of the three water molecules (60 % of the total uptake) in the pressure range of $p/p_0 = 0.001 \dots 0.03$. Still, a fraction of the initial water uptake is irreversible (a little less than 20 % of the total uptake), attributable to coordinating water (at the first site). This suggests that, again, coordination of some water molecules to the open metal site results in more favorable conditions for the second and third site (*i.e.,* similar sorption energies after adsorption of enough water molecules, contrary to CPO-27-Mg and CPO-27-Mn). Eventually, this leads to the formation of water clusters along the pore walls with similar characteristics as previously described (Fig. 5c). Then, the fourth water molecule is adsorbed in a clear step (*ca.* $p/p_0 = 0.03 \dots 0.05$; Fig. 5d), before the adsorption of the fifth molecule takes place over the wide remaining pressure range ($p/p_0 = 0.05 \dots 1$; Fig. 5e). This time, no significant hysteresis is observed. However, we suggest that a process similar to the previously noted phenomenon of preliminary pore saturation (as described for most other members) occurs after the second sorption step. Here, no large density changes seem to be present, enabling a reversible process. We determined the total water adsorption capacity after the first cycle as 23.2 (±2.9) mmol g^{-1}, which agrees with literature data (25.9 mmol g^{-1}, mostly defect-free framework) [48].

Finally, the water sorption isotherms of CPO-27-Ni (Fig. 6f) are comparable in shape to those of CPO-27-Co, but also reveal decisive differences. The first defined step occurs in a pressure range of $p/p_0 = 0.001 \dots 0.03$ and corresponds to *ca.* 40 % of the total uptake (two water molecules). We note that the desorption data are inconclusive with respect to reversibility, because, as mentioned above, the low-pressure data are missing for technical reasons. However, it is reasonable to assume that, as for the other materials, adsorption of water in CPO-27-Ni starts with coordination to the Ni^{2+} sites. In this case, the interaction between water and the metal sites is slightly less attractive, which may stem from rather strong Ni–O interactions (second behind CPO-27-Cu, as discussed above) in the inorganic building units influencing the atomic charges on the metal center as well as the preferred coordination environment of Ni^{2+} (*i.e.*, square planar, similar to Cu^{2+}). As a result, both the coordination of water molecules to the metal center and the H-bonding with framework O atoms becomes less attractive, causing similar adsorption energies of the first and second site. Furthermore, the third site also becomes less attractive, possibly due to either an increased electron density in the linker backbone and/or steric effects (*i.e.*, H-bond distances between water and oxygen atoms of the inorganic unit at the second site). As a consequence, adsorption of two water molecules instead of one is preferred to create the previously mentioned metastable state (step at $p/p_0 = 0.03 \dots 0.05$; Fig. 5d) instead of a water cluster along the pore walls. Afterward, gradual saturation is observed over a larger pressure range (Fig. 5e). In both isotherms, a slightly more pronounced hysteresis is observed (compared to CPO-27-Co), indicative of a less drastic density change.

Summarizing the water sorption data, we can conclude that the high water uptake at low relative pressure ($p/p_0 < 0.1$) is clear evidence of the hydrophilic nature of the CPO-27-*M* series (see Supporting Information, Fig. S29). The affinity of the open metal sites towards water is characteristic for each metal M^{2+} (except for Cu^{2+}) and becomes evident by the coordination of water (*i.e.*, chemisorption, 20 % of total water uptake). The irreversibility of this sorption process verifies the existence of vacant coordination sites prior to sorption measurements (*i.e.*, after activation, Fig. 5a). Deviating from this behavior, CPO-27-Cu shows a (nearly) reversible pore condensation behavior driven by water-water interactions, which is a result of changes in the local coordination environment and atomic charges, causing one oxygen atom of the inorganic building unit to move slightly towards the pore center, thereby initiating water cluster formation (*via* H-bonding) while blocking the Cu^{2+} site [53]. For all other materials, the precise water adsorption/desorption behavior (number of steps, adsorbed amounts, relative pressure ranges) depends on the metal center M^{2+}, consistent with the previously observed dehydration behavior [23]. With the exception of CPO-27-Zn, which reveals a prototypical water sorption behavior with clear identification of the chemisorbed water during adsorption (*i.e.*, occupation of the first sorption site; Fig. 5b) [53], all other members reveal a simultaneous adsorption processe (*i.e.*, occupation of the first two sites; first three for Co). Interestingly, the defined adsorption step at $p/p_0 = 0.03 \dots 0.05$ that corresponds to the uptake of one water molecule is virtually independent of the metal center (for M = Co, Mg, Mn, Ni, Zn) and characterized by comparable relative amounts of water uptake. This step describes the water cluster formation along the walls of the one-dimensional channels (high occupation of the first three sorption sites, Fig. 5c, except for Ni). After this step, additional adsorption (up to 80 %) leads to a metastable state (*i.e.,* preliminary pore saturation, Fig. 5d). Lastly, re-orientation of water molecules enables additional water uptake at higher relative pressures (Fig. 5e), which also explains the hysteresis in some water sorption isotherms due to the (for most members) irreversible increase in density of the adsorbed water [47,83,89,91–95]. However, CPO-27-Ni differs slightly from the above-described behavior, showing an uptake of two water molecules during the aforementioned step at $p/p_0 = 0.03 \ldots 0.05$. Here, the strong Ni–O interactions along with occupation of the first two sorption sites leads to significantly less attractive interactions at the third site (*i.e.*, phenylene ring). As a result, preliminary pore saturation (Fig. 5d) is observed instead of the formation of water clusters along the pore walls. We conclude that the formation of the above-discussed metastable state during adsorption is mostly unaffected by the type of metal center and purely based on confinement effects, as it is observed at similar relative pressures for all materials. Based on our findings, we suggest that the water affinity of the CPO-27-*M* series decreases in the order of $Mg^{2+} > Ni^{2+} > Co^{2+} > Mn^{2+} > Zn^{2+} \gg Cu^{2+}$ (Supporting Information Fig. S29), which is mostly consistent with previous studies on other guest molecules [15,19,57,98].

4. Conclusion

Our study reveals a strong impact of the choice of the metal center in CPO-27 on the water arrangement inside the one-dimensional micropores and the adsorption mechanism. In addition to the contact time, the extent to which water molecules interact with adjacent atoms in hydrated CPO-27-*M*, plays a major role on its durability against water. A high tendency of water molecules to form H-bonds seems to facilitate protonation of the phenolate and carboxylate groups (*M* = Zn, Mn, Co; large network contribution, *i.e.*, more static water) because of water accumulation near the pore walls. On the other hand, weaker interactions seem to inhibit this (*M* = Cu, Mg, Ni; large intermediate contribution), resulting in higher water stability. The precise hydration/dehydration behavior is governed by the given metal center. While CPO-27-Cu shows a drastically different behavior, revealing reversible pore condensation with the adsorbed water adopting a bulk-like behavior (with symmetric H-bonding) without any involvement of the metal site, CPO-27-Zn proves to possess a prototypical water sorption behavior with different, easily distinguishable sites, including the preferred occupation of the open metal site (first adsorption site). The other members of series (*M* = Co, Mg, Mn, Ni) show similarities and differences in their sorption behavior when compared to CPO-27-Zn. The precise hydration behavior is governed by the metal center, influencing the respective occupation of the five distinct sorption sites. Consequently, different adsorption mechanisms are observed. However, formation of water clusters along the walls of the one-dimensional channels is present in most compounds (except Ni). All materials reveal the formation of a metastable state at 80 % hydration (with respect to the total water uptake), which is characterized by a continuous H-bond network. This effect causes a hysteresis in some water sorption isotherms due to an irreversible density increase of the adsorbed water. In the completely hydrated state, highly located water molecules in an asymmetric H-bonding situation are observed in most materials.

CRediT authorship contribution statement

Marvin Kloß: Writing – original draft, Investigation, Formal analysis, Data curation. **Christian Weinberger:** Writing – review & editing, Validation, Methodology, Data curation, Conceptualization. **Michael Tiemann:** Writing – review & editing, Validation, Supervision, Project administration, Conceptualization.

Declaration of competing interest

The authors declare that they have no known competing financial interests or personal relationships that could have appeared to influence the work reported in this paper.

Data availability

Data will be made available on request.

Appendix A. Supplementary data

Supplementary data to this article can be found online at https://doi.org/10.1016/j.micromeso.2024.113352.

References

[1] C. Janiak, J.K. Vieth, MOFs, MILs and more: concepts, properties and applications for porous coordination networks (PCNs), New J. Chem. 34 (2010) 2366–2388.

[2] A.V. Desai, E. Lizundia, A. Laybourn, D.N. Rainer, A.R. Armstrong, R.E. Morris, S. Wuttke, R. Ettlinger, Green synthesis of reticular materials, Adv. Funct. Mater. (2023) 2304660.

[3] Ü. Kökçam-Demir, A. Goldman, L. Esrafili, M. Gharib, A. Morsali, O. Weingart, C. Janiak, Coordinatively unsaturated metal sites (open metal sites) in metal–organic frameworks: design and applications, Chem. Soc. Rev. 49 (2020) 2751–2798.

[4] P.D.C. Dietzel, Y. Morita, R. Blom, H. Fjellvåg, An in situ high-temperature single-crystal investigation of a dehydrated metal–organic framework compound and field-induced magnetization of one-dimensional metal–oxygen chains, Angew. Chem. Int. Ed. 44 (2005) 6354–6358.

[5] N.L. Rosi, J. Kim, M. Eddaoudi, B. Chen, M. O'Keeffe, O.M. Yaghi, Rod packings and Metal−Organic frameworks constructed from rod-shaped secondary building units, J. Am. Chem. Soc. 127 (2005) 1504–1518.

[6] P.D.C. Dietzel, B. Panella, M. Hirscher, R. Blom, H. Fjellvåg, Hydrogen adsorption in a nickel based coordination polymer with open metal sites in the cylindrical cavities of the desolvated framework, Chem. Commun. (2006) 959–961.

[7] E.D. Bloch, L.J. Murray, W.L. Queen, S. Chavan, S.N. Maximoff, J.P. Bigi, R. Krishna, V.K. Peterson, F. Grandjean, G.J. Long, B. Smit, S. Bordiga, C.M. Brown, J.R. Long, Selective binding of O_2 over N_2 in a redox–active metal–organic framework with open iron(II) coordination sites, J. Am. Chem. Soc. 133 (2011) 14814–14822.

[8] M. Märcz, R.E. Johnsen, P.D.C. Dietzel, H. Fjellvåg, The iron member of the CPO-27 coordination polymer series: synthesis, characterization, and intriguing redox properties, Microporous Mesoporous Mater. 157 (2012) 62–74.

[9] W. Zhou, H. Wu, T. Yildirim, Enhanced H_2 adsorption in isostructural Metal−Organic frameworks with open metal sites: strong dependence of the binding strength on metal ions, J. Am. Chem. Soc. 130 (2008) 15268–15269.

[10] G. Calleja, R. Sanz, G. Orcajo, D. Briones, P. Leo, F. Martínez, Copper-based MOF-74 material as effective acid catalyst in Friedel–Crafts acylation of anisole, Catal. Today 227 (2014) 130–137.

[11] M. Díaz-García, M. Sánchez-Sánchez, Synthesis and characterization of a new Cd-based metal-organic framework isostructural with MOF-74/CPO-27 materials, Microporous Mesoporous Mater. 190 (2014) 248–254.

[12] T.T. Zheng, J. Zhao, Z.W. Fang, M.T. Li, C.Y. Sun, X. Li, X.L. Wang, Z.M. Su, A luminescent metal organic framework with high sensitivity for detecting and removing copper ions from simulated biological fluids, Dalton Trans. 46 (2017) 2456–2461.

[13] P.D.C. Dietzel, R. Blom, H. Fjellvåg, Base-induced formation of two magnesium metal-organic framework compounds with a bifunctional tetratopic ligand, Eur. J. Inorg. Chem. (2008) 3624–3632.

[14] P.D.C. Dietzel, V. Besikiotis, R. Blom, Application of metal–organic frameworks with coordinatively unsaturated metal sites in storage and separation of methane and carbon dioxide, J. Mater. Chem. 19 (2009) 7362–7370.

[15] B. Pato-Doldán, M.H. Rosnes, P.D.C. Dietzel, An in-depth structural study of the carbon dioxide adsorption process in the porous metal–organic frameworks CPO-27-M, ChemSusChem 10 (2017) 1710–1719.

[16] E.O. Fetisov, M.S. Shah, J.R. Long, M. Tsapatsis, J.I. Siepmann, First principles Monte Carlo simulations of unary and binary adsorption: CO_2, N_2, and H_2O in Mg-MOF-74, Chem. Commun. 54 (2018) 10816–10819.

[17] W.L. Queen, M.R. Hudson, E.D. Bloch, J.A. Mason, M.I. Gonzalez, J.S. Lee, D. Gygi, J.D. Howe, K. Lee, T.A. Darwish, M. James, V.K. Peterson, S.J. Teat, B. Smit, J. B. Neaton, J.R. Long, C.M. Brown, Comprehensive study of carbon dioxide adsorption in the metal–organic frameworks M_2(dobdc) (M = Mg, Mn, Fe, Co, Ni, Cu, Zn), Chem. Sci. 5 (2014) 4569–4581.

[18] N. Drenchev, M.H. Rosnes, P.D.C. Dietzel, A. Albinati, K. Hadjiivanov, P. A. Georgiev, Open metal sites in the metal–organic framework CPO-27-Cu: detection of regular and defect copper species by CO and NO probe molecules, J. Phys. Chem. C 122 (2018) 17238–17249.

[19] M.H. Rosnes, M. Opitz, M. Frontzek, W. Lohstroh, J.P. Embs, P.A. Georgiev, P.D. C. Dietzel, Intriguing differences in hydrogen adsorption in CPO-27 materials induced by metal substitution, J. Mater. Chem. A 3 (2015) 4827–4839.

[20] F. Bonino, S. Chavan, J.G. Vitillo, E. Groppo, G. Agostini, C. Lamberti, P.D. C. Dietzel, C. Prestipino, S. Bordiga, Local structure of CPO-27-Ni metallorganic framework upon dehydration and coordination of NO, Chem. Mater. 20 (2008) 4957–4968.

[21] W.S. Drisdell, R. Poloni, T.M. McDonald, J.R. Long, B. Smit, J.B. Neaton, D. Prendergast, J.B. Kortright, Probing adsorption interactions in metal–organic frameworks using X-ray spectroscopy, J. Am. Chem. Soc. 135 (2013) 18183–18190.

[22] I. Strauss, A. Mundstock, D. Hinrichs, R. Himstedt, A. Knebel, C. Reinhardt, D. Dorfs, J. Caro, The interaction of guest molecules with Co-MOF-74: a vis/NIR and Raman approach, Angew. Chem. Int. Ed. 57 (2018) 7434–7439.

[23] M.H. Rosnes, B. Pato-Doldán, R.E. Johnsen, A. Mundstock, J. Caro, P.D.C. Dietzel, Role of the metal cation in the dehydration of the microporous metal–organic frameworks CPO-27-M, Microporous Mesoporous Mater. 309 (2020) 110503.

[24] J. Liu, L. Chen, H. Cui, J. Zhang, L. Zhang, C.Y. Su, Applications of metal–organic frameworks in heterogeneous supramolecular catalysis, Chem. Soc. Rev. 43 (2014) 6011–6061.

[25] S.M.J. Rogge, A. Bavykina, J. Hajek, H. Garcia, A.I. Olivos-Suarez, A. Sepúlveda-Escribano, A. Vimont, G. Clet, P. Bazin, F. Kapteijn, M. Daturi, E.V. Ramos-Fernandez, F.X. Xamena, V. Van Speybroeck, J. Gascon, Metal–organic and covalent organic frameworks as single-site catalysts, Chem. Soc. Rev. 46 (2017) 3134–3184.

[26] Y.S. Wei, M. Zhang, R. Zou, Q. Xu, Metal–organic framework-based catalysts with single metal sites, metal–organic framework-based catalysts with single metal sites, Chem. Rev. 120 (2020) 12089–12174.

[27] I. Strauss, A. Mundstock, M. Treger, K. Lange, S. Hwang, C. Chmelik, P. Rusch, N. C. Bigall, T. Pichler, H. Shiozawa, J. Caro, Metal–organic framework Co-MOF-74-Based host–guest composites for resistive gas sensing, ACS Appl. Mater. Interfaces 11 (2019) 14175–14181.

[28] L.T. Zhang, Y. Zhou, S.T. Han, The role of metal–organic frameworks in electronic sensors, Angew. Chem. Int. Ed. 60 (2021) 15192–15212.

[29] C. Solís, D. Palaci, F.X. Llabres i Xamena, J.M. Serra, Proton transport through robust CPO-27-type metal organic frameworks, J. Phys. Chem. C 118 (2014) 21663–21670.

[30] S. Hwang, E.J. Lee, D. Song, N.C. Jeong, High proton mobility with high directionality in isolated channels of MOF-74, ACS Appl. Mater. Interfaces 10 (2018) 35354–35360.

[31] A. Javed, I. Strauss, H. Bunzen, J. Caro, M. Tiemann, Humidity-mediated anisotropic proton conductivity through the 1D channels of Co-MOF-74, Nanomaterials 10 (2020) 1263.

[32] M.K. Sarango-Ramírez, D.-W. Lim, D.I. Kolokolov, A.E. Khudozhitkov, A. G. Stepanov, H. Kitagawa, Superprotonic conductivity in metal–organic framework via solvent-free coordinative urea insertion, J. Am. Chem. Soc. 142 (2020) 6861.

[33] M. Lupa, P. Kozyra, G. Jajko, D. Matoga, ACS Appl. Mater. Interfaces 13 (2021) 29820.

[34] M. Lupa, P. Kozyra, D. Matoga, Solvent-free mechanochemical dense pore filling yields CPO-27/MOF-74 metal–organic frameworks with high anhydrous and water-assisted proton conductivity, ACS Appl. Energy Mater. 6 (2023) 9118.

[35] I.E. Khalil, J. Fonseca, M.R. Reithofer, T. Eder, J.M. Chin, Tackling orientation of metal-organic frameworks (MOFs): the quest to enhance MOF performance, Coord. Chem. Rev. 481 (2023) 215043.

[36] Y.R. Liu, Y.Y. Chen, H.Y. Zhao, G. Li, Exploration of single-crystal proton conduction in ordered networks, Coord. Chem. Rev. 499 (2024) 215516.

[37] T. Chen, S. Chen, Y. Chen, M. Zhao, D. Losic, S. Zhang, Metal-organic frameworks containing solid-state electrolytes for lithium metal batteries and beyond, Mater. Chem. Front. 5 (2021) 1771–1794.

[38] T.M. McDonald, W.R. Lee, J.A. Mason, B.M. Wiers, C.S. Hong, J.R. Long, Capture of carbon dioxide from air and flue gas in the alkylamine-appended metal–organic framework mmen-Mg_2(dobpdc), J. Am. Chem. Soc. 134 (2012) 7056–7065.

[39] C.A. Trickett, A. Helal, B.A. Al-Maythalony, Z.H. Yamani, K.E. Cordova, O. M. Yaghi, The chemistry of metal–organic frameworks for CO_2 capture, regeneration and conversion, Nat. Rev. Mater. 2 (2017) 17045.

[40] M.J. Kalmutzki, C.S. Diercks, O.M. Yaghi, Metal–organic frameworks for water harvesting from air, Adv. Mater. 30 (2018) 1704304.

[41] N. Hanikel, M.S. Prévot, O.M. Yaghi, MOF water harvesters, Nat. Nanotechnol. 15 (2020) 348–355.

[42] Y.S. Bae, C.Y. Lee, K.C. Kim, O.K. Farha, P. Nickias, J.T. Hupp, S.T. Nguyen, R. Q. Snurr, High propene/propane selectivity in isostructural metal-organic frameworks with high densities of open metal sites, Angew. Chem. Int. Ed. 51 (2012) 1857–1860.

[43] P. Vervoorts, A. Schneemann, I. Hante, J. Pirillo, Y. Hijikata, T. Toyao, K. Kon, K. I. Shimizu, T. Nakamura, S.I. Noro, R.A. Fischer, Coordinated water as new binding sites for the separation of light hydrocarbons in metal-organic frameworks with open metal sites, ACS Appl. Mater. Interfaces 12 (2020) 9448–9456.

[44] J.-B. Brubach, A. Mermet, A. Filabozzi, A. Gerschel, P. Roy, Signatures of the hydrogen bonding in the infrared bands of water, J. Chem. Phys. 122 (2005) 184509.

[45] G. Onori, A. Santucci, IR investigations of water structure in Aerosol OT reverse micellar aggregates, J. Phys. Chem. 97 (1993) 5430–5434.

[46] H. MacDonald, B. Bedwell, E. Gulari, FTIR spectroscopy of microemulsion structure, Langmuir 2 (1986) 704–708.

[47] C. Weinberger, F. Zysk, M. Hartmann, N.K. Kaliannan, W. Keil, T.D. Kühne, M. Tiemann, The structure of water in silica mesopores – influence of the pore wall polarity, Adv. Mater. Interfac. 9 (2022) 2200245.

[48] H. Furukawa, F. Gándara, Y.B. Zhang, J. Jiang, W.L. Queen, M.R. Hudson, O. M. Yaghi, Water adsorption in porous metal–organic frameworks and related materials, J. Am. Chem. Soc. 136 (2014) 4369–4381.

[49] B. Zhang, Z. Zhu, X. Wang, X. Liu, F. Kapteijn, Water adsorption in MOFs: structures and applications, Adv. Funct. Mater. (2023) 2304788.

[50] J.B. DeCoste, G.W. Peterson, B.J. Schindler, K.L. Killops, M.A. Browe, J.J. Mahle, The effect of water adsorption on the structure of the carboxylate containing metal–organic frameworks Cu-BTC, Mg-MOF-74, and UiO-66, J. Mater. Chem. A 1 (2013) 11922–11932.

[51] P.M. Schoenecker, C.G. Carson, H. Jasuja, C.J.J. Flemming, K.S. Walton, Effect of water adsorption on retention of structure and surface area of metal–organic frameworks, Ind. Eng. Chem. Res. 51 (2012) 6513–6519.

[52] A. Metrane, A. Delhali, M. Ouikhalfan, A.H. Assen, Y. Belmabkhout, Water vapor adsorption by porous materials: from chemistry to practical applications, J. Chem. Eng. Data 67 (2022) 1617–1653.

[53] M. Kloß, M. Beerbaum, D. Baier, C. Weinberger, F. Zysk, H. Elgabarty, T.D. Kühne, M. Tiemann, Understanding hydration in CPO-27 metal-organic frameworks: strong impact of the chemical nature of the metal (Cu, Zn), Adv. Mater. Interfaces (2024) 2400476.

[54] K. Lee, J.D. Howe, L.-C. Lin, B. Smit, J.B. Neaton, Small-molecule adsorption in open-site metal–organic frameworks: a systematic density functional theory study for rational design, Chem. Mater. 27 (2015) 668–678.

[55] Y. Li, X. Wang, D. Xu, J.D. Chung, M. Kaviany, B. Huang, H_2O adsorption/desorption in MOF-74: *Ab initio* molecular dynamics and experiments, J. Phys. Chem. C 119 (2015) 13021–13031.

[56] X. Peng, L. Lin, W. Sun, B. Smit, Water adsorption in metal–organic frameworks with open-metal sites, AIChE J. 61 (2) (2015) 677–687.

[57] M.G. Lopez, P. Canepa, T. Thonhauser, NMR study of small molecule adsorption in MOF-74-Mg, J. Chem. Phys. 138 (2013) 154704.

[58] L.J. Wang, H. Deng, H. Furukawa, F. Gándara, K.E. Cordova, D. Peri, O.M. Yaghi, Synthesis and characterization of metal–organic framework-74 containing 2, 4, 6, 8, and 10 different metals, Inorg. Chem. 53 (2014) 5881–5883.

[59] S.E. Henkelis, S.M. Vornholt, D.B. Cordes, A.M.Z. Slawin, P.S. Wheatley, R. E. Morris, A single crystal study of CPO-27 and UTSA-74 for nitric oxide storage and release, CrystEngComm 21 (2019) 1857–1861.

[60] K. Momma, F. Izumi, *VESTA 3* for three-dimensional visualization of crystal, volumetric and morphology data, J. Appl. Crystallogr. 44 (2011) 1272–1276.

[61] Q. Song, Y. Li, Z. Cao, H. Liu, C. Tian, Z. Yang, X. Qiang, Z. Tan, Y. Deng, Discovery of novel 2,5-dihydroxyterephthalamide derivatives as multifunctional agents for the treatment of Alzheimer's disease, Bioorg. Med. Chem. 26 (2018) 6115–6127.

[62] J. Rouquerol, P. Llewellyn, F. Rouquerol, Is the bet equation applicable to microporous adsorbents? Stud. Surf. Sci. Catal. 160 (2007) 49–56.

[63] M. Thommes, K. Kaneko, A.V. Neimark, J.P. Olivier, F. Rodriguez-Reinoso, J. Rouquerol, K.S.W. Sing, Physisorption of gases, with special reference to the evaluation of surface area and pore size distribution (IUPAC Technical Report), Pure Appl. Chem. 87 (2015) 1051–1069.

[64] S.S. Han, S.-H. Choi, A.C.T. van Duin, Molecular dynamics simulations of stability of metal–organic frameworks against H_2O using the ReaxFF reactive force field, Chem. Commun. 46 (2010) 5713–5715.

[65] M.V. Veidis, G.H. Schreiber, T.E. Gough, G.J. Palenik, Jahn-Teller distortions in octahedral copper(II) complexes, J. Am. Chem. Soc. 91 (1969) 1859–1860.

[66] T. Pham, K.A. Forrest, J. Eckert, B. Space, Dramatic effect of the electrostatic parameters on H_2 sorption in an M-MOF-74 analogue, Cryst. Growth Des. 16 (2016) 867–874.

[67] K. Schlichte, T. Kratzke, S. Kaskel, Improved synthesis, thermal stability and catalytic properties of the metal-organic framework compound $Cu_3(BTC)_2$, Microporous Mesoporous Mater. 73 (2004) 81–88.

[68] N. Heidary, D. Chartrand, A. Guiet, N. Kornienko, Rational incorporation of defects within metal–organic frameworks generates highly active electrocatalytic sites, Chem. Sci. 12 (2021) 7324–7333.

[69] R.M. Badger, A relation between internuclear distances and bond force constants, J. Chem. Phys. 2 (1934) 128–131.

[70] L. Verdonck, G.P. Van der Kelen, Z. Eeckhaut, Benzyl compounds—VII: the far infrared and Raman spectra of *meta*-substituted benzyl compounds, Spectrochim. Acta Part A Mol. Spectrosc. 29 (1973) 813–816.

[71] R.J. Jakobsen, F.F. Bentley, Vibrational spectra of benzene derivatives. II. Frequency assignments in the CsBr region, Appl. Spectrosc. 18 (1964) 88–92.

[72] E.F. De Oliveira, Y. Hase, Infrared study of magnesium–nickel hydroxide solid solutions, Vib. Spectrosc. 31 (2003) 19–24.

[73] X. Wang, L. Andrews, Infrared spectra of $M(OH)_{1,2,3}$ (M = Mn, Fe, Co, Ni) molecules in solid argon and the character of first row transition metal hydroxide bonding, J. Phys. Chem. A 110 (2006) 10035–10045.

[74] C. Henrist, K. Traina, C. Hubert, G. Toussaint, A. Rulmont, R. Cloots, Study of the morphology of copper hydroxynitrate nanoplatelets obtained by controlled double jet precipitation and urea hydrolysis, J. Cryst. Growth 254 (2003) 176–187.

[75] R.H.P. Devamani, M. Alagar, Synthesis and characterisation of copper II hydroxide nano particles, Nano Biomed. Eng. 5 (2013) 116–120.

[76] E.F. De Oliveira, Y. Hase, Infrared study and isotopic effect of magnesium hydroxide, Vib. Spectrosc. 25 (2001) 53–56.

[77] H. Lin, Y. Wang, J. Niu, Z. Yue, Q. Huang, Efficient sorption and removal of perfluoroalkyl acids (PFAAs) from aqueous solution by metal hydroxides generated in situ by electrocoagulation, Environ. Sci. Technol. 49 (2015) 10562–10569.

[78] L. Gong, X. Liu, L. Su, Facile solvothermal synthesis $Ni(OH)_2$ nanostructure for electrochemical capacitors, J. Inorg. Organomet. Polym. Mater. 21 (2011) 866–870.

[79] P.D.C. Dietzel, R.E. Johnsen, R. Blom, H. Fjellvåg, Structural changes and coordinatively unsaturated metal atoms on dehydration of honeycomb analogous microporous metal–organic frameworks, Chem. Eur J. 14 (2008) 2389–2397.

[80] Y. Fu, Y. Yao, A.C. Forse, J. Li, K. Mochizuki, J.R. Long, J.A. Reimer, G. De Paëpe, X. Kong, Solvent-derived defects suppress adsorption in MOF-74, Nat. Commun. 14 (2023) 2386.

[81] R.D. Shannon, Revised effective ionic radii and systematic studies of interatomic distances in halides and chalcogenides, Acta Crystallogr., Sect. A 32 (1976) 751–767.

[82] S.D. Bernardina, E. Paineau, J.-B. Brubach, P. Judeinstein, S. Rouzière, P. Launois, P. Roy, Water in carbon nanotubes: the peculiar hydrogen bond network revealed by infrared spectroscopy, J. Am. Chem. Soc. 138 (2016) 10437–10443.

[83] M. Sadeghi, G.A. Parsafar, Density-induced molecular arrangements of water inside carbon nanotubes, Phys. Chem. Chem. Phys. 15 (2013) 7379–7388.

[84] I. Hanasaki, A. Nakatani, Flow structure of water in carbon nanotubes: Poiseuille type or plug-like? J. Chem. Phys. 124 (2006) 144708.

[85] C. Zhang, R.Z. Khaliullin, D. Bovi, L. Guidoni, T.D. Kühne, Vibrational signature of water molecules in asymmetric hydrogen bonding environments, J. Phys. Chem. Lett. 4 (2013) 3245–3250.

[86] C. Zhang, L. Guidoni, T.D. Kühne, Competing factors on the frequency separation between the OH stretching modes in water, J. Mol. Liq. 205 (2015) 42–45.

[87] A. Kaufman Katz, J.P. Glusker, G.D. Markham, C.W. Bock, Deprotonation of water in the presence of carboxylate and magnesium ions, J. Phys. Chem. B 102 (1998) 6342–6350.

[88] N. Al-Janabi, A. Alfutimie, F.R. Siperstein, X. Fan, Front, Underlying mechanism of the hydrothermal instability of $Cu_3(BTC)_2$ metal-organic framework, Chem. Sci. Eng. 10 (2016) 103–107.

[89] T. Iiyama, M. Ruike, K. Kaneko, Structural mechanism of water adsorption in hydrophobic micropores from in situ small angle X-ray scattering, Chem. Phys. Lett. 331 (2000) 359–364.

[90] J. Alcañiz-Monge, A. Linares-Solano, B. Rand, Mechanism of adsorption of water in carbon micropores as revealed by a study of activated carbon fibers, J. Phys. Chem. B 106 (2002) 3209–3216.

[91] I. Brovchenko, A. Geiger, A. Oleinikova, Water in nanopores: II. The liquid–vapour phase transition near hydrophobic surfaces, J. Phys. Condens. Matter 16 (2004) S5345.

[92] T. Ohba, H. Kanoh, K. Kaneko, Cluster-growth-induced water adsorption in hydrophobic carbon nanopores, J. Phys. Chem. B 108 (2004) 14964–14969.

[93] T. Ohba, H. Kanoh, K. Kaneko, Structures and stability of water nanoclusters in hydrophobic nanospaces, Nano Lett. 5 (2005) 227–230.

[94] P. Gallo, M. Rovere, S.-H. Chen, Anomalous dynamics of water confined in MCM-41 at different hydrations, J. Phys. Condens. Matter 22 (2010) 284102.

[95] M. Thommes, J. Morell, K.A. Cychosz, M. Fröba, Combining nitrogen, argon, and water adsorption for advanced characterization of ordered mesoporous carbons (CMKs) and periodic mesoporous organosilicas (PMOs), Langmuir 29 (2013) 14893–14902.

[96] J.B. Mietner, F.J. Brieler, Y.J. Lee, M. Fröba, Properties of water confined in periodic mesoporous organosilicas: nanoimprinting the local structure, Angew. Chem. Int. Ed. 56 (2017) 12348–12351.

[97] B. Malfait, A. Moréac, A. Jani, R. Lefort, P. Huber, M. Fröba, D. Morineau, Structure of water at hydrophilic and hydrophobic interfaces: Raman spectroscopy of water confined in periodic mesoporous (Organo)Silicas, J. Phys. Chem. C 126 (2022) 3520–3531.

[98] R. Mercado, B. Vlaisavljevich, L.C. Lin, K. Lee, Y. Lee, J.A. Mason, D.J. Xiao, M. I. Gonzalez, M.T. Kapelewski, J.B. Neaton, B. Smit, Force field development from periodic density functional theory calculations for gas separation applications using metal–organic frameworks, J. Phys. Chem. C 120 (2016) 12590–12604.

Water in the Micropores of CPO-27 Metal-Organic Frameworks: A Comprehensive Study

Supporting Information

Marvin Kloß,[1] Christian Weinberger,[1] and Michael Tiemann*,[1]

[1] *Department of Chemistry – Inorganic Chemistry, Faculty of Science, Paderborn University*
Warburger Str. 100, 33098, Paderborn, Germany

Synthesis of 2,5-dihydroxyterephthalic acid (H_4dhtp): Dimethyl 2,5-dioxo-cyclohexane-1,4-dicarboxylic acid (11.4 g, 51.4 mmol, 1.0 eq) was dissolved in glacial acetic acid (50 mL). The mixture was heated to 80 °C and *N*-chlorosuccinimide (NCS, 7.22 g, 54.2 mmol, 1.08 eq) was added portion-wise over the course of 30 minutes. During this process, a yellow precipitate was formed. After complete addition of NCS, the mixture was heated for additional 2 hours to 80 °C. After cooling back to room temperature, a bright yellow solid was filtered off and washed with copious amounts of deionized water (300-400 mL) and methanol (2 x 10 mL). The product was dried overnight at 60 °C. Dimethyl 2,5-dihydroxyterephthalate (8.34 g, 36.9 mmol, 74 %) was isolated as a bright yellow, crystalline solid. ^{1}H NMR (700 MHz, $CDCl_3$): δ = 10.05 (s, 2H), 7.46 (s, 2H), 3.97 (s, 6H) ppm. ^{13}C NMR (175 MHz, $CDCl_3$) δ = 169.7, 153.1, 118.5, 118.0, 53.0 ppm (see Supporting Information, Fig. S1). Dimethyl 2,5-dihydroxyterephthalate (8.34 g, 36.9 mmol, 1 eq.) was dissolved in a solution of sodium hydroxide (6.71 g, 167.7 mmol, 4.55 eq) in deionized water (130 mL). The mixture was heated to 80 °C for 6 h, during which the initially yellow solution turned into an orange and finally dark brown solution. After cooling to room temperature, the solution was poured into a mixture of concentrated aqueous hydrochloric acid and ice. During this process, a light-yellow precipitate was formed. The pH was adjusted to 1. The product was separated by filtration and washed with copious amounts of water (approx. 700 mL) until the pH was neutral. The product was dried overnight at 60 °C in an oven to afford 2,5-dihydroxyterephthalic acid (H_4dhtp, 5.27 g, 26.6 mmol, 72 %) as a light-yellow solid. ^{1}H NMR (500 MHz, dmso-d_6): δ = 11.34 (brs, 2H), 7.27 (s, 2H) ppm. ^{13}C NMR (125 MHz, DMSO-d_6) δ = 170.8, 152.5, 119.8, 117.8 ppm (see Supporting Information, Fig. S2).

Preparation of CPO-27-Co: Cobalt(II) nitrate hexahydrate (2.0 g, 6.86 mmol, 1.0 eq) was dissolved in deionized water (54 mL) in a glass insert (250 mL). Then, 2,5-dihydroxyterephthalic acid (H_4dhtp, 1.58 g, 8.0 mmol, 1.17 eq) was dissolved in a mixture of ethanol (54 mL) and *N,N*-dimethylformamide (DMF, 54 mL) under sonification. The obtained linker solution was transferred to the glass insert containing the cobalt salt solution and the mixture was stirred briefly. The insert was placed in a stainless-steel reactor (*Parr Instruments*), sealed, and reacted in a preheated oven at 130 °C for 24 h. After cooling, the dark red solid was separated by filtration over a glass frit and washed with deionized water (4 x 30 mL) and methanol (30 mL). Afterwards, the solvent was exchanged by methanol (four times), leaving each portion to stand for 30 to 45 minutes. The obtained product was dried in multiple steps. For the first step, the product was placed in a round flask under dynamic vacuum for 20 h. Then, the product was heated in three steps from 60 °C (hold for 90 minutes) to 100 °C (hold for 90 minutes) and 150 °C (hold for 20 h). The desolvated product (brown solid) was stored in a glove box under argon atmosphere.

Preparation of CPO-27-Cu: Copper(II) nitrate trihydrate (2.414 g, 10.0 mmol, 1.0 eq) was dissolved in DMF (15 mL) under sonification and transferred to a Teflon-lined insert (125 mL). Then, 2,5-dihydroxyterephthalic acid (H_4dhtp, 0.99 g, 5.0 mmol, 0.5 eq) and 1,4-diazabicyclo[2.2.2]octan (dabco, 0.28 g, 2.5 mmol, 0.25 eq) were separately dissolved in DMF (H_4dhtp in 40 mL, dabco in 10 mL) under sonification. The obtained solutions were combined in the insert and the mixture was stirred briefly. The insert was placed in a stainless-steel reactor (*Parr Instruments*), sealed, and reacted in a preheated oven at 60 °C for 72 h. After cooling, the dark red solid was separated by filtration over a glass frit and washed with deionized water (4 x 30 mL) and methanol (30 mL). Afterwards, the solvent was exchanged by methanol (four times), leaving each portion to stand for 30 to 45 minutes. The obtained product was dried in multiple steps. For the first step, the product was placed in a round flask under dynamic vacuum for 20 h. Then, the product was heated in three steps from 60 °C (hold for 90 minutes) to 100 °C (hold for 90 minutes) and 120 °C (hold for 20 h). The desolvated product (dark brown solid) was stored in a glove box under argon atmosphere.

Preparation of CPO-27-Mg: Magnesium(II) acetate tetrahydrate (1.93 g, 9.0 mmol, 1.0 eq) was dissolved in deionized water (6 mL) and transferred to a Teflon-lined insert (125 mL). Then, 2,5-dihydroxyterephthalic acid (H_4dhtp, 0.89 g, 4.5 mmol, 0.5 eq) was dissolved in *N*-methyl-2-pyrrolidone (NMP, 54 mL) under sonification. The obtained solution was transferred to the insert containing the magnesium salt solution and the mixture was stirred briefly. The insert was placed in a stainless-steel reactor (*Parr Instruments*), sealed, and reacted in a preheated oven at 120 °C for 24 h. After cooling, the yellow-brown solid was separated by filtration over a glass frit and washed with deionized water (4 x 30 mL) and methanol (30 mL). Afterwards, the solvent was exchanged by methanol (four times), leaving each portion to stand for 30 to 45 minutes. The obtained product was dried in multiple steps. For the first step, the product was placed in a round flask under dynamic vacuum for 20 h. Then, the product was heated in three steps from 60 °C (hold for 90 minutes) to 100 °C (hold for 90 minutes) and 150 °C (hold for 20 h). The desolvated product (yellow solid) was stored in a glove box under argon atmosphere.

Preparation of CPO-27-Mn: Manganese(II) acetate tetrahydrate (1.84 g, 7.5 mmol, 1.0 eq) was dissolved in deionized water (6 mL) and transferred to a Teflon-lined insert (125 mL). Then, 2,5-dihydroxyterephthalic acid (H_4dhtp, 0.74 g, 3.75 mmol, 0.5 eq) was dissolved in *N*-methyl-2-pyrrolidone (NMP, 54 mL) under sonification. The obtained solution was transferred to the insert containing the manganese salt solution and the mixture was stirred briefly. The insert was placed in a stainless-steel reactor (*Parr Instruments*), sealed, and reacted in a preheated oven at 110 °C for 24 h. After cooling, the brown solid was separated by filtration over a glass frit and washed with deionized water (4 x 30 mL) and methanol (30 mL). Afterwards, the solvent was exchanged by methanol (four times), leaving each portion to stand for 30 to 45 minutes. The obtained product was dried in multiple steps. For the first step, the product was placed in a round flask under dynamic vacuum for 20 h. Then, the product was heated in three steps from 60 °C (hold for 90 minutes) to 100 °C (hold for 90 minutes) and 150 °C (hold for 20 h). The desolvated product (brown solid) was stored in a glove box under argon atmosphere.

Preparation of CPO-27-Ni: Nickel(II) acetate tetrahydrate (1.79 g, 7.2 mmol, 1.0 eq) was dissolved in deionized water (6 mL) and transferred to a Teflon-lined insert (45 mL). Then, 2,5-dihydroxyterephthalic acid (H_4dhtp, 0.74 g, 3.6 mmol, 0.5 eq) was dispersed in deionized water (16 mL). The obtained dispersion was transferred to the insert and the mixture was stirred briefly. The insert was placed in a stainless-steel reactor (*Parr Instruments*), sealed, and reacted in a preheated oven at 110 °C for 24 h. After cooling, the yellow solid was separated by filtration over a glass frit and washed with deionized water (4 x 30 mL) and methanol (30 mL). Afterward, the solvent was exchanged by methanol (four times), leaving each portion to stand for 30 to 45 minutes. The obtained product was dried in multiple steps. For the first step, the product was placed in a round flask under dynamic vacuum for 20 h. Then, the product was heated in three steps from 60 °C (hold for 90 minutes) to 100 °C (hold for 90 minutes) and 150 °C (hold for 20 h). The desolvated product (orange-yellow solid) was stored in a glove box under argon atmosphere.

Preparation of CPO-27-Zn: Zinc(II) nitrate hexahydrate (4.19 g, 14.1 mmol, 1.0 eq) was dissolved in a mixture of DMF (30 mL) and deionized water (3.6 mL) and transferred to a Teflon-lined insert (125 mL). Then, 2,5-dihydroxyterephthalic acid (H_4dhtp, 0.9 g, 4.55 mmol, 0.33 eq) was dissolved in a mixture of DMF (30 mL) and ethanol (3.6 mL). The obtained solution was transferred to the insert containing the zinc salt solution and the mixture was stirred briefly. The insert was placed in a stainless-steel reactor (*Parr Instruments*), sealed, and reacted in a preheated oven at 120 °C for 24 h. After cooling, the yellow solid was separated by filtration over a glass frit and washed with deionized water (4 x 30 mL) and methanol (30 mL). Afterwards, the solvent was exchanged by methanol (four times), leaving each portion to stand for 30 to 45 minutes. The obtained product was dried in multiple steps. For the first step, the product was placed in a round flask under dynamic vacuum for 20 h. Then, the product was heated in three steps from 60 °C (hold for 90 minutes) to 100 °C (hold for 90 minutes) and 150 °C (hold for 20 h). The desolvated product (orange-yellow solid) was stored in a glove box under argon atmosphere.

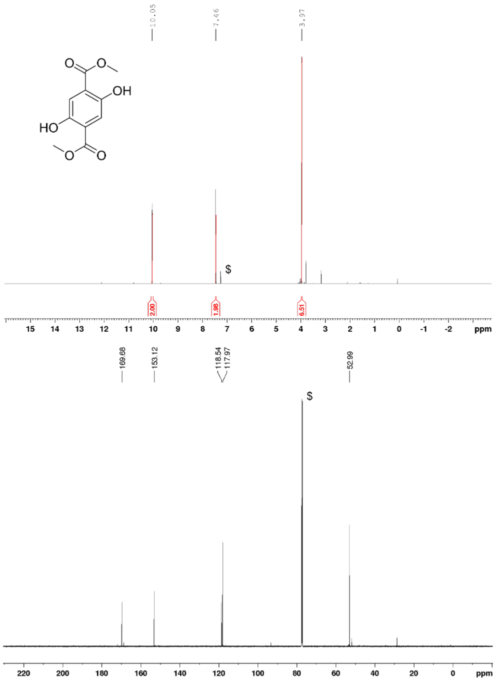

Fig. S1. ^{1}H NMR (top) and ^{13}C NMR spectrum (bottom) of dimethyl 2,5-dihydroxyterephthalate in $CDCl_3$ (marked with $).

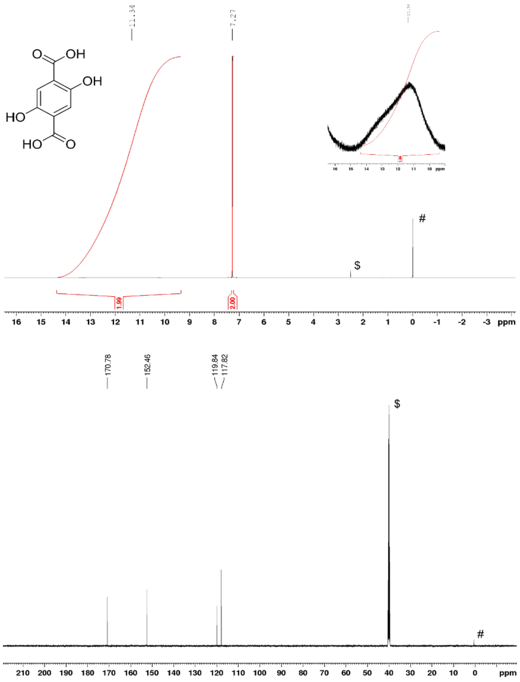

Fig. S2. ^{1}H NMR (top) and ^{13}C NMR spectrum (bottom) of 2,5-dihydroxyterephthalic acid in dmso-d_6 (marked with $). TMS (marked with #) has been used as internal standard.

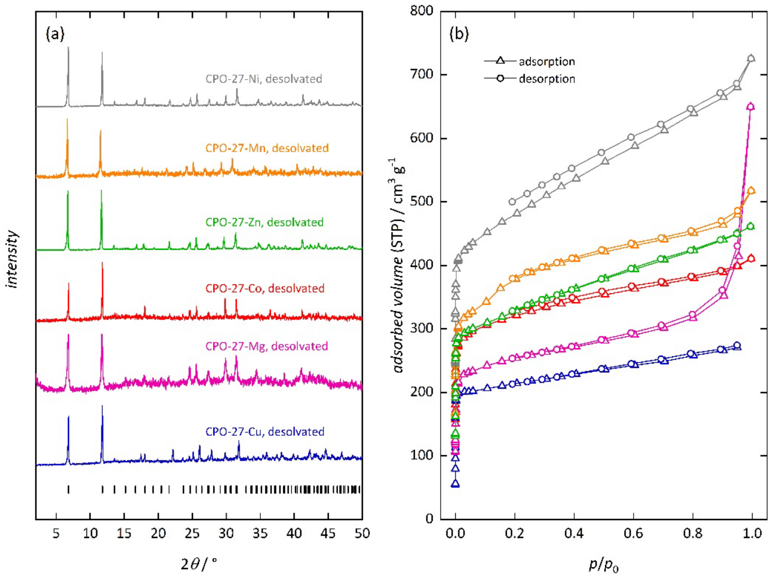

Fig. S3. Powder X-ray diffraction pattern of desolvated (ds) frameworks of the isoreticular CPO-27-*M* framework series (a) in comparison with the theoretical peak positions for the zinc compound (tik marks). The patterns are normalized for comparison. (b) Nitrogen sorption isotherms of the isoreticular CPO-27-*M* series in linear scale, measured at 77 K. The color code is the same as in (a).

Tab. S1. Specific surface area and pore volume (determined at $p/p_0 \approx 0.5$) obtained from the sorption isotherms of the CPO-27-*M* materials.

	S_{BET} / m^2 g^{-1}	V_{Pore} / m^3 g^{-1}
Co	1220	0.56
Cu	860	0.37
Mg	980	0.44
Mn	1350	0.66
Ni	1790	0.90
Zn	1240	0.59

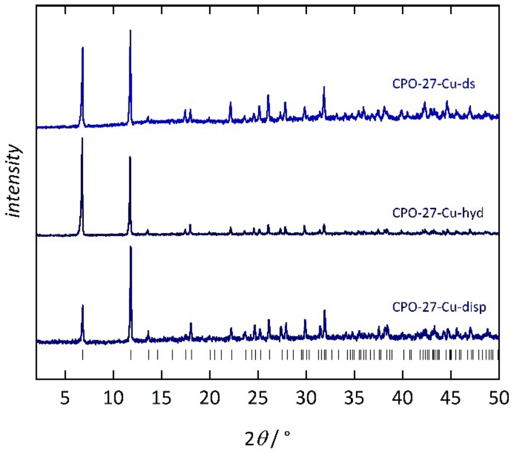

Fig. S4. Powder X-ray diffraction pattern of desolvated (ds), hydrated (hyd), and dispersed (disp) CPO-27-Cu in comparison with the theoretical peak positions.

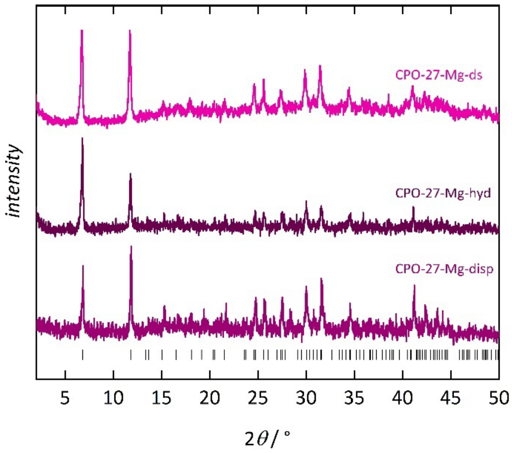

Fig. S5. Powder X-ray diffraction pattern of desolvated (ds), hydrated (hyd), and dispersed (disp) CPO-27-Mg in comparison with the theoretical peak positions.

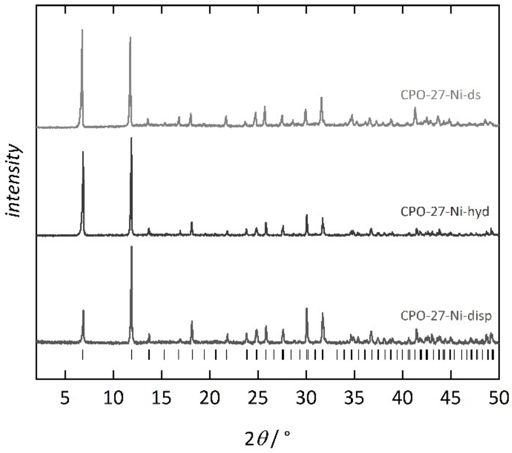

Fig. S6. Powder X-ray diffraction pattern of desolvated (ds), hydrated (hyd), and dispersed (disp) CPO-27-Ni in comparison with the theoretical peak positions.

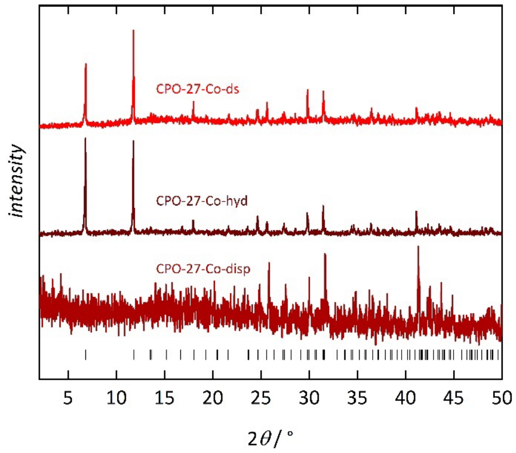

Fig. S7. Powder X-ray diffraction pattern of desolvated (ds), hydrated (hyd), and dispersed (disp) CPO-27-Co in comparison with the theoretical peak positions.

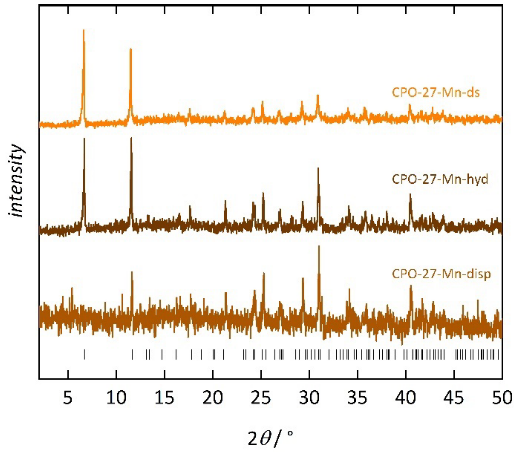

Fig. S8. Powder X-ray diffraction pattern of desolvated (ds), hydrated (hyd), and dispersed (disp) CPO-27-Mn in comparison with the theoretical peak positions.

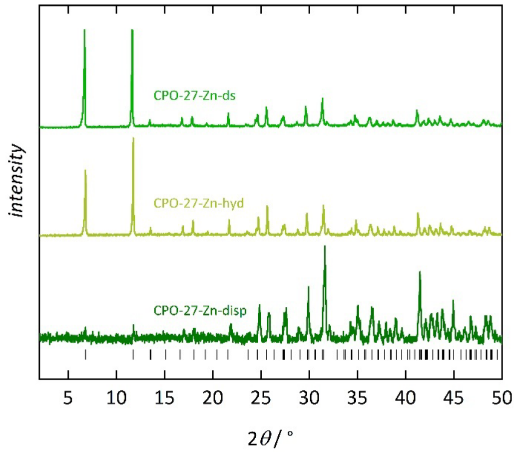

Fig. S9. Powder X-ray diffraction pattern of desolvated (ds), hydrated (hyd), and dispersed (disp) CPO-27-Zn in comparison with the theoretical peak positions.

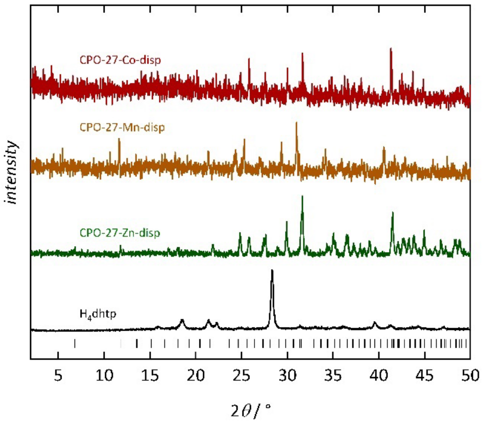

Fig. S10. Powder X-ray diffraction pattern of dispersed (disp) CPO-27-*M* (*M* = Co, Mn, Zn) samples in comparison with the protonated dhtp linker molecule and theoretical peak positions.

Tab. S2. Elemental analysis (C, H) of dispersed and hydrated CPO-27-*M* materials (2 individually synthesized batches of each material; two samples of each batch) and the amounts of water molecules *x* per formula unit M_2(dhtp)(H_2O)$_x$ calculated from the measured data.

	dispersed			*hydrated*		
	C	H	*x*	C	H	*x*
Co	20.9	4.53	8	20.3	4.5	9
	20.88	4.29	8	20.22	4.55	9
	20.23	4.18	9	19.84	4.18	10
	20.22	4.19	9	19.93	4.45	10
Cu	21.11	4.46	8	20.08	4.14	9
	21.28	3.79	8	20.14	4.13	9
	20.8	3.73	8	20.09	4.27	9
	20.75	3.41	8	19.95	4.12	9
Mg	25.11	4.38	8	20.78	5.21	10+
	25.05	4.48	8	21.81	4.83	10+
	23.83	5.02	9	21.98	5.01	10+
	23.38	4.85	9	22.44	5.07	10+
Mn	20.97	4.18	9	20.09	4.8	10
	21.02	4.13	9	20	4.64	10
	21.1	4.09	8	19.49	4.24	10
	21.03	3.94	8	19.62	4.35	10
Ni	20.1	4.31	9	19.6	4.51	10
	20.09	4.31	9	19.67	4.59	10
	20.04	4.42	9	19.82	4.35	10
	20.02	4.47	9	19.78	4.48	10
Zn	19.67	4.05	9	19.03	4.41	10
	19.54	4.06	9	19.05	4.42	10
	19.66	4.04	9	19.32	5.44	10
	19.48	3.88	9	19.22	4.31	10

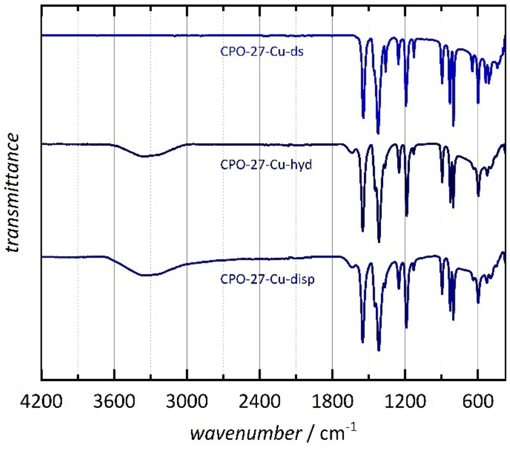

Fig. S11. Comparison of the FT-IR spectra of desolvated (ds), hydrated (hyd) and dispersed (disp) CPO-27-Cu. The spectra are normalized and vertically offset.

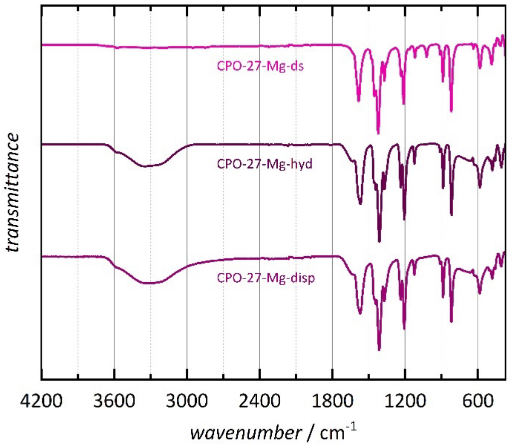

Fig. S12. Comparison of the FT-IR spectra of desolvated (ds), hydrated (hyd) and dispersed (disp) CPO-27-Mg. The spectra are normalized and vertically offset.

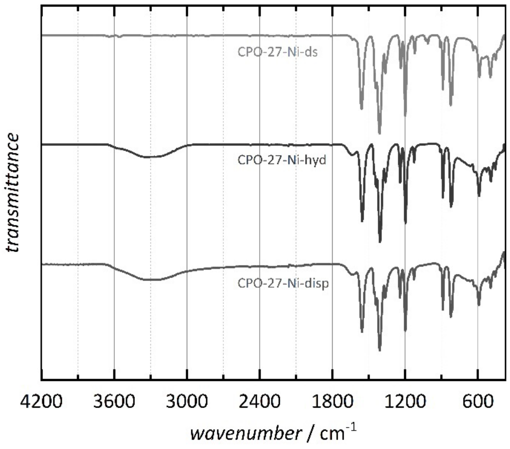

Fig. S13. Comparison of the FT-IR spectra of desolvated (ds), hydrated (hyd) and dispersed (disp) CPO-27-Ni. The spectra are normalized and vertically offset.

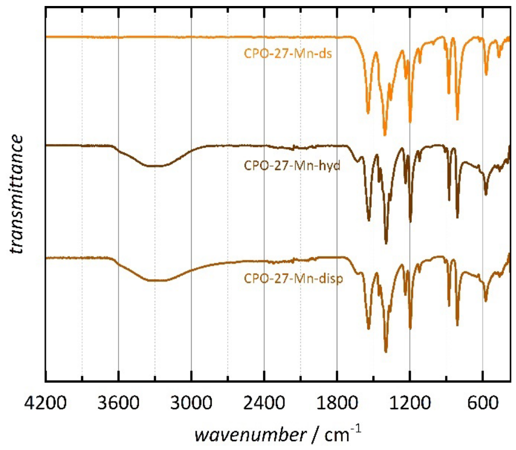

Fig. S14. Comparison of the FT-IR spectra of desolvated (ds), hydrated (hyd) and dispersed (disp) CPO-27-Mn. The spectra are normalized and vertically offset.

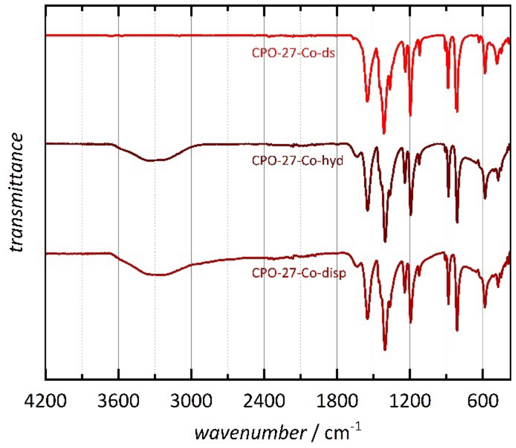

Fig. S15. Comparison of the FT-IR spectra of desolvated (ds), hydrated (hyd) and dispersed (disp) CPO-27-Co. The spectra are normalized and vertically offset.

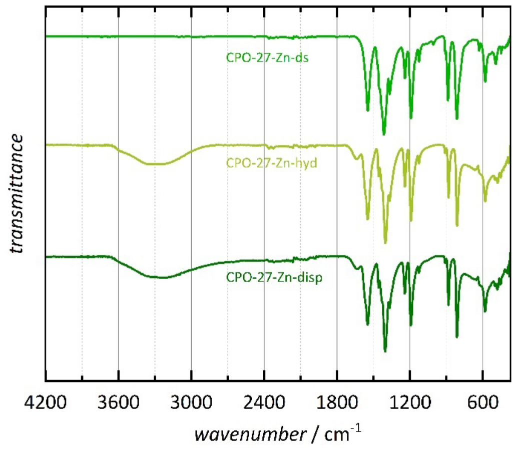

Fig. S16. Comparison of the FT-IR spectra of desolvated (ds), hydrated (hyd) and dispersed (disp) CPO-27-Zn. The spectra are normalized and vertically offset.

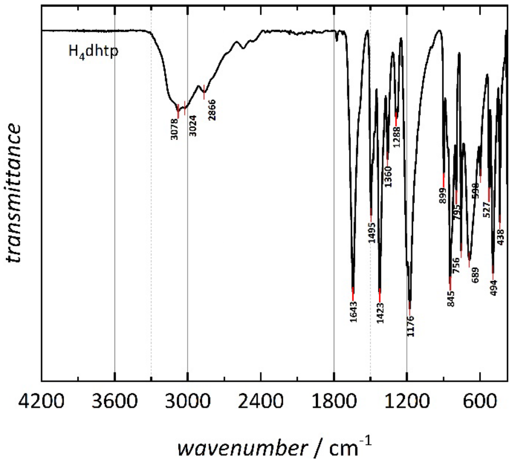

Fig. S17. FT-IR spectra of the 2,5-dihydroxyterephthalic acid linker molecule used for the synthesis of CPO-27-M frameworks.

Table S3. Initial dehydration (T_{dehyd}) and framework decomposition (T_{dec}) of CPO-27-*M* samples determined by thermal analysis.

	mass loss / %	T_{dehyd} (°C)	$T_{\text{dehyd, literature}}$* (°C)	T_{dec}** (°C)	$T_{\text{dec, literature}}$* (°C)
Co	31.5	210	230	439 (525)	407
Cu	26.5	90	90	295 (380)	300
Mg	30.5	360	380	467 (625)	607
Mn	28.8	205	280	219 (527)	500
Ni	30.5	250	280	360 (520)	330
Zn	29.2	205	210	325 (500)	230 (440)

* M. H. Rosnes, B. Pato-Doldán, R. E. Johnsen, A. Mundstock, J. Caro, P. D. C. Dietzel, *Microporous Mesoporous Mater.* 309 (2020) 110503.

** onset (complete decomposition)

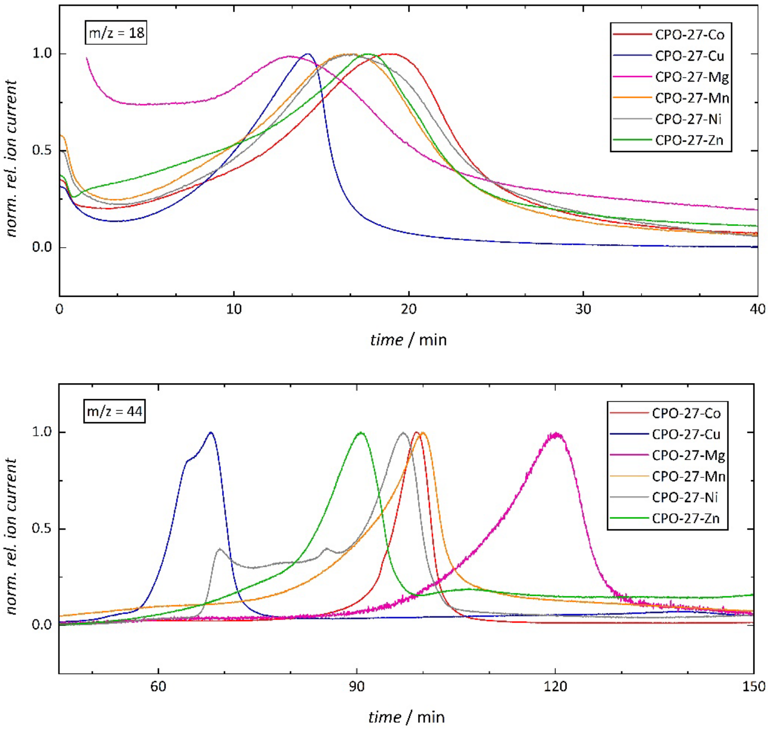

Fig. S18. Zoom-in of the MS traces (m/z = 18 and m/z = 44) of the measured CPO-27-*M*-hyd samples. For CPO-27-Mg, the first 90 seconds of the m/z = 18 trace were discarded due to a high initial signal stemming from residual atmospheric water in the sample chamber.

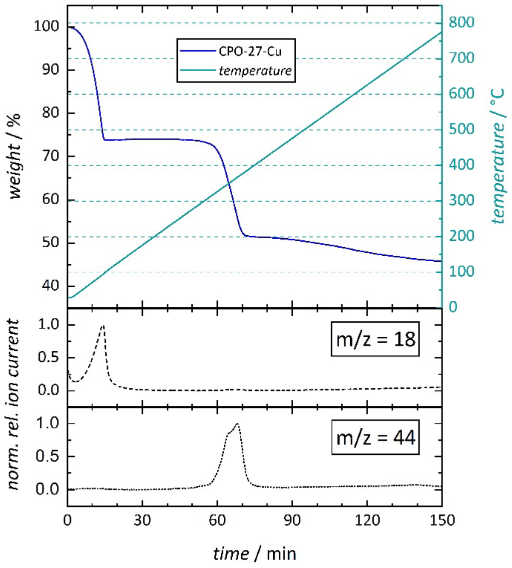

Fig. S19. Thermogravimetric analysis of the hydrated CPO-27-Cu. The MS traces (m/z = 18 and m/z = 44) are shown as dashed and doted lines, respectively.

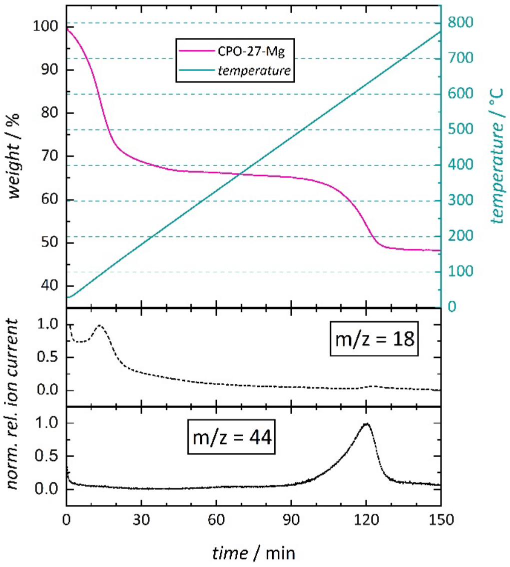

Fig. S20. Thermogravimetric analysis of the hydrated CPO-27-Mg. The MS traces (*m*/*z* = 18 and *m*/*z* = 44) are shown as dashed and doted lines, respectively. The first 90 seconds of the *m*/*z* = 18 trace were discarded due to a high initial signal stemming from residual atmospheric water in the sample chamber.

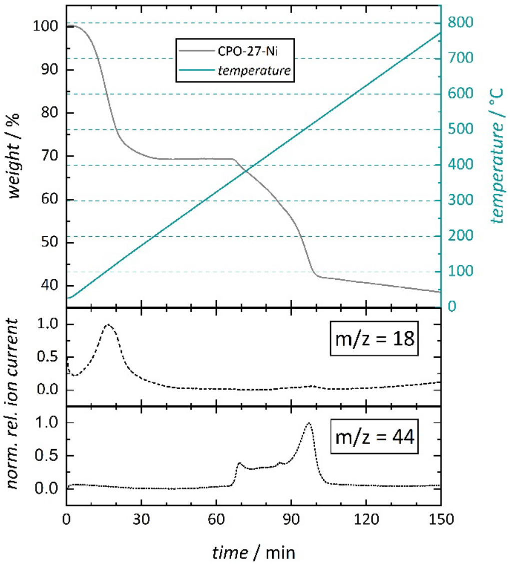

Fig. S21. Thermogravimetric analysis of the hydrated CPO-27-Ni. The MS traces (*m*/*z* = 18 and *m*/*z* = 44) are shown as dashed and doted lines, respectively.

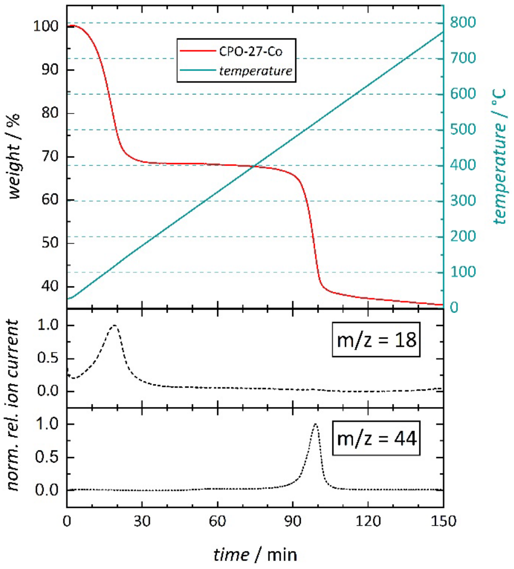

Fig. S22. Thermogravimetric analysis of the hydrated CPO-27-Co. The MS traces (m/z = 18 and m/z = 44) are shown as dashed and doted lines, respectively.

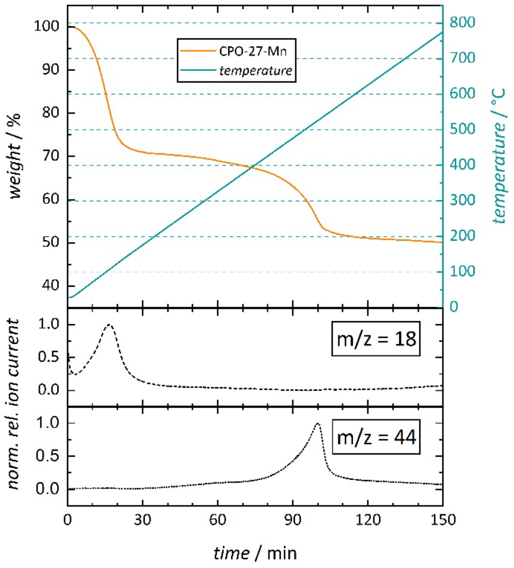

Fig. S23. Thermogravimetric analysis of the hydrated CPO-27-Mn. The MS traces (m/z = 18 and m/z = 44) are shown as dashed and doted lines, respectively.

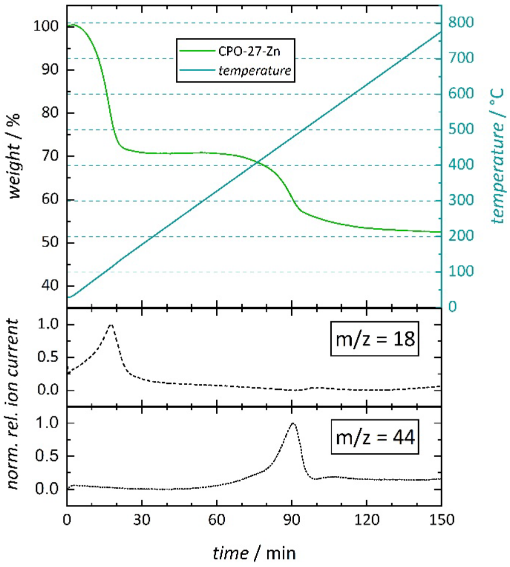

Fig. S24. Thermogravimetric analysis of the hydrated CPO-27-Zn. The MS traces (m/z = 18 and m/z = 44) are shown as dashed and doted lines, respectively.

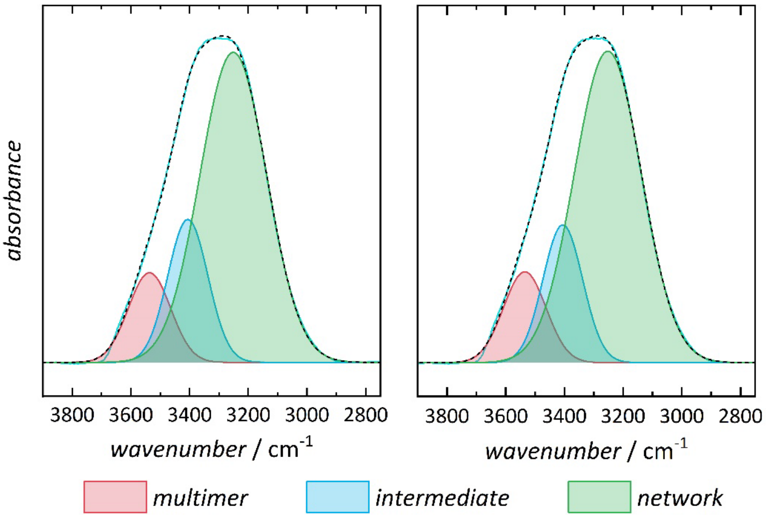

Fig. S25. FT-IR spectra of pure HPLC grade water (two sample preparations). The doted lines represent the cumulative fit of the three distinct water bending vibration modes.

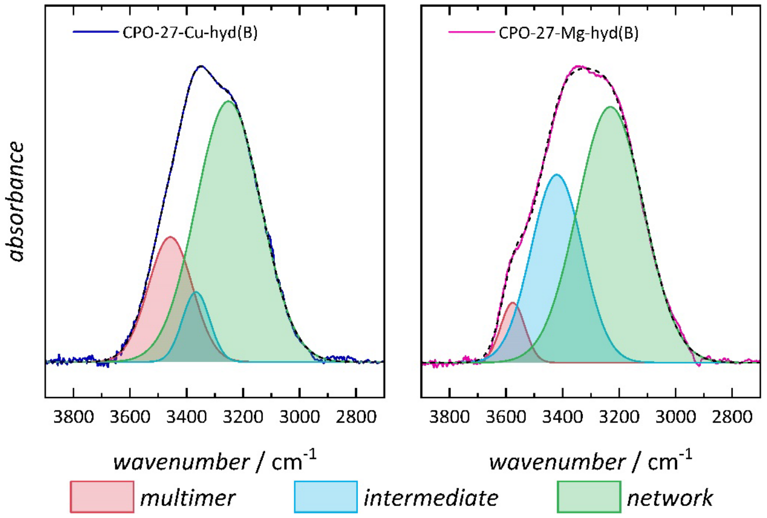

Fig. S26. FT-IR spectra of additional CPO-27-Cu-hyd and CPO-27-Mg-hyd samples. The doted lines represent the cumulative fit of the three distinct water bending vibration modes.

Tab. S4. Results of the least-square fits, showing the contribution of the different vibrational modes to the water stretching vibration for hydrated CPO-27-*M* materials (two independently synthesized samples).

M	multimer water			intermediate water			network water		
	area %	*mean %*	*error*	*area %*	*mean %*	*error*	*area %*	*mean %*	*error*
Co	6.11 5.80	5.95	1.15	29.55 28.77	29.16	5.26	64.34 65.43	64.89	4.53
Cu	6.05 22.64	14.34	6.41	52.65 7.85	30.25	14.24	41.29 69.51	55.40	9.18
Mg	4.65 5.15	4.90	0.79	50.19 34.41	42.30	5.68	45.16 60.44	52.80	5.11
Mn	4.77 5.32	5.04	1.01	25.30 30.96	28.13	5.41	69.93 63.72	66.83	4.84
Ni	4.88 4.87	4.87	1.05	51.47 51.50	51.49	9.07	43.65 43.63	43.64	7.97
Zn	4.71 4.80	4.75	0.90	24.88 23.43	24.16	4.47	70.41 71.77	71.09	4.05
water	12.55 12.78	12.67	1.99	19.00 18.06	18.53	3.21	68.45 69.15	68.80	1.66

Tab. S5. Peak center positions and their errors obtained by the least-square fits of the different modes of the water stretching vibration for hydrated CPO-27-*M*-hyd materials (two independently synthesized samples).

M	multimer water		intermediate water		network water	
	wavenumber / cm^{-1}	*error* / cm^{-1}	*wavenumber* / cm^{-1}	*error* / cm^{-1}	*wavenumber* / cm^{-1}	*error* / cm^{-1}
Co	3559.3	1.5	3406.8	1.3	3221.8	2.9
	3558.7	1.7	3406.0	1.5	3223.0	3.3
Cu	3518.9	10.8	3377.6	3.7	3207.4	9.5
	3457.3	6.9	3366.7	2.3	3251.8	2.0
Mg	3577.4	0.8	3395.3	3.4	3208.0	3.9
	3576.2	0.8	3420.5	1.7	3230.9	2.7
Mn	3566.3	1.1	3417.4	1.2	3222.1	2.7
	3565.3	1.6	3410.9	2.0	3229.6	3.9
Ni	3566.5	1.4	3376.6	4.8	3193.7	5.2
	3567.3	1.4	3375.6	5.0	3193.0	5.4
Zn	3566.1	1.1	3412.7	1.2	3208.8	2.7
	3563.8	1.3	3412.2	1.2	3215.4	2.8
water	3536.7	3.7	3406.0	1.8	3251.2	1.1
	3535.2	3.7	3405.6	1.8	3252.0	1.0

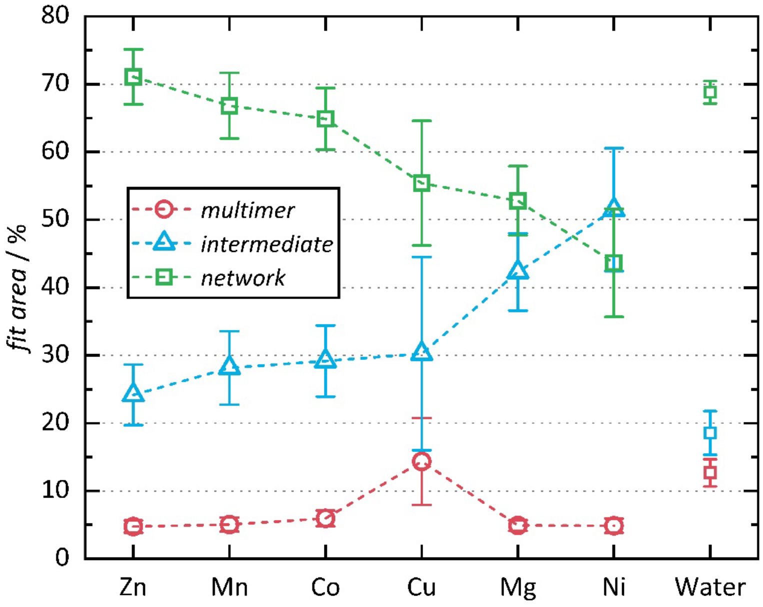

Fig. S27. Results of the least-square fits, showing the area percentages of the three distinct vibration modes for CPO-27-*M*-hyd and for pure water. (Doted lines are a guide to the eye.)

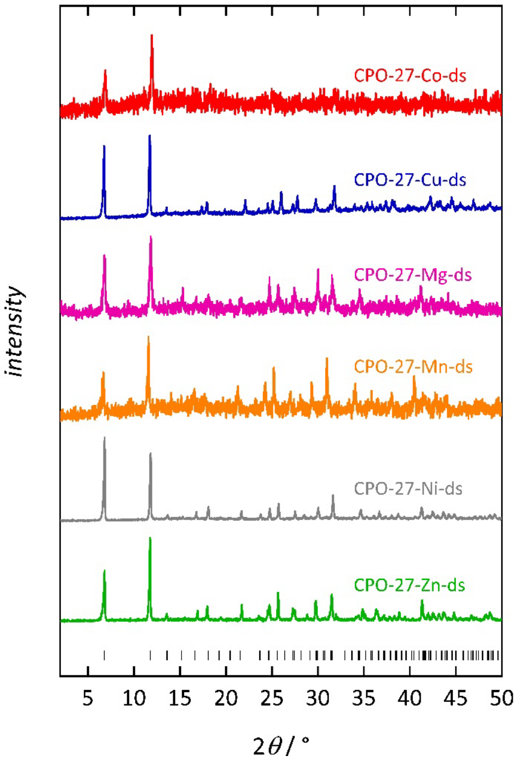

Fig. S28. XRD patterns of re-isolated CPO-27-*M* samples, previously used for water vapor sorption measurements.

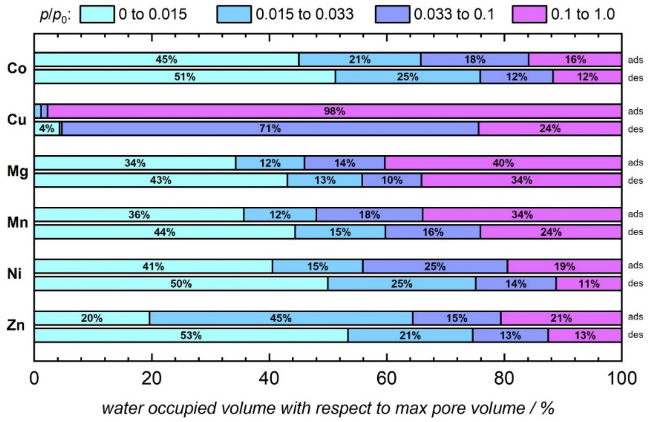

Fig. S29. Pore filling percentages of CPO-27-*M* within different p/p_0 ranges with respect to the maximum uptake after the first adsorption branch, calculated for the first cycles of the respective water sorption isotherms. It shall be noted that the first measurement point CPO-27-Cu ($p/p_0 \approx 0.06$) is taken as the respective starting point. The labeling refers to the additional water uptake within the given pressure range.

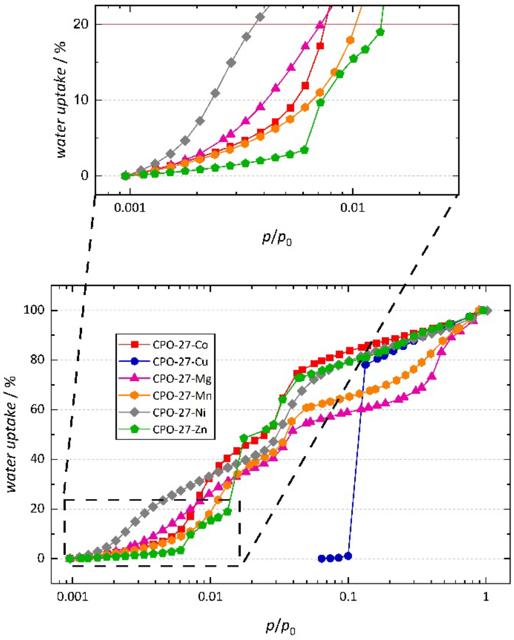

Fig. S30. First adsorption branch for the water vapor sorption isotherms (25 °C) of CPO-27-*M*. Data was normalized to the maximum uptake after the first adsorption branch. Horizontal lines mark 20%, 40%, 60%, 80%, and 100% of the total water uptake.

CHAPTER

4

WATER SORPTION BEHAVIOR OF PORE ENGINEERED CPO-27-NI

Multiple studies on porous compounds revealed that the interactions of water molecules in confinement are influenced by various factors such as the surface polarity, the density of functional groups as well as the diameter of the respective pores. The interplay of these properties affects the given sorption mechanism, resulting in drastically altered water sorption isotherms, *i.e.*, with respect to the isotherm shape and the inflection point. Water adsorption studies on MOFs often focus on materials with strong binding sites, either presented by OMS or hydrophilic functional groups. Water predominantly adsorbs to these sites, providing additional H-bonding opportunities, enabling water cluster formation. As a result, pore condensation occurs. Additionally, the vast variety of possible modification makes MOFs exceptionally well suited to systematically study the effect of different factors such as pore size and pore wall functionality on the water sorption properties.

4.1 Water Sorption Studies on Isoreticular CPO-27-type MOFs

Previous studies on the water adsorption of MOFs highlighted that the pore size and pore wall functionality affects of the water adsorption behavior. Driven by this, the influence of the pore size, the pore wall polarity, and pore wall uniformity on the water adsorption/desorption mechanism within a series of six isoreticular, CPO-27-type frameworks was investigated by water vapor sorption analysis. Pore engineering *via* substitution of the regular dhtp^{4-} linker with different dicarboxylate-based linker molecules offered precise control of the pore diameter and pore wall functionality of these isoreticular frameworks. Information on the water arrangement under MOF confinement was obtained by thermogravimetric analysis (TGA) analysis and Fourier transform infrared (FTIR) spectroscopy. Finally, defect analysis was performed by ^{1}H nuclear magnetic resonance (NMR) spectroscopy. Results revealed that the sorption mechanism of CPO-27, characterized by the occupation of discrete positions with water in a highly asymmetric H-bonding environment, is rather unique and can be altered by defect sites. In larger pores, water molecules adsorbed to the OMS act as H-bonding anchor sites, resulting in the formation of discrete water clusters. Uptake of more water molecules enables the construction of water-bridges between adjacent inorganic secondary building units, leading to pore condensation in a single step with no effect of incorporated defects. Further, similarities of adsorbed water with bulk water do increase with pore size.

M. Kloß, L. Schäfers, Z. Zhao, C. Weinberger, M. Tiemann Water Sorption Studies on Isoreticular CPO-27-type MOFs: From Discrete Sorption Sites to Water-Bridge-Mediated Pore Condensation *Nanomaterials* **2024**, *14*, 1791.

- Digital Object Identifier: 10.3390/nano14221791

Participation in this publication

M. Kloß, L. Schäfers, Z. Zhao, C. Weinberger, M. Tiemann: Experimental work (data evaluation and synthesis), writing and editing of the manuscript, project idea and conceptualization

nanomaterials

Article

Water Sorption on Isoreticular CPO-27-Type MOFs: From Discrete Sorption Sites to Water-Bridge-Mediated Pore Condensation

Marvin Kloß, Lara Schäfers, Zhenyu Zhao, Christian Weinberger, Hans Egold and Michael Tiemann *

Department of Chemistry, Paderborn University, 33098 Paderborn, Germany
* Correspondence: michael.tiemann@upb.de

Abstract: Pore engineering is commonly used to alter the properties of metal–organic frameworks. This is achieved by incorporating different linker molecules (L) into the structure, generating isoreticular frameworks. CPO-27, also named MOF-74, is a prototypical material for this approach, offering the potential to modify the size of its one-dimensional pore channels and the hydrophobicity of pore walls using various linker ligands during synthesis. Thermal activation of these materials yields accessible open metal sites (i.e., under-coordinated metal centers) at the pore walls, thus acting as strong primary binding sites for guest molecules, including water. We study the effect of the pore size and linker hydrophobicity within a series of Ni^{2+}-based isoreticular frameworks (i.e., Ni_2L, L = dhtp, dhip, dondc, bpp, bpm, tpp), analyzing their water sorption behavior and the water interactions in the confined pore space. For this purpose, we apply water vapor sorption analysis and Fourier transform infrared spectroscopy. In addition, defect degrees of all compounds are determined by thermogravimetric analysis and solution ^1H nuclear magnetic resonance spectroscopy. We find that larger defect degrees affect the preferential sorption sites in Ni_2dhtp, while no such indication is found for the other materials in our study. Instead, strong evidence is found for the formation of water bridges/chains between coordinating water molecules, as previously observed for hydrophobic porous carbons and mesoporous silica. This suggests similar sorption energies for additional water molecules in materials with larger pore sizes after saturation of the primary binding sites, resulting in more bulk-like water arrangements. Consequently, the sorption mechanism is driven by classical pore condensation through H-bonding anchor sites instead of sorption at discrete sites.

Keywords: metal–organic frameworks; MOF-74; IRMOF-74; open metal sites; water vapor sorption; hydrophobicity

check for updates

Citation: Kloß, M.; Schäfers, L.; Zhao, Z.; Weinberger, C.; Egold, H.; Tiemann, M. Water Sorption on Isoreticular CPO-27-Type MOFs: From Discrete Sorption Sites to Water-Bridge-Mediated Pore Condensation. *Nanomaterials* **2024**, *14*, 1791. https://doi.org/10.3390/nano14221791

Academic Editor: Antonios Kelarakis

Received: 18 September 2024
Revised: 4 November 2024
Accepted: 6 November 2024
Published: 7 November 2024

1. Introduction

The concept of reticular synthesis [1] has proven to be one of the most fundamental concepts within the field of metal–organic frameworks (MOFs), a class of porous inorganic–organic hybrid materials. On the one hand, it provides a systematic approach to reduce the complexity of numerous MOFs [2,3] by simplifying their extended structures, reducing them to simple geometric building blocks, so-called secondary building units (SBUs). On the other hand, it guides chemists to rationally design new frameworks adopting the same framework connectivity, i.e., network topology, referring to the structure and connectivity of the underlying periodic network [4,5]. Substitution of geometrically identical units allows creation of precisely tailored pore environments by inclusion of new functionalities [6–10], pore size modification [6,10–13] or the use of different metal cations [14].

One of the most extensively studied examples of the applicability of this concept is CPO-27-M [15] (i.e., M_2dhtp, dhtp = 2,5-dihydroxyterephthalate, also known as dobdc), also well-known as MOF-74-M [16]. Substitution of the dhtp-linker molecule [11,17–19] generates three-dimensional, isoreticular MOFs (i.e., IRMOF-74) with a honeycomb-like cross section and one-dimensional, cylindrical pores. This pore engineering concept resulted in multiple compounds with different pore sizes and functionalities such as M_2dondc [20] (dondc = 1,5-dihydroxynaphthalene-2,6-dicarboxylate), M_2bpp [11,17–19,21] (bpp = 3,3′-dihydroxy-[1,1′-biphenyl]-4,4′-dicarboxylate, also known as dobpdc) and M_2tpp [11,17,19,21] (tpp = 3,3″-dihydroxy-2′,5′-dimethyl-[1,1′:4′,1″-terphenyl]-4,4″-dicarboxylate). Further studies showed that modification of the linker substitution pattern (i.e., from para- to meta-arrangement of carboxylic acid groups) results in frameworks with bended, 'banana-like' pore walls as in the cases of M_2dhip [22] (dhip = 4,6-dihydroxyisophthalate, also known as *m*-dobdc) and M_2bpm [21–24] (bpm = 4,4′-Dihydroxy [1,1′-biphenyl]-3,3′-dicarboxylate). All IRMOF-74 frameworks have accessible open metal sites [25] (i.e., under-coordinated metal centers) created by removing coordinating solvent molecules. These sites are exposed to the pores, acting as attractive sorption sites for various guest molecules such as CO_2 [26–29] or water [28,30–32]. Therefore, these isostructural frameworks offer unique possibilities for sorption-based applications.

In order to evaluate the material performance, a deep understanding of the water sorption properties is needed, since applications either heavily rely on the absence (e.g., battery technology [33] and carbon capture [34,35]) or presence of water (e.g., proton conduction [36–40] and water harvesting [12,41]). Hence, a comprehensive knowledge of the interactions of water molecules inside the pores of the host framework is necessary. One powerful method to study the adsorption/desorption behavior of MOFs is water vapor sorption analysis. The isothermal water uptake of the sample is measured, typically applying either gravimetric methods (microbalance) [42,43] or manometric techniques [44,45]. For the latter method, we recently demonstrated the potential provided by high accuracy in the low-pressure range, i.e., for small amounts of water, studying the sorption mechanism of M_2dhtp (M^{2+} = Co, Cu, Mg, Mn, Ni and Zn) [46,47], unveiling distinct differences of the sorption mechanisms, depending on the respective type of metal center.

In general, different sorption sites and unique sorption properties in MOFs [48,49] are a consequence of the chemical nature of the surface of these porous frameworks, gathered by a complex interplay of the hydrophilic inorganic building units and the (mostly) hydrophobic organic domains (i.e., linker molecules). However, discrete information on the polarity of the framework surface is obtained by determination of the inflection point α, i.e., the point at which half of the maximum adsorption is observed, of water adsorption steps. For polar materials, this point is shifted toward lower relative pressures (p/p_0), when compared to less polar compounds [1,50]. Many MOF materials tend to lack sufficient hydrolytic stability [51,52], which is an immediate consequence of the dynamic nature of the coordinative bonds in competition with water molecules [53]. Nevertheless, the above-discussed isoreticular approaches to modulate the pore properties in MOFs make them interesting materials for detailed water sorption studies. Qian et al. [10] systematically studied UiO-66(Zr) by independently analyzing the effect of the pore wall polarity (via linker functionalization) and pore size (via incorporation of larger linker moieties) on its water sorption behavior. Linkers with higher hydrophilicity revealed a pronounced shift of the observed sorption step toward lower relative pressures, suggesting stronger water–framework interactions. Similar observations were also made for other MOFs [13]. However, incorporation of highly polar linkers drastically altered the water sorption behavior, changing the shape of the observed water sorption isotherm (from type IV to type I [54]), suggesting highly attractive conditions for water adsorption, as similarly observed for porous carbon [55]. In contrast, hydrophobic groups only led to severely reduced water uptake without further visible changes. Further, pore size-dependent shifts of the sorption step toward higher pressures were observed, indicating that micropore filling is highly affected by the given pore diameter and the increased size of hydrophobic domains, since pore condensation relies on water cluster formation, as similarly observed for other MOFs [56–58].

We present a comprehensive study on the effects of pore size and linker substitution pattern on the water sorption mechanism and water arrangement within the one-dimensional, cylindrical pores of a series of isoreticular MOFs (i.e., Ni_2L; L = dhtp, dhip, dondc, bpp, bpm and tpp). We utilize thermogravimetric analysis (TGA) and Fourier transform infrared (FTIR) spectroscopy to monitor the interactions of water with its environment in the confined space. In addition, we apply solution ^{1}H nuclear magnetic resonance (NMR) spectroscopy to monitor the number of defects from missing linker molecules. Finally, manometric water vapor sorption analysis is used to study the adsorption/desorption behavior of the IRMOF-74 series.

2. Materials and Methods

2.1. Linker and MOF Synthesis

All M_2L MOF materials (i.e., Ni_2dhtp [59], Ni_2dhip [22], Ni_2dondc [20], Ni_2bpp [11], Ni_2bpm [11], Ni_2tpp [11]) were synthesized under solvothermal conditions according to modified reported procedures (details are given in the Supplementary Materials). Solvent was removed by heating under dynamic vacuum conditions to obtain desolvated samples, which were stored in a glove box under Ar atmosphere until further use. All products were characterized by powder X-ray diffraction (XRD) and compared with literature results, ensuring structural integrity with no evidence of crystalline impurities.

H_4dhtp [46,60], H_4dondc [20], H_4bpp [17,61] and H_4tpp [17,61] linker molecules were synthesized according to modified literature procedures (details are given in the Supplementary Materials). All other chemicals (including H_4dhip and H_4bpm) and solvents were purchased from commercial suppliers and used without further purification. All air- or water-sensitive reactions were carried out under standard Schlenk techniques using a dry argon atmosphere.

2.2. Preparation of Hydrated Samples

The desolvated samples were placed in a closed vessel with a separate water reservoir (1 mL per sample, ca. 10 to 15 mg) to load them via the gas phase at 40 °C for 24 h. Afterwards, we refer to them as hydrated samples (Ni_2L-hyd).

2.3. General Characterization Techniques

Powder X-ray diffraction (XRD) data were collected on a Bruker D8 Advance diffractometer (Bruker, Karlsruhe, Germany) with a step size of 0.02° and a counting time of 3 s per step. Patterns are normalized (data range from 0, 1) to the most intense reflection for better comparison of relative intensities. ^{1}H and ^{13}C nuclear magnetic resonance (NMR) spectra were recorded using Bruker Advance 500 and Bruker Ascent 700 spectrometers (Bruker, Ettlingen, Germany). Chemical shifts were calibrated to the resonance of residual non-deuterated solvent. For defect analysis, small amounts of the samples (ca. 3 to 5 mg) were diluted overnight in 600 μL of a solvent mixture prepared from dmso-d_6 (10 mL) and deuterium chloride (20 wt% in D_2O; 0.5 mL). Thermogravimetric analysis (TGA) was performed using a TGA/DSC1 STAR System thermobalance from Mettler-Toledo (Gießen, Germany). Samples were placed in a 70 μL corundum crucible. Measurements were performed under a constant nitrogen gas flow (50 mL min^{-1}, purity 5.0) in a temperature range from 40 °C to 800 °C using a heating rate of 10 °C min^{-1}.

2.4. Fourier Transform Infrared (FTIR) Spectroscopy

FTIR spectroscopy was performed using a Bruker Vertex 70 spectrometer (Bruker, Ettlingen, Germany) in annual total reflection (ATR) mode utilizing the Platinum ATR unit A225 with a diamond ATR crystal. Powdered samples were pressed on the crystal during the measurement. After the measurement of hydrated samples, an automatic baseline correction was applied using the OPUS 7.2.1 software package. The correction was performed using a concave rubberband correction, with 10 iterations and 32 baseline points. Gaussian least square fits of the water stretching band were performed individually using the peak analyzer function of the Origin23b software package. First, the data within the range from 4500 to 2400 cm^{-1} were normalized (data range from 0.1) to the maximum absorbance. For the fitting procedure, the data from 3900 to 2400 cm^{-1} were selected.

Baseline correction was performed, using a linear baseline. Then, three peaks were set with the starting positions near 3560 cm^{-1} (multimer water), 3380 cm^{-1} (intermediate water) and 3210 cm^{-1} (network water). Only positive peak areas were allowed, while the previously corrected baseline was set constant. No further restrictions were used. It was noted that the fit results possess a small error, caused by the overlap of the aromatic C-H vibration of the linker molecules with the water stretching bands.

2.5. Sorption Analysis

2.5.1. Nitrogen Physisorption Measurements

N_2 physisorption analysis was performed with a Quantachrome Autosorb 6B (Quantechrome Instruments, Boca Raton, FL, USA) at 77 K. The relative pressure range suitable for the BET area calculation was determined using the Rouquerol [62] criteria. Total pore volumes were determined from the uptake at $p/p_0 \approx 0.9$. Activation of the samples was performed in a stepwise manner. The desolvated samples were transferred to the measurement cell and dispersed in methanol twice for 45 min. After each step, the solvent was removed under dynamic vacuum. The pre-dried samples were degassed for approximately 17 h applying the following procedure: Samples were heated from room temperature to 60 °C with a heating rate of 2 °C min^{-1} after which the temperature was held for two hours. Then, the sample was heated to 100 °C with the same heating rate (2 °C min^{-1}) and the temperature was held for another two hours. Finally, the sample was heated (2 °C min^{-1}) to 150 °C and the temperature held for an additional 12 h, after which the sample was allowed to cool to room temperature. Pore size analysis was accomplished with the supplied AS-Multistation 2.01 software package using the NLDFT data-based method (N_2 at 77 K on silica, cylind. pore, NLDFT adsorption branch data kernel), treating the samples as silica.

2.5.2. Water Vapor Sorption Measurements

Water vapor sorption experiments were performed on a 3Flex instrument (Micromeritics, Unterschleißheim, Germany) at 298 K (25 °C) with double distilled (and degassed) water. Activation of the samples was performed in a stepwise manner, applying the same procedure as mentioned in the N_2 physisorption section.

3. Results and Discussion

3.1. General Characterization

All members of our nickel-based frameworks, i.e., Ni_2L (L = linker molecule), were prepared using six linker molecules, each presenting either a different substitution pattern (para- vs. meta-position of carboxylate groups) or different sizes, resulting in isoreticular materials with tunable size and pore wall polarities (Figure 1).

Powder X-ray diffraction (XRD) data of the prepared frameworks (i.e., Ni_2L) are in agreement with literature data [11,17,20,21], confirming the periodic, three-dimensional framework structure with a honeycomb-like cross section, with no evidence of crystalline impurities in any of the prepared samples (Figure 2a). The respective (110) lattice plane distances, characteristic for the perpendicular arrangement of the one-dimensional cylindrical pores, indicate the expected pore diameters in the range 13 . . . 23 Å (Table 1). We note that the broad reflections for most materials indicate small crystallite size, while the signal-to-noise ratio is attributed to sample preparation and the crystallinity of the frameworks (longer measurement times were avoided to minimize the influence of humidity).

N_2 physisorption analysis enabled us to confirm the permanent porosity of all products, revealing type I sorption isotherms [64] for most frameworks in our series, consistent with the existence of micropores (Figure 2b). In contrast, Ni_2tpp reveals a type IV(b) isotherm shape typical of mesoporous materials with pore diameters below 40 Å. The suitable pressure range for BET area determination was selected using the Rouquerol [62] criteria. The high specific surface areas (560 . . . 2320 m^2 g^{-1}) and large specific pore volumes (0.38 . . . 1.03 cm^3 g^{-1}, at $p/p_0 \approx 0.9$) of the networks mostly align with literature data (reference data only for Mn_2dondc) [17,20–23]. We note that the comparable low surface areas for some materials hint toward the existence of amorphous byproduct, while the increase in the adsorbed volume at high relative pressures generally indicates interparticle porosity as a consequence of small crystallite size Observed differences for Ni_2dhip and Ni_2bpm are slightly larger. Pore sizes analysis (Figure 2c) is in good agreement with previous studies [21] and our XRD results, verifying that the pore size within our series approximately doubles from Ni_2dhip to Ni_2tpp (see Table 1, details are shown in the Supplementary Materials; NLDFT-based fits displayed in Figures S6–S11). However, the uniformity of the pore sizes is seemingly affected by the average pore diameters, resulting in a broadening of the distribution curve, in agreement with the expectation that larger inorganic moieties negatively influence the frameworks crystallinity.

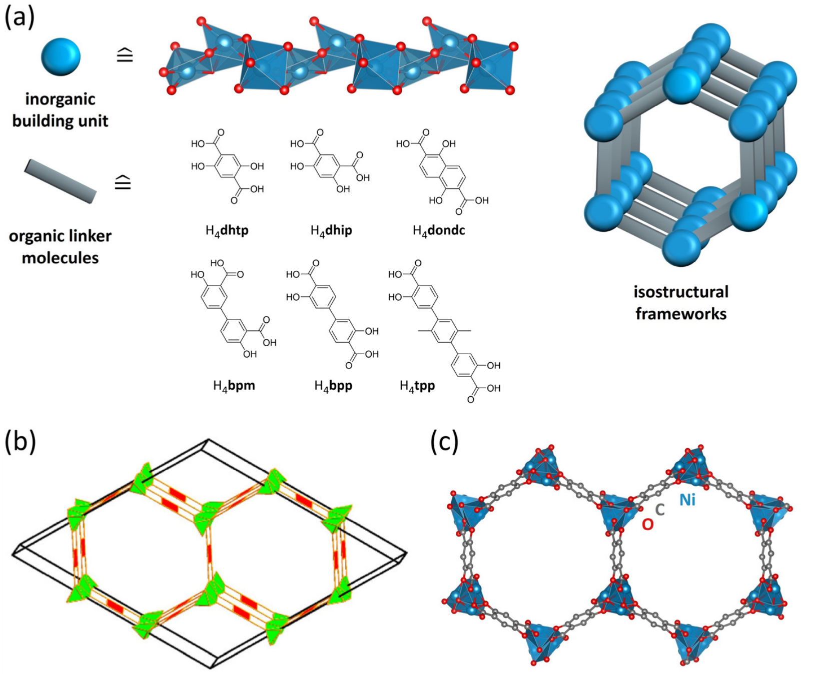

Figure 1. (**a**) Illustration of the inorganic building units and used linker molecules in this research, forming isostructural Ni_2L frameworks. (**b**) Network topology of Ni_2dhtp (msf, reprinted from ref. [3]) and (**c**) representation of the honeycomb-like cross section along the crystallographic *c*-axis, showing Ni_2dhtp as an example.

Table 1. Determined lattice plane distance d_{110} calculated from the Bragg equitation as well as surface areas S_{BET}, pore volumes V_{Pore} and pore sizes $d_{Pore,NLDFT}$ of Ni_2L materials determined from nitrogen sorption data at 77 K.

	d_{110} (Å)	S_{BET} ($m^2\ g^{-1}$)	V_{Pore} ($cm^3\ g^{-1}$)	$d_{Pore,NLDFT}$ (Å)
Ni_2dhtp	12.93 ± 0.02	1240 ± 80	0.55 ± 0.07	12.73 ± 0.22
Ni_2dhip	12.97 ± 0.06	560 ± 120	0.38 ± 0.09	11.93 ± 0.30
Ni_2dondc	14.57 ± 0.10	1010 ± 10	0.55 ± 0.03	13.63 ± 0.42
Ni_2bpp	18.36 ± 0.04	1660 ± 230	0.74 ± 0.02	16.68 ± 0.57
Ni_2bpm	18.87 ± 0.00	1200 ± 50	0.58 ± 0.02	18.52 ± 0.52
Ni_2tpp	23.05 ± 0.06	2320 ± 140	1.03 ± 0.06	25.09 ± 0.67

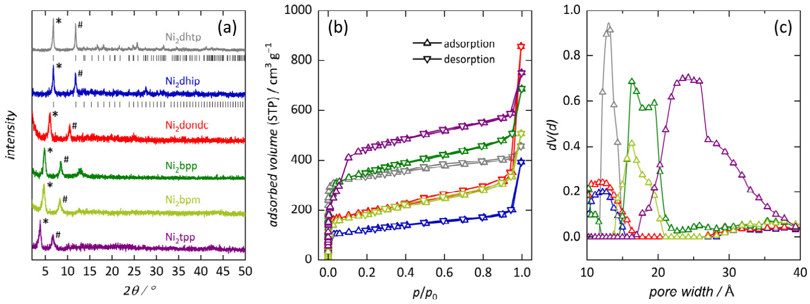

Figure 2. XRD patterns of Ni$_2$*L* frameworks (**a**). The most intense reflections represent the (110) and (300) lattice planes (marked with * and # respectively), being shifted toward lower angles with increasing pore diameter. Patterns are normalized and compared to literature data where accessible [22,63]. N$_2$ physisorption isotherms of Ni$_2$*L* (**b**) measured at 77 K and their respective NLDFT-based pore size plots (**c**).

Recent studies analyzed formate defects in Ni$_2$dhtp stemming from decomposed DMF (DMF = *N*,*N*-dimethylformamide) solvent molecules. They found that the number of defect sites increases with the metal-to-linker ratio [65]. Therefore, we applied ^{1}H NMR spectroscopy to analyze potential defects within our series. Samples were diluted in a solvent mixture of dmso-d$_6$ and deuterium chloride (20 wt% in D$_2$O). We note that acid-caused decomposition of formate anions [66] is a possible error source. However, we suggest that the impact of this is comparably low due to the reasonably low acid concentration used for decomposition. NMR spectra of diluted frameworks are shown in the Supplementary Materials (Figures S12–S17). Respective ratios of the linker molecules and formate anions (For$^-$), or acetate (OAc$^-$) anions for Ni$_2$dondc, were calculated considering the different charges of the coordinating ligands, i.e., one linker (L^{4-}) must be replaced by four For$^-$/OAc$^-$ ions (capping ligand) to maintain charge balance. This enabled us to determine the respective sum formula for our materials (see Table 2). We found that even for low metal-to-linker ratios (e.g., Ni$_2$dhtp) the amount of incorporated formate ions is significant (i.e., 0.62, suggesting 0.16 dhtp^{4-} molecules are replaced). However, we see the reported trend of increased defect sites with increasing metal-to-linker ratios for all materials in our series. The precise amount of the capping ligands depends on the nature of the linker molecule (acidity, solubility, . . .) and the precise reaction conditions. Ni$_2$dhip revealed the largest differences between individually synthesized samples, indicating that its synthesis is more sensitive to minor changes compared to the other materials in this study. Further, we found formate ions in diluted samples of Ni$_2$dondc (Figure S18), which we attribute to thermally decomposed DMF used for the replacement of *N*-methyl-2-pyrrolidone (NMP) solvent molecules. We suggest that these post-synthetically generated formate ions do not affect the defect degree of the pristine framework but coordinate to the open metal sites. Hence, these molecules can be replaced by additional solvent exchange procedures, as performed prior to sorption analysis. However, this suggests that the determined formate ion concentration in diluted samples is slightly overestimated as a consequence of residual DMF solvent molecules. Nevertheless, the amount of incorporated capping ligands clearly is another contributing factor for the broadening of the pore size distribution (see above), in agreement with the negative effect of defect sites on the materials' crystallinity. For the sake of simplicity, all materials are referred to Ni$_2$*L*, and presented defects are discussed when necessary.

Table 2. Determined linker and formate (For$^-$) or acetate (OAc$^-$) capping ligand concentrations of Ni$_2$*L* materials derived from solution ^{1}H NMR and their respective sum formulas, considering charge balance. (Sum formula for a defect free material would be Ni$_2$*L*.).

	Linker Molecules per Formula Unit	**For$^-$/OAc$^-$ Ligands per Formula Unit**	**Sum Formula**
Ni_2dhtp	0.84 ± 0.02	0.62 ± 0.10	$Ni_2(dhtp)_{0.84}(For)_{0.62}$
Ni_2dhip	0.65 ± 0.09	1.41 ± 0.35	$Ni_2(dhip)_{0.65}(For)_{1.41}$
Ni_2dondc	0.65 ± 0.01	1.39 ± 0.00	$Ni_2(dondc)_{0.65}(OAc)_{1.39}$
Ni_2bpp	0.49 ± 0.06	2.04 ± 0.25	$Ni_2(bpp)_{0.49}(For)_{2.04}$
Ni_2bpm	0.61 ± 0.06	1.54 ± 0.25	$Ni_2(bpm)_{0.61}(For)_{1.54}$
Ni_2tpp	0.54 ± 0.04	1.85 ± 0.16	$Ni_2(tpp)_{0.54}(For)_{1.85}$

3.2. Thermal Analysis

To evaluate the thermal stability of our frameworks and provide an ideal starting point for our hydration/dehydration experiments, we performed thermogravimetric analysis (TGA) of the hydrated frameworks (Ni$_2$*L*-hyd, Figure 3). Samples were prepared by loading the desolvated materials with water through the gas phase. Therefore, samples were placed in a closed vessel with a separate water reservoir to load them with water above room temperature (i.e., 40 °C) for 24 h; for more details, see Section 2.2.

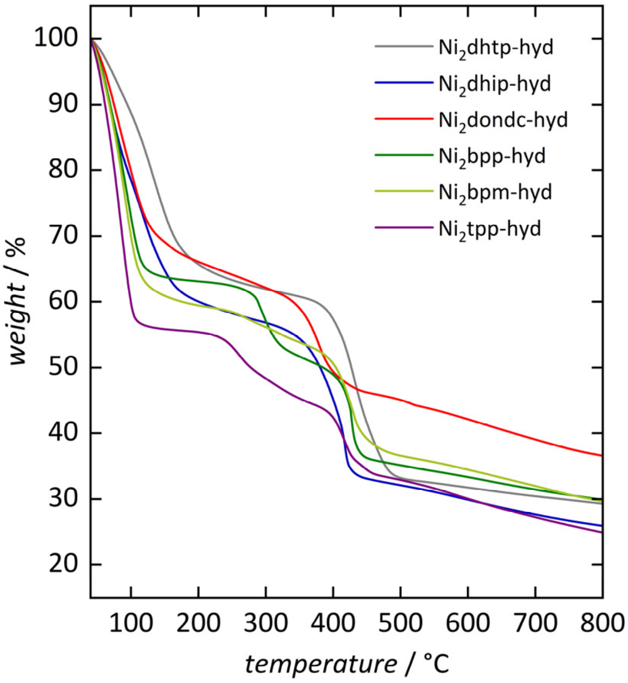

Figure 3. Thermogravimetric analysis of the hydrated materials (Ni$_2$*L*-hyd) from 40 to 800 °C under N_2 atmosphere (heating rate: 10 °C min^{-1}).

In general, framework decomposition is observed in the range 350 . . . 450 °C, comparable with previous reports [17,21]. However, the above-mentioned formate/acetate defects affect the thermal stability of the frameworks. Prior to framework decomposition, an additional smaller mass loss step around 250 °C (Ni$_2$tpp) and 300 °C (Ni$_2$bpp) is observed for some frameworks. This is in accordance with previous studies on defect engineering in Ni_2dhtp, revealing additional decomposition steps, becoming more pronounced with higher defect degrees [67]. Our results on Ni_2bpp and Ni_2tpp are comparable to previous studies, although the here-observed steps are more pronounced and, for Ni_2tpp, shifted toward lower temperatures [17,21]. These differences are likely to arise from slightly different synthetic approaches (here: mostly DMF [59] vs. DMF/EtOH/water (1/1/1) mixture with lower Ni-to-*L* ratios), resulting in varying defect sites [65]. TGA data further indicate that the mass stability, i.e., formation of a stable plateau, depends on the defect degree, as increasing amounts of For^-/OAc^- lead to the loss of a stable mass plateau after the water loss step and finally, an additional pronounced decomposition step. We note that our results for Ni_2dhtp deviate from our previous studies [46], where larger amounts of OAc^- ions were incorporated (stemming from the metal source), visible in an additional decomposition step prior to the collapse of the framework. This suggests that the herein-found formate defects do not significantly alter the thermal stability of Ni_2dhtp, agreeing with the above-referenced studies.

Next, we determined the amount of adsorbed water in all hydrated Ni_2L-hyd materials by considering the first mass loss step between 40 and 250 °C. (We note that the adsorbed amount of water is generally underestimated due to its strong bonding to the Ni^{2+} sites, being slowly desorbed over a broad temperature range as well as during framework collapse [32,46]). All materials reveal similar values (21 . . . 25% weight loss, Supplementary Materials Table S1), slightly increasing with pore size. However, Ni_2tpp deviates from this trend, indicating that some loosely bonded water molecules could desorb during sample preparation, as indicated by a less stable sample mass during measurement setup. In general, the dehydration step shifts toward lower temperatures with increasing pore diameter, indicating water–framework interactions become less attractive and the adsorbed water becomes more comparable to bulk water.

3.3. FTIR Spectra of Hydrated Samples

Our results presented above indicate the expected effect of the channel size on water–framework interactions and hint toward different water arrangements in the one-dimensional channels. Thus far, infrared spectroscopy is frequently used to analyze the interactions of water molecules at surfaces (e.g., inverse micelles [68,69]) or within pores (e.g., mesoporous silica [45,70] and MOFs [46,71]). This possibility arises from the deconvolution of the O–H stretching vibration, a superposition of vibrational bands, typically located in the range of 2800 to 3700 cm^{-1} [72]. Least squares fitting of three Gaussian profiles enables us to determine the respective contributions (peak areas) of the different vibrational bands assigned to water in a particular H-bonding environment [45,68,69]. Brubach et al. [72] designated these water molecules as different types with respect to their coordination numbers (CN), i.e., numbers of H-bonding partners. These three types are termed 'network water' (NW), 'intermediate water' (IW) and 'multimer water' (MW), as their respective stretching frequencies reveal a red shift, i.e., toward lower wavenumbers, with an increasing number of intermolecular interactions. NW resembles highly H-bonded water molecules interacting strongly with their respective environment, forming roughly four H-bonds (CN $\geq$ 4) with adjacent atoms. These structures are often referred to as 'ice-like' arrangements, possessing oscillation frequencies around 3260 cm^{-1}. As the number of interactions decreases, IW water populations form, showing frequencies around 3460 cm^{-1}. These populations offer a 'bulk-like' water arrangement of more dynamic water molecules. Lastly, MW resembles poorly connected water molecules, often found at interfaces, forming only few H-bonds (as found in dimeric/trimeric structures). These MW water molecules are also referred to 'dangling' water molecules, being a consequence of their isolation, i.e., low connectivity, to other water molecules. MW typically shows vibration frequencies located around 3600 cm^{-1}.

We carried out Fourier transform infrared (FTIR) spectroscopic measurements in attenuated total reflection (ATR) mode on hydrated samples (i.e., Ni_2L-hyd) to analyze the effect of the pore size and linker substitution pattern on the arrangement and interactions of adsorbed water molecules. The spectra reveal the integrity of the organic linker molecules as well as the presence of three of the characteristic vibration bands of water, i.e., the stretching band (3750 … 2800 cm^{-1}), the bending band (1700 … 1650 cm^{-1}), and the libration band (1000 … 400 cm^{-1}) (see Supplementary Materials Figures S19–S24) [72]. Next, least squares fitting was performed for a pure liquid water film located at the surface of the ATR crystal (Supplementary Materials Figure S25), as a reference to quantify the relative contributions of the different water vibrations. We observed a contribution of 13% from multimer water (3535 cm^{-1}), stemming from water in the liquid film that is located at either of the two interfaces (ATR diamond crystal or air) [46]. Further, contributions of 18% from intermediate water (3405 cm^{-1}) and 69% from network water (3251 cm^{-1}) indicate that most of the water molecules not located at the interfaces form multiple H-bonds with surrounding molecules. All Ni$_2$*L*-hyd samples possess significantly lower contributions for the multimer peak (5–6%) (Figure 4 and Supplementary Materials Table S2) when compared to the pure water film. This suggests that, similar to M_2dhtp [46], water molecules in these confined environments show a higher tendency for H-bonding than interface-near water molecules of a pure liquid water film. This further suggests that additional water molecules interact strongly with the coordinating water molecules, located at the primary binding sites, and with oxygen atoms of the inorganic building unit, giving rise to further H-bonding possibilities. Further, all Ni$_2$*L*-hyd networks show slightly higher contributions from network water (73–78%) as well as similar contributions from intermediate water (17–22%) when compared to the pure water film, suggesting that multiple water molecules form a highly connected H-bonding network.

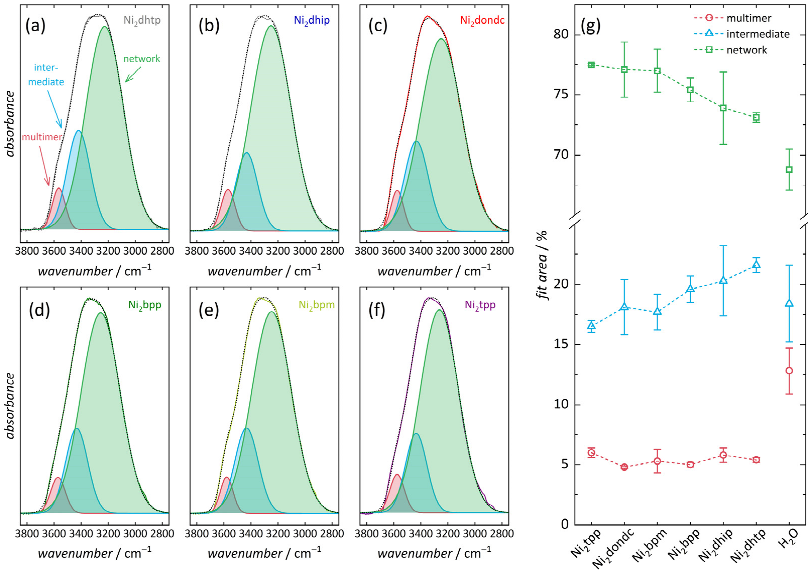

Figure 4. Deconvolution of the FTIR O–H stretching vibration band of water in hydrated Ni$_2$L-hyd samples (**a**–**f**) by least squares fitting (Dotted lines: sums of the three Gaussians). Relative contributions of multimer, intermediate and network water in comparison with a pure liquid water film (**g**).

We note that the observed relative contributions of the three vibrational bands in Ni$_2$dhtp-hyd differ from earlier results [46]. As mentioned above, this is explained by different synthetic procedures, resulting in more defect sites caused by significant incorporation of acetate anions (from the metal source). These capping ligands alter the pore surface, resulting in a less uniform pore wall structure, causing less attractive interactions of water with the framework because of reduced H-bonding possibilities. Further, the precise adsorption mechanism is affected (as discussed below). As stated above, the Ni_2dhtp formed here possess fewer defects, which is typical for reactions applying small metal to linker rations [65]. Consequently, a more uniform pore wall structure and stronger interactions with more H-bonding opportunities are found. Expecting crystallographically defined water positions in Ni_2dondc, similarly for Mn_2dondc [20], we found different MW (lowest observed) and NW (second highest) contributions, suggesting a similar number of water molecules within the hydrated framework (ca. five molecules per Ni^{2+}). However, defects within the other frameworks seem to play a minor role for these interactions, since most water molecules form multiple H-bonds even in the presence of significant amounts of capping ligands. This indicates that potential binding sites near the pore walls are significantly less attractive for frameworks with larger hydrophobic domains. We hypothesize that the high NW contributions found therein stem from inner pore, more bulk-like water, rather than from interfacial water (i.e., MOF–water interactions as found for M_2dhtp [46]).

Consideration of the respective wavenumbers $\widetilde{v}$ (peak positions, see Supplementary Materials Table S3) of the three Gaussian contributions allows us to gain more information on the O–H bond situation of confined water. When compared to the pure water film, all Ni_2L-hyd samples show a blue shift (i.e., toward higher $\widetilde{v}$) of the multimer and intermediate water peak. Observed shifts are comparable for all materials except for Ni_2dhtp-hyd, which reveals a less pronounced blue shift, generally indicating O–H bond strengthening upon hydration. In addition, most compounds reveal no significant changes of the network water peak. However, Ni_2dhtp-hyd reveals a red shift (toward lower $\widetilde{v}$), indicating weakening of the O–H bonds in NW water stemming from highly confined water molecules. For Ni_2tpp-hyd, the opposite, i.e., blue shift, is found, being a consequence of less confined water molecules.

The local H-bonding situation inside the one-dimensional pores of hydrated frameworks is another aspect to bear in mind to monitor pore-size-dependent differences. Information on this is derived from the respective differences between the peak center positions x and y of different vibrational bands, i.e., from the wavenumber splitting $\Delta\widetilde{v}_{xy}$ (Table 3). Smaller $\Delta\widetilde{v}$ values suggest a higher symmetry in the local H-bonding of water, indicating more mobile water molecules with high rotational degrees of freedom and vice versa [73,74]. We determined higher values for all Ni_2L-hyd materials than found for a pure water film. This indicates a higher degree of H-bonding asymmetry, which is consistent with the expectation of confined water molecules. Despite the similar trend, the precise $\Delta\widetilde{v}$ values differ for any given compound. For Ni_2L-hyd materials with smaller pore diameters, i.e., L = dhtp, dhip and dondc, generally higher wavenumber splitting is found. In the particular cases of Ni_2dhtp [32] and Ni_2dondc [20], this is in accordance with the expectation of crystallographically defined water positions in a fixed, highly asymmetric local H-bonding situation. However, frameworks with larger pore diameters, i.e., L = bpp, bpm and tpp, show the opposite trend, revealing lower $\Delta\widetilde{v}$ values. H-bonding becomes more symmetric, and thus are more comparable with bulk water because of the less pronounced confinement effects. These observations are in accordance with our TGA experiments and previous results on mesoporous silica revealing similar effects of the pore size [70], highlighting a more bulk-like behavior with more flexible water molecules. Considering these results, the members with larger pores (Ni_2L, L = bpp, bpm and tpp) should reveal a water sorption behavior that mostly resembles classical pore condensation (i.e., water cluster formation), rather than the occupation of discrete positions and confinement effects (as expected for the smaller pores).

Table 3. Wavenumber splitting $\Delta\widetilde{v}$ of the stretching vibration bands of water in the Ni_2L-hyd materials and of pure water.

	$\Delta\widetilde{v}_{\text{multimer-network}}$ (cm^{-1})	$\Delta\widetilde{v}_{\text{multimer-intermed.}}$ (cm^{-1})	$\Delta\widetilde{v}_{\text{network-intermed.}}$ (cm^{-1})
Ni_2dhtp	336.2 ± 2.5	146.1 ± 1.1	190.1 ± 2.5
Ni_2dhip	325.4 ± 1.8	142.2 ± 1.2	183.2 ± 1.8
Ni_2dondc	337.0 ± 2.5	141.3 ± 1.2	181.7 ± 1.7
Ni_2bpp	321.0 ± 1.9	140.9 ± 1.5	182.9 ± 1.6
Ni_2bpm	320.6 ± 1.7	142.6 ± 1.4	178.8 ± 1.5
Ni_2tpp	309.1 ± 2.2	140.0 ± 2.0	169.1 ± 1.8
water	284.4 ± 1.5	130.2 ± 2.9	154.2 ± 1.5

3.4. Water Vapor Sorption

To prove our hypothesis regarding the effect of the pore size on the sorption mechanism, we analyzed the hydration/dehydration behavior of the Ni_2L with manometric water vapor sorption measurements at 25 °C. We carried out two consecutive adsorption/desorption cycles without additional thermal activation in between the two cycles (i.e., samples were not removed from the device), since our previous water sorption studies on M_2dhtp [46,47] highlighted that coordination of water to the open metal site during the first sorption isotherm results in different starting conditions ascribed to strongly bound (chemisorbed) water molecules. These cannot be removed during the desorption process without additional thermal activation.

We observed an overall higher total uptake during the second adsorption/desorption cycle when compared to the first cycle for Ni_2dhtp. This is explained by a partial degradation of the frameworks resulting in the formation of additional open metal sites caused by cleavage of metal–linker bonds [42,46,47] during the time-consuming measurements (several days). Results on Ni_2dhip indicate a poor hydrolytically stability since we observe a decrease in water uptake during the first desorption isotherm, reflected by the crossing of the adsorption and desorption branch and large equilibrium times, making it impossible to further evaluate its water sorption behavior in detail. On the other hand, Ni_2L frameworks containing larger linker moieties (i.e., L = dondc, bpp, bpm and tpp), and thus possessing larger pores, reveal a severely decreased total water uptake during the second cycle, indicating that water molecules affect the framework's longevity. All observations are consistent with the decreased crystallinity of all samples after water sorption experiments (Supplementary Materials Figure S26), while most materials maintain a larger degree of their initial pore ordering (except for Ni_2dondc, which reveals complete loss of crystallinity). Since all M_2L frameworks adsorb water at low relative pressure ($p/p_0 < 0.1$) due to highly attractive interactions with vacant coordination sites, we displayed all isotherms, both in a linear and in a semi-logarithmic representation, to analyze differences in the sorption behavior. In addition, first derivatives of the isotherms ($\delta V/\delta(p/p_0)$) were calculated to highlight the distinct water sorption steps in all isotherms (see Supplementary Materials Figures S27–S32) (Missing data points below p/p_0 = ca. 0.002, except in the first adsorption isotherms, are due to technical experimental restrictions).

The water sorption isotherms of Ni_2dhtp (Figure 5a,b), reveal similar characteristics as observed in previous studies on M_2dhtp [46,47], revealing a type I [54] water sorption isotherm. However, differences arise as both materials are compared with each other. Accordingly, uptake of the first 20% (with respect to the total uptake) occurs at particularly low pressures ($p/p_0 < 0.003$), attributed to the coordination of water to open meal sites, even though the desorption data are inconclusive with respect to the irreversibility of this process, i.e., missing low-pressure data due to technical limitations. The further course of the isotherms suggests a slightly different sorption mechanism: The observed sorption step at $p/p_0 = 0.03 \ldots 0.05$ in this study corresponds to the uptake of one rather than two water molecules in our previous study (ca. 20%, resulting in 60% of the total water uptake vs. 40%, resulting in 80%) and presumably results in the formation of a uniform water cluster along the pore walls of the framework, being in agreement with the water sorption mechanisms found for most other metals within the M_2dhtp series (except M = Cu) [46,47]. As mentioned above, these findings result from varying defect degrees. Significant incorporation of acetate anions (and presumably capping ligands in general), results in less uniform pore walls within the Ni_2dhtp framework, and thus less attractive interactions of water with the pore walls, i.e., via H-bonding with the phenylene backbone at the proposed third adsorption site. Consequently, the adsorption mechanism is altered, making the adsorption of two water molecules more attractive to create a metastable state (i.e., preliminary pore saturation). However, the further cause of our isotherm suggests that the here observed formation of a continuous water layer along the pore walls seems to be a meta-stable state, since gradual absorption of additional water molecules occurs afterwards until complete hydration is observed, without any sign of additional sorption steps. We attribute this to stronger Ni–O interactions in the inorganic SBU when compared to the other members of the M_2dhtp series [47], affecting atomic charges on the metal center, thus preferring a square planer coordination environment of Ni^{2+}. Consequently, chemisorption of water molecules to the metal center as well as H-bonding with framework O atoms becomes less attractive, i.e., larger H-bonding distances, causing similar adsorption energies of both sorption sites. Subsequent occupation of the third site (near the phenylene backbone) results in more water molecules arranged in the confined environment. Hence, preliminary pore saturation is observed at lower relative pressures when compared to M_2dhtp [46,47]. Then, uptake of additional water molecules with increasing vapor pressure (i.e., during adsorption) is enabled by relaxation of previously adsorbed molecules, providing additional space while decreasing their respective mobility. This phenomenon creates a hysteresis because of an increased density of the adsorbed water, which is irreversible during the desorption, i.e., with decreasing pressure. We previously ascribed this effect to the alternating hydrophobic (phenylene) and hydrophilic (coordinated metal centers) domains within M_2dhtp [46,47], which is in accordance with similar effects found for other porous materials possessing larger and/or more hydrophobic pores [45,75–84]. The total water uptake after the first adsorption branch was determined to be 0.51 ± 0.06 g g^{-1}, which is in agreement with earlier studies [17,85]. Our findings on Ni_2dhtp indicate that the precise sorption mechanism can be tailored by selective incorporation of defects, giving rise to tailor-made water sorption properties [59,65,67,86]. We will carry out further experiments in the future to validate this hypothesis and confirm if this is a general property of the M_2dhtp framework series.

Continuing with Ni_2dhip, the water sorption isotherms reveal a similar shape compared to Ni_2dhtp (Figure 5c,d). Slight differences within the low-pressure range $p/p_0 < 0.05$ suggest that the less uniform structure of the pore walls because of the different substitution patterns (i.e., para- vs. meta-arrangements of the carboxylate groups) has only a minor influence on the possible sorption sites within the one-dimensional pores. In addition, the total water uptake is slightly lower (0.41 ± 0.06 g g^{-1}), which is probably due to the decreased void spaces, affecting especially sorption sites near the pore center. We note that these effects could also stem from the observed higher defect-degrees within Ni_2dhip when compared to Ni_2dhtp. As mentioned above, the framework decomposes during the first desorption branch, making it impossible to analyze any effects of the chemisorbed water on the second cycle.

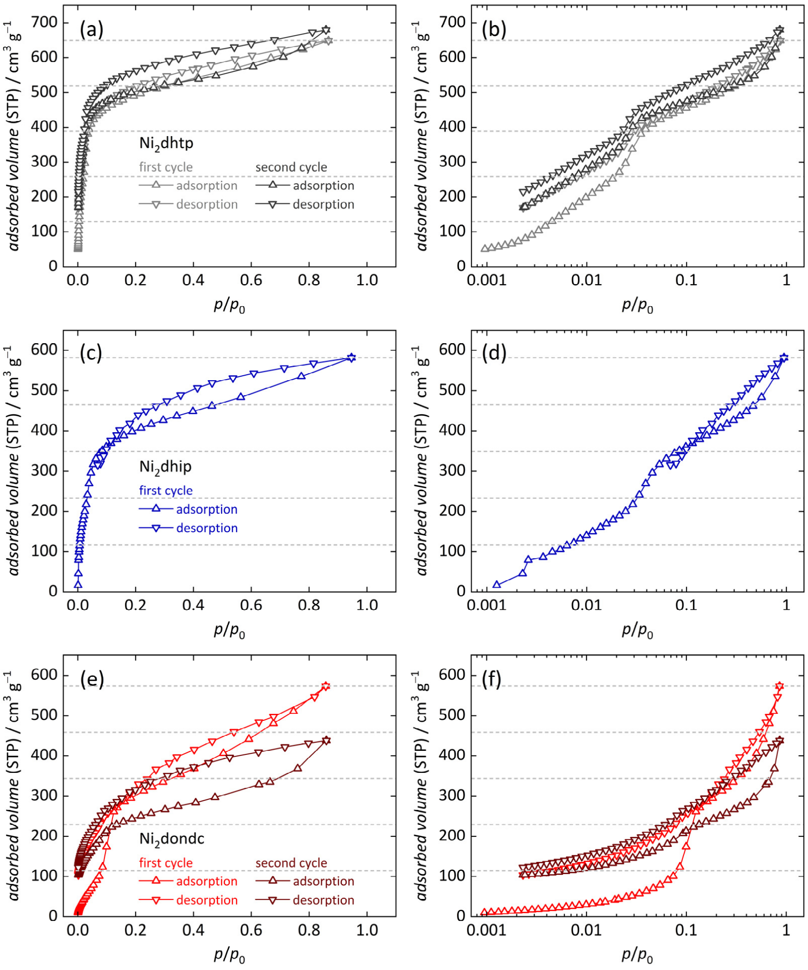

Figure 5. Water vapor sorption isotherms (25 °C) of Ni_2dhtp, Ni_2dhip and Ni_2dondc (two consecutive adsorption/desorption cycles). Data are shown at linear scale (**a**,**c**,**e**) and in semi-logarithmic representation (**b**,**d**,**f**). Horizontal lines mark 20%, 40%, 60%, 80% and 100% of the total water uptake during the first cycle.

The water sorption isotherms of Ni_2dondc (Figure 5e,f) offer fewer similarities to the previously discussed Ni_2dhtp, displaying a type IV [54] water sorption isotherm. Here, water adsorption proceeds less at low relative pressures ($p/p_0 < 0.1$) and is attributed to the irreversible saturation of the open metal sites, i.e., chemisorption to the primary binding sites (ca. 20% of the total uptake remain adsorbed after completed desorption). Following this, a pronounced adsorption step at $p/p_0 = 0.1$ is detected, accountable for a majority of the water uptake. This indicates less favorable conditions for water adsorption, i.e., similar sorption energies of additional water molecules after chemisorption, because of the larger pore diameter and hydrophobic moieties. Therefore, water cluster formation is the driving force for pore condensation, initiated by previously adsorbed water molecules coordinating to the metal centers [56,57]. After this step, more water molecules are gradually adsorbed over a large pressure range. Desorption proceeds gradually as no pronounced desorption steps are visible. This results in a hysteresis between the first adsorption and desorption branch, again suggesting the formation of a meta-stable state during the adsorption process. The total water uptake after the first adsorption branch (0.43 ± 0.03 g g^{-1}) is slightly smaller than for Ni_2dhtp, which is attributed to the higher molecular mass of the used dondc^{4-} ligand, resulting in a larger molecular mass. However, our results are in agreement with single crystal data on as-synthesized Mn_2dondc [20], suggesting that, once completely hydrated, water occupies similar positions in fully hydrated M_2dhtp (i.e., five distinct positions) (We note that the authors mentioned significant disorder of the water molecules due to residual *N*-Methyl-2-pyrolidone solvent molecules). However, unlike for Ni_2dhtp, these distinct positions do not stem from the occupation of preferred sorption sites during the adsorption but rather from an attractive configuration of adsorbed water molecules in hydrated pores. Continuing with the second cycle, a lower overall uptake is observed after the adsorption branch, suggesting decomposition of the framework during the measurement, applying a similar mechanism as discussed for Ni_2dhtp [42,46,47], i.e., with partial pore blockage, resulting in decreased water uptake.

Finally, we investigated the adsorption/desorption behavior of the remaining Ni_2L materials (i.e., L = bpp, bpm and tpp). These compounds offer even larger pores than Ni_2dondc, but reveal distinct similarities, showing type IV [54] water sorption isotherms. All these Ni_2L materials reveal only minor adsorption below a pressure of $p/p_0 < 0.2$, which is again attributed to the irreversible adsorption to the primary sorption sites (Ni^{2+} metal sites, Figure 6a–f). The amount of irreversibly bond water molecules decreases as shown by 13% (Ni_2bpp) > 11% (Ni_2bpm) > 8% (Ni_2tpp), suggesting a smaller amount of water strongly interacting with the framework, resulting in a more bulk-like state, agreeing with our FTIR experiments. Slight differences in the trend presumably stem from the significantly higher incorporation of For^{-} within Ni_2bpp, resulting in lower hydrolytic stability. As the relative water pressure increases, one large adsorption step is visible in all isotherms, which is shifted toward higher pressures with increasing pore size: $p/p_0 \approx 0.21$ for (Ni_2bpp and Ni_2bpm) < $p/p_0 \approx 0.46$ for (Ni_2tpp). Similar dependencies of the condensation of water on the pore size were reported for other MOFs [10] and carbon nanotubes [81,87,88]. These pronounced sorption steps are accountable for the majority of the total water uptake, indicating that for Ni_2dondc and other MOFs [56,57], water adsorption is driven by water cluster formation initiated by chemisorbed water molecules, facilitating pore condensation. Over the remaining pressure ranges, water is gradually adsorbed until complete hydration is observed. During desorption, a small hysteresis is observed, attributed to the above-stated preliminary pore condensation. However, a rather unusual behavior is found for Ni_2bpp and Ni_2bpm, as the first desorption branch crosses the first adsorption branch within the pressure range $p/p_0 = 0.25 \ldots 0.41$ (Figure 6a–d). This is assigned to structural degradation of the framework [89], adopting a similar decomposition mechanism as reported for Ni_2dhtp [42,47]. There, additional open metal sites are formed with individual pores tilting against each other, resulting in decreased porosity. Further evidence for this is found as the second adsorption/desorption cycle is considered, revealing a significantly reduced water uptake after the second adsorption branch when compared to the first adsorption branch. We note that a similar phenomenon might occur for Ni_2tpp (see data range from $p/p_0 = 0.5 \ldots 0.7$) although data are inconclusive in this respect (Figure 6e,f). In addition to this crossing, the second cycles are mostly identical to the first ones, clearly indicating that this effect is caused by framework degradation rather than unique material properties. The maximum water uptake after the first sorption branch increases with pore size, 0.57 ± 0.02 g g^{-1} (Ni_2bpp) < 0.65 ± 0.07 g g^{-1} (Ni_2bpm) < 0.80 ± 0.01 g g^{-1} (Ni_2tpp). Except for the observed crossing of the branches, our results on Ni_2bpp and Ni_2tpp are generally in agreement with previous studies, revealing a slightly lower total water uptake [17]. Differences are attributed to either different measurement settings (fewer data points in the respective crossing regions) or lower defect amounts (not analyzed therein).

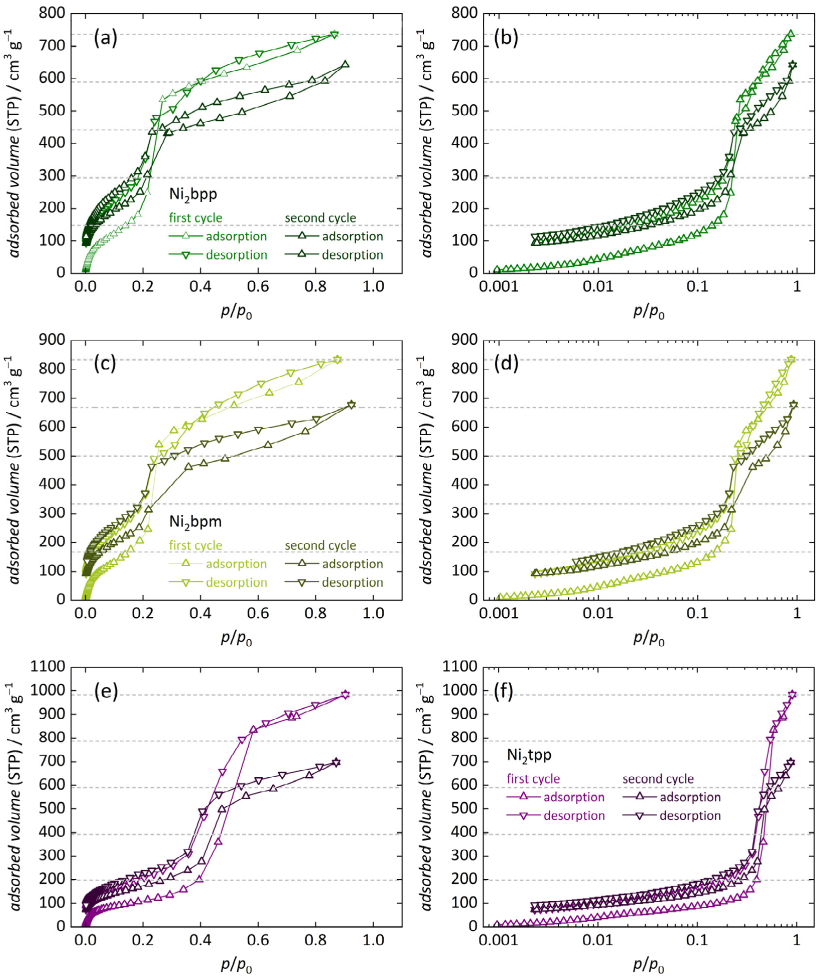

Figure 6. Water vapor sorption isotherms (25 °C) of Ni_2bpp, Ni_2bpm and Ni_2tpp (two consecutive adsorption/desorption cycles). Data are shown at linear scale (**a**,**c**,**e**) and in semi-logarithmic representation (**b**,**d**,**f**). Horizontal lines mark 20%, 40%, 60%, 80% and 100% of the total water uptake during the first cycle (Missing data points for Ni_2bpm below ca. p/p_0 = 0.006 stem from technical difficulties).

When compared to our TGA results, the overall water uptake determined by water vapor sorption experiments (see Supplementary Materials Table S4) is higher for all frameworks (23 . . . 48 mmol g^{-1}). Differences become larger with increasing pore size. As stated above, our TGA analysis underestimates the amount of adsorbed water because the chemisorbed water is strongly bound and gradually released over a larger temperature range and during decomposition. Hence, it is not considered in the initial dehydration step. While this is sufficient to explain the difference for Ni_2L frameworks with a smaller pore apparatus, i.e., L = dhtp, dhip and dondc, additional factors for larger pores must be considered. We hypothesize that some water molecules in these frameworks, i.e., L = bpp, bpm, tpp, are loosely bond and could leave prior to the TGA measurements during sample preparation. Further, we note that we do not see a clear trend of the maximum adsorbed volumes in our nitrogen sorption and water sorption experiments (see Table S6), as found in other studies [82]. Nevertheless, our water vapor sorption analysis indicates that additional hydrophilic sorption sites for H-bonding, besides the open metal sites, i.e., near the inorganic SBUs as present in Ni_2dhtp, are optimal for high water sorption at low relative pressures (Figure 7a). Those additional sorption sites are not found in the other members of the Ni_2L series, which is an immediate consequence of the larger hydrophobic domains. We suggest that water adsorption within the more porous Ni_2L frameworks (L = dondc, bpp, bpm, tpp), is dominated by water cluster formation and follows a similar mechanism in the low-pressure region, as previously reported for other MOFs with strong sorption sites [56–58]. First, the open metal sites are saturated before additional, low-entropy water molecules adsorb thereon, forming distinct water clusters driven by large hydration enthalpies (We note that this could also be a simultaneous process). With increasing pressures, previously adsorbed water molecules initiate the formation of water bridges/chains between adjacent chemisorbed water molecules, acting as hydrophilic anchor sites (Figure 7b–d), similar to studies previously reported for mesoporous silica [83,90] and porous carbons [91] possessing similar hydrophobic domain size. As soon as enough water molecules are present in the gas phase to connect enough adjacent anchor sites, the formation of a continuous H-bonding network is initiated, resulting in pore condensation with minimal framework–water interactions. This process is shifted toward higher relative pressures p/p_0 with increasing hydrophobic domain size, i.e., larger distances of adjacent chemisorbed water molecules, revealing a direct correlation of the inflection point α and the linker polarity (i.e., octanol–water partition coefficients [92,93], see Table S5). Further, this suggests that the pore wall surface polarity is mostly controlled by the inorganic domains, even at small domain sizes. These effects are a direct consequence of the Gibbs hydration energy $\Delta G_{\text{hydration}}$ being dominated by the enthalpy term for larger hydrophobic domains, with water molecules avoiding these units. Conversely, smaller units are viewed as discrete perturbations, forcing a high-entropy water arrangement near the hydrophobic surface, resulting in dominant entropic contributions as suggested for Ni_2dhtp (i.e., dominant surface–water interactions) [94–96]. The transition length for the reversal of entropy/enthalpy-driven hydration lies around 10 Å (or 1 nm), which is within the same range as water–water distances for coordination water molecules in Ni_2bpp and Ni_2bpm. Following the condensation step, the relaxation of adsorbed water molecules provides additional room for further water molecules until complete hydration is observed. Consequently, a more bulk-like water arrangement with increased H-bonding symmetry is found, as suggested by our FTIR experiments. Hence, the observed H-bonding in NW water is dominated by water–water interactions for larger pores, which is additionally supported by the observation of a decreasing amount of irreversible bond water molecules with increasing pore size. For Ni_2dondc, this relaxation process initiates the formation of more entropic water molecules with more asymmetric H-bonding forced to interact with the pore walls. Eventually, this results in the occupation of discrete positions, as suggested by XRD data [20], even though the initial hydration mechanism, i.e., pore condensation, is enthalpy-driven. This is supported by our spectroscopic results, highlighting a more asymmetric H-bonding situation.

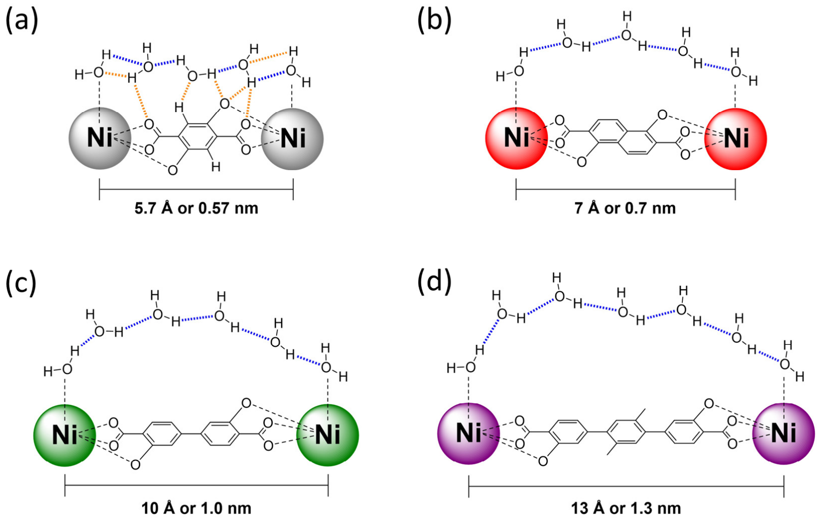

Figure 7. Illustration of the different arrangements of water molecules near the framework pore walls in hydrated Ni_2L frameworks. (**a**) Ni_2dhtp reveals multiple attractive H-bonding interactions with framework atoms (dashed orange lines) and surrounding water molecules (dashed blue lines), located at distinct positions. Formed water bridges, avoiding the hydrophobic domains in (**b**) Ni_2dondc, (**c**) Ni_2bpp and (**d**) Ni_2tpp, suggest that the size of the water bridges/chains increases with larger distances of adjacent coordinating water molecules, i.e., H-bonding anchors (distances estimated from XRD data [11,20,97]).

4. Conclusions

Our study on the isoreticular Ni_2L framework series enabled us to analyze the effects of the pore size and linker hydrophobicity on the water sorption mechanism and the arrangement of confined water. We found evidence that defects in Ni_2dhtp play an important role on the given sorption mechanism. Higher amounts of formate defects result in a less uniform pore wall, reducing the attractiveness of the third sorption site (near the phenylene backbone), offering less H-bonding possibilities. Conversely, incorporation of fewer defect sites results in a sorption mechanism, more comparable to those discussed for most other M_2dhtp frameworks. This suggests that selective incorporation of defects enables one to precisely tune the water sorption properties in the M_2dhtp series. On the other hand, these effects play a minor role for larger pores (i.e., Ni_2L; L = dondc, bpp, bpm, tpp). Within the low-pressure range, water predominantly adsorbs to the open metal sites while additional molecules adsorb thereon as a result of large hydration enthalpies, forming distinct water clusters. Water bridges between adjacent chemisorbed water molecules, located at the primary binding sites, form thereafter, providing additional H-bonding opportunities. Consequently, the sorption process is facilitated, resulting in classical pore condensation characterized by a continuous H-bonding network. The observed sorption step is governed by the pore size, with the pressure range additionally depending on the linker hydrophobicity/hydrophobic domain size. We found that H-bonding is generally more asymmetric in smaller pores, consistent with the expectation of defined water positions in fully hydrated Ni_2dhtp and Ni_2dondc, offering multiple attractive water–framework interactions. Larger pores offer a more symmetric H-bonding situation, suggesting a more bulk-like water arrangement under less confinement, dominated by water–water interactions, as indicated by decreasing dehydration temperatures with increasing pore size.

Supplementary Materials: The following supporting information can be downloaded at: https://www.mdpi.com/article/10.3390/nano14221791/s1, Synthetic procedures (linker and MOF synthesis), Figures S1–S5: NMR spectra of organic compounds; Figures S6–S11: Pore size distribution fits by NLDFT methods; Figures S12–S18: NMR spectra of digested MOFs; Figures S19–S24: FTIR spectra of MOFs in comparison with the used linkers; Figure S25: Deconvolution of the O-H stretching vibration of liquid water; Figure S26: XRD data of re-isolated MOF samples after water vapor sorption analysis; Figures S27–S32: Normalized first derivatives ($\delta V/\delta(p/p_0)$) of water vapor sorption data; Table S1: Total water uptake of MOF samples, determined by TGA analysis; Table S2: Results of least square fits of hydrated MOF samples in comparison with pure water; Table S3: Peak center position of the O-H stretching vibration of water in hydrated MOFs; Table S4: Total water uptake of MOF samples, determined by water vapor sorption analysis; Table S5: Octanol–water partition coefficients of protonated linker molecules; Table S6: Comparison of the maximum adsorption of the nitrogen and water sorption isotherms.

Author Contributions: Conceptualization, M.K. and M.T.; methodology, M.K.; validation, M.K., L.S., Z.Z., C.W. and M.T.; formal analysis, M.K., L.S., Z.Z., C.W. and H.E.; investigation, M.K. and L.S.; resources, M.T.; data curation, M.K.; writing—original draft preparation, M.K., C.W. and M.T.; writing—review and editing, M.K., C.W. and M.T.; visualization, M.K. and Z.Z.; supervision, M.T.; project administration, M.T. All authors have read and agreed to the published version of the manuscript.

Funding: This research received no external funding.

Data Availability Statement: Dataset available on request from the authors.

Acknowledgments: The authors thank Michael Reimer and Tamay Meric from the working group for Plastics Technology and Plastics Processing of the Faculty of Mechanical Engineering of Paderborn University for performing the TGA experiments.

Conflicts of Interest: The authors declare no conflicts of interest.

References

1. Yaghi, O.M.; O'Keeffe, M.; Ockwig, N.W.; Chae, H.K.; Eddaoudi, M.; Kim, J. Reticular synthesis and the design of new materials. *Nature* **2003**, *423*, 705–714. [CrossRef] [PubMed]
2. Janiak, C.; Vieth, J.K. MOFs, MILs and more: Concepts, properties and applications for porous coordination networks (PCNs). *New J. Chem.* **2010**, *34*, 2366. [CrossRef]
3. Schoedel, A.; Li, M.; Li, D.; O'Keeffe, M.; Yaghi, O.M. Structures of Metal–Organic Frameworks with Rod Secondary Building. Units. *Chem. Rev.* **2016**, *116*, 12466–12535. [CrossRef]
4. Keeffe, M.O.; Peskov, M.A.; Ramsden, S.J.; Yaghi, O.M. The Reticular Chemistry Structure Resource (RCSR) Database of, and Symbols for, Crystal Nets. *Acc. Chem. Res.* **2008**, *41*, 1782–1789. [CrossRef]
5. Zhao, D.; Timmons, D.J.; Yuan, D.; Zhou, H.-C. Tuning the Topology and Functionality of Metal−Organic Frameworks by Ligand Design. *Acc. Chem. Res.* **2011**, *44*, 123–133. [CrossRef]
6. Eddaoudi, M.; Kim, J.; Rosi, N.; Vodak, D.; Wachter, J.; O'Keeffe, M.; Yaghi, O.M. Systematic Design of Pore Size and Functionality in Isoreticular MOFs and Their Application in Methane Storage. *Science* **2002**, *295*, 469–472. [CrossRef]
7. Pallach, R.; Keupp, J.; Terlinden, K.; Frentzel-Beyme, L.; Kloß, M.; Machalica, A.; Kotschy, J.; Vasa, S.K.; Chater, P.A.; Sternemann, C.; et al. Frustrated flexibility in metal-organic frameworks. *Nat. Commun.* **2021**, *12*, 4097. [CrossRef]
8. Frentzel-Beyme, L.; Kloß, M.; Kolodzeiski, P.; Pallach, R.; Henke, S. Meltable Mixed-Linker Zeolitic Imidazolate Frameworks and Their Microporous Glasses: From Melting Point Engineering to Selective Hydrocarbon Sorption. *J. Am. Chem. Soc.* **2019**, *141*, 12362–12371. [CrossRef]
9. Henke, S.; Schneemann, A.; Wütscher, A.; Fischer, R.A. Directing the Breathing Behavior of Pillared-Layered Metal–Organic Frameworks via a Systematic Library of Functionalized Linkers Bearing Flexible Substituents. *J. Am. Chem. Soc.* **2012**, *134*, 9464–9474. [CrossRef]
10. Lu, F.-F.; Gu, X.-W.; Wu, E.; Li, B.; Qian, G. Systematic evaluation of water adsorption in isoreticular UiO-type metal–organic frameworks. *J. Mater. Chem. A* **2023**, *11*, 1246–1255. [CrossRef]
11. Deng, H.; Grunder, S.; Cordova, K.E.; Valente, C.; Furukawa, H.; Hmadeh, M.; Gándara, F.; Whalley, A.C.; Liu, Z.; Asahina, S.; et al. Large-Pore Apertures in a Series of Metal-Organic Frameworks. *Science* **2012**, *336*, 1018–1023. [CrossRef] [PubMed]
12. Kalmutzki, M.J.; Diercks, C.S.; Yaghi, O.M. Metal–Organic Frameworks for Water Harvesting from Air. *Adv. Mater.* **2018**, *30*, 1704304. [CrossRef]
13. Akiyama, G.; Matsuda, R.; Sato, H.; Hori, A.; Takata, M.; Kitagawa, S. Effect of functional groups in MIL-101 on water sorption behavior. *Microporous Mesoporous Mater.* **2012**, *157*, 89–93. [CrossRef]

14. Frentzel-Beyme, L.; Kloß, M.; Pallach, R.; Salamon, S.; Moldenhauer, H.; Landers, J.; Wende, H.; Debus, J.; Henke, S. Porous purple glass—A cobalt imidazolate glass with accessible porosity from a meltable cobalt imidazolate framework. *J. Mater. Chem. A* **2019**, *7*, 985–990. [CrossRef]
15. Dietzel, P.D.C.; Morita, Y.; Blom, R.; Fjellvåg, H. An In Situ High-Temperature Single-Crystal Investigation of a Dehydrated Metal–Organic Framework Compound and Field-Induced Magnetization of One-Dimensional Metal–Oxygen Chains. *Angew. Chem. Int. Ed.* **2005**, *44*, 6354–6358. [CrossRef]
16. Rosi, N.L.; Kim, J.; Eddaoudi, M.; Chen, B.; O'Keeffe, M.; Yaghi, O.M. Rod Packings and Metal−Organic Frameworks Constructed from Rod-Shaped Secondary Building Units. *J. Am. Chem. Soc.* **2005**, *127*, 1504–1508. [CrossRef] [PubMed]
17. Zheng, J.; Vemuri, R.S.; Estevez, L.; Koech, P.K.; Varga, T.; Camaioni, D.M.; Blake, T.A.; Mcgrail, B.P.; Motkuri, R.K. Pore-Engineered Metal–Organic Frameworks with Excellent Adsorption of Water and Fluorocarbon Refrigerant for Cooling Applications. *J. Am. Chem. Soc.* **2017**, *139*, 10601–10604. [CrossRef]
18. Gheorghe, A.; Reus, S.; Koenis, M.; Dubbeldam, D.; Woutersen, S.; Tanase, S. Role of additives and solvents in the synthesis of chiral isoreticular MOF-74 topologies. *Dalt. Trans.* **2021**, *50*, 12159–12167. [CrossRef]
19. Peng, S.; Bie, B.; Jia, H.; Tang, H.; Zhang, X.; Sun, Y.; Wei, Q.; Wu, F.; Yuan, Y.; Deng, H.; et al. Efficient Separation of Nucleic Acids with Different Secondary Structures by Metal–Organic Frameworks. *J. Am. Chem. Soc.* **2020**, *142*, 5049–5059. [CrossRef]
20. Dietzel, P.D.C.; Georgiev, P.A.; Frøseth, M.; Johnsen, R.E.; Fjellvåg, H.; Blom, R. Effect of Larger Pore Size on the Sorption Properties of Isoreticular Metal–Organic Frameworks with High Number of Open Metal Sites. *Chem. A Eur. J.* **2020**, *26*, 13523–13531. [CrossRef]
21. Zheng, J.; Barpaga, D.; Trump, B.A.; Shetty, M.; Fan, Y.; Bhattacharya, P.; Jenks, J.J.; Su, C.Y.; Brown, C.M.; Maurin, G.; et al. Molecular Insight into Fluorocarbon Adsorption in Pore Expanded Metal–Organic Framework Analogs. *J. Am. Chem. Soc.* **2020**, *142*, 3002–3012. [CrossRef]
22. Kapelewski, M.T.; Geier, S.J.; Hudson, M.R.; Stück, D.; Mason, J.A.; Nelson, J.N.; Xiao, D.J.; Hulvey, Z.; Gilmour, E.; Fitzgerald, S.A.; et al. M_2(*m*-dobdc) (M = Mg, Mn, Fe, Co, Ni) Metal–Organic Frameworks Exhibiting Increased Charge Density and Enhanced H_2 Binding at the Open Metal Sites. *J. Am. Chem. Soc.* **2014**, *136*, 12119–12129. [CrossRef] [PubMed]
23. Gygi, D.; Bloch, E.D.; Mason, J.A.; Hudson, M.R.; Gonzalez, M.I.; Siegelman, R.L.; Darwish, T.A.; Queen, W.L.; Brown, C.M.; Long, J.R. Hydrogen Storage in the Expanded Pore Metal–Organic Frameworks M_2(dobpdc) (M = Mg, Mn, Fe, Co, Ni, Zn). *Chem. Mater.* **2016**, *28*, 1128–1138. [CrossRef]
24. Forse, A.C.; Gonzalez, M.I.; Siegelman, R.L.; Witherspoon, V.J.; Jawahery, S.; Mercado, R.; Milner, P.J.; Martell, J.D.; Smit, B.; Blümich, B.; et al. Unexpected Diffusion Anisotropy of Carbon Dioxide in the Metal–Organic Framework Zn_2(dobpdc). *J. Am. Chem. Soc.* **2018**, *140*, 1663–1673. [CrossRef]
25. Kökçam-Demir, Ü.; Goldman, A.; Esrafili, L.; Gharib, M.; Morsali, A.; Weingart, O.; Janiak, C. Coordinatively unsaturated metal sites (open metal sites) in metal–organic frameworks: Design and applications. *Chem. Soc. Rev.* **2020**, *49*, 2751. [CrossRef]
26. Dietzel, P.D.C.; Besikiotis, V.; Blom, R. Application of metal–organic frameworks with coordinatively unsaturated metal sites in storage and separation of methane and carbon dioxide. *J. Mater. Chem.* **2009**, *19*, 7362–7370. [CrossRef]
27. Pato-Doldán, B.; Rosnes, M.H.; Dietzel, P.D.C. An In-Depth Structural Study of the Carbon Dioxide Adsorption Process in the Porous Metal–Organic Frameworks CPO-27-M. *ChemSusChem* **2017**, *10*, 1710–1719. [CrossRef] [PubMed]
28. Fetisov, E.O.; Shah, M.S.; Long, J.R.; Tsapatsis, M.; Siepmann, J.I. First principles Monte Carlo simulations of unary and binary adsorption: CO_2, N_2, and H_2O in Mg-MOF-74. *Chem. Commun.* **2018**, *54*, 10816–10819. [CrossRef]
29. Queen, W.L.; Hudson, M.R.; Bloch, E.D.; Mason, J.A.; Gonzalez, M.I.; Lee, J.S.; Gygi, D.; Howe, J.D.; Lee, K.; Darwish, T.A.; et al. Comprehensive study of carbon dioxide adsorption in the metal–organic frameworks M_2(dobdc) (M = Mg, Mn, Fe, Co, Ni, Cu, Zn). *Chem. Sci.* **2014**, *5*, 4569–4581. [CrossRef]
30. Drisdell, W.S.; Poloni, R.; McDonald, T.M.; Long, J.R.; Smit, B.; Neaton, J.B.; Prendergast, D.; Kortright, J.B. Probing Adsorption Interactions in Metal–Organic Frameworks using X-ray Spectroscopy. *J. Am. Chem. Soc.* **2013**, *135*, 18183–18190. [CrossRef]
31. Strauss, I.; Mundstock, A.; Hinrichs, D.; Himstedt, R.; Knebel, A.; Reinhardt, C.; Dorfs, D.; Caro, J. The Interaction of Guest Molecules with Co-MOF-74: A Vis/NIR and Raman Approach. *Angew. Chemie Int. Ed.* **2018**, *57*, 7434–7439. [CrossRef] [PubMed]
32. Rosnes, M.H.; Pato-Doldán, B.; Johnsen, R.E.; Mundstock, A.; Caro, J.; Dietzel, P.D.C. Role of the metal cation in the dehydration of the microporous metal–organic frameworks CPO-27-M. *Microporous Mesoporous Mater.* **2020**, *309*, 110503. [CrossRef]
33. Chen, T.; Chen, S.; Chen, Y.; Zhao, M.; Losic, D.; Zhang, S. Metal-organic frameworks containing solid-state electrolytes for lithium metal batteries and beyond. *Mater. Chem. Front.* **2021**, *5*, 1771–1794. [CrossRef]
34. McDonald, T.M.; Lee, W.R.; Mason, J.A.; Wiers, B.M.; Hong, C.S.; Long, J.R. Capture of Carbon Dioxide from Air and Flue Gas in the Alkylamine-Appended Metal–Organic Framework mmen-Mg_2(dobpdc). *J. Am. Chem. Soc.* **2012**, *134*, 7056–7065. [CrossRef] [PubMed]
35. Trickett, C.A.; Helal, A.; Al-Maythalony, B.A.; Yamani, Z.H.; Cordova, K.E.; Yaghi, O.M. The chemistry of metal–organic frameworks for CO_2 capture, regeneration and conversion. *Nat. Rev. Mater.* **2017**, *2*, 17045. [CrossRef]
36. Solís, C.; Palaci, D.; Llabres i Xamena, F.X.; Serra, J.M. Proton Transport through Robust CPO-27-type Metal Organic Frameworks. *J. Phys. Chem. C* **2014**, *118*, 21663–21670. [CrossRef]
37. Hwang, S.; Lee, E.J.; Song, D.; Jeong, N.C. High Proton Mobility with High Directionality in Isolated Channels of MOF-74. *ACS Appl. Mater. Interfaces* **2018**, *10*, 35354–35360. [CrossRef]

38. Javed, A.; Strauss, I.; Bunzen, H.; Caro, J.; Tiemann, M. Humidity-Mediated Anisotropic Proton Conductivity through the 1D Channels of Co-MOF-74. *Nanomaterials* **2020**, *10*, 1263. [CrossRef]
39. Khalil, I.E.; Fonseca, J.; Reithofer, M.R.; Eder, T.; Chin, J.M. Tackling orientation of metal-organic frameworks (MOFs): The quest to enhance MOF performance. *Coord. Chem. Rev.* **2023**, *481*, 215043. [CrossRef]
40. Liu, Y.R.; Chen, Y.Y.; Zhao, H.Y.; Li, G. Exploration of single-crystal proton conduction in ordered networks. *Coord. Chem. Rev.* **2024**, *499*, 215516. [CrossRef]
41. Hanikel, N.; Prévot, M.S.; Yaghi, O.M. MOF water harvesters. *Nat. Nanotechnol.* **2020**, *15*, 348. [CrossRef] [PubMed]
42. DeCoste, J.B.; Peterson, G.W.; Schindler, B.J.; Killops, K.L.; Browe, M.A.; Mahle, J.J. The effect of water adsorption on the structure of the carboxylate containing metal–organic frameworks Cu-BTC, Mg-MOF-74, and UiO-66. *J. Mater. Chem. A* **2013**, *1*, 11922–11932. [CrossRef]
43. Schoenecker, P.M.; Carson, C.G.; Jasuja, H.; Flemming, C.J.J.; Walton, K.S. Effect of Water Adsorption on Retention of Structure and Surface Area of Metal–Organic Frameworks. *Ind. Eng. Chem. Res.* **2012**, *51*, 6513–6519. [CrossRef]
44. Metrane, A.; Delhali, A.; Ouikhalfan, M.; Assen, A.H.; Belmabkhout, Y. Water Vapor Adsorption by Porous Materials: From Chemistry to Practical Applications. *J. Chem. Eng. Data* **2022**, *67*, 1617–1653. [CrossRef]
45. Weinberger, C.; Zysk, F.; Hartmann, M.; Kaliannan, N.K.; Keil, W.; Kühne, T.D.; Tiemann, M. The Structure of Water in Silica Mesopores—Influence of the Pore Wall Polarity. *Adv. Mater. Interfaces* **2022**, *9*, 2200245. [CrossRef]
46. Kloß, M.; Beerbaum, M.; Baier, D.; Weinberger, C.; Zysk, F.; Elgabarty, H.; Kühne, T.D.; Tiemann, M. Understanding Hydration in CPO-27 Metal-Organic Frameworks: Strong Impact of the Chemical Nature of the Metal (Cu, Zn). *Adv. Mater. Interfaces* **2024**, 2400476. [CrossRef]
47. Kloß, M.; Weinberger, C.; Tiemann, M. Water in the Micropores of CPO-27 Metal-Organic Frameworks: A Comprehensive Study. *Microporous Mesoporous Mater.* **2024**, *381*, 113352. [CrossRef]
48. Furukawa, H.; Gándara, F.; Zhang, Y.B.; Jiang, J.; Queen, W.L.; Hudson, M.R.; Yaghi, O.M. Water Adsorption in Porous Metal–Organic Frameworks and Related Materials. *J. Am. Chem. Soc.* **2014**, *136*, 4369–4381. [CrossRef]
49. Zhang, B.; Zhu, Z.; Wang, X.; Liu, X.; Kapteijn, F. Water Adsorption in MOFs: Structures and Applications. *Adv. Funct. Mater.* **2023**, *34*, 2304788. [CrossRef]
50. Yaghi, O.M.; Kalmutzki, M.J.; Diercks, C.S. Water Sorption Applications of MOFs. In *Introduction to Reticular Chemistry: Metal-Organic Frameworks and Covalent Organic Frameworks*; Wiley-VCH: Weinheim, Germany, 2019; pp. 359–427. [CrossRef]
51. Tan, K.; Nijem, N.; Canepa, P.; Gong, Q.; Li, J.; Thonhauser, T.; Chabal, Y.J. Stability and Hydrolyzation of Metal Organic Frameworks with Paddle-Wheel SBUs upon Hydration. *Chem. Mater.* **2012**, *24*, 3153–3167. [CrossRef]
52. Tan, K.; Nijem, N.; Gao, Y.; Zuluaga, S.; Li, J.; Thonhauser, T.; Chabal, Y.J. Water interactions in metal organic frameworks. *CrystEngComm* **2015**, *17*, 247–260. [CrossRef]
53. Lincoln, S.F. Mechanistic Studies of Metal Aqua Ions: A Semi-Historical Perspective. *Helv. Chim. Acta* **2005**, *88*, 523–545. [CrossRef]
54. Ng, E.-P.; Mintova, S. Nanoporous materials with enhanced hydrophilicity and high water sorption capacity. *Microporous Mesoporous Mater.* **2008**, *114*, 1–26. [CrossRef]
55. Liu, L.; Zeng, W.; Tan, S.J.; Liu, M.; Do, D.D. Microscopic insights into water adsorption in carbon nanopores—The role of acidic and basic functional groups and their configurations. *Phys. Chem. Chem. Phys.* **2021**, *23*, 18369–18377. [CrossRef]
56. Mileo, P.G.M.; Cho, K.H.; Park, J.; Devautour-Vinot, S.; Chang, J.S.; Maurin, G. Unraveling the Water Adsorption Mechanism in the Mesoporous MIL-100(Fe) Metal−Organic Framework. *J. Phys. Chem. C* **2019**, *123*, 23014–23025. [CrossRef]
57. Ho, C.-H.; Valentine, M.L.; Chen, Z.; Xie, H.; Farha, O.; Xiong, W.; Paesani, F. Structure and thermodynamics of water adsorption in NU-1500-Cr. *Commun. Chem.* **2023**, *6*, 70. [CrossRef]
58. Hanikel, N.; Pei, X.; Chheda, S.; Lyu, H.; Jeong, W.S.; Sauer, J.; Gagliardi, L.; Yaghi, O.M. Evolution of water structures in metal-organic frameworks for improved atmospheric water harvesting. *Science* **2021**, *374*, 454–459. [CrossRef]
59. Heidary, N.; Chartrand, D.; Guiet, A.; Kornienko, N. Rational incorporation of defects within metal–organic frameworks generates highly active electrocatalytic sites. *Chem. Sci.* **2021**, *12*, 7324–7333. [CrossRef] [PubMed]
60. Song, Q.; Li, Y.; Cao, Z.; Liu, H.; Tian, C.; Yang, Z.; Qiang, X.; Tan, Z.; Deng, Y. Discovery of novel 2,5-dihydroxyterephthalamide derivatives as multifunctional agents for the treatment of Alzheimer's disease. *Bioorg. Med. Chem.* **2018**, *26*, 6115–6127. [CrossRef]
61. Schukraft, G.E.M.; Ayala, S.; Dick, B.L.; Cohen, S.M. Isoreticular expansion of polyMOFs achieves high surface area materials. *Chem. Commun.* **2017**, *53*, 10684–10687. [CrossRef]
62. Rouquerol, J.; Llewellyn, P.; Rouquerol, F. Is the bet equation applicable to microporous adsorbents? *Stud. Surf. Sci. Catal.* **2007**, *160*, 49–56. [CrossRef]
63. Kim, H.; Sohail, M.; Yim, K.; Park, Y.C.; Chun, D.H.; Kim, H.J.; Han, S.O.; Moon, J.-H. Effective CO_2 and CO Separation Using [M_2(DOBDC)] (M = Mg, Co, Ni) with Unsaturated Metal Sites and Excavation of Their Adsorption Sites. *ACS Appl. Mater. Interfaces* **2019**, *11*, 7014–7021. [CrossRef] [PubMed]
64. Thommes, M.; Kaneko, K.; Neimark, A.V.; Olivier, J.P.; Rodriguez-Reinoso, F.; Rouquerol, J.; Sing, K.S.W. Physisorption of gases, with special reference to the evaluation of surface area and pore size distribution (IUPAC Technical Report) Pure. *Appl. Chem.* **2015**, *87*, 1051. [CrossRef]
65. Fu, Y.; Yao, Y.; Forse, A.C.; Li, J.; Mochizuki, K.; Long, J.R.; Reimer, J.A.; De Paëpe, G.; Kong, X. Solvent-derived defects suppress adsorption in MOF-74. *Nat. Commun.* **2023**, *14*, 2386. [CrossRef] [PubMed]

66. Yasaka, Y.; Yoshida, K.; Wakai, C.; Matubayasi, N.; Nakahara, M. Kinetic and Equilibrium Study on Formic Acid Decomposition in Relation to the Water-Gas-Shift Reaction. *J. Phys. Chem. A* **2006**, *110*, 11082–11090. [CrossRef]
67. Lim, J.; Lee, S.; Sharma, A.; Seong, J.; Baek, S.B.; Lah, M.S. Ligand functionalization of defect-engineered Ni-MOF-74. *RSC Adv.* **2022**, *12*, 31451–31455. [CrossRef]
68. Onori, G.; Santucci, A. IR investigations of water structure in Aerosol OT reverse micellar aggregates. *J. Phys. Chem.* **1993**, *97*, 5430. [CrossRef]
69. MacDonald, H.; Bedwell, B.; Gulari, E. FTIR spectroscopy of microemulsion structure. *Langmuir* **1986**, *2*, 704. [CrossRef]
70. Knight, A.W.; Kalugin, N.G.; Coker, E.; Ilgen, A.G. Water properties under nano-scale confinement. *Sci. Rep.* **2019**, *9*, 8246. [CrossRef]
71. Wagner, J.C.; Hunter, K.M.; Paesani, F.; Xiong, W. Water Capture Mechanisms at Zeolitic Imidazolate Framework Interfaces. *J. Am. Chem. Soc.* **2021**, *143*, 21189–21194. [CrossRef]
72. Brubach, J.-B.; Mermet, A.; Filabozzi, A.; Gerschel, A.; Roy, P. Signatures of the hydrogen bonding in the infrared bands of water. *J. Chem. Phys.* **2005**, *122*, 184509. [CrossRef] [PubMed]
73. Zhang, C.; Khaliullin, R.Z.; Bovi, D.; Guidoni, L.; Kühne, T.D. Vibrational Signature of Water Molecules in Asymmetric Hydrogen Bonding Environments. *J. Phys. Chem. Lett.* **2013**, *4*, 3245–3250. [CrossRef]
74. Zhang, C.; Guidoni, L.; Kühne, T.D. Competing factors on the frequency separation between the OH stretching modes in water. *J. Mol. Liq.* **2015**, *205*, 42–45. [CrossRef]
75. Iiyama, T.; Ruike, M.; Kaneko, K. Structural mechanism of water adsorption in hydrophobic micropores from in situ small angle X-ray scattering. *Chem. Phys. Lett.* **2000**, *331*, 359–364. [CrossRef]
76. Alcañiz-Monge, J.; Linares-Solano, A.; Rand, B. Mechanism of Adsorption of Water in Carbon Micropores As Revealed by a Study of Activated Carbon Fibers. *J. Phys. Chem. B* **2002**, *106*, 3209–3216. [CrossRef]
77. Brovchenko, I.; Geiger, A.; Oleinikova, A. Water in nanopores: II. The liquid–vapour phase transition near hydrophobic surfaces. *J. Phys. Condens. Matter* **2004**, *16*, S5345–S5370. [CrossRef]
78. Ohba, T.; Kanoh, H.; Kaneko, K. Cluster-Growth-Induced Water Adsorption in Hydrophobic Carbon Nanopores. *J. Phys. Chem. B* **2004**, *108*, 14964–14969. [CrossRef]
79. Ohba, T.; Kanoh, H.; Kaneko, K. Structures and Stability of Water Nanoclusters in Hydrophobic Nanospaces. *Nano Lett.* **2005**, *5*, 227–230. [CrossRef] [PubMed]
80. Gallo, P.; Rovere, M.; Chen, S.-H. Anomalous dynamics of water confined in MCM-41 at different hydrations. *J. Phys. Condens. Matter* **2010**, *22*, 284102. [CrossRef]
81. Sadeghi, M.; Parsafar, G.A. Density-induced molecular arrangements of water inside carbon nanotubes. *Phys. Chem. Chem. Phys.* **2013**, *15*, 7379–7388. [CrossRef]
82. Thommes, M.; Morell, J.; Cychosz, K.A.; Fröba, M. Combining Nitrogen, Argon, and Water Adsorption for Advanced Characterization of Ordered Mesoporous Carbons (CMKs) and Periodic Mesoporous Organosilicas (PMOs). *Langmuir* **2013**, *29*, 14893–14902. [CrossRef] [PubMed]
83. Mietner, J.B.; Brieler, F.J.; Lee, Y.J.; Fröba, M. Properties of Water Confined in Periodic Mesoporous Organosilicas: Nanoimprinting the Local Structure. *Angew. Chem. Int. Ed.* **2017**, *56*, 12348–12351. [CrossRef] [PubMed]
84. Malfait, B.; Moréac, A.; Jani, A.; Lefort, R.; Huber, P.; Fröba, M.; Morineau, D. Structure of Water at Hydrophilic and Hydrophobic Interfaces: Raman Spectroscopy of Water Confined in Periodic Mesoporous (Organo)Silicas. *J. Phys. Chem. C* **2022**, *126*, 3520–3531. [CrossRef]
85. Liu, J.; Wang, Y.; Benin, A.I.; Jakubczak, P.; Willis, R.R.; LeVan, M.D. CO_2/H_2O Adsorption Equilibrium and Rates on Metal−Organic Frameworks: HKUST-1 and Ni/DOBDC. *Langmuir* **2010**, *26*, 14301–14307. [CrossRef]
86. Villajos, J.A.; Jagorel, N.; Reinsch, S.; Emmerling, F. Increasing Exposed Metal Site Accessibility in a Co-MOF-74 Material with Induced Structure-Defects. *Front. Mater.* **2019**, *6*, 230. [CrossRef]
87. Dalla Bernardina, S.; Paineau, E.; Brubach, J.-B.; Judeinstein, P.; Rouzière, S.; Launois, P.; Roy, P. Water in Carbon Nanotubes: The Peculiar Hydrogen Bond Network Revealed by Infrared Spectroscopy. *J. Am. Chem. Soc.* **2016**, *138*, 10437–10443. [CrossRef] [PubMed]
88. Hanasaki, I.; Nakatani, A. Hydrogen bond dynamics and microscopic structure of confined water inside carbon nanotubes. *J. Chem. Phys.* **2006**, *124*, 144708. [CrossRef]
89. Küsgens, P.; Rose, M.; Senkovska, I.; Fröde, H.; Henschel, A.; Siegle, S.; Kaskel, S. Characterization of metal-organic frameworks by water adsorption. *Microporous Mesoporous Mater.* **2009**, *120*, 325–330. [CrossRef]
90. Moon, H.; Collanton, R.P.; Monroe, J.I.; Casey, T.M.; Shell, M.S.; Han, S.; Scott, S.L. Evidence for Entropically Controlled Interfacial Hydration in Mesoporous. Organosilicas. *J. Am. Chem. Soc.* **2022**, *144*, 1766–1777. [CrossRef]
91. Wang, C.; Xing, Y.; Lei, Y.; Xia, Y.; Zhang, C.; Zhang, R.; Wang, S.; Chen, P.; Zhu, S.; Li, J.; et al. Adsorption of water on carbon materials: The formation of "water bridge" and its effect on water adsorption. *Colloids Surf. A Physicochem. Eng. Asp.* **2021**, *631*, 127719. [CrossRef]
92. Harris, M.F.; Logan, J.L. Determination of log K_{ow} Values for Four Drugs. *J. Chem. Educ.* **2014**, *91*, 915–918. [CrossRef]
93. Paschke, A.; Neitzel, P.L.; Walther, W.; Schüürmann, G. Octanol/Water Partition Coefficient of Selected Herbicides: Determination Using Shake-Flask Method and Reversed-Phase High-Performance Liquid Chromatography. *J. Chem. Eng. Data* **2004**, *49*, 1639–1642. [CrossRef]

94. Lum, K.; Chandler, D.; Weeks, J.D. Hydrophobicity at Small and Large Length Scales. *J. Phys. Chem. B* **1999**, *103*, 4570–4577. [CrossRef]
95. Huang, D.M.; Chandler, D. Temperature and length scale dependence of hydrophobic effects and their possible implications for protein folding. *Proc. Natl. Acad. Sci. USA* **2000**, *97*, 8324–8327. [CrossRef]
96. Huang, D.M.; Geissler, P.L.; Chandler, D. Scaling of Hydrophobic Solvation Free Energies. *J. Phys. Chem. B* **2001**, *105*, 6704–6709. [CrossRef]
97. Wong-Ng, W.; Kaduk, J.A.; Wu, H.; Suchomel, M. Synchrotron X-ray studies of metal-organic framework M_2(2,5-dihydroxyterephthalate), M = (Mn, Co, Ni, Zn) (MOF74). *Powder Diffr.* **2012**, *27*, 256–262. [CrossRef]

Water Sorption Studies on Isoreticular CPO-27-type MOFs: From Discrete Sorption Sites to Water-Bridge-Mediated Pore Condensation

Supporting Information

Marvin Kloß, Lara Schäfers, Zhenyu Zhao, Christian Weinberger, Hans Egold and Michael Tiemann*

Department of Chemistry, Faculty of Science, Paderborn University
Warburger Str. 100 D-33098, Paderborn, Germany

Inorganic Chemistry (michael.tiemann@upb.de)

EXPERIMENTAL (LINKER SYNTHESIS)

Synthesis of 1,5-dihydroxynaphthalene-2,6-dicarboxylic acid (H_4dondc): Synthesis was performed using a previously published protocol under slight modifications.[1] 1,5-dihydroxynaphtalene (9.75 g, 60 mmol, 1.0 eq) and potassium bicarbonate (20.25 g, 202.5 mmol, 3.375 eq) were finely grounded in a mortar. The solid mixture was transferred to a Teflon-lined inlay (125 mL), placed in a stainless-steel reactor (*Parr Instruments*), sealed, and reacted in a pre-heated oven at 230 °C for 20 h. After cooling to room temperature, the mixture was carefully acidified using aqueous hydrochloric acid (2 M). The solid was separated by centrifugation (4000 rpm, 30 min) and washed three time with desalinated water. The obtained green solid residue was dried at 60 °C over the course of three days before it was re-dissolved in tetrahydrofuran (THF) and subsequently filtered to get rid of solid impurities. Then, THF was removed under reduced pressure, yielding a brown solid. Finally, dispersion of the solid in fresh methanol and removal of the solvent under reduced pressure yielded 1,5-dihydroxynaphthalene-2,6-dicarboxylic acid (H_4dondc) as a green-brown powder (13.28 g, 53.5 mmol, 88%).

^{1}H NMR (500 MHz, dmso-d_6): δ = 14.02 (brs, 2H), 12.7 (brs, 2H), 7.81 (d, 2H, $^3J_{HH}$ = 8.8 Hz), 7.74 (d, 2H, $^3J_{HH}$ = 8.8 Hz) ppm.

^{13}C NMR (125 MHz, dmso-d_6) δ = 172.5, 159.3, 127.6, 124.9, 113.1, 109.0 ppm (see **Figure S1**).

Synthesis of 3,3'-dihydroxy-[1,1'-biphenyl]-4,4'-dicarboxylic acid (H_4bpp): For the first step, a Suzuki-Miyaura cross coupling reaction was performed following a literature protocol with slight modifications.[2] Potassium acetate (2.52 g, 25.71 mmol, 6.3 eq), and Pd(dppf)Cl_2·DCM (200 mg, 0.245 mmol, 0.06 eq) were placed in a Schlenk-flask (100 mL) inside an argon glovebox. Then, 3-methoxy-4-methoxycarbonylphenyl boronic acid (1.03 g, 4.9 mmol, 1.2 eq) and methyl-4-bromo-2-methoxybenzoat (1.0 g, 4.08 mmol, 1.0 eq) were added under a constant argon gas flow. All compounds were suspended in a solvent mixture of *p*-dioxane/water (25/10 ml, previously degassed for 45 min). The mixture was heated to 80 °C for 19 h. After cooling to room temperature, the solid residue was filtrated and washed with water (total of 200 mL in several portions). Subsequent drying for 48 h at 60 °C in an oven yielded dimethyl-3,3′-dimethoxy-[1,1′-biphenyl]-4,4′-dicarboxylate as a brown solid (1.3 g, 3.94 mmol, 96%).

^{1}H NMR (500 MHz, $CDCl_3$): δ=7.89 (d, $^3J_{HH}$ = 8 Hz, 1H), 7.20 (dd, $^3J_{HH}$ = 8 Hz, $^4J_{HH}$ =1.5Hz, 1H), 7,15 (d, $^4J_{HH}$ = 1.5Hz, 1H), 3.98 (s, 6H), 3.92 (s, 6H) ppm. (see **Figure S2**).

For the second step, two subsequent deprotection reactions were performed with slight deviation from previously published protocols.[3] Dimethyl-3,3′-dimethoxy-[1,1′-biphenyl]-4,4′-dicarboxylate (1.3 g, 3.94 mmol, 1 eq) was dissolved in dry dichloromethane (DCM, 15mL). The solution was cooled to –78 °C using an acetone cooling bath. Then, boron tribromide solution, 1 M in *n*-hexane, (13 mL, 13 mmol, 3.3 eq) was slowly added with a syringe. After complete addition, the mixture was cooled for additional 5 min before removal of the cooling bath. The mixture was stirred over night at room temperature. The reaction was quenched using ice cold water (same volume than DCM). The solid residue was isolated by filtration and dried at 60 °C overnight. Then, the filtrate was saturated with sodium chloride and extracted with ethyl acetate (3 x 50 mL). Combined organic layers were dried over $MgSO_4$ and the solvent was removed under reduced pressure. The obtained solid was then dried at 60 °C overnight. For the next step, both crude products were combined (1.41 g, 4.67 mmol, *ca.* 1 eq) and dissolved in a mixture of THF (12 mL) and aqueous sodium hydroxide (1.87 g, 46.7 mmol, 10 eq, 12 mL) to obtain a 0.2 M solution. Mixture was heated to 50 °C for 24h. After cooling to room temperature, THF was removed under reduced pressure. Next, aqueous hydrochloric acid was added to the suspension until a pH < 2 was reached. The precipitate was filtered, washed with copious amounts of water, and dried for 48 h at 60 °C. 3,3′-Dihydroxy-[1,1′-biphenyl]-4,4′-dicarboxylic acid (H_4bpp) was isolated as an off-white solid (0.91, 3.0 mmol, 76%).

^{1}H NMR (500 MHz, dmso-d$_6$): δ= 11.41 (brs, 2H), 7.87 (d, $^3J_{HH}$ = 8.0 Hz, 1H), 7.20 (dd, $^3J_{HH}$ = 8.0 Hz, $^4J_{HH}$ =1.5Hz, 1H), 7,15 (d, $^4J_{HH}$ =1.5Hz, 1H), 3.98 (s, 6H), 3.92 (s, 6H) ppm.

^{13}C NMR (125 MHz, dmso-d$_6$) δ = 166.5, 159.7, 145.8, 132.5, 119.8, 119.4, 111.3, 56.4, 52.2 ppm (see **Figure S3**).

Synthesis of 3,3''-dihydroxy-2',5'-dimethyl-[1,1':4',1''-terphenyl]-4,4''-dicarboxylic acid (H_4tpp):

For the first step, a Suzuki-Miyaura cross coupling reaction was performed following a literature protocol under slight modifications.[2] Potassium acetate (2.23 g, 22.73 mmol, 12 eq), and Pd(dppf)Cl_2·DCM (155 mg, 0.189 mmol, 0.1 eq) were placed in a Schlenk-flask (50 mL) inside an argon glovebox. Then, 3-methoxy-4-methoxycarbonylphenyl boronic acid (0.955 g, 4.55 mmol, 2.4 eq) and 1,4-dibromo-2,5-dimethylbenzene (0.5 g, 1.89 mmol, 1.0 eq) were added under a constant argon gas flow. All compounds were suspended in a solvent mixture of *p*-dioxane/water (25/10 ml, previously degassed for 45 min). The mixture was refluxed overnight (*ca.* 16 h). After cooling to room temperature, water (20 mL) was added, and the aqueous phase was extracted with DCM (3 x 25ml). Combined organic phases were dried over $MgSO_4$. Removing of the solvent under reduced pressure and subsequent drying at 60 °C over 48 h yielded dimethyl-3,3′-dimethoxy-2,5-dimethyl-[1,4-terphenyl]-4,4′-dicarboxylate as a off-white solid (0.55 g, 1.22 mmol, 67%).

^{1}H-NMR δ=7.86 (d, $^3J_{HH}$ = 7.8 Hz, 2H), 7.16 (s, 2H), 6.98 (dd, $^3J_{HH}$ = 7.8 Hz, $^4J_{HH}$ = 1.4 Hz, 2H), 6.96 (d, $^4J_{HH}$ = 1.4 Hz, 2H), 3.93 (s, 6H), 3.92 (s, 3H), 2.28 (s, 6H) ppm (see **Figure S4**).

For the second step, two subsequent deprotection reactions were performed with slight deviation from previously published protocols.[3] Dimethyl-3,3′-dimethoxy-2,5-dimethyl-[1,4-terphenyl]-4,4′-dicarboxylat (1.14 g, 2.62 mmol, 1 eq) was dissolved in dry DCM (15 mL). The solution was cooled to -78 C using an acetone cooling bath. Then, boron tribromide solution, 1 M in *n*-hexane, (7.8 mL, 7.8 mmol, 3.3 eq) was slowly added with a syringe. After complete addition, the mixture was cooled for additional 5 min before removal of the cooling bath. The mixture was stirred over night at room temperature (*ca.* 16 h). The reaction was quenched using ice cold water (same volume than DCM). The solid residue was isolated by filtration and dried at 60 °C overnight. Then, the filtrate was saturated with sodium chloride and extracted with ethyl acetate (3 x 50 mL). Combined organic layers dried over $MgSO_4$ and the solvent was removed under reduced pressure. The obtained solid was then dried at 60 °C overnight. For the next step, both crude products were combined (0.754 g, 1.86 mmol, 1 eq) and dissolved in a mixture of THF (5 mL) and aqueous sodium hydroxide (0.742 g, 18.6 mmol, 10 eq, 5 mL) to obtain a 0.2 M solution. The mixture was heated to 50 °C for 24h. After cooling to room temperature, THF was removed under reduced pressure. Aqueous hydrochloric acid was added to the suspension until a pH <2 was reached. The precipitate was filtered, washed with copious amounts of water, and dried for 48 h at 60 °C. 3,3′-Dihydroxy-[1,1′-biphenyl]-4,4′-dicarboxylic acid (H_4tpp) was isolated as an off-whit solid (0.91, 1.65 mmol, 91 %).

^1H NMR (700 MHz, $CDCl_3$): δ= 7.85 (d, $^3J_{HH}$ = 8.4 Hz, 2H), 7.17 (s, 2H), 6.93 (dd, $^3J_{HH}$ = 8.4 Hz, $^4J_{HH}$ = 1.5 Hz, 1H), 6.92 (d, $^4J_{HH}$ =1.5 Hz, 2H), 2.24 (s, 6H) ppm.

^{13}C NMR (175 MHz, dmso-d_6) δ = 171.8, 160.9, 148.2, 139.6, 132.2, 131.3, 130.1, 120.2, 117.3, 111.7, 19.5 ppm (see **Figure S5**).

EXPERIMENTAL (MOF SYNTHESIS)

Preparation of Ni_2(dhtp)[4]: H_4dhtp (349 mg, 1.76 mmol, 0.6 eq) was dissolved in *N,N*-dimethylformamide (DMF, 50 mL) using ultra sonification. Separately, nickel(II) nitrate hexahydrate (854 mg, 2.94 mmol, 1.0 eq) was dissolved in DMF (12.5 mL) and deionized water (3.2 mL). Both solutions were combined in a Teflon-lined insert (125 mL) and the mixture was stirred briefly. The insert was placed in a stainless-steel reactor (*Parr Instruments*), sealed, and reacted in a preheated oven at 100 °C for 24 h. After cooling, the solid was separated by filtration and washed with DMF (2 x 20 mL) deionized water (3 x 30 mL) and methanol (3 x 30 mL). Then, the solvent was exchanged using methanol (three times over the course of four days). The obtained product was dried in multiple steps. For the first step, the product was placed in a round flask under dynamic vacuum for 16 h. Then, the product was heated in 70 °C (hold for 18 h). The desolvated product (orange) was stored in a glove box under argon atmosphere.

Preparation of Ni_2(dhip)[5]: H_4dhip (149 mg, 0.75 mmol, 1.0 eq) was dissolved in DMF (12.5 mL) using ultra sonification. Separately, nickel(II) chloride hexahydrate (446 mg, 1.88 mmol, 2.5 eq) was dissolved in a mixture of DMF (20 mL) and methanol (17.5 mL). Both solutions were portioned equally to five screw-top jars (20 mL, with PTFE seal). The sealed jars were heated to 120 °C for 18 h in a pre-heated oven. After cooling to room temperature, the solid residues were combined and washed with DMF (3 x 25 mL) and methanol (3 x 25 mL). Then, the solvent was exchanged using methanol (four times *ca.* 15mL over the course of four days). The obtained product was dried in multiple steps. For the first step, the product was placed in a round flask under dynamic vacuum for 16 h. Then, the product was heated to 70 °C (hold for 18 h). The desolvated product (light-green) was stored in a glove box under argon atmosphere.

Preparation of Ni_2(dondc)[1]: H_4dondc (310 mg, 1.25 mmol, 1.0 eq) was dissolved in *N*-Methyl-2-pyrrolidon (NMP, 40 mL) using ultra sonification. Separately, nickel(II) acetate tetrahydrate (620 mg, 2.5 mmol, 2.0 eq) were dissolved in deionized water (5 mL). Both solutions were portioned equally to five screw-top jars (20 mL, with PTFE seal). The sealed jars were heated to 110 °C for 48 h in a pre-heated oven. After cooling to room temperature, the solid residues were combined and washed with DMF (3 x 25 mL), and methanol (3 x 25 mL). Then, the solvent was exchanged using methanol (three times 15 mL over the course of four days). The obtained product was dried in multiple steps. For the first step, the product was placed in a round flask under dynamic vacuum for 16 h. Then, the product was heated in 70 °C (hold for 18 h). The desolvated product (brown) was stored in a glove box under argon atmosphere.

Preparation of Ni_2(bpp): Synthesis was performed by upscaling of a previously reported procedure.[6] H_4bpp (153 mg, 0.57 mmol, 1.0 eq) was dissolved in DMF (39 mL). Separately, nickel(II) nitrate hexahydrate (540 mg, 1.86 mmol, 3.3 eq) was dissolved in DMF (6 mL). Both solutions were transferred to a Teflon-lined insert (125 mL). Then, ethanol (1 mL) and deionized water (1 mL) were added. The insert was placed in a stainless-steel reactor (*Parr Instruments*), sealed, and reacted in a preheated oven at 120 °C for 24 h. After cooling to room temperature, the overstanding solution was separated, and the solid residue was dispersed in DMF (15 mL). The solvent was replaced four-times over the course of several days. Then, the solvent was exchanged using methanol (2 x 20mL over the course of four days). The obtained product was dried in multiple steps. For the first step, the product was placed in a round flask under dynamic vacuum for 16 h. Then, the product was heated in 70 °C (hold for 18 h). The desolvated product (light-green) was stored in a glove box under argon atmosphere.

Preparation of Ni_2(bpm): Synthesis was performed by upscaling of a previously reported procedure under use of the H_4bpm linker molecule.[6] H_4bpm (156 mg, 0.57mmol, 1.0 eq) was dissolved in DMF (39 mL) using ultra sonification and transferred into a Teflon-lined inlay (125 ml). Separately, nickel(II) nitrate hexahydrate (540 mg, 1.86 mmol, 3.3 eq) was dissolved in DMF (6 mL) separately and added to the linker solution. Then, ethanol (3 mL) and deionized water (3 mL) were added, and the solution was briefly stirred. The inlay was transferred into a stainless-steel autoclave reactor (*Paar Instruments*), sealed, and heated to 120 °C for 24 h in a pre-heated oven. After cooling to room temperature, the solid residue was filtered of and washed with methanol (5 x 25 mL). Then, the solvent was exchanged using methanol (2 x 25mL over the course of four days). The obtained product was dried in multiple steps. For the first step, the product was placed in a round flask under dynamic vacuum for 16 h. Then, the product was heated in 70 °C (hold for 18 h). The desolvated product (light-green) was stored in a glove box under argon atmosphere.

Preparation of Ni_2(tpp): Synthesis is based on a previously published procedure.[6] H_4tpp (71 mg, 0.188 mmol, 1.0 eq) was dissolved in DMF (13 mL) in a screw-top jar with PTFE-sealed cap (20 mL) using ultra sonification. Separately, nickel(II) nitrate hexahydrate (180 mg, 0.62 mmol, 3.3 eq) was dissolved in DMF (2 mL) and added to the screw-top jar. Then, ethanol (1 mL) und deionized water (1 mL) were added. The jar war sealed, briefly shacked, and heated to 120 C for 24 h in a pre-heated oven. After cooling to room temperature, the overstanding solution was separated, and the solid residue was dispersed in DMF (5 mL). The solvent was replaced four-times over the course of several days. Then, the solvent was exchanged using methanol (2 x 8mL over the course of four days). The obtained product was dried in multiple steps. For the first step, the product was placed in a round flask under dynamic vacuum for 16 h. Then, the product was heated in 70 °C (hold for 18 h). The desolvated product (brown-green) was stored in a glove box under argon atmosphere.

NMR (LINKER SYNTHESIS)

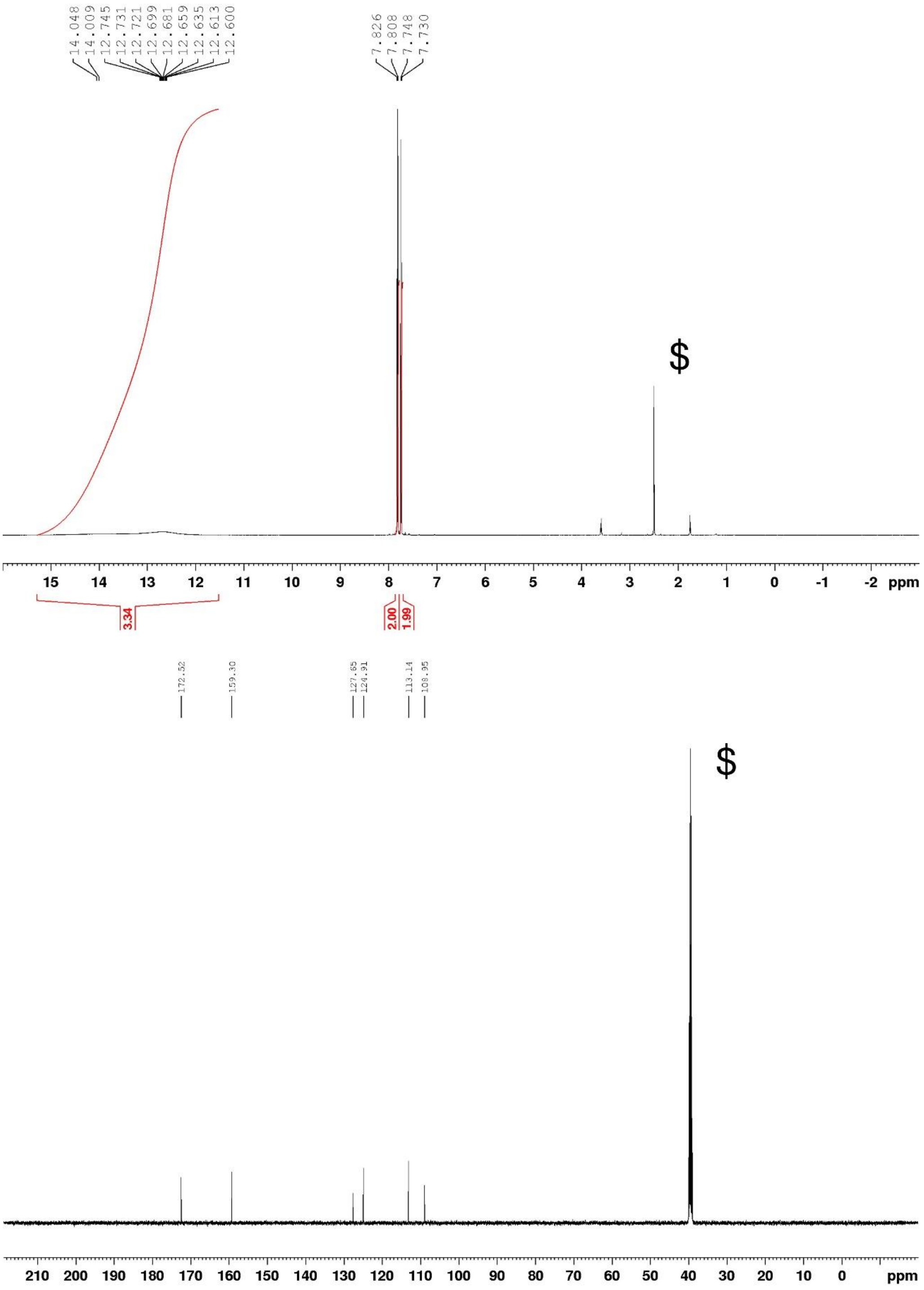

Figure S1. ^{1}H NMR (top) and ^{13}C NMR spectrum (bottom) of 1,5-dihydroxynaphthalene-2,6-dicarboxylic acid (H_4dondc) in dmso-d_6 (marked with $).

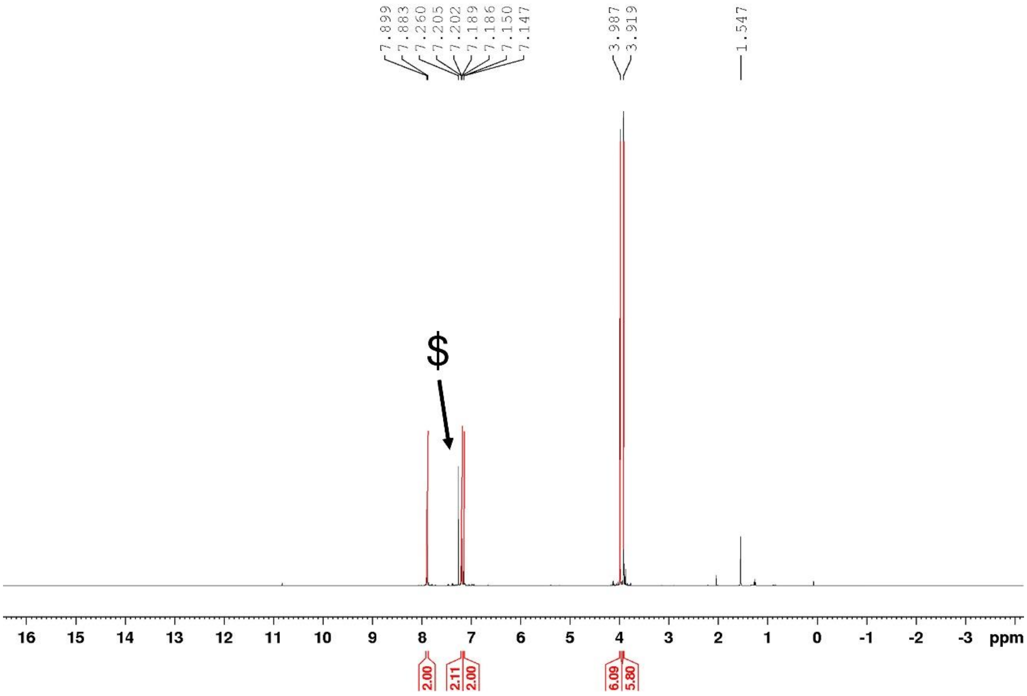

Figure S2. ^{1}H NMR spectrum of dimethyl-3,3'-dimethoxy-[1,1'-biphenyl]-4,4'-dicarboxylate in $CDCl_3$ (marked with $).

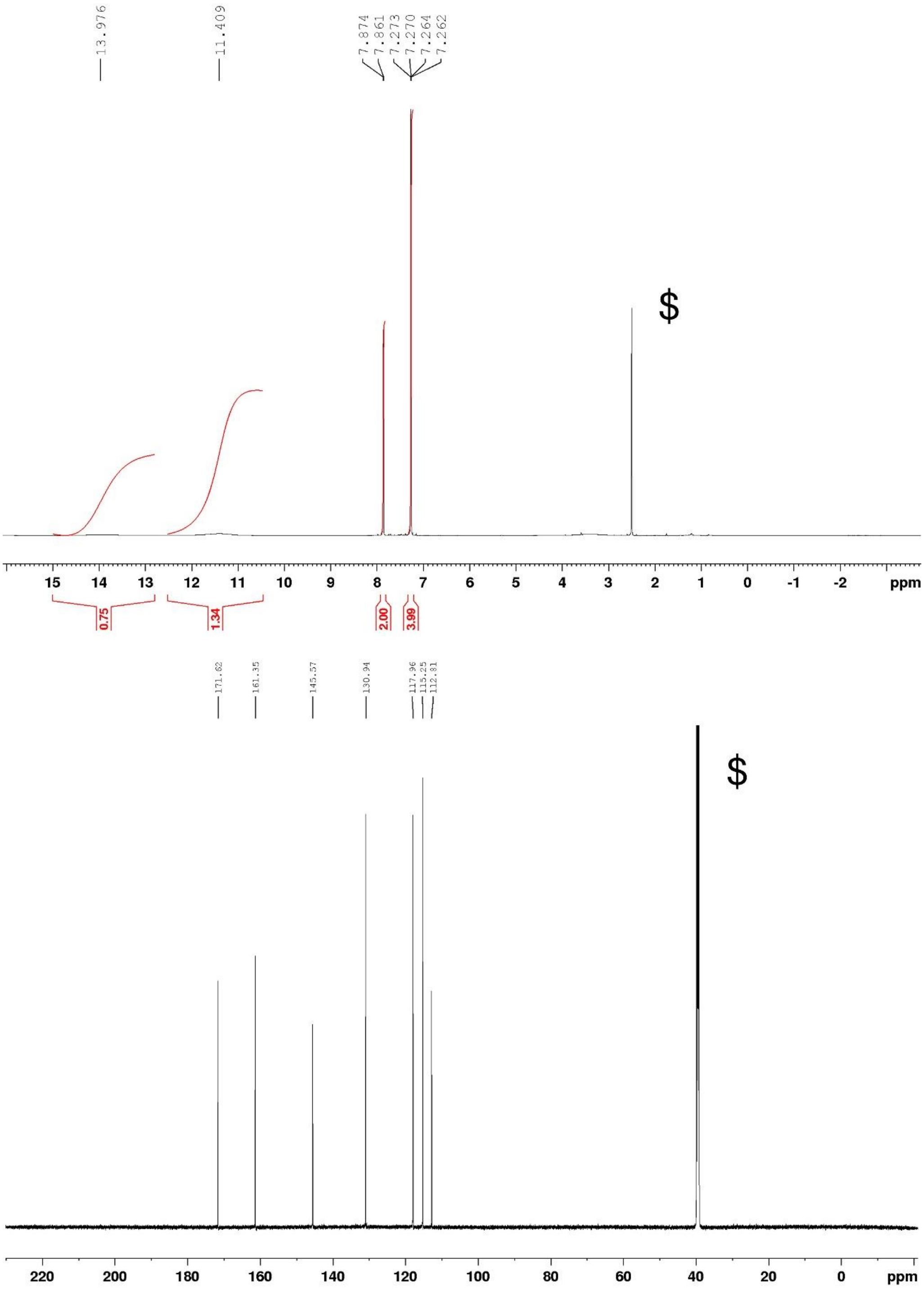

Figure S3. ^{1}H NMR (top) and ^{13}C NMR spectrum (bottom) of 3,3′-Dihydroxy-[1,1′-biphenyl]-4,4′-dicarboxylic acid (H_4bpp) in dmso-d_6 (marked with $).

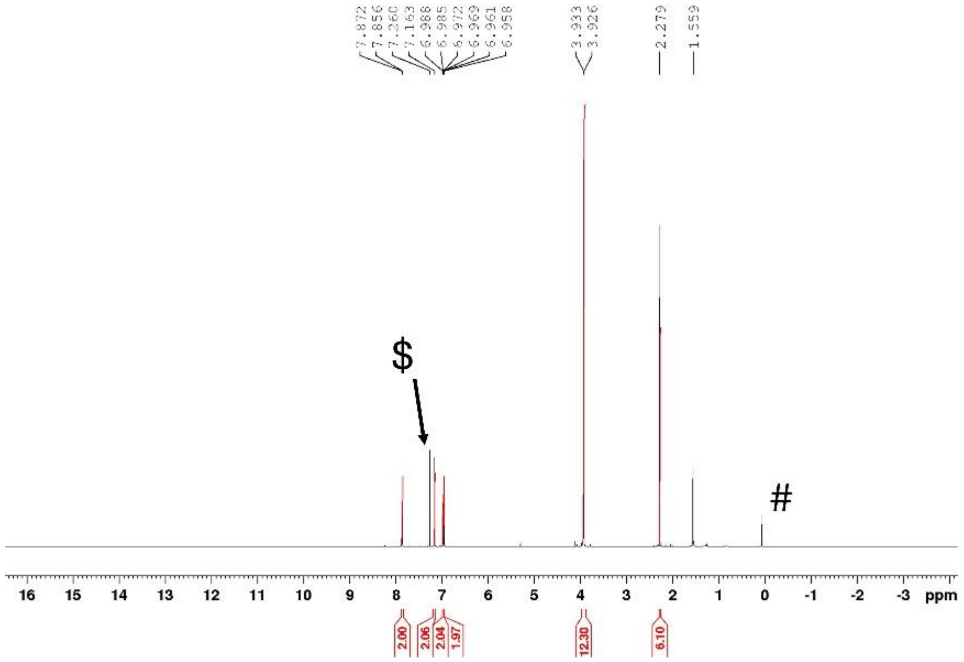

Figure S4. ^{1}H NMR spectrum of dimethyl-3,3′-dimethoxy-2,5-dimethyl-[1,4-terphenyl]-4,4′-dicarboxylate in CDCl$_3$ (marked with $). TMS (marked with #) has been used as internal standard.

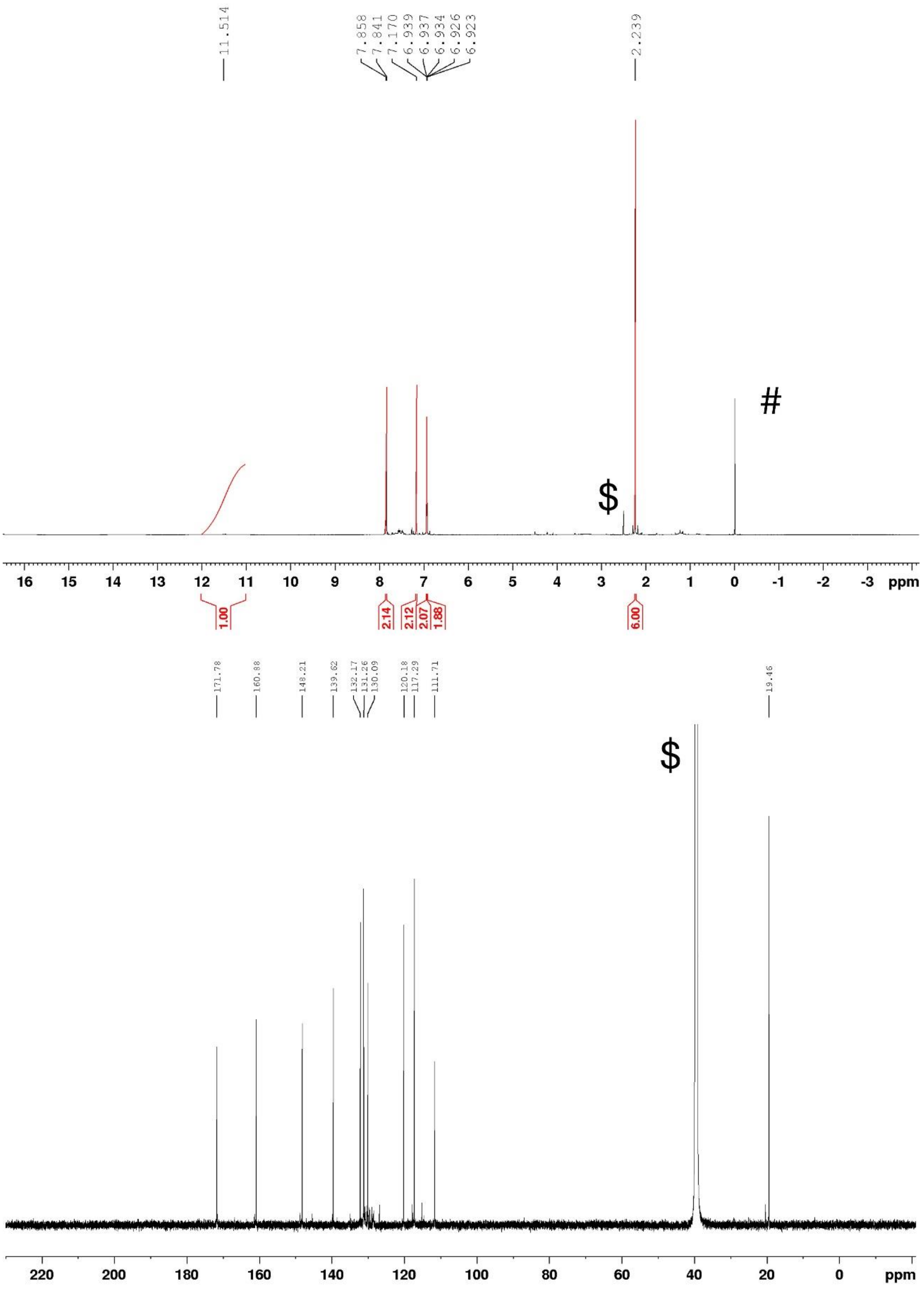

Figure S5. ^1H NMR (top) and ^{13}C NMR spectrum (bottom) of 3,3'-Dihydroxy-[1,1'-biphenyl]-4,4'-dicarboxylic acid (H_4tpp) in dmso-d_6 (marked with $). Internal standard: TMS (marked with #).

NITROGEN SORPTION DATA

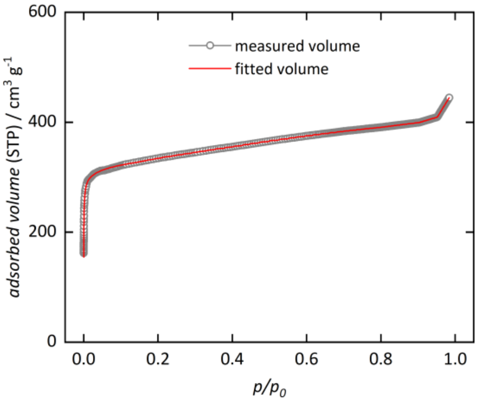

Figure S6. N_2 sorption data for Ni_2dhtp, obtained at 77 K, fitted by a NLDFT data-based method (Fitting error 0.2%).

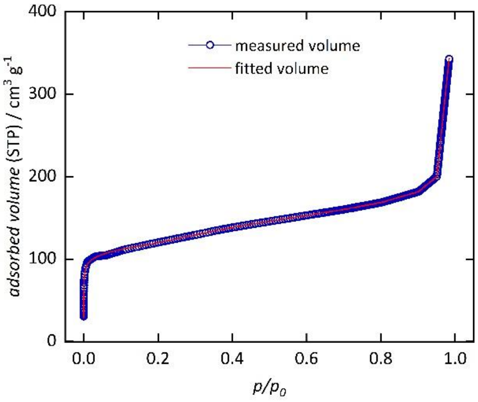

Figure S7. N_2 sorption data for Ni_2dhip, obtained at 77 K, fitted by a NLDFT data-based method (Fitting error 0.5%).

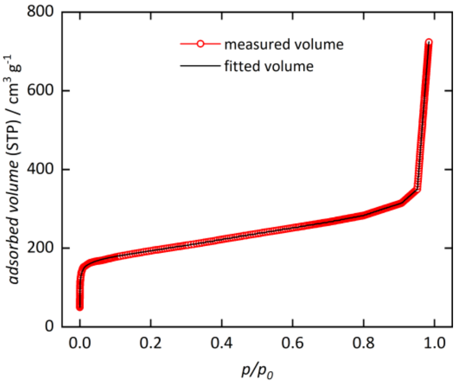

Figure S8. N_2 sorption data for Ni_2dondc, obtained at 77 K, fitted by a NLDFT data-based method (Fitting error 0.6%).

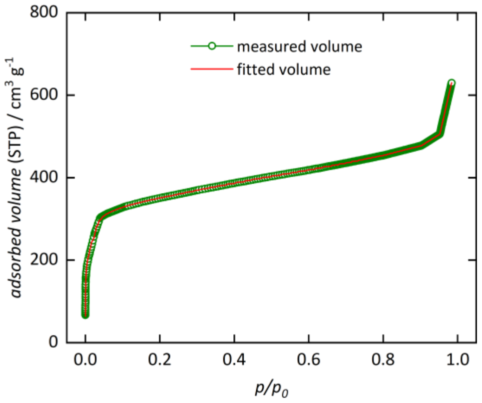

Figure S9. N_2 sorption data for Ni_2bpp, obtained at 77 K, fitted by a NLDFT data-based method (Fitting error 0.3%).

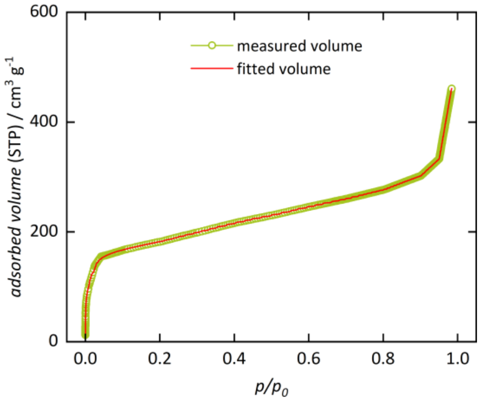

Figure S10. N_2 sorption data for Ni_2bpm, obtained at 77 K, fitted by a NLDFT data-based method (Fitting error 0.3%).

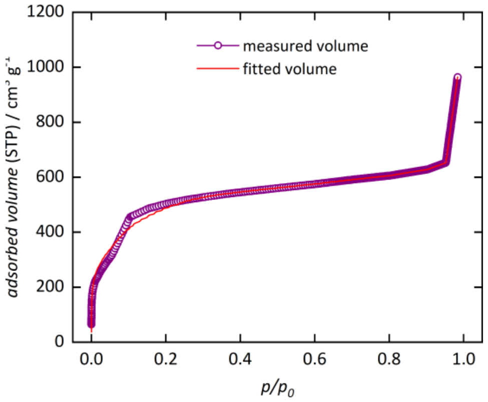

Figure S11. N_2 sorption data for Ni_2tpp, obtained at 77 K, fitted by a NLDFT data-based method (Fitting error 1.7%).

NMR (DIGESTED SAMPLES FOR DEFECT ANALYSIS)

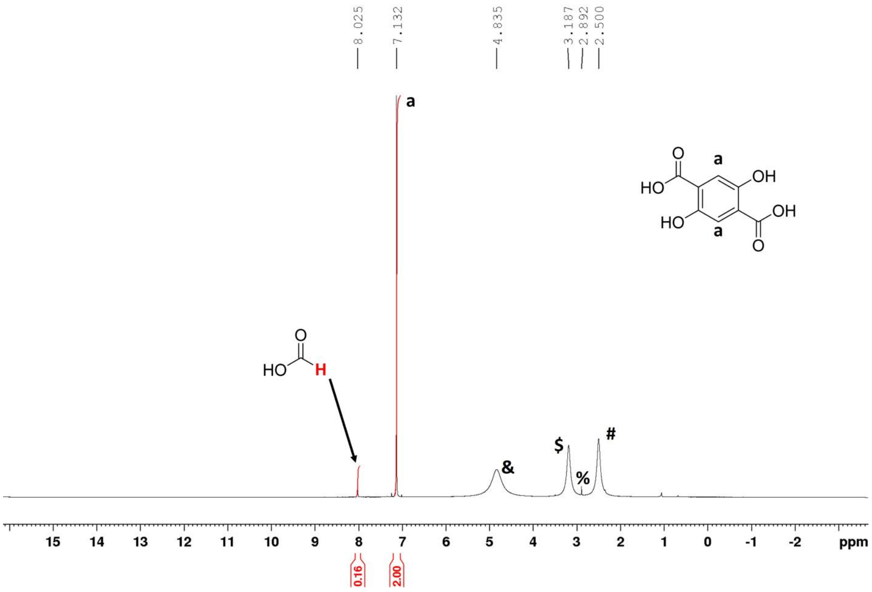

Figure S12. ^{1}H NMR Ni_2dhtp diluted in a mixture of dmso-d_6 (marked with #) and DCl (20wt% in D_2O, marked with $). The signal at 4.8 ppm is a superposition of all acidic protons (-OH and -COOH groups, marked with &), stemming from a fast chemical proton exchange. Residual DMF solvent molecules are marked with %. The remaining two DMF signals are not visible due to signal overlap or the low relative intensity.

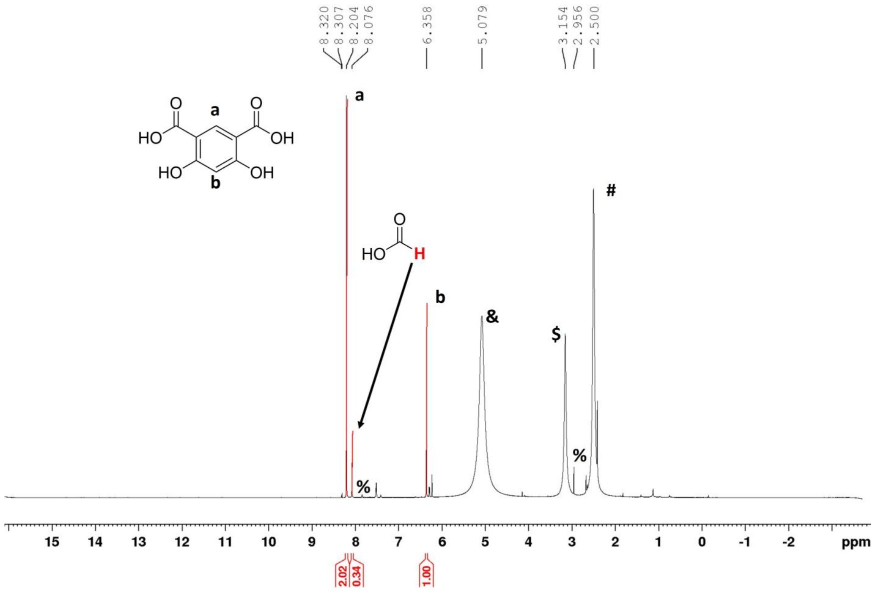

Figure S13. ^{1}H NMR Ni$_2$dhip diluted in a mixture of dmso-d$_6$ (marked with #) and DCl (20wt% in D_2O, marked with $). The signal at 4.8 ppm is a superposition of all acidic protons (-OH and -COOH groups, marked with &), stemming from a fast chemical proton exchange. Residual DMF solvent molecules are marked with %. The third DMF signal (methyl group) is not visible due to signal overlap.

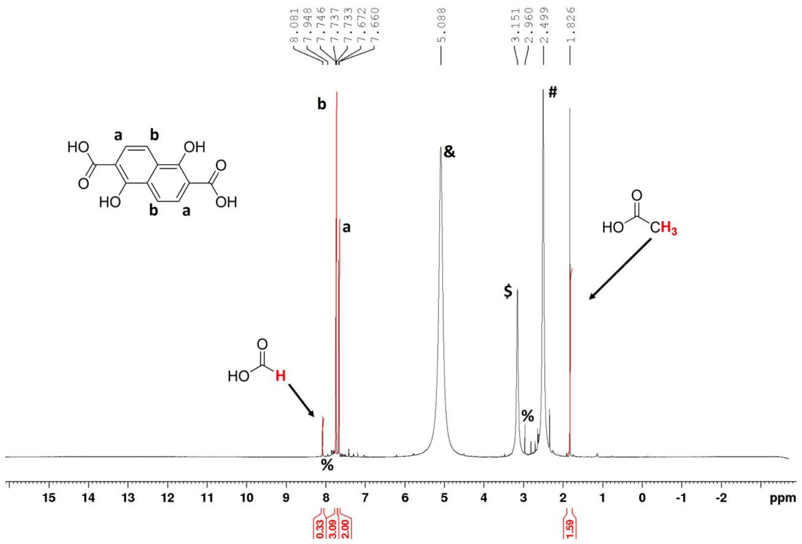

Figure S14. ^{1}H NMR Ni_2dondc diluted in a mixture of dmso-d_6 (marked with #) and DCl (20wt% in D_2O, marked with $). The signal at 5.1 ppm is a superposition of all acidic protons (-OH and -COOH groups, marked with &), stemming from a fast chemical proton exchange. Residual DMF solvent molecules are marked with %. The remaining DMF signal (methyl group) is not visible due to signal overlap. In addition, traces of formic acids are found, stemming from partial thermal decomposition of DMF during the desolvation procedure.

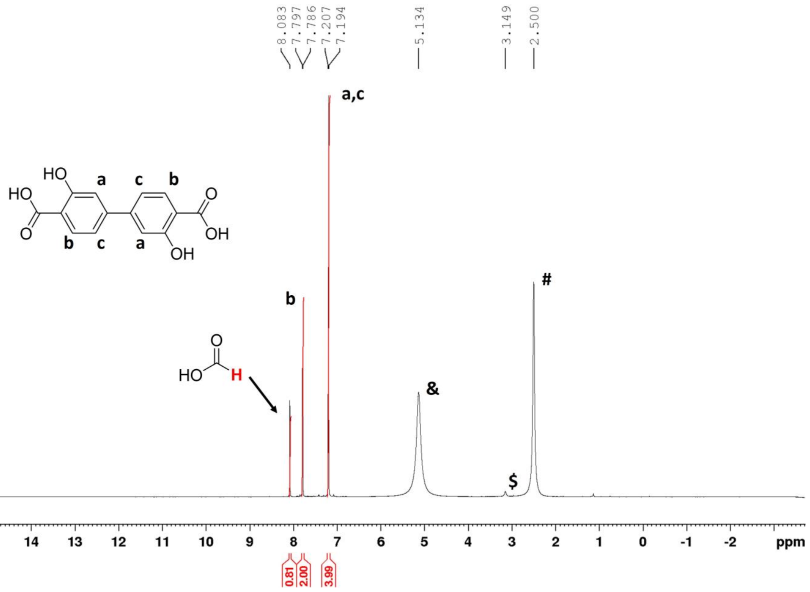

Figure S15. ^{1}H NMR Ni_2bpp diluted in a mixture of dmso-d_6 (marked with #) and DCl (20wt% in D_2O, marked with $). The signal at 5.1 ppm is a superposition of all acidic protons (-OH and -COOH groups, marked with &), stemming from a fast chemical proton exchange.

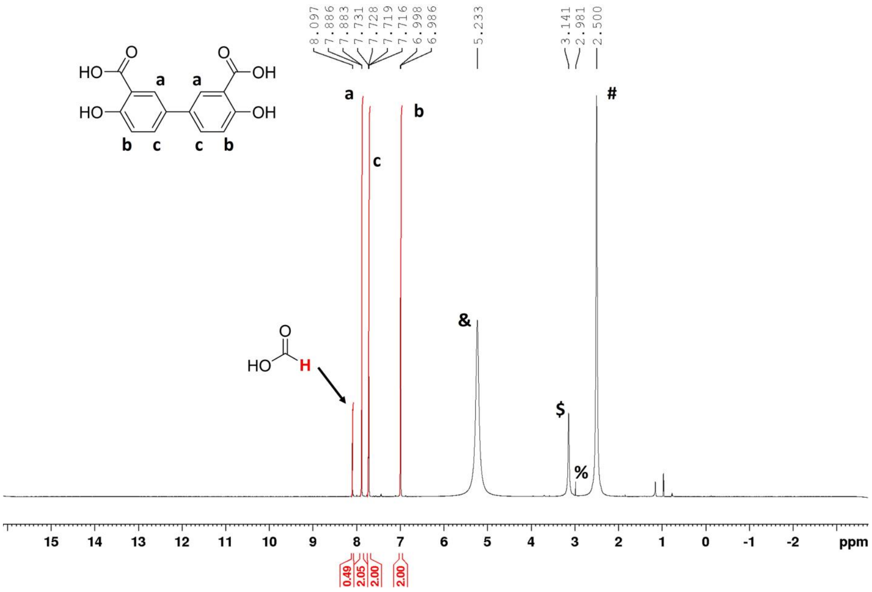

Figure S16. ^{1}H NMR Ni$_2$bpm diluted in a mixture of dmso-d$_6$ (marked with #) and DCl (20wt% in D$_2$O, marked with $). The signal at 5.1 ppm is a superposition of all acidic protons (-OH and -COOH groups, marked with &), stemming from a fast chemical proton exchange. Residual DMF solvent molecules are marked with %. The remaining two DMF signals are not visible due to signal overlap and low relative intensities.

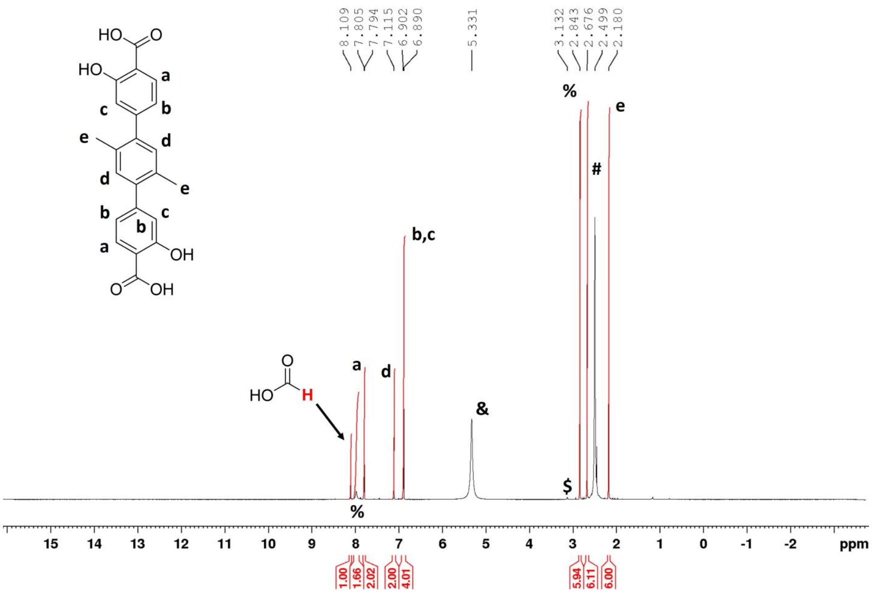

Figure S17. ^{1}H NMR Ni_2tpp diluted in a mixture of dmso-d_6 (marked with #) and DCl (20wt% in D_2O, marked with $). The signal at 5.1 ppm is a superposition of all acidic protons (-OH and -COOH groups, marked with &), stemming from a fast chemical proton exchange. Residual DMF solvent molecules are marked with %.

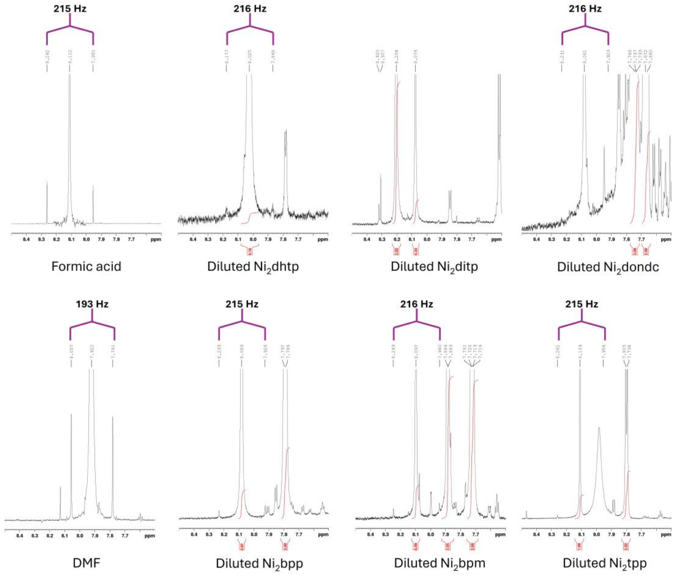

Figure S18. ^{1}H NMR of diluted Ni$_2$*L* frameworks in the region from 8.5 to 7.5 ppm in comparison with formic acid and DMF, showing the $^1J_{CH}$ coupling constants of the ^{13}C satellites, highlighting that the signal at *ca.* 8.1 originates from formate ions. No satellites were found for Ni$_2$dhip.

TGA (SUPPORTING DATA)

Table S1. Total water uptake determined from the first water mass loss step of the TGA data for hydrated Ni$_2$*L* materials.

	$n_{\text{water,TGA}}$ **(mmol g^{-1})**	$n_{\text{water,TGA}}$* **(mmol mmol^{-1} of MOF)**
Ni$_2$dhtp	20.84 ± 0.14	6.35 ± 0.93
Ni$_2$dhip	20.95 ± 2.13	6.27 ± 0.20
Ni$_2$dondc	21.14 ± 2.89	7.91 ± 0.06
Ni$_2$bpp	21.06 ± 1.48	7.16 ± 0.98
Ni$_2$bpm	24.97 ± 2.39	8.77 ± 1.13
Ni$_2$tpp	23.22 ± 1.41	9.30 ± 1.44

* based on sum formulas determined by solution ^{1}H NMR

FTIR (SUPPORTING DATA)

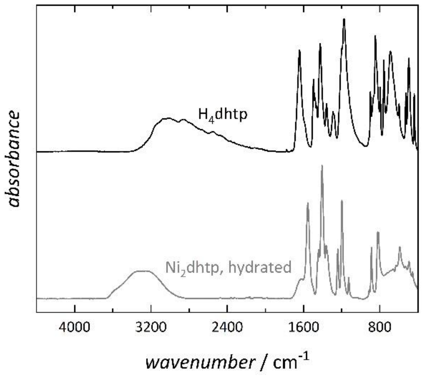

Figure S19. FTIR spectra of hydrated Ni$_2$dhtp in comparison with spectra of the H$_4$dhtp linker molecule. The spectra are normalized and vertically offset.

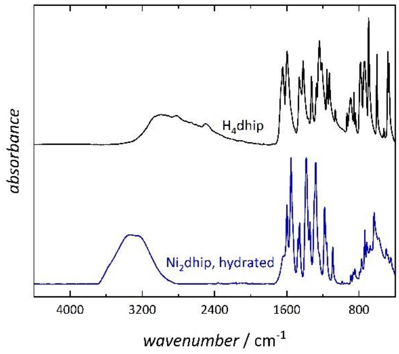

Figure S20. FTIR of hydrated Ni$_2$dhip in comparison with spectra of the H$_4$dhip linker molecule. The spectra are normalized and vertically offset.

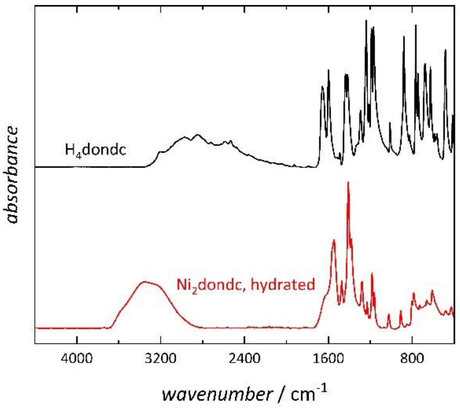

Figure S21. FTIR spectra of hydrated Ni2dondc in comparison with spectra of the H4dondc linker molecule. The spectra are normalized and vertically offset.

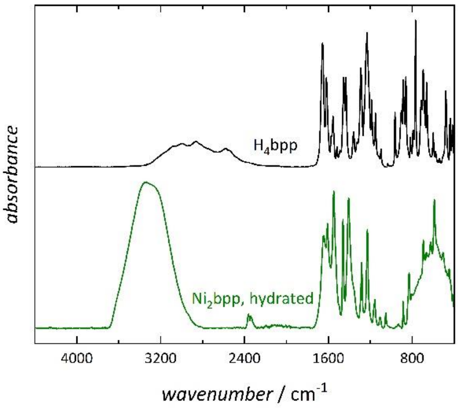

Figure S22. FTIR spectra of hydrated Ni2bpp in comparison with spectra of the H4bpp linker molecule. The spectra are normalized and vertically offset.

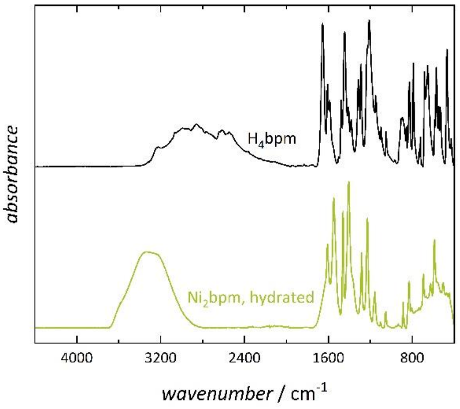

Figure S23. FTIR spectra of hydrated Ni2bpm in comparison with spectra of the H4bpm linker molecule. The spectra are normalized and vertically offset.

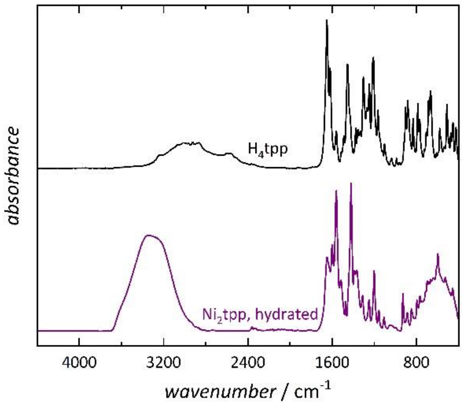

Figure S24. FTIR spectra of hydrated Ni_2tpp in comparison with spectra of the H_4tpp linker molecule. The spectra are normalized and vertically offset.

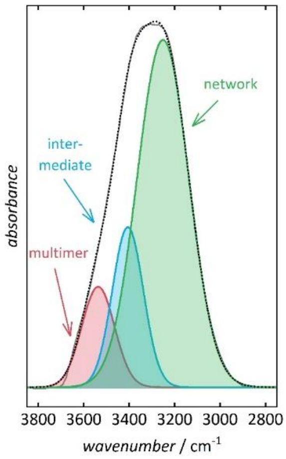

Figure S25. FTIR spectra of pure HPLC grade water, showing the three different vibrational modes of the O-H stretching vibration. The doted lines represent the cumulative fit of the three distinct water bending vibration modes.

Table S2. Results of the least-square fits, showing the contribution of the different vibrational modes to the water stretching vibration for hydrated Ni_2L materials (two or three independently synthesized samples).

	multimer water		**intermediate water**		**network water**	
	***area* / %**	***error***	***area* / %**	***error***	***area* / %**	***error***
Ni_2dhtp	5.4	0.2	21.6	0.6	73.1	0.4
Ni_2dhip	5.8	0.6	20.3	2.9	73.9	3.0
Ni_2dondc	4.8	0.1	18.1	2.3	77.1	2.3
Ni_2bpp	5.0	0.2	19.6	1.1	75.4	1.0
Ni_2bpm	5.3	1.0	17.7	1.5	77.0	1.8
Ni_2tpp	6.0	0.4	16.5	0.5	77.5	0.1
water	12.8	1.9	18.4	3.2	68.8	1.7

Table S3. Peak center positions and their errors obtained by the least-square fits of the different modes of the water stretching vibration for hydrated $Ni_2\mathit{L}$ materials (two or three independently synthesized samples).

	multimer water		**intermediate water**		**network water**	
	wavenumber / **cm^{-1}**	***error***	***wavenumber /*** **cm^{-1}**	***error***	***wavenumber /*** **cm^{-1}**	***error***
Ni_2dhtp	3565.1	0.8	3419.1	0.7	3228.9	2.4
Ni_2dhip	3573.6	0.8	3431.4	0.8	3248.2	1.6
Ni_2dondc	3573.7	0.8	3432.4	0.8	3250.7	1.5
Ni_2bpp	3574.5	1.2	3433.5	0.9	3253.4	1.4
Ni_2bpm	3573.7	1.2	3431.0	0.8	3253.1	1.3
Ni_2tpp	3571.3	1.7	3431.3	1.1	3262.2	1.5
water	3535.9	2.6	3405.8	1.3	3251.6	0.7

WATER SORPTION (SUPPORTING DATA)

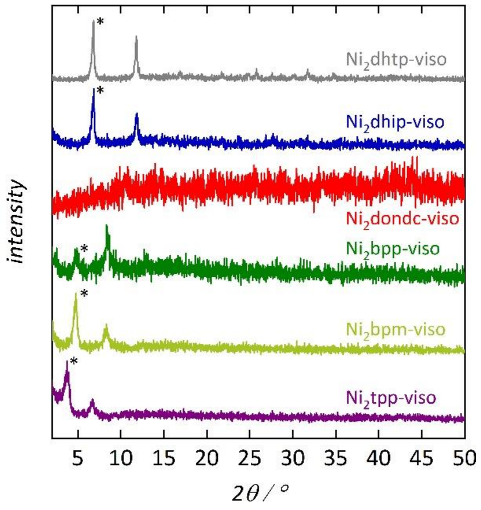

Figure S26. XRD patterns of re-isolated Ni_2L samples, previously used for water vapor sorption measurements. The (110) lattice plane is marked with an asterisk (*).

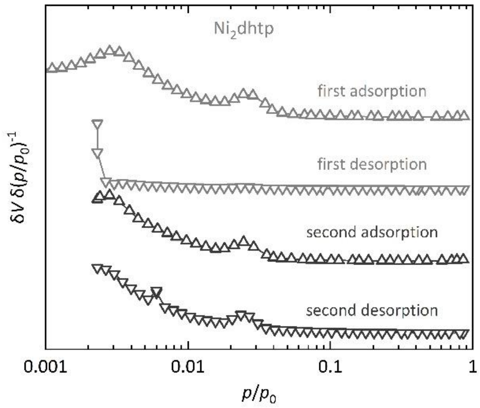

Figure S27. Normalized first derivatives (δV/δ(p/p_0)) of the water vapor sorption isotherms (25 °C) of Ni$_2$dhtp.

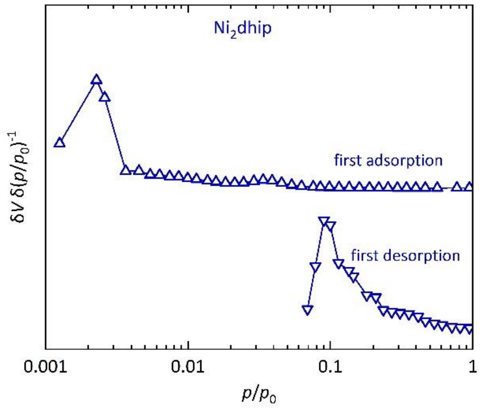

Figure S28. Normalized first derivatives (δV/δ(p/p_0)) of the water vapor sorption isotherms (25 °C) of Ni$_2$dhip.

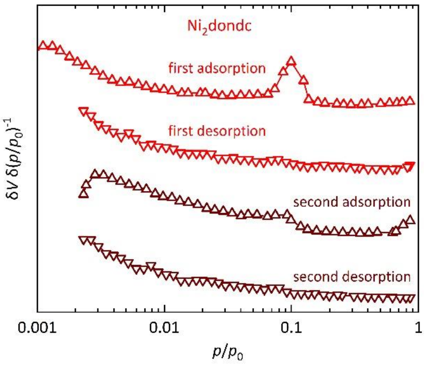

Figure S29. Normalized first derivatives (δV/δ(p/p_0)) of the water vapor sorption isotherms (25 °C) of Ni$_2$dondc.

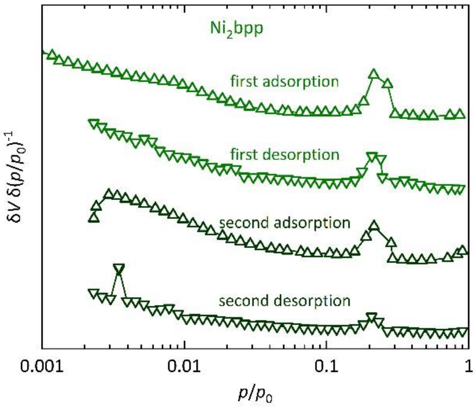

Figure S30. Normalized first derivatives (δV/δ(p/p_0)) of the water vapor sorption isotherms (25 °C) of Ni$_2$bpp.

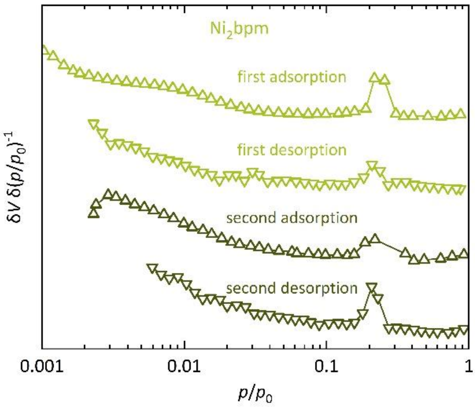

Figure S31. Normalized first derivatives (δV/δ(p/p_0)) of the water vapor sorption isotherms (25 °C) of Ni$_2$bpm.

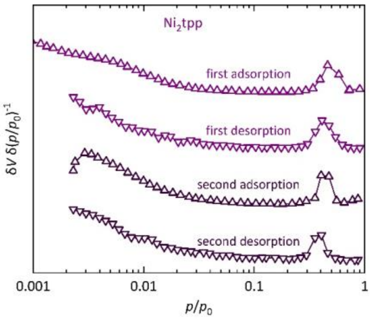

Figure S32. Normalized first derivatives (δV/δ(p/p_0)) of the water vapor sorption isotherms (25 °C) of Ni$_2$tpp.

Table S4. Determined total water uptake after the first adsorption branch $n_{\mathrm{water,total}}$ determined from water vapor sorption data.

	$n_{\mathrm{water,total}}$ **(mmol g^{-1})**	$n_{\mathrm{water,total}}$* **(mmol mmol^{-1} of MOF)**
Ni_2dhtp	29.89 ± 0.96	9.11 ± 1.34
Ni_2dhip	22.69 ± 3.27	6.92 ± 0.23
Ni_2dondc	24.13 ± 1.43	7.55 ± 0.06
Ni_2bpp	31.67 ± 1.20	10.78 ± 1.48
Ni_2bpm	41.82 ± 4.00	14.46 ± 1.86
Ni_2tpp	47.91 ± 4.04	19.19 ± 2.96

* based on sum formulas determined by solution ^{1}H NMR

Table S5. Octanol-water partition coefficients *log* (P_{OW}) of the H_4L linker molecules, obtained from the ChemDraw (*V21.0.0*) software package.

	log P_{OW}
H_4dhtp	0.37
H_4dhip	0.37
H_4dondc	1.37
H_4bpp	2.04
H_4bpm	2.04
H_4tpp	4.69

Table S6. Comparison of the maximum adsorption of the nitrogen and water sorption isotherms during the first desorption branches.

	V_{nitrogen} **(cm^3 g^{-1})**	V_{water} **(cm^3 g^{-1}) At p/p_0 0.55**	V_{water} / V_{nitrogen}
Ni_2dhtp	0.55 ± 0.07	0.48 ± 0.01	0.87 ± 0.01
Ni_2dhip	0.38 ± 0.09	0.37 ± 0.06	0.97 ± 0.17
Ni_2dondc	0.55 ± 0.03	0.36 ± 0.01	0.66 ± 0.02
Ni_2bpp	0.74 ± 0.02	0.50 ± 0.03	0.67 ± 0.04
Ni_2bpm	0.58 ± 0.02	0.62 ± 0.04	1.08 ± 0.08
Ni_2tpp	1.03 ± 0.06	0.78 ± 0.04*	0.75 ± 0.04

* pore volume determined at p/p_0 0.7

References

---

[1] Dietzel, P. D. C.; Georgiev, P. A.; Frøseth, M.; Johnsen, R. E.; Fjellvåg, H.; Blom, R. Effect of Larger Pore Size on the Sorption Properties of Isoreticular Metal–Organic Frameworks with High Number of Open Metal Sites *Chem. – A Eur. J.* **2020**, *26*, 13523–13531. 10.1002/chem.202001825.

[2] Schukraft, G. E. M.; Ayala, S.; Dick, B. L.; Cohen, S. M. Isoreticular expansion of polyMOFs achieves high surface area materials *Chem. Commun.* **2017**, 53, 10684–10687. 10.1039/C7CC04222A

[3] Zheng, J.; Vemuri, R. S.; Estevez, L.; Koech, P. K.; Varga, T.; Camaioni, D. M.; Blake, T. A.; Mcgrail, B. P.; Motkuri, R. K. Pore-Engineered Metal–Organic Frameworks with Excellent Adsorption of Water and Fluorocarbon Refrigerant for Cooling Applications *J. Am. Chem. Soc.* **2017**, *139*, 10601–10604. 10.1021/jacs.7b04872

[4] Heidary, N.; Chartrand, D.; Guiet, A.; Kornienko, N. Rational incorporation of defects within metal–organic frameworks generates highly active electrocatalytic sites *Chem. Sci.* **2021**, *12*, 7324–7333. 10.1039/D1SC00573A.

[5] Kapelewski, M. T.; Geier, S. J.; Hudson, M. R.; Stück, D.; Mason, J. A.; Nelson, J. N.; Xiao, D. J.; Hulvey, Z.; Gilmour, E.; Fitzgerald, S. A.; Head-Gordon, M.; Brown, C. M.; Long, J. R. M_2(*m*-dobdc) (M = Mg, Mn, Fe, Co, Ni) Metal–Organic Frameworks Exhibiting Increased Charge Density and Enhanced H_2 Binding at the Open Metal Sites *J. Am. Chem. Soc.* **2014**, *136*, 12119–12129. 10.1021/ja506230r

[6] Deng, H.; Grunder, S.; Cordova, K. E.; Valente, C.; Furukawa, H.; Hmadeh, M.; Gándara, F.; Whalley, A. C.; Liu, Z.; Asahina, S.; Kazumori, H.; O'Keeffe, M.; Terasaki, O.; Stoddart, J. F.; Yaghi, O. M. Large-Pore Apertures in a Series of Metal-Organic Frameworks *Science* **2012**, *336*, 1018–1023. 10.1126/science.1220131

CHAPTER 5

SUMMARY AND OUTLOOK

The water sorption behavior of MOFs proves to be a complex interplay of multiple factors such as the chemical nature of framework metal cations, pore diameter of the channels and the uniformity of the pore walls, altered by incorporated defects. Application of different experimental techniques (manometric water vapor sorption analysis, FTIR spectroscopy, TGA and NMR spectroscopy) in combination with theoretical methods (DFT and MD simulations) allows to analyze differences in the precise sorption mechanism of water into the pores of CPO-27 and isoreticular frameworks and how the water arrangement influences the materials hydrolytic stability.

5.1 Comprehensive Summary

This thesis aims to obtain a comprehensive overview on the water adsorption/desorption characteristics of CPO-27-*M* and isoreticular frameworks. Particular interest lies in the arrangement of adsorbed water molecules within the one-dimensional channels. The presented work focuses on two key-aspects: First, the influence of the incorporated metal center within the CPO-27-*M* series on the adsorption/desorption behavior and its hydrolytic stability. Second, the effect of the pore size, pore wall polarity and defect sites on the given water adsorption mechanism of different CPO-27-type materials.

In the first part of this work, the hydration behavior of CPO-27-*M* (*M* = Co, Cu, Mg, Mn, Ni, Zn), a MOF offering vacant coordination sites, *i.e.*, open metal site (OMS), as strong binding sites, is analyzed. The uptake of water into the micropores in these topologically identical framework proceeds *via* different mechanisms and is characterized by an entirely different structure of the adsorbed water. It is found that CPO-27-Zn possesses a prototypical sorption behavior. Uptake of water starts with the coordination of water to the undercoordinated Zn^{2+} center in a single step (*ca.* 20% hydration). These water molecules further serve as H-bonding anchors for the adsorption of additional water molecules, which also strongly interact with framework oxygen atoms *via* H-bonding (*ca.* 60% hydration). A continuous water layer along the pore walls is formed, with few water molecules residing in the pore center. Afterward, more water molecules adsorb, occupying positions near the pore center (*ca.* 80% hydration). This state marks a metastable conformation with water molecules freely exchanging between distinct positions. Additionally, this effect causes a pronounced hysteresis in the water sorption isotherms, being a consequence of irreversible density changes of adsorbed water. Finally, water is gradually adsorbed over a larger pressure range until complete hydration, with water molecules occupying distinct, crystal-like positions in a highly asymmetric environment.

Most other materials (*M* = Co, Mg, Mn, Ni) reveal rather comparable sorption characteristics, with the respective metal center orchestrating the adsorption behavior in the one-dimensional micropores, resulting in altered sorption steps. However, coordination of the OMS does not occur in a single step but simultaneously with the adsorption of additional molecules to chemisorbed ones. Nevertheless, the adsorption of water results in the occupation of similar sorption sites, providing comparable configurations of adsorbed water. Contrary, CPO-27-Cu reveals an entirely different behavior. Here, water does not coordinate to the metal center, but only interacts with the framework *via* H-bonding. This is a consequence of large changes in the electron density distribution and an altered coordination environment, *i.e.*, nearly square planar instead of octahedral coordination with one oxygen atom blocking the metal center, acting as a H-bonding anchor side. Pore filling is mostly accomplished in a single step (*ca.* 80% hydration), characterized by the formation of water clusters along the pore axis. These clusters provide a high degree in H-bonding, similarly to bulk water.

Further, it is found that the hydrolytic stability of CPO-27-*M* compounds is largely determined by two factors: (i) The contact time of the framework with water and (ii) the extent to which adsorbed water molecules form H-bonds with the host framework. Presence of more static water in the channels (as found for M = Zn, Mn, Co) facilitates the protonation of the linker molecules, *i.e.*, phenolate and carboxylate groups. Contrary, weaker interactions inhibit this (as found for M = Cu, Mg, Ni), yielding frameworks with higher water stability.

The second part of this thesis focuses on six CPO-27-type isoreticular frameworks with different pore sizes and pore wall polarities. Ni^{2+} based frameworks are investigated as they displayed good hydrolytic stability in previous studies. Evidence is found that defects in Ni_2dhtp play a key role for the observed sorption mechanism, affecting interactions at sorption sites near the pore wall. This suggests that selective incorporation of defect sites allows to precisely tune the water sorption properties of this framework.

Contrary, defects do not influence the hydration behavior of frameworks with larger pores (*i.e.*, Ni_2L; L = dondc, bpp, bpm, tpp). Here, adsorption of water is initiated by coordination to the OMS, acting as primary binding sites in the low-pressure range. Additional molecules adsorb thereon, resulting in the formation of distinct water clusters. Subsequently, water bridges between adjacent chemisorbed water molecules are formed to avoid the hydrophobic pore walls. This is a consequence of the dominant enthalpy term for larger hydrophobic domains (> 10 Å/1 nm) in the Gibbs hydration energy $\Delta G_{\text{hydration}}$. Formed bridges yield further H-bonding opportunities, facilitating the adsorption process. As a result, classical pore condensation is observed in a single step, with the pressure range depending on the pore size and the hydrophobic domain size, confirming previous results on other MOFs. As for CPO-27-*M*, gradual adsorption of water proceeds over a larger pressure range until complete hydration.

In general, H-bonding of adsorbed water in CPO-27-type frameworks is more asymmetric than found for bulk water. However, this effect is more pronounced in smaller pores, consistent with the expectation of water molecules located at defined positions with highly directed water-framework interactions in fully hydrated frameworks (as found for Ni_2dhtp and Ni_2dondc). This leads to high-entropy water arrangements near the hydrophobic surface, resulting from the entropy-driven $\Delta G_{\text{hydration}}$, typically found for small hydrophobic domains (< 10 Å/1 nm). With increasing pore size, water molecules adopt a more symmetric H-bonding environment with dominating contributions of water-water interactions. Thus, a more bulk-like state is observed, being a consequence of the less confined environment.

5.2 Outlook

Following the results of this thesis, further investigations on the effect of defect sites in CPO-27 frameworks are needed in order to verify the assumption that the water sorption mechanism can be precisely modified. This can be accomplished by selective incorporation of linker molecules with missing functional groups or by altered synthetic procedures. Previous studies on mixed-metal CPO-27 reveal better hydrolytic stabilities, indicating different water arrangements and consequently, altered sorption properties. Hence, additional studies should focus on the effects of multiple metal centers in CPO-27, providing more information, enabling to modify the hydrolytic stability of these materials. Finally, modification of the pore wall surface in CPO-27-type frameworks should be considered. This may, like observed for mesoporous silica, positively influence the water-adsorbent interactions, resulting in different water arrangements.

BIBLIOGRAPHY

[1] C. Janiak, J. K. Vieth, *New J. Chem.* **2010**, *34*(11), 2366.

[2] F. Ahmadijokani, H. Molavi, M. Rezakazemi, S. Tajahmadi, A. Bahi, F. Ko, T. M. Aminabhavi, J. R. Li, M. Arjmand, *Prog. Mater. Sci.* **2022**, *125*, 100904.

[3] J. Liu, Y. Wang, *Molecules* **2023**, *28*(5), 2141.

[4] A. Kathuria, A. El Badawy, S. Al-Ghamdi, L. S. Hamachi, M. B. Kivy, *Trends Food Sci. Technol.* **2023**, *138*, 323–338.

[5] T. M. McDonald, W. R. Lee, J. A. Mason, B. M. Wiers, C. S. Hong, J. R. Long, *J. Am. Chem. Soc.* **2012**, *134*(16), 7056–7065.

[6] C. A. Trickett, A. Helal, B. A. Al-Maythalony, Z. H. Yamani, K. E. Cordova, O. M. Yaghi, *Nat. Rev. Mater.* **2017**, *2*(8), 17045.

[7] J. Liu, L. Chen, H. Cui, J. Zhang, L. Zhang, C. Y. Su, *Chem. Soc. Rev.* **2014**, *43*(16), 6011–6061.

[8] S. M. Rogge, A. Bavykina, J. Hajek, H. Garcia, A. I. Olivos-Suarez, A. Sepúlveda-Escribano, A. Vimont, G. Clet, P. Bazin, F. Kapteijn, M. Daturi, E. V. Ramos-Fernandez, F. X. Llabrés Xamena, V. Van Speybroeck, J. Gascon, *Chem. Soc. Rev.* **2017**, *46*(11), 3134–3184.

[9] Y. S. Wei, M. Zhang, R. Zou, Q. Xu, *Chem. Rev.* **2020**, *120*(21), 12089–12174.

[10] M. J. Kalmutzki, C. S. Diercks, O. M. Yaghi, *Adv. Mater.* **2018**, *30*(37), 1704304.

[11] N. Hanikel, M. S. Prévot, O. M. Yaghi, *Nat. Nanotechnol.* **2020**, *15*(5), 348–355.

[12] P. D. Dietzel, Y. Morita, R. Blom, H. Fjellvåg, *Angew. Chem. Int. Ed.* **2005**, *44*(39), 6354–6358.

[13] N. L. Rosi, J. Kim, M. Eddaoudi, B. Chen, M. O'Keeffe, O. M. Yaghi, *J. Am. Chem. Soc.* **2005**, *127*(5), 1504–1518.

[14] M. Díaz-García, M. Sánchez-Sánchez, *Microporous Mesoporous Mater.* **2014**, *190*, 248–254.

[15] J. Zheng, R. S. Vemuri, L. Estevez, P. K. Koech, T. Varga, D. M. Camaioni, T. A. Blake, B. P. Mcgrail, R. K. Motkuri, *J. Am. Chem. Soc.* **2017**, *139*(31), 10601–10604.

[16] G. Calleja, R. Sanz, G. Orcajo, D. Briones, P. Leo, F. Martínez, *Catal. Today* **2014**, *227*, 130–137.

[17] E. D. Bloch, L. J. Murray, W. L. Queen, S. Chavan, S. N. Maximoff, J. P. Bigi, R. Krishna, V. K. Peterson, F. Grandjean, G. J. Long, B. Smit, S. Bordiga, C. M. Brown, J. R. Long, *J. Am. Chem. Soc.* **2011**, *133*(37), 14814–14822.

[18] M. Märcz, R. E. Johnsen, P. D. Dietzel, H. Fjellvåg, *Microporous Mesoporous Mater.* **2012**, *157*, 62–74.

[19] P. D. Dietzel, R. Blom, H. Fjellvåg, *Eur. J. Inorg. Chem.* **2008**, (23), 3624–3632.

[20] W. Zhou, H. Wu, T. Yildirim, *J. Am. Chem. Soc.* **2008**, *130*(46), 15268–15269.

[21] P. D. Dietzel, B. Panella, M. Hirscher, R. Blom, H. Fjellvåg, *Chem. Commun.* **2006**, (9), 959–961.

[22] Ü. Kökçam-Demir, A. Goldman, L. Esrafili, M. Gharib, A. Morsali, O. Weingart, C. Janiak, *Chem. Soc. Rev.* **2020**, *49*(9), 2751–2798.

[23] L. J. Wang, H. Deng, H. Furukawa, F. Gándara, K. E. Cordova, D. Peri, O. M. Yaghi, *Inorg. Chem.* **2014**, *53*(12), 5881–5883.

[24] S. Li, *J. Porous Mater.* **2023**, *30*(2), 421–432.

[25] N. E. El-Gamel, *Eur. J. Inorg. Chem.* **2015**, *2015*(8), 1351–1358.

[26] D. Wu, W. Yan, H. Xu, E. Zhang, Q. Li, *Inorganica Chim. Acta* **2017**, *460*, 93–98.

[27] J. A. Villajos, N. Jagorel, S. Reinsch, F. Emmerling, *Front. Mater.* **2019**, *6*, 230.

[28] J. Lim, S. Lee, A. Sharma, J. Seong, S. B. Baek, M. S. Lah, *RSC Adv.* **2022**, *12*(48), 31451–31455.

[29] A. C. Kizzie, A. G. Wong-Foy, A. J. Matzger, *Langmuir* **2011**, *27*(10), 6368–6373.

[30] A. A. Voskanyan, A. A. Voskanyan, V. G. Goncharov, N. Novendra, X. Guo, A. Navrotsky, A. Navrotsky, *ACS Omega* **2020**, *5*(22), 13158–13163.

[31] B. Shi, R. AL-Dadah, S. Mahmoud, A. Elsayed, E. Elsayed, *Appl. Therm. Eng.* **2016**, *106*, 325–333.

[32] J. B. Decoste, G. W. Peterson, B. J. Schindler, K. L. Killops, M. A. Browe, J. J. Mahle, *J. Mater. Chem. A* **2013**, *1*(38), 11922–11932.

[33] S. S. Han, S.-H. Choi, A. C. T. van Duin, *Chem. Commun.* **2010**, *46*(31), 5713.

[34] Y. Jiao, C. R. Morelock, N. C. Burtch, W. P. Mounfield, J. T. Hungerford, K. S. Walton, *Ind. Eng. Chem. Res.* **2015**, *54*(49), 12408–12414.

[35] J. Liu, Y. Tan, E. Shen, B. Liu, Y. Tian, L. Liang, X. Yan, H. Wu, *Biomed. Mater.* **2022**, *17*(6), 065026.

[36] L. Valenzano, B. Civalleri, S. Chavan, G. T. Palomino, C. O. Areán, S. Bordiga, *J. Phys. Chem. C* **2010**, *114*(25), 11185–11191.

[37] K. Lee, J. D. Howe, L.-C. C. Lin, B. Smit, J. B. Neaton, *Chem. Mater.* **2015**, *27*(3), 668–678.

[38] T. Pham, K. A. Forrest, J. Eckert, B. Space, *Cryst. Growth Des.* **2016**, *16*(2), 867–874.

[39] X. Peng, L. Lin, W. Sun, B. Smit, *AIChE J.* **2015**, *61*(2), 677–687.

[40] P. D. Dietzel, R. E. Johnsen, R. Blom, H. Fjellvåg, *Chem. Eur. J.* **2008**, *14*(8), 2389–2397.

[41] M. H. Rosnes, B. Pato-Doldán, R. E. Johnsen, A. Mundstock, J. Caro, P. D. Dietzel, *Microporous Mesoporous Mater.* **2020**, *309*, 110503.

[42] O. M. Yaghi, M. O'Keeffe, N. W. Ockwig, H. K. Chae, M. Eddaoudi, J. Kim, *Nature* **2003**, *423*(6941), 705–714.

[43] O. M. Yaghi, M. J. Kalmutzki, C. S. Diercks, *Introduction to Reticular Chemistry*, Wiley-VCH, **2019**.

[44] A. Schoedel, M. Li, D. Li, M. O'Keeffe, O. M. Yaghi, *Chem. Rev.* **2016**, *116*, 12466–12535.

[45] R. Banerjee, A. Phan, B. Wang, C. Knobler, H. Furukawa, M. O'Keeffe, O. M. Yaghi, *Science* **2008**, *319*(5865), 939–943.

[46] C. Férey, C. Mellot-Draznieks, C. Serre, F. Millange, J. Dutour, S. Surblé, I. Margiolaki, *Science* **2005**, *309*(5743), 2040–2042.

[47] S. S.-Y. Chui, S. M.-F. Lo, J. P. H. Charmant, A. G. Orpen, I. D. Williams, *Science* **1999**, *283*(5405), 1148–1150.

[48] D. N. Dybtsev, H. Chun, K. Kim, *Angew. Chem. Int. Ed.* **2004**, *43*(38), 5033–5036.

[49] M. O. Keeffe, M. A. Peskov, S. J. Ramsden, O. M. Yaghi, *Acc. Chem. Res.* **2008**, *41*(12), 1782–1789.

[50] D. Zhao, D. J. Timmons, D. Yuan, H.-C. Zhou, *Acc. Chem. Res.* **2011**, *44*(2), 123–133.

[51] M. Eddaoudi, J. Kim, N. Rosi, D. Vodak, J. Wachter, M. O'Keeffe, O. M. Yaghi, *Science* **2002**, *295*(5554), 469–472.

[52] S. T. Meek, J. J. Perry, S. L. Teich-McGoldrick, J. A. Greathouse, M. D. Allendorf, *Cryst. Growth Des.* **2011**, *11*(10), 4309–4312.

[53] V. Guillerm, F. Ragon, M. Dan-Hardi, T. Devic, M. Vishnuvarthan, B. Campo, A. Vimont, G. Clet, Q. Yang, G. Maurin, G. Férey, A. Vittadini, S. Gross, C. Serre, *Angew. Chem. Int. Ed.* **2012**, *51*(37), 9267–9271.

[54] S. Henke, A. Schneemann, A. Wütscher, R. A. Fischer, *J. Am. Chem. Soc.* **2012**, *134*(22), 9464–9474.

[55] L. Frentzel-Beyme, M. Kloß, P. Kolodzeiski, R. Pallach, S. Henke, *J. Am. Chem. Soc.* **2019**, *141*(31), 12362–12371.

[56] R. Pallach, J. Keupp, K. Terlinden, L. Frentzel-Beyme, M. Kloß, A. Machalica, J. Kotschy, S. K. Vasa, P. A. Chater, C. Sternemann, M. T. Wharmby, R. Linser, R. Schmid, S. Henke, *Nat. Commun.* **2021**, *12*(1), 4097.

[57] H. Deng, S. Grunder, K. E. Cordova, C. Valente, H. Furukawa, M. Hmadeh, F. Gándara, A. C. Whalley, Z. Liu, S. Asahina, H. Kazumori, M. O'Keeffe, O. Terasaki, J. F. Stoddart, O. M. Yaghi, *Science* **2012**, *336*(6084), 1018–1023.

[58] L. Frentzel-Beyme, M. Kloß, R. Pallach, S. Salamon, H. Moldenhauer, J. Landers, H. Wende, J. Debus, S. Henke, *J. Mater. Chem. A* **2019**, *7*(3), 985–990.

[59] P. D. Dietzel, P. A. Georgiev, M. Frøseth, R. E. Johnsen, H. Fjellvåg, R. Blom, *Chem. – A Eur. J.* **2020**, *26*(59), 13523–13531.

[60] A. Gheorghe, S. Reus, M. Koenis, D. Dubbeldam, S. Woutersen, S. Tanase, *Dalton Trans.* **2021**, *50*(35), 12159–12167.

[61] S. Peng, B. Bie, H. Jia, H. Tang, X. Zhang, Y. Sun, Q. Wei, F. Wu, Y. Yuan, H. Deng, X. Zhou, *J. Am. Chem. Soc.* **2020**, *142*(11), 5049–5059.

[62] J. Zheng, D. Barpaga, B. A. Trump, M. Shetty, Y. Fan, P. Bhattacharya, J. J. Jenks, C. Y. Su, C. M. Brown, G. Maurin, B. P. McGrail, R. K. Motkuri, *J. Am. Chem. Soc.* **2020**, *142*(6), 3002–3012.

[63] H. Montes-Andrés, G. Orcajo, C. Martos, J. A. Botas, G. Calleja, *Int. J. Hydrogen Energy* **2019**, *44*(33), 18205–18213.

[64] M. T. Kapelewski, S. J. Geier, M. R. Hudson, D. Stück, J. A. Mason, J. N. Nelson, D. J. Xiao, Z. Hulvey, E. Gilmour, S. A. Fitzgerald, M. Head-Gordon, C. M. Brown, J. R. Long, *J. Am. Chem. Soc.* **2014**, *136*(34), 12119–12129.

[65] D. Gygi, E. D. Bloch, J. A. Mason, M. R. Hudson, M. I. Gonzalez, R. L. Siegelman, T. A. Darwish, W. L. Queen, C. M. Brown, J. R. Long, *Chem. Mater.* **2016**, *28*(4), 1128–1138.

[66] A. C. Forse, M. I. Gonzalez, R. L. Siegelman, V. J. Witherspoon, S. Jawahery, R. Mercado, P. J. Milner, J. D. Martell, B. Smit, B. Blümich, J. R. Long, J. A. Reimer, *J. Am. Chem. Soc.* **2018**, *140*(5), 1663–1673.

[67] G. Q. Lu, X. S. Zhao, „Nanoporous materials - An Overview“ in *Nanoporous Materials - Science and Engineering*, Imperial College Press, **2004**, S. 1–13.

[68] J. Canivet, A. Fateeva, Y. Guo, B. Coasne, D. Farrusseng, *Chem. Soc. Rev.* **2014**, *43*(16), 5594–5617.

[69] T. Wagner, S. Haffer, C. Weinberger, D. Klaus, M. Tiemann, *Chem. Soc. Rev.* **2013**, *42*(9), 4036–4053.

[70] W. K. Han, W. Yuan, Z. G. Gu, Y. Zhao, *ACS Mater. Lett.* **2024**, *6*(6), 2276–2294.

[71] Q. Sun, B. Aguila, Y. Song, S. Ma, *Acc. Chem. Res.* **2020**, *53*(4), 812–821.

[72] A. Javed, I. Strauss, H. Bunzen, J. Caro, M. Tiemann, *Nanomaterials* **2020**, *10*(7), 1263.

[73] L. Feng, S. Bian, K. Zhang, H. Zhou, *Dalton Trans.* **2022**, *51*(36), 13742–13748.

[74] K. Geng, T. He, R. Liu, S. Dalapati, K. T. Tan, Z. Li, S. Tao, Y. Gong, Q. Jiang, D. Jiang, *Chem. Rev.* **2020**, *120*(16), 8814–8933.

[75] D. J. Wales, J. Grand, V. P. Ting, R. D. Burke, K. J. Edler, C. R. Bowen, S. Mintova, A. D. Burrows, *Chem. Soc. Rev.* **2015**, *44*(13), 4290–4321.

[76] H. Kim, S. R. Rao, E. A. Kapustin, L. Zhao, S. Yang, O. M. Yaghi, E. N. Wang, *Nat. Commun.* **2018**, *9*(1), 1–8.

[77] N. Hanikel, M. S. Prévot, F. Fathieh, E. A. Kapustin, H. Lyu, H. Wang, N. J. Diercks, T. G. Glover, O. M. Yaghi, *ACS Cent. Sci.* **2019**, *5*(10), 1699–1706.

[78] M. F. De Lange, K. J. Verouden, T. J. Vlugt, J. Gascon, F. Kapteijn, *Chem. Rev.* **2015**, *115*(22), 12205–12250.

[79] R. AL-Dadah, S. Mahmoud, E. Elsayed, P. Youssef, F. Al-Mousawi, *Energy* **2020**, *190*, 116356.

[80] M. Tiemann, *Chem. Eur. J.* **2007**, *13*(30), 8376–8388.

[81] J. Zhang, Y. Tan, W.-J. Song, *Microchim. Acta* **2020**, *187*(4), 234.

[82] R. E. Morris, P. S. Wheatley, *Angew. Chem. Int. Ed.* **2008**, *47*(27), 4966–4981.

[83] Z. Chang, D. S. Zhang, Q. Chen, X. H. Bu, *Phys. Chem. Chem. Phys.* **2013**, *15*(15), 5430–5442.

[84] X. Yang, Q. Xu, *Cryst. Growth Des.* **2017**, *17*(4), 1450–1455.

[85] K. S. Song, D. Kim, A. Coskun, *ACS Appl. Nano Mater.* **2020**, *3*(2), 985–991.

[86] P. Vervoorts, A. Schneemann, I. Hante, J. Pirillo, Y. Hijikata, T. Toyao, K. Kon, K. I. Shimizu, T. Nakamura, S. I. Noro, R. A. Fischer, *ACS Appl. Mater. Interfaces* **2020**, *12*(8), 9448–9456.

[87] U. Böhme, B. Barth, C. Paula, A. Kuhnt, W. Schwieger, A. Mundstock, J. Caro, M. Hartmann, *Langmuir* **2013**, *29*(27), 8592–8600.

[88] A. Corma, H. García, F. X. Llabrés I Xamena, *Chem. Rev.* **2010**, *110*(8), 4606–4655.

[89] M. Bhadra, H. S. Sasmal, A. Basu, S. P. Midya, S. Kandambeth, P. Pachfule, E. Balaraman, R. Banerjee, *ACS Appl. Mater. Interfaces* **2017**, *9*(15), 13785–13792.

[90] Y. S. Bae, C. Y. Lee, K. C. Kim, O. K. Farha, P. Nickias, J. T. Hupp, S. T. Nguyen, R. Q. Snurr, *Angew. Chem. Int. Ed.* **2012**, *51*(8), 1857–1860.

[91] K. Tan, N. Nijem, P. Canepa, Q. Gong, J. Li, T. Thonhauser, Y. J. Chabal, *Chem. Mater.* **2012**, *24*(16), 3153–3167.

[92] K. Tan, N. Nijem, Y. Gao, S. Zuluaga, J. Li, T. Thonhauser, Y. J. Chabal, *CrystEngComm* **2015**, *17*(2), 247–260.

[93] Y. Li, T. Jin, G. Ma, Y. Li, L. Fan, X. Li, *Dalton Trans.* **2019**, *48*(17), 5649–5655.

[94] J. F. Young, *J. Appl. Chem.* **1967**, *17*(9), 241–245.

[95] P. P. Lewicki, W. Pomaranska-Lazuka, *Int. J. Food Prop.* **2003**, *6*(3), 557–563.

[96] S. J. Schmidt, J. W. Lee, *Int. J. Food Prop.* **2012**, *15*(2), 236–248.

[97] S. L. Zelinka, K. J. Bourne, S. V. Glass, C. R. Boardman, L. Lorenz, E. E. Thybring, *Wood Fiber Sci.* **2018**, *50*(3), 244–253.

[98] X. Ma, W. Shen, X. Li, Y. Hu, X. Liu, X. Lu, *Sci. Rep.* **2020**, *10*(1), 1–12.

[99] S. Gal, „Recent Developments in Techniques for Obtaining Complete Sorption Isotherms“ in *Water Act. Influ. Food Qual.*, Academic Press, **1981**, S. 89–110.

[100] M.-B. Kim, Y.-K. Ryu, C.-H. Lee, *J. Chem. Eng. Data* **2005**, *50*(3), 951–955.

[101] Y. Wang, M. D. LeVan, *J. Chem. Eng. Data* **2009**, *54*(10), 2839–2844.

[102] H. Furukawa, F. Gándara, Y. B. Zhang, J. Jiang, W. L. Queen, M. R. Hudson, O. M. Yaghi, *J. Am. Chem. Soc.* **2014**, *136*(11), 4369–4381.

[103] K.-M. Kim, H.-T. Oh, S.-J. Lim, K. Ho, Y. Park, C.-H. Lee, *J. Chem. Eng. Data* **2016**, *61*(4), 1547–1554.

[104] K. N. Son, T.-M. J. Richardson, G. E. Cmarik, *J. Chem. Eng. Data* **2019**, *64*(3), 1063–1071.

[105] E.-P. Ng, S. Mintova, *Microporous Mesoporous Mater.* **2008**, *114*(1-3), 1–26.

[106] M. Thommes, K. Kaneko, A. V. Neimark, J. P. Olivier, F. Rodriguez-Reinoso, J. Rouquerol, K. S. Sing, *Pure Appl. Chem.* **2015**, *87*(9-10), 1051–1069.

[107] A. Metrane, A. Delhali, M. Ouikhalfan, A. H. Assen, Y. Belmabkhout, *J. Chem. Eng. Data* **2022**, *67*(7), 1617–1653.

[108] L. Liu, S. J. Tan, T. Horikawa, D. Do, D. Nicholson, J. Liu, *Adv. Colloid Interface Sci.* **2017**, *250*, 64–78.

[109] M. Nakamura, T. Ohba, P. Branton, H. Kanoh, K. Kaneko, *Carbon* **2010**, *48*(1), 305–308.

[110] T. Ohba, K. Kaneko, *Langmuir* **2011**, *27*(12), 7609–7613.

[111] A. M. Ribeiro, T. P. Sauer, C. A. Grande, R. F. P. M. Moreira, J. M. Loureiro, A. E. Rodrigues, *Ind. Eng. Chem. Res.* **2008**, *47*(18), 7019–7026.

[112] T. Horikawa, T. Muguruma, D. Do, K.-I. Sotowa, J. R. Alcántara-Avila, *Carbon* **2015**, *95*, 137–143.

[113] M. Thommes, J. Morell, K. A. Cychosz, M. Fröba, *Langmuir* **2013**, *29*(48), 14893–14902.

[114] T. Ohba, H. Kanoh, K. Kaneko, *J. Phys. Chem. B* **2004**, *108*(39), 14964–14969.

[115] L. Liu, W. Zeng, S. J. Tan, M. Liu, D. D. Do, *Phys. Chem. Chem. Phys.* **2021**, *23*(34), 18369–18377.

[116] C. Wang, Y. Xing, Y. Lei, Y. Xia, C. Zhang, R. Zhang, S. Wang, P. Chen, S. Zhu, J. Li, X. Gui, *Colloids Surfaces A* **2021**, *631*, 127719.

[117] H. Moon, R. P. Collanton, J. I. Monroe, T. M. Casey, M. S. Shell, S. Han, S. L. Scott, *J. Am. Chem. Soc.* **2022**, *144*(4), 1766–1777.

[118] S. K. Henninger, F. Jeremias, H. Kummer, P. Schossig, H.-M. Henning, *Energy Procedia* **2012**, *30*, 279–288.

[119] J. S. Oh, W. G. Shim, J. W. Lee, J. H. Kim, H. Moon, G. Seo, *J. Chem. Eng. Data* **2003**, *48*(6), 1458–1462.

[120] Q. Li, Y. Zhou, *Molecules* **2023**, *28*(5), 2013.

[121] C. Weinberger, F. Zysk, M. Hartmann, N. K. Kaliannan, W. Keil, T. D. Kühne, M. Tiemann, *Adv. Mater. Interfaces* **2022**, *9*(20), 2200245.

[122] H. Naono, M. Hakuman, T. Tanaka, N. Tamura, K. Nakai, *J. Colloid Interface Sci.* **2000**, *225*(2), 411–420.

[123] A. Han, Y. Qiao, *J. Phys. D. Appl. Phys.* **2007**, *40*(18), 5743–5746.

[124] C. Yoshina-Ishii, T. Asefa, N. Coombs, M. J. MacLachlan, G. A. Ozin, *Chem. Commun.* **1999**, (24), 2539–2540.

[125] F. Hoffmann, M. Cornelius, J. Morell, M. Fröba, *Angew. Chem. Int. Ed.* **2006**, *45*(20), 3216–3251.

[126] S. Inagaki, Y. Fukushima, *Microporous Mesoporous Mater.* **1998**, *21*(4-6), 667–672.

[127] H. Sohrabi, S. Ghasemzadeh, S. Shakib, M. R. Majidi, A. Razmjou, Y. Yoon, A. Khataee, *Ind. Eng. Chem. Res.* **2023**, *62*(11), 4611–4627.

[128] S. F. Lincoln, *Helv. Chim. Acta* **2005**, *88*(3), 523–545.

[129] M. Zou, M. Dong, T. Zhao, *Int. J. Mol. Sci.* **2022**, *23*(16), 9396.

[130] G. Akiyama, R. Matsuda, H. Sato, A. Hori, M. Takata, S. Kitagawa, *Microporous Mesoporous Mater.* **2012**, *157*, 89–93.

[131] G. Férey, C. Serre, C. Mellot-Draznieks, F. Millange, S. Surblé, J. Dutour, I. Margiolaki, *Angew. Chem. Int. Ed.* **2004**, *43*(46), 6296–6301.

[132] P. G. Mileo, K. Ho Cho, J. Park, S. Devautour-Vinot, J. S. Chang, G. Maurin, *J. Phys. Chem. C* **2019**, *123*(37), 23014–23025.

[133] F.-F. Lu, X.-W. Gu, E. Wu, B. Li, G. Qian, *J. Mater. Chem. A* **2023**, *11*(3), 1246–1255.

[134] J. H. Cavka, S. Jakobsen, U. Olsbye, N. Guillou, C. Lamberti, S. Bordiga, K. P. Lillerud, *J. Am. Chem. Soc.* **2008**, *130*(42), 13850–13851.

[135] F. Yang, H. Huang, X. Wang, F. Li, Y. Gong, C. Zhong, J. R. Li, *Cryst. Growth Des.* **2015**, *15*(12), 5827–5833.

[136] W. J. Phang, H. Jo, W. R. Lee, J. H. Song, K. Yoo, B. Kim, C. S. Hong, *Angew. Chem. Int. Ed.* **2015**, *54*(17), 5142–5146.

[137] W. Zhang, H. Huang, D. Liu, Q. Yang, Y. Xiao, Q. Ma, C. Zhong, *Microporous Mesoporous Mater.* **2013**, *171*, 118–124.

[138] N. X. Zhu, Z. W. Wei, C. X. Chen, X. H. Xiong, Y. Y. Xiong, Z. Zeng, W. Wang, J. J. Jiang, Y. N. Fan, C. Y. Su, *Angew. Chem. Int. Ed.* **2022**, *61*(4).

[139] T. Grant Glover, G. W. Peterson, B. J. Schindler, D. Britt, O. Yaghi, *Chem. Eng. Sci.* **2011**, *66*(2), 163–170.

[140] H. Y. Cho, D. A. Yang, J. Kim, S. Y. Jeong, W. S. Ahn, *Catal. Today* **2012**, *185*, 35–40.

[141] P. M. Schoenecker, C. G. Carson, H. Jasuja, C. J. J. Flemming, K. S. Walton, *Ind. Eng. Chem. Res.* **2012**, *51*(18), 6513–6519.

[142] D. A. Yang, H. Y. Cho, J. Kim, S. T. Yang, W. S. Ahn, *Energy Environ. Sci.* **2012**, *5*(4), 6465–6473.

[143] E. Elsayed, R. AL-Dadah, S. Mahmoud, P. A. Anderson, A. Elsayed, P. G. Youssef, *Desalination* **2017**, *406*, 25–36.

[144] Y. Gong, C. Chen, R. P. Lively, K. S. Walton, *Ind. Eng. Chem. Res.* **2021**, *60*(27), 9940–9947.

[145] Y. Li, X. Wang, D. Xu, J. D. Chung, M. Kaviany, B. Huang, *J. Phys. Chem. C* **2015**, *119*(23), 13021–13031.

[146] M. G. Lopez, P. Canepa, T. Thonhauser, *J. Chem. Phys.* **2013**, *138*(15), 154704.

[147] P. W. Siu, Z. J. Brown, O. K. Farha, J. T. Hupp, K. A. Scheidt, *Chem. Commun.* **2013**, *49*(93), 10920.

[148] M. Yoshizawa, M. Tamura, M. Fujita, *Science* **2006**, *312*(5771), 251–254.

[149] S. Kowalak, A. Jankowska, *Microporous Mesoporous Mater.* **2003**, *61*(1-3), 213–222.

[150] J.-M. Lehn, *Science* **1993**, *260*(5115), 1762–1763.

[151] J. Jiou, K. Chiravuri, A. Gudapati, J. Gassensmith, *Curr. Org. Chem.* **2014**, *18*(15), 2002–2009.

[152] K. B. Jinesh, J. W. M. Frenken, *Phys. Rev. Lett.* **2008**, *101*(3), 036101.

[153] A. Vila Verde, R. Lipowsky, *J. Phys. Chem. B* **2013**, *117*(36), 10556–10566.

[154] S. Takahara, S. Kittaka, T. Mori, Y. Kuroda, T. Yamaguchi, M.-C. Bellissent-Funel, *Adsorption* **2005**, *11*(S1), 479–483.

[155] A. Lerbret, G. Lelong, P. E. Mason, M.-L. Saboungi, J. W. Brady, *Food Biophys.* **2011**, *6*(2), 233–240.

[156] U. Raviv, P. Laurat, J. Klein, *Nature* **2001**, *413*(6851), 51–54.

[157] E. A. Jagla, *Phys. Rev. Lett.* **2002**, *88*(24), 245504.

[158] Y.-C. Liu, Q. Wang, L.-H. Lu, *Chem. Phys. Lett.* **2003**, *381*(1-2), 210–215.

[159] S. Chakraborty, H. Kumar, C. Dasgupta, P. K. Maiti, *Acc. Chem. Res.* **2017**, *50*(9), 2139–2146.

[160] J. B. Mietner, F. J. Brieler, Y. J. Lee, M. Fröba, *Angew. Chem. Int. Ed.* **2017**, *56*(40), 12348–12351.

[161] K. Lum, D. Chandler, J. D. Weeks, *J. Phys. Chem. B* **1999**, *103*(22), 4570–4577.

[162] D. M. Huang, D. Chandler, *Proc. Natl. Acad. Sci. U. S. A.* **2000**, *97*(15), 8324–8327.

[163] D. M. Huang, P. L. Geissler, D. Chandler, *J. Phys. Chem. B* **2001**, *105*(28), 6704–6709.

[164] C. Yang, X. Wang, M. A. Omary, *J. Am. Chem. Soc.* **2007**, *129*(50), 15454–15455.

[165] N. Nijem, P. Canepa, U. Kaipa, K. Tan, K. Roodenko, S. Tekarli, J. Halbert, I. W. Oswald, R. K. Arvapally, C. Yang, T. Thonhauser, M. A. Omary, Y. J. Chabal, *J. Am. Chem. Soc.* **2013**, *135*(34), 12615–12626.

[166] K. M. Hunter, J. C. Wagner, M. Kalaj, S. M. Cohen, W. Xiong, F. Paesani, *J. Phys. Chem. C* **2021**, *125*(22), 12451–12460.

[167] J. C. Wagner, K. M. Hunter, F. Paesani, W. Xiong, *J. Am. Chem. Soc.* **2021**, *143*(50), 21189–21194.

[168] H. Zhang, R. Q. Snurr, *J. Phys. Chem. C* **2017**, *121*(43), 24000–24010.

[169] J. B. Brubach, A. Mermet, A. Filabozzi, A. Gerschel, P. Roy, *J. Chem. Phys.* **2005**, *122*(18), 184509.

[170] H. MacDonald, B. Bedwell, E. Gulari, *Langmuir* **1986**, *2*(6), 704–708.

[171] G. Onori, A. Santucci, *J. Phys. Chem.* **1993**, *97*(20), 5430–5434.

[172] A. W. Knight, N. G. Kalugin, E. Coker, A. G. Ilgen, *Sci. Rep.* **2019**, *9*(1), 8246.

[173] C. Zhang, R. Z. Khaliullin, D. Bovi, L. Guidoni, T. D. Kühne, *J. Phys. Chem. Lett.* **2013**, *4*(19), 3245–3250.

[174] C. Zhang, L. Guidoni, T. D. Kühne, *J. Mol. Liq.* **2015**, *205*, 42–45.

APPENDIX

Comprehensive Tables

Table A.1: Metal-organic frameworks discussed in this thesis and their respective full names and incorporated metal cations.

Framework	Full name	Metal centers
CPO-27 or MOF-74	CPO = coordination polymer of Oslo MOF = metal-organic framework	Cd^{2+}, Co^{2+}, Cu^{2+}, Fe^{2+}, Mg^{2+}, Mn^{2+}, Ni^{2+}, Zn^{2+}
FMOF-1	FMOF = fluorinated MOF	Ag^{+}
MIL-101	MIL = Matériaux de l'Institut Lavoisier	Cr^{3+}
UiO-66	UiO = Universitetet i Oslo	Zr^{4+}
DUT-52	DUT = Dresden University of Technology	Zr^{4+}
UiO-67	UiO = Universitetet i Oslo	Zr^{4+}
ZIF-67	ZIF = zeolitic imidazolate framework	Zn^{2+}

Table A.2: Organic linker molecules mentioned in this thesis, referring to their commonly known abbreviations, full names and molecular structures.

Abbreviation	Full name	Molecular structure
dhtp/dobdc	2,5-dioxidoterephthalate	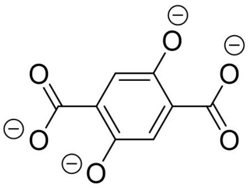
dondc	1,5-dioxidonaphthalene-2,6-dicarboxylate	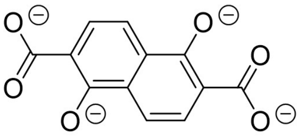
bpp/dobpdc	3,3’-dioxido-[1,1’-biphenyl]-4,4’-dicarboxylate	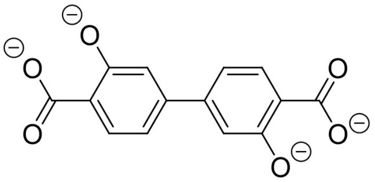
tpp	2’,5’-dimethyl-3,3”-dioxido-[1,1’:4’,1”-terphenyl]-4,4”-dicarboxylate	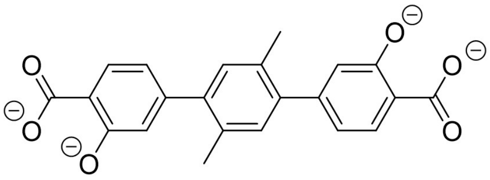
dhip/*m*-dhtp/*m*-dobdc	4,6-dioxidoisophthalate	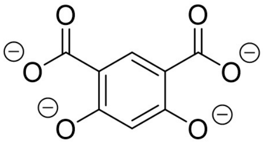
bpm	4,4’-dioxido-[1,1’-biphenyl]-3,3’-dicarboxylate	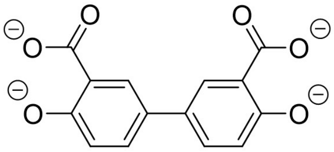

Table A.2: Organic linker molecules mentioned in this thesis, referring to their commonly known abbreviations, full names and molecular structures. (Continued)

Abbreviation	Full name	Molecular structure
bdc	terephthalate	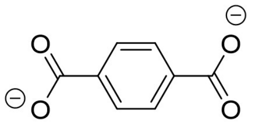
bdc-NH_2	2-aminoterephthalate	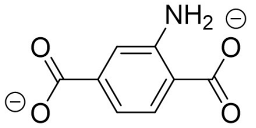
bdc-SO_3H	2-aminoterephthalate	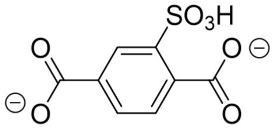
bdc-N	pyridine-2,5-dicarboxylate	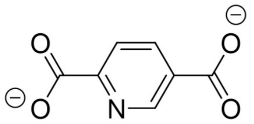
bdc-$(OH)_2$	2,5-dihydroxyterephthalate	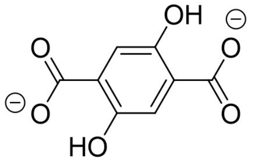
bdc-OH	2-hydroxyterephthalate	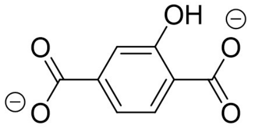
bdc-CH_3	2-methylterephthalate	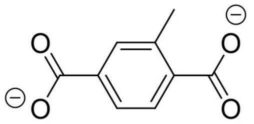
bdc-NO_2	2-nitroterephthalate	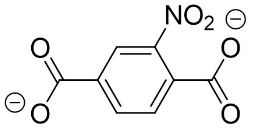
bdc-Cl	2-chloroterephthalate	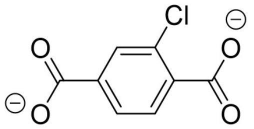

Table A.2: Organic linker molecules mentioned in this thesis, referring to their commonly known abbreviations, full names and molecular structures. (Continued)

Abbreviation	Full name	Molecular structure
bdc-Br	2-bromoterephthalate	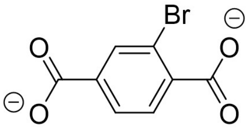
ndc	naphthalene-2,6-dicarboxylate	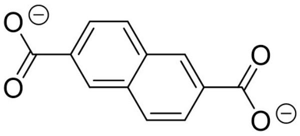
bpdc	[1,1'-biphenyl]-4,4'-dicarboxylate	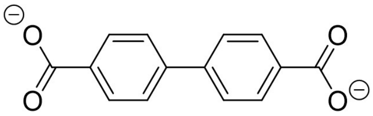
tz	3,5-bis(trifluoromethyl)-1,2,4-triazolate	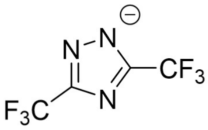
imCa	imidazole-2- carboxaldehyde	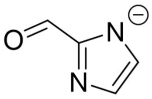

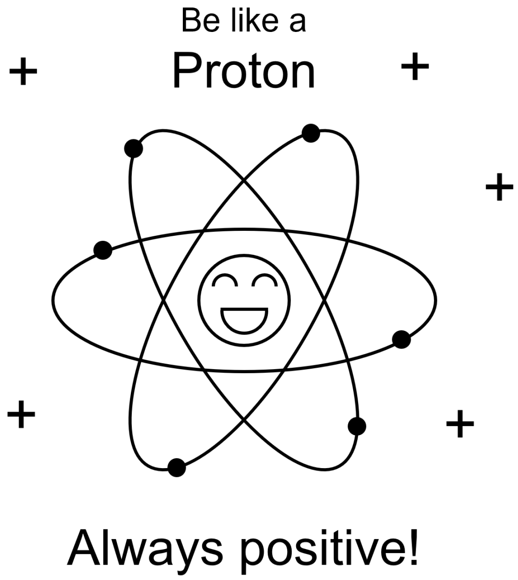
Be like a
Proton
+
+
+
+
+
Always positive!

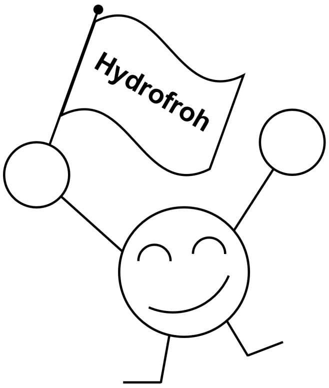
Hydrofroh

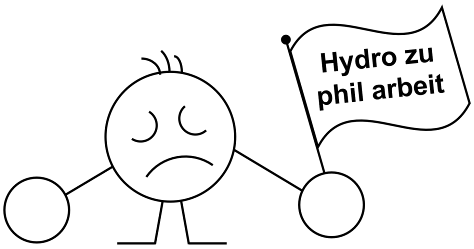
Hydro zu
phil arbeit